

ABSTRACT

JOHNSON, SPENCER JOSEPH. Modulation of Radio Frequency Signals by Nonlinearly Generated Acoustic Fields. (Under the direction of Michael B. Steer and Mohammed A. Zikry.)

Acousto-electromagnetic scattering is a process in which an acoustic excitation is utilized to induce modulation on an electromagnetic (EM) wave. This phenomenon can be exploited in remote sensing and detection schemes whereby target objects are mechanically excited by high powered acoustic waves resulting in unique object characterizations when interrogated with EM signals. Implementation of acousto-EM sensing schemes, however, are limited by a lack of fundamental understanding of the nonlinear interaction between acoustic and EM waves and inefficient simulation methods in the determination of the radiation patterns of higher order scattered acoustic fields. To address the insufficient simulation issue, a computationally efficient mathematical model describing higher order scattered sound fields, particularly of third-order in which a 40x increase in computation speed is achieved, is derived using a multi-Gaussian beam (MGB) expansion that expresses the sound field of any arbitrary axially symmetric beam as a series of Gaussian base functions. The third-order intermodulation (IM3) frequency components are produced by considering the cascaded nonlinear second-order effects when analyzing the interaction between the first- and second-order frequency components during the nonlinear scattering of sound by sound from two noncollinear ultrasonic baffled piston sources. The theory is extended to the modeling of the sound beams generated by parametric transducer arrays, showing that the MGB model can be efficiently used to calculate both the second- and third-order sound fields of the array. Additionally, a near-to-far-field (NTFF) transformation method is developed to model the far-field characteristics of scattered sound fields, extending Kirchhoff's theorem, typically applied to EM waves, determining the far-field patterns of an acoustic source from amplitude and phase measurements made in the near-field by including the higher order sound fields generated by the nonlinear scattering of sound by sound as the acoustic waves propagate into the far-field.

With improvements in the sensitivity of radio frequency (RF) receivers, spectral content previously below the measurable noise floor, such as the nonlinear content produced by acousto-EM scattering, can now be examined and analyzed. Through the use of a high dynamic range nonlinear measurement system based on analog cancellation, the ability to experimentally investigate the effects of nonlinear interaction between acoustic and EM waves previously unattainable is enabled. To further the understanding of the effects of acousto-EM scattering and verify experimental results, a mathematical description of the periodic change in the medium characteristics due to the propagation of a high powered acoustic wave through a medium that modulates an EM signal proportional to the acoustic frequency is developed.

© Copyright 2014 by Spencer Joseph Johnson

All Rights Reserved

Modulation of Radio Frequency Signals by Nonlinearly Generated Acoustic Fields

by
Spencer Joseph Johnson

A dissertation submitted to the Graduate Faculty of
North Carolina State University
in partial fulfillment of the
requirements for the Degree of
Doctor of Philosophy

Electrical Engineering

Raleigh, North Carolina

2014

APPROVED BY:

Michael B. Steer
Co-chair of Advisory Committee

Mohammed A. Zikry
Co-chair of Advisory Committee

Griff L. Bilbro

H. Joel Trussell

Richard Keltie

DEDICATION

To my beautiful and supportive fiancée, Salma.

BIOGRAPHY

Spencer Joseph Johnson was born in Spotsylvania, Virginia in 1987. He attended North Carolina State University on the Park Scholarship for his undergraduate studies, where he received a Bachelor of Science degree in Electrical Engineering with a minor in Business Administration in 2009. He continued his studies at North Carolina State University, earning a Master of Science degree in Electrical Engineering in 2011. He began work towards his Ph.D. degree as a research assistant for the Electronics Research Laboratory at North Carolina State University in 2010 under the direction of Lampe Distinguished Professor of Electrical Engineering, Dr. Michael Steer.

His research interests include nonlinear acoustic modeling, high powered acoustics, electromagnetics, RF system design, and nonlinear RF effects. After graduation, he will join the Massachusetts Institute of Technology Lincoln Laboratory located in Lexington, Massachusetts.

ACKNOWLEDGEMENTS

I would like to thank my graduate advisor, Dr. Michael Steer, for providing guidance and assistance throughout my time in the Ph.D. program at North Carolina State University. His experience and insight throughout the course of my research were invaluable in defining the scope of my work and in the development of the quality journal publications that followed. I would also like to thank the members of my advisory committee, Drs. Mohammed Zikry, Griff Bilbro, Joel Trussell, and Richard Keltie, for the numerous discussions and feedback that helped to shape my research. I would also like to thank Dr. Ginger Yu for her mentorship and the countless conversations that helped to guide me throughout my graduate school experience.

In addition, I would like to thank my colleagues while at North Carolina State University, Drs. Josh Wetherington, Peter Gadfort, Glen Garner, Robert Harris, and Harun Demircioglu, for their technical expertise, stimulating conversation, and camaraderie during our time as graduate students, as well as Carter Harris and Joseph Betthauser whose work as undergraduate assistants was immensely valuable.

I would also like to thank Dr. Sergey Leble from the Gdańsk University of Technology for his insights into numerical simulation techniques when dealing with highly oscillatory functions and Dr. Jarle Berntsen from the University of Bergen for generously sharing his numerical approaches and published code for solving the nonlinear KZK parabolic wave equation.

Lastly, I would like to thank my family and friends who have supported me through the years and given me the courage to pursue and achieve goals I never imagined.

This work was funded by the U.S. Office of Naval Research as part of a Multi-disciplinary University Research Initiative on Sound and Electromagnetic Interacting Waves under grant number N00014-10-1-0958.

TABLE OF CONTENTS

LIST OF TABLES	vii
LIST OF FIGURES	viii
Chapter 1 Introduction	1
1.1 Overview	1
1.2 Motivation	4
1.3 Original Contributions	5
1.3.1 Efficient Modeling of Third-Order Scattering of Sound by Sound	5
1.3.2 Scattered Acoustic Field Modeling using Near-to-Far-Field Transformations	5
1.3.3 Advancements in the Design of Third-Order Parametric Arrays	6
1.3.4 Effects of High Powered Acoustic Excitation on Electromagnetic Scattering	6
1.4 Dissertation Outline	6
1.5 Authored Works	8
1.5.1 Journal Articles	8
1.5.2 Patents	8
Chapter 2 Literature and Concepts Review	9
2.1 Introduction	9
2.2 Nonlinear Acoustics Theory	10
2.2.1 Acoustic Source Modeling	15
2.2.2 The Scattering of Sound by Sound and the Parametric Array	23
2.3 Computation of the Equations of Nonlinear Acoustics	32
2.3.1 Direct Numerical Evaluation of the KZK Equation	32
2.3.2 Calculation of Multidimensional Integrals	33
2.4 Acousto-Electromagnetic Scattering	36
2.4.1 Doppler Theory	37
2.4.2 Amplitude Modulation	39
2.5 High Dynamic Range Nonlinear Measurement	43
2.5.1 Analog Cancellation	44
2.6 Summary	46
Chapter 3 Computationally Efficient Modeling of Third-Order Scattering of Sound by Sound	48
3.1 Introduction	48
3.2 Third-Order Quasilinear Solution	50
3.3 Gaussian Beam Expansion	54
3.3.1 Application to Parametric Transducer Arrays	57
3.4 Sound Field Measurement	58
3.4.1 Measurement Equipment	59
3.4.2 Single Uniform Planar Piston	59
3.4.3 Parametric Transducer Array	62
3.5 Comparison of Computation Methods	64

3.6	Third-Order Parametric Array Design Enhancements	66
3.6.1	Relationship of Transmitted Signals	66
3.6.2	Modulation Schemes	67
3.6.3	System Architecture	68
3.7	Summary	70
Chapter 4 Determination of Nonlinearly Generated Scattered Acoustic Fields using a Near-to-Far-Field Transformation Method		71
4.1	Introduction	71
4.2	Transformation Development for Acoustic Fields	74
4.3	Measurement with High Powered Acoustic Sources	78
4.3.1	Near-Field Measurement Architecture	79
4.3.2	NTFF Transformation for a Single Uniform Planar Piston	80
4.3.3	NTFF Transformation for a Parametric Transducer Array	84
4.4	Summary	87
Chapter 5 Near-Field Radio Frequency Scattering from Vibrating Structures in an Acoustically-Excited Environment		90
5.1	Introduction	90
5.2	Radio Frequency Scattering from Medium Property Fluctuations due to High Powered Acoustic Sources	92
5.2.1	Comparison with Other Acousto-Electromagnetic Modulation Effects . . .	96
5.3	Vibration Modulation Detection from Stand-off Excitation	99
5.3.1	Measurement Architecture	100
5.3.2	Zero Span Frequency Measurement	101
5.4	Spectral Measurement	102
5.5	Summary	105
Chapter 6 Conclusions		107
6.1	Summary of Research and Original Contributions	107
6.2	Future Research	109
References		112
Appendices		125
Appendix A Gaussian Beam Expansion Coefficient Sets		126
Appendix B LabVIEW Measurement and Automation Code		129
B.1 Acoustic Signal Generation and Measurement Code		129
B.2 Zero Span Frequency Measurement Analog Cancellation Code		130
Appendix C MATLAB Simulation Code		133
C.1 Multi-Gaussian Beam Expansion Code		133
C.2 Near-to-Far-Field Transformation Code		157
C.3 Acousto-Electromagnetic Interaction Code		169

LIST OF TABLES

Table 5.1	Comparison of sideband tone power for various modulation types normalized to the RF carrier. The sideband amplitude is normalized to the primary unmodulated RF signal amplitude.	99
Table A.1	Ten term coefficient set defining an edge supported piston, as given by Wen. .	126
Table A.2	Ten term coefficient set given by Ding using a simplified method of calculation.	127
Table A.3	Fifteen term coefficient set given by Wei and Jun using an optimization method that combines solutions of linear equations with Fourier series expansions.	127
Table A.4	Four term coefficient set given by Cervenka using a heuristic evolutionary algorithm.	127
Table A.5	Twenty-five term coefficient set given by Kim <i>et al.</i> that increased the precision of the expansion for a piston radiator into the near-field.	128
Table A.6	Six term coefficient set defining a rigid piston, as given by Wen.	128

LIST OF FIGURES

Figure 2.1	The normalized pressure amplitudes for the fundamental and second harmonic frequencies generated from a Gaussian source along the normalized radial axis, r/a , at a distance of 150 m from the source.	18
Figure 2.2	Comparison of the on-axis acoustic pressure for the primary frequency using the MGB method with $n = 10, 15$, and 25 as given in [15], [58], and [59], respectively.	22
Figure 2.3	The normalized pressure amplitudes for the fundamental and second harmonic frequencies generated from a circular piston source using the MGB expansion model along the normalized radial axis ξ at a distance of 150 m from the source.	23
Figure 2.4	Normalized pressure amplitudes of the second-order sound field distributions (a) on the acoustic axis of the harmonic, sum, and difference frequencies where $A_i = \pi a^2$ is the area of the source for the i th primary frequency and at various distances from the source for (b) the second harmonic, (c) sum frequency, and (d) difference frequency as described in [16] and [17].	29
Figure 2.5	Frequency spectrum for the interacting primary (f_1 and f_2) and secondary ($2f_2$ and $f_D = f_1 - f_2$) sound fields with the resultant third-order fields ($f_L = (2f_2 - f_1) + (f_2 - f_D)$).	30
Figure 2.6	Frequency spectrum of an RF signal scattered by a vibrating object with modulation sidebands produced by the Doppler effect. The spectrum is centered at the frequency of the transmitted RF signal f_{RF} with modulation sidebands at $f_{\text{RF}} \pm n f_V$	39
Figure 2.7	Feedforward analog cancellation implementation block diagram for use in high dynamic range nonlinear measurement systems.	45
Figure 3.1	Acoustic measurement system used to determine the sound field distributions of the acoustic sources discussed in Sections 3.4.2 and 3.4.3.	60
Figure 3.2	The third-order sound field distribution. The pressure amplitudes of the first three harmonic sound fields (a) on the acoustic axis and (b) normalized at a distance of 6 m from the source as described in [34]. The measured and theoretical pressure amplitude at a distance 2 m from the source for (c) the IM3 upper and (d) the IM3 lower tones.	61
Figure 3.3	The sound field distribution generated by a 19 element parametric array. The measured and theoretical pressure amplitudes of the primary frequencies, (a) $f_1 = 51$ kHz and (b) $f_2 = 49$ kHz. The measured and theoretical pressure amplitudes of (c) the difference and (d) the IM3 lower frequencies.	63
Figure 3.4	The sound field distribution generated by a 81 element parametric array. The measured and theoretical pressure amplitudes of the primary frequencies, (a) $f_1 = 51$ kHz and (b) $f_2 = 49$ kHz. The measured and theoretical pressure amplitudes of (c) the difference frequency and (d) the IM3 lower tone.	64

Figure 3.5	The sound field distribution generated by a 81 element parametric array as a comparison to [39]. The measured and theoretical pressure amplitudes of the primary frequencies (a) $f_1 = 72$ kHz and (c) $f_2 = 70$ kHz that generate (e) the difference frequency at $f_D = f_1 - f_2 = 2$ kHz. Additionally, the measured and theoretical pressure amplitudes of the primary frequencies (b) $f_1 = 70$ kHz, and (d) $f_2 = 36$ kHz that generate (f) the third-order lower frequency at $f_L = 2f_2 - f_1 = 2$ kHz.	65
Figure 3.6	Frequency spectrum for the interacting primary sound fields utilized to produce the third-order parametric array having a finite bandwidth, with a single frequency signal, f_2 , a finite bandwidth signal, f_1 , and the resultant finite bandwidth third-order intermodulation product, f_L	68
Figure 3.7	Block diagram of the third-order parametric array implementation utilizing separate narrowband and broadband amplifiers and transducers as to improve the efficiency of generating the interacting primary sound fields that produce the third-order intermodulation product.	69
Figure 4.1	Geometry of coordinate system used in the NTFF transformation. The near-field points along the closed surface are at an angle α from the x -axis and at a distance a and elevation y from the source. Similarly, the field point is located at $P(R, \psi, \theta)$	79
Figure 4.2	Acoustic measurement system employed to ascertain the near-field data on the surface of a cylinder enclosing the acoustic sources required by the linear and nonlinear NTFF transformations to determine the far-field responses discussed in Sections 4.3.2 and 4.3.3.	80
Figure 4.3	The primary sound field generated from a 22 mm diameter transducer operating at $f = 50$ kHz demonstrating the ability of the linear NTFF transformation, (4.6), to accurately produce the far-field pressure amplitude from near-field data: (a) the measured near-field data obtained at 10λ from the source and (b) a comparison of the normalized far-field pressure amplitude at 150 m obtained using direct calculation and using the linear NTFF transformation of the measured near-field data.	81
Figure 4.4	The pressure amplitudes for the second harmonic: (a) the near-field data at 100λ from the source used in the nonlinear NTFF transformation and (b) a comparison of the normalized far-field pressure amplitudes produced using the nonlinear NTFF transformation and direct computation. The radial distance is the distance from the axis normal to the direction of propagation.	82
Figure 4.5	Sound pressure amplitudes for the second-order sum and difference frequencies: the near-field data at 100λ from the source used in the nonlinear NTFF transformation for (a) the sum frequency and (c) the difference frequency and a comparison of the normalized far-field pressure amplitudes calculated using the nonlinear NTFF transformation of the near-field data found using the implicit backward finite difference method and direct computation for (b) the sum frequency and (d) the difference frequency. The radial distance is the distance from the axis normal to the direction of propagation.	83

Figure 4.6	The primary sound field at 51 kHz for the 19 element parametric transducer array: (a) the near-field data experimentally sampled at 25λ from the source and (b) a comparison of the normalized far-field pressure amplitudes using the linear NTFF transformation of the measured near-field data and direct computation.	85
Figure 4.7	Sound pressure amplitudes for the second-order sum and difference frequencies generated from the 19 element parametric transducer array: the near-field data experimentally sampled at 25λ from the source for (a) the sum frequency and (c) the difference frequency and a comparison of the normalized far-field pressure amplitudes calculated using the nonlinear NTFF transformation of the measured near-field data and direct computation for (b) the sum frequency and (d) the difference frequency.	86
Figure 4.8	The primary sound field for the LRAD parametric transducer array: (a) the near-field data experimentally sampled at 10λ from the source and (b) a comparison of the normalized far-field pressure amplitudes calculated using the linear NTFF transformation and direct computation.	87
Figure 4.9	Sound pressure amplitudes for the second-order sum and difference frequencies generated from the LRAD parametric transducer array: the near-field data experimentally sampled at 10λ from the source for (a) the sum frequency and (c) the difference frequency and a comparison of the normalized far-field pressure amplitudes calculated using the nonlinear NTFF transformation of the measured near-field data and direct computation for (b) the sum frequency and (d) the difference frequency.	88
Figure 5.1	Expected power relative to the RF carrier tone of the first eight normalized modulation sideband tones for an acoustically-induced linearly vibrating plate using $d_V = 0.03\lambda_{\text{RF}}$, $R_0 = 3\lambda_{\text{RF}}$, $\lambda_{\text{RF}} = \frac{1}{3}$ m, and $f_V = 2$ kHz	100
Figure 5.2	Block diagram of the pseudo-transient zero span frequency measurement architecture as an extension of the analog canceller used in the high dynamic range nonlinear measurement system.	101
Figure 5.3	Top view of the experimental setup for the bistatic radar measurement of the vibrating plate acoustically-induced by an LRAD.	103
Figure 5.4	Measured narrowband RF power spectrum showing the modulation of an RF carrier at 915 MHz by an acoustic excitation tone at 2.18 kHz compared to the expected model results, i.e., using (5.23). On this scale, the predicted spectrum consists of the RF carrier at 0 kHz and the modulation tones offset from the carrier at ± 2.18 kHz. Except for noise evident in the measured results, the responses are almost identical.	104
Figure 5.5	Measured response showing the modulation of an RF carrier at 915 MHz by an aluminum annular disc excited at its mechanical resonance of 2.18 kHz in the (a) frequency and (b) time domains. The transient response in (b) was found using a zero span frequency measurement centered around a single modulation sideband.	105

Figure B.1	Front panel of user interface of the high dynamic range nonlinear measurement system with zero span frequency measurement incorporated.	131
Figure B.2	Block diagram of zero span frequency measurement implementation in the measurement system.	132

Chapter 1

Introduction

1.1 Overview

High frequency acoustic signals for remote sensing applications have regained interest in recent years as field simulation techniques have improved and alternatives to common electromagnetic (EM) sensing methods have gained favor for countering limitations in many environments. Typically, remote sensing refers to the use of propagating EM signals to interrogate an object at distance without making direct physical contact in an effort to gather information about that object; however, sensing techniques do not have to be restricted solely to EM radiation as there are a variety of other mechanisms that provide the ability to induce a response by an object at distance, such as acoustics, thereby enabling the acquisition of information. In a process analogous to that found in EM, the interaction of an incident acoustic wave on an object generates a scattered acoustic field that contains information about the scattering object and, since acoustic signals provide an orthogonal sensing modality to the more conventional EM methods, this acoustic interrogation can provide distinctive information about the excited environment not achievable by EM sensing, making it an attractive option for remote sensing applications. Additionally, due to the orthogonal nature of the methods, acoustic interrogation can be combined with common EM sensing to allow for further information to be ascertained within an excited environment through the use of dual remote sensing techniques, referred to as acousto-EM sensing. The implementation of acousto-EM sensing, however, has traditionally been infeasible as the fundamental understanding of the interacting processes have been limited by difficulties in experimentally detecting and verifying the effects of the interacting acoustic and EM waves as well as inadequate modeling capabilities for propagating acoustic fields.

Acousto-EM sensing has been investigated primarily as a potential means of improving buried object detection schemes, whereby the acoustic signals act as an excitation source inducing vibrations on an object that scatter the interrogating EM signal. Early endeavors to

develop an acousto-EM approach for buried object detection employed acoustic transducers and RF antennas that were configured specifically to the testing environment and operated at small distances from the target [1–4], limiting the feasibility of the approach in unknown environments and at stand-off ranges. More recent efforts have focused primarily on theoretical investigations, utilizing high power acoustic sources and vibrational targets chosen for their mathematical tractability rather than practicality [5–11], ignoring any attempt to experimentally verify their results. The theoretical investigations were performed at stand-off ranges but required a high power acoustic source capable of generating plane waves at 150 dB sound pressure level (SPL), where strong acoustic nonlinearities occur during propagation, while simultaneously measuring mechanical vibrational effects on targets that were typically very small and often dominated by the excitation from the source; thus, the investigations become extremely difficult to implement experimentally.

Numerical techniques employed to model interacting EM and acoustic energies also have a unique set of challenges due to the physical properties of the different wave types. The discrepancy in wavelength between EM and acoustic signals can be quite large, requiring simulations to have a considerable time-scale disparity. Additionally, vibrating objects have very small displacements, rarely over 1 mm, necessitating fine mesh sizes to accurately capture the response while under interrogation. Typically, the acoustic effects are accounted for as a time-varying perturbation [5, 7] or boundary condition [10, 11] within the EM domain, however, not as an independent scattering phenomenon.

A major obstacle in the implementation of acousto-EM sensing schemes is the inability to calculate the acoustic field solutions efficiently. Traditional techniques for calculating sound field radiation patterns require substantial computation, particularly in the determination of the higher order scattered sound fields, limiting their use in real-time sensing applications. The scattered sound fields that radiate energy into the harmonics, sum-, difference-, and intermodulation frequencies of the primary interacting signals are produced by the nonlinear interactions of high frequency acoustic signals and the nonlinearity of the medium in which the signals propagate, a phenomenon known as the scattering of sound by sound. These higher order sound signals, generated by the nonlinear scattering, have a narrower beamwidth than that of the primary interacting signals, making them ideal for use in remote sensing and detection applications. To model the nonlinearities required to generate these higher order acoustic signals, the Khokhlov-Zabolotskaya-Kuznetsov (KZK) partial differential equation (PDE) [12, 13] was developed. However, conventional methods used to solve this equation are computationally inefficient and, therefore, efforts to improve the computational efficiency of the sound field calculations have recently emerged. Expansion techniques based upon the idea that sound beams generated from acoustic sources can be expressed as a series of base functions have become the foundation for deriving more computationally efficient sound field solutions. The initial works

used a series of Gaussian-Laguerre [14] and Gaussian [15] base functions to develop numerical models for the primary field of a circular plane baffled transducer. The expansion technique was then extended to the second-order sound fields generated by arbitrary axial-symmetric acoustic sources [16–18], allowing for simple analytic solutions that are computationally more efficient than previous methods that relied on cumbersome numerical techniques such as finite difference methods to yield sound field solutions. However, the expansion technique has been confined solely to the primary and secondary sound fields generated by a single transducer, neglecting higher order fields as well as common acoustic devices such as transducer arrays.

Since the initial work on scattering of sound by sound using two independent acoustic waves [19,20], scattered sound fields have been widely studied for their applications in sound projection [21], acoustic radar [22], and sonar [23], primarily focusing on modeling the radiation of the acoustic fields from a variety of sources. Expressions for the primary, harmonic, and secondary sound fields have been developed in the near- and far-field [24–26] showing the legitimacy of the fully nonlinear wave equation in both regions; but these solutions are valid under very limited constraints, otherwise requiring the solving of volumetric field integrals commonly done using slow numerical simulation techniques. Similar efforts have been applied to analyzing the primary and secondary sound fields generated from parametric radiation [27–36] but emphasis was placed on comparing numerical results obtained with theory and measurements from earlier works and not on computational efficiency.

Considerable effort has been put forth to expand the idea of parametric radiation for practical applications. A variety of mathematical models have been developed that yield solutions for the radiated sound fields, utilizing various techniques to solve the wave equation [31,32,35], accounting for different types of acoustic sources [28,33], and incorporating effects such as spherical spreading of the primary sound beams [37]. Additionally, explorations into the resultant acoustic fields generated from the intersection of two independent sound sources at varying intersection angles [29,30,33,36] as well as from transducer arrays [27,34,38,39] have been significant areas of interest due to their application in detection schemes.

The focus of this work is on improving acoustic field simulation techniques to enable real-time implementation in systems and using these improvements to enhance the understanding of the coupling between acoustic and EM energies during remote sensing. A mathematical model is developed solving the fully nonlinear acoustic wave equation that is computationally efficient and valid for the higher order harmonics and intermodulation frequencies that are primarily ignored in previous literature. In addition, a near-to-far-field (NTFF) transformation technique that is commonly implemented in EM to determine the far-field radiation patterns of antennas is established for radiated acoustic fields in an effort to further improve the computational efficiency of acoustic simulations. These techniques are then exploited to extend acousto-EM sensing methods to stand-off ranges by modeling the response of an object under acoustic

illumination and its effects on a scattered EM wave. To continue the investigation of acousto-EM coupling, analysis is also provided on the physical changes in the medium caused by the propagation of high powered acoustic waves that lead to additional distortion of an EM signal.

1.2 Motivation

Remote sensing and detection schemes have improved in recent years as there have been many advancements in implementation algorithms and receiver performance capabilities; however, complications remain in these systems resulting from the difficulty in distinguishing objects of interest from clutter in the background environment. These problems are further exacerbated as the knowledge and ability to manipulate propagating waves, notably EM waves, have become common, leading to structures intelligently designed to avoid exposure by conventional detection schemes. Therefore, interest has been growing in the development of alternative sensing modalities that can provide unique methods of characterizing unknown objects, particularly at stand off distances.

As a means of developing an alternative sensing technique, the use of acoustic signals to interrogate remote objects has received much research attention as it is an orthogonal modality to EM sensing. Traditional acoustic sensing schemes utilizing linear and nonlinear excitation methods suffer from similar difficulties in distinguishing objects of interest from the environment; however, it has been shown that acoustic signals can produce a scattered EM spectrum within an environment by generating vibrations that cause phase modulation on the EM signal. This scattering effect has prompted the development of a hybrid acousto-EM sensing technique, particularly as a potential means of enhancing buried object detection schemes. Although an improvement, current acousto-EM approaches have practicality concerns, as investigations have been either purely theoretical using acoustic power levels not easily produced to analyze objects with the simplest of geometries or experimental conditions unrealistically configured to yield optimal results. Additionally, acousto-EM techniques experience difficulties in determining the acoustic fields as computation methods to ascertain the nonlinear sound field solutions are inefficient.

Experimental investigations utilizing practical sources and target structures that are verifiable by theoretical results in addition to the development of acoustic field solutions that are calculable in real-time can enable a realistic implementation of an acousto-EM sensing technique, thereby achieving an alternative sensing modality with the capability of providing unique object characterization at stand off ranges.

1.3 Original Contributions

During the culmination of this research, a number of original techniques and algorithms were developed in order to accomplish the work described. This section provides a brief summary of those original research contributions by the author to the fields of nonlinear acoustics and remote RF and microwave sensing.

1.3.1 Efficient Modeling of Third-Order Scattering of Sound by Sound

The determination of the radiation patterns of higher order sound fields has been of great interest in nonlinear acoustics; however, the computational effort required to calculate these field solutions remains quite high. Without making simplifying approximations, the analytical solutions for these fields are typically in the form of PDEs or multi-variable field integrals, thereby necessitating the use of numerical computation methods that are often difficult to compute and time intensive. One method of alleviating these computation issues is to determine a mathematical representation for the acoustic source that enables the higher order PDEs and field integrals to be simplified analytically. Following this approach, a mathematical model is developed in Chapter 3 to describe the third-order sound field, generated through the physical process known as scattering of sound by sound, by defining the acoustic source as a superposition of Gaussian functions and, thus, enabling a simplified solution for the third-order sound field to be derived.

1.3.2 Scattered Acoustic Field Modeling using Near-to-Far-Field Transformations

The issue of slow computation time is further exacerbated when the acoustic waves radiate into the far-field, requiring mesh grids that are extremely fine to account for the hundreds of acoustic wavelengths to be computed in the determination of the field patterns. This problem is not unique to acoustics, however, as the modeling of EM propagation and antenna radiation patterns suffer from similar situations. In EM, a common method of handling these simulation concerns is to implement a NTFF transformation technique whereby the field pattern in the near-field is extrapolated to determine the equivalent far-field radiation characteristics. Applying this concept in an attempt to mitigate large computation efforts, a NTFF transformation method is developed in Chapter 4 to determine the acoustic far-field radiation patterns for the higher order scattered fields using known near-field data. Implementation of this technique, along with the improved efficiency gained by simplifying the third-order sound field solution, allows for a much more computationally efficient means of determining the higher order scattered fields radiated from an acoustic source.

1.3.3 Advancements in the Design of Third-Order Parametric Arrays

The second-order parametric array has become a useful and common acoustic source for generating highly directional sound signals, as much research effort has been put into understanding the second-order nonlinear interaction between two ultrasonic signals. However, the third-order parametric array has garnered much less attention despite the advantages gained in signal directivity from this alternate array configuration. By investigating the implementation of the fundamental components comprising the array, a design for the third-order parametric array is developed in Chapter 3 with improvements in the overall efficiency of the system. The design considers the frequency location and relative power of the ultrasonic signals, implemented modulation schemes, and architecture of the electrical system used in the generation of the acoustic signals.

1.3.4 Effects of High Powered Acoustic Excitation on Electromagnetic Scattering

Scattering of EM signals within an acoustically-excited environment with vibrating objects has traditionally been attributed to phase modulation associated with the Doppler effect. Recent advancements in receiver capabilities have prompted a reevaluation of the fundamental physical mechanisms related to the scattering of an EM signal from a vibrating object, however, the effects of the acoustic wave on the propagation medium have been ignored. When the vibrating objects are acoustically-induced at stand-off ranges, particularly for high powered acoustic signals, the propagating wave can cause considerable time-harmonic changes in the medium that can lead to modulation of the EM signal comparable to those generated by the vibrations. By analyzing the fluctuations in the medium over time, an analytical model is developed in Chapter 5 that describes the modulation on a scattered EM signal propagating in an acoustically-excited environment. Additionally, in order to measure the modulations due to the time-harmonic fluctuations, transient capabilities were developed for the high dynamic range measurement system by incorporating a zero-span frequency measurement into the architecture of the analog canceller.

1.4 Dissertation Outline

Chapter 2 of this dissertation presents a literature review of the theory of nonlinear acoustics and the approaches utilized in generating solutions to the nonlinear wave equations. It discusses the development of the second-order parametric array and the scattering of sound by sound through the radiation of acoustic signals generated by a single transducer as well as a multi-element transducer array. Additionally, a discussion on acousto-electromagnetic interac-

tion theory is given, outlining the various physical mechanisms in which a vibrating object can produce modulation on a scattered RF wave. A brief description of the high dynamic range measurement system used to generate the acousto-electromagnetic measurements is also provided.

Chapter 3 develops an approach for determining the third-order scattered acoustic fields that is computationally more efficient than previously implemented methods. It begins by deriving the third-order quasilinear solution of the fully nonlinear KZK parabolic wave equation that is used to develop a solution for the third-order scattered sound fields by expressing the acoustic source as a superposition of Gaussian functions. By defining the source in this manner, mathematical simplifications for the third-order fields are made that lead to improvements in computation time. With the ability to produce simplified solutions for the scattered acoustic fields, the mathematical model is then utilized to determine the radiation patterns generated by parametric transducer arrays. The simulation results given by the model are compared with sound field measurements and previously presented results showing that the model is computationally more efficient than previous methods while accurately representing the sound fields. The advancement of the design of the third-order parametric array is also detailed, improving the overall efficiency of the system by optimizing the relationship between the transmitted signals as well as the architecture of the system.

Chapter 4 continues the development of efficient computation of scattered sound fields by implementing a NTFF transformation method that uses known sound field data in the near-field to determine the far-field radiation characteristics. The mathematical model extends Kirchhoff's Theorem from the linear solution valid for only the primary acoustic fields to the higher order scattered fields by deriving a comparable solution from the KZK nonlinear wave equation. The method provides a significant increase in efficiency since it utilizes near-field data that can be computed relatively easily or provided prior to far-field calculation. Measurements are made of the second-order scattered sound fields generated from a single transducer as well as a multi-element transducer array and compared to the results provided from the NTFF transformation method illustrating that the model produces accurate sound field radiation patterns.

Chapter 5 explores the effect of a high powered acoustic signal on the medium in which it propagates and the modulation on a scattered RF signal directly related to this medium fluctuation. The analysis begins by establishing a relationship between the periodic pressure changes in the medium and the propagating acoustic wave then introduces that time-dependent fluctuation into Maxwell's equations, deriving an EM wave equation that defines a propagating signal in the sound perturbed medium. The resultant solution includes spectral components corresponding to the propagating acoustic frequency that are interpreted as acoustic modulation of the EM signal. Those components are then compared to other known phase and amplitude modulations that have been investigated in an acoustically-excited environment with vibrating

objects to determine the relative importance of this effect when detecting modulation due to the presence of an acoustic transmission. The additional capability of transient measurement using the high dynamic range measurement system is also described, implementing a zero-span frequency measurement and using the recorded I/Q data of the system to capture the measured power over time. Spectral and transient measurements are then taken to correlate the acoustic excitation with the observed modulations on the scattered EM signal.

Chapter 6 concludes with a summary of the presented research and a discussion of potential future work to continue the advancement of research in this area.

1.5 Authored Works

1.5.1 Journal Articles

S. J. Johnson and M. B. Steer, “An Efficient Approach to Computing Third-Order Scattering of Sound by Sound with Application to Parametric Arrays,” *IEEE Trans. Ultrason., Ferroelectr., Freq. Control*, accepted for publication.

S. J. Johnson and M. B. Steer, “A Near-to-Far-Field Transformation Method for the Determination of Nonlinearly Generated Scattered Acoustic Fields,” submitted to *IEEE Trans. Ultrason., Ferroelectr., Freq. Control*.

S. J. Johnson, J. M. Wetherington, and M. B. Steer, “Near-Field Radio Frequency Scattering from Acoustically-Excited Vibrating Structures,” submitted to *IEEE Trans. Antennas Propag.*

1.5.2 Patents

M. B. Steer and S. J. Johnson. 2014. High-Order Parametric Sound System. US Provisional Patent Application No. 62/005,477, filed May 30, 2014.

Chapter 2

Literature and Concepts Review

2.1 Introduction

Remote sensing using acousto-EM scattering is an appealing alternative to conventional sensing methods as the use of two orthogonal modalities enables the acquisition of information not attainable through the use of sensing schemes employing only a single modality. Implementation of the acousto-EM sensing schemes is hindered, however, by inadequate modeling capabilities for the radiation of scattered acoustic fields and ability to experimentally verify the effects of the nonlinear interaction between the acoustic and EM waves at stand off distances. To provide a foundation from which the development of the solutions to improve these shortcomings and facilitate practical application of acousto-EM sensing methods are built, the fundamentals of nonlinear acoustics and the effects of incident acoustic signals on objects are presented along with a discussion of the current theoretical development of acousto-EM scattering as it pertains to remote sensing.

Section 2.2 establishes the nonlinear acoustic wave equation for plane waves and sound beams beginning with the general motion of a fluid and building to the KZK parabolic wave equation. Mathematical models are then developed that solve the nonlinear acoustic wave equation and define the sound fields emitted from several types of acoustic sources. With models describing a single sound field generated by a single source, the concept of scattering of sound by sound where multiple sound fields exist in a single environment is discussed. Section 2.3 then reviews a variety of methods currently utilized to compute the equations of nonlinear acoustics. Section 2.4 provides background for the current state of the theoretical and experimental development of acousto-EM scattering theory. A brief discussion is given on Doppler theory and the different modulation effects that contribute to the resultant distortion of an EM signal in an acoustically-excited environment. Prior research studying the use of acousto-EM scattering in detection schemes is also examined. Section 2.5 discusses the development of a high dynamic

range measurement system created using analog cancellation that will be employed in the measurement of the EM modulation induced by acousto-EM scattering. Section 2.6 summarizes the key concepts of this chapter to be used in the development of the original contributions in Chapters 3, 4, and 5.

2.2 Nonlinear Acoustics Theory

Acoustic waves are interpreted as fluid particles in motion, therefore it is necessary to establish a description of the fundamental movement of a fluid in a medium to facilitate the development of the equations of nonlinear acoustics. The general motion of a fluid can be defined by the conservation laws of fluid dynamics (for mass, momentum, and energy) along with the thermodynamic equation of state [40]. Beginning with these equations for fluid motion, the nonlinear wave equation for acoustic propagation in a fluid can be derived, following a similar method as provided by Hamilton [41].

The conservation of mass in a fluid volume yields the acoustic equation of continuity, given by

$$\frac{D\rho}{Dt} + \nabla \cdot (\rho u) = 0, \quad (2.1)$$

where ρ is the mass density, u is the fluid particle velocity, ∇ is the material time derivative, and $D/Dt = \partial/\partial t + u \cdot \nabla$. Similarly, from the conservation of momentum, the momentum equation is

$$\rho \frac{Du}{Dt} + \nabla P = \mu \nabla^2 u + (\mu_B + \frac{1}{3}\mu) \nabla(\nabla \cdot u), \quad (2.2)$$

where P is the thermodynamic pressure, μ is the shear viscosity considering the momentum diffusion between adjacent fluid particles, and μ_B is the bulk viscosity describing the variations between the local and thermodynamic pressures. Equation (2.2) is valid when the relaxation times in the system are shorter than the acoustic time scale. Under these conditions, the conservation of energy produces the entropy equation, expressed as

$$\rho T \frac{Ds}{Dt} = \kappa \nabla^2 T + \mu_B (\nabla \cdot u)^2 + \frac{1}{2} \mu \left(\frac{\partial u_i}{\partial x_j} + \frac{\partial u_j}{\partial x_i} - \frac{1}{2} \delta_{ij} \frac{\partial u_k}{\partial x_k} \right)^2, \quad (2.3)$$

where T is the absolute temperature, s is the specific entropy per unit mass, κ is the thermal conductivity, and δ_{ij} is the Kronecker delta equal to unity for $i = j$ and zero otherwise where the final term in (2.3) is written in Cartesian tensor notation so that u_i indicates the fluid particle velocity in the direction x_i . With expressions for the laws of conservation, the final expression required to develop the equations of nonlinear acoustics is the thermodynamic equation of state:

$$P = P(\rho, s). \quad (2.4)$$

To simplify the analysis, a plane wave in a lossless fluid is considered where the sound of speed, c_a , is defined as

$$c_a^2 = \left(\frac{\partial P}{\partial \rho} \right)_s. \quad (2.5)$$

By assuming the condition of a lossless fluid, the shear and bulk viscosities along with the thermal conductivity become zero, indicating that the fluid is uniform with specific entropy equivalent to its ambient state, s_0 , and the thermodynamic equation of state in (2.4) simplifies to $P = P(\rho)$. A common form of the thermodynamic equation of state is that for a perfect gas, found using the ideal gas law [42], and, using (2.5), can be expressed in a lossless fluid as

$$\frac{P}{P_0} = \left(\frac{\rho}{\rho_0} \right)^\gamma \exp \left(\frac{s - s_0}{c_v} \right) = \left(\frac{c_a}{c_0} \right)^{2\gamma/(\gamma-1)}, \quad (2.6)$$

where P_0 and ρ_0 are the ambient pressure and density reference values, respectively, c_0 is the small-signal sound speed, c_p and c_v are the specific heats at constant pressure and constant volume, and $\gamma = c_p/c_v$ is the ratio of the specific heats. Additionally, for a perfect gas, (2.5) reduces to $c_a^2 = \gamma P/\rho$. Thus, (2.1), (2.2), (2.3), and (2.6) describe the conservation laws of fluid dynamics and the thermodynamic equation of state for a plane wave in a lossless fluid.

Extending the discussion to include nonplanar waves, also in a lossless fluid, (2.1) and (2.2) can be expressed in terms of velocity potential, ϕ , with $u = \nabla \phi$ and $Ds/Dt = 0$ (since the viscosities and thermal conductivity are zero), as

$$\frac{\partial \rho}{\partial t} + \nabla \rho \cdot \nabla \phi + \rho \nabla^2 \phi = 0, \quad (2.7)$$

$$\nabla \left(\frac{\partial \phi}{\partial t} + \frac{1}{2} |\nabla \phi|^2 \right) + \frac{\nabla P}{\rho} = 0, \quad (2.8)$$

where $|\nabla \phi|^2 = \nabla \phi \cdot \nabla \phi$ and $\nabla P = \rho \nabla q$, found with the relation

$$q = \int_{P_0}^P \frac{dP}{\rho} = \int_{\rho_0}^\rho \frac{c_a^2}{\rho} d\rho = \frac{c_a^2 - c_0^2}{\gamma - 1}, \quad (2.9)$$

where the integrals are solved for a perfect gas along $s = s_0$. Integrating (2.8) with respect to the spatial coordinates, the momentum equation simplifies to

$$\frac{\partial \phi}{\partial t} + \frac{1}{2} |\nabla \phi|^2 + q = 0. \quad (2.10)$$

Substituting the solution for a perfect gas in (2.9) into (2.10), the speed of sound becomes

$$c_a^2 = c_0^2 - (\gamma - 1) \left(\frac{\partial \phi}{\partial t} + \frac{1}{2} |\nabla \phi|^2 \right), \quad (2.11)$$

which enables (2.7) to be rewritten as

$$\frac{\partial c_a^2}{\partial t} + \nabla c_a^2 \cdot \nabla \phi + (\gamma - 1)c_a^2 \nabla^2 \phi = 0. \quad (2.12)$$

Finally, substituting (2.11) into (2.12), the wave equation expressed in terms of the velocity potential is

$$c_0^2 \nabla^2 \phi - \frac{\partial^2 \phi}{\partial t^2} = \left(2\nabla \frac{\partial \phi}{\partial t} + \frac{1}{2} |\nabla \phi|^2 \right) \cdot \nabla \phi + (\gamma - 1) \left(\frac{\partial \phi}{\partial t} + \frac{1}{2} |\nabla \phi|^2 \right) \nabla^2 \phi. \quad (2.13)$$

This is the exact solution describing the propagation of a wave for a lossless perfect gas.

To this point, the development of the wave equation has solely considered a lossless fluid, however, for practical application, attention needs to be given to the nonlinear acoustic propagation of a wave in a dissipative fluid. In this fluid, the dissipation losses introduced are primarily due to thermoviscous effects caused by the medium in which the wave propagates: thermal losses from increased particle velocity resulting in heat generation and viscous losses from resistance by the medium due to shear and compressive stress. When these effects are included, exact analytical solutions for the wave equation are unobtainable, thus approximations are required to develop model equations that describe nonlinear acoustic propagation. A common approximation method is to utilize perturbation techniques as a means of deriving an analytical solution, whereby small disturbances from equilibrium are introduced into the variables of the linearized equations for the laws of conservation and equation of state (i.e., $p = P - P_0$, $\rho' = \rho - \rho_0$, $s' = s - s_0$, and $T = T - T_0$).

Beginning again with the conservation of mass and including the perturbed medium density ρ' into (2.1), the continuity equation remains exact for higher-order approximations and can be expressed as

$$\frac{\partial \rho'}{\partial t} + \rho_0 \nabla \cdot u = -\rho' \nabla \cdot u - u \cdot \nabla \rho'. \quad (2.14)$$

Similarly, for the conservation of momentum, incorporating the pressure perturbation p into (2.2), discarding terms higher than second-order, and rearranging terms, the second-order momentum equation can be written as

$$\rho_0 \frac{\partial u}{\partial t} + \nabla p = (\mu_B + \frac{4}{3}\mu) \nabla^2 u - \frac{1}{2} \rho_0 \nabla u^2 - \rho' \frac{\partial u}{\partial t}. \quad (2.15)$$

Examining the entropy equation, it can be seen from the terms on the right hand side of (2.3) that the entropy perturbations s' are of second-order and that the amplitude of the viscosity

terms are much less than that of the thermal conductivity. Therefore, (2.3) simplifies to

$$\rho_0 T_0 \frac{\partial s'}{\partial t} = \kappa \nabla^2 T'. \quad (2.16)$$

Finally, to determine the second-order equation of state, (2.4) is expanded using a Taylor series evaluated about the equilibrium point (ρ_0, s_0) so that

$$P - P_0 = \left(\frac{\partial P}{\partial \rho} \right)_{s,0} (\rho - \rho_0) + \frac{1}{2} \left(\frac{\partial^2 P}{\partial \rho^2} \right)_{s,0} (\rho - \rho_0)^2 + \dots, \quad (2.17)$$

which can be expressed using the perturbed states as

$$p = A \left(\frac{\rho'}{\rho_0} \right) + \frac{B}{2} \left(\frac{\rho'}{\rho_0} \right)^2 + \frac{C}{3} \left(\frac{\rho'}{\rho_0} \right)^3 + \dots, \quad (2.18)$$

where

$$A = \rho_0 \left(\frac{\partial P}{\partial \rho} \right)_{s,0} = \rho_0 c_0^2, \quad B = \rho_0^2 \left(\frac{\partial^2 P}{\partial \rho^2} \right)_{s,0}, \quad C = \rho_0^3 \left(\frac{\partial^3 P}{\partial \rho^3} \right)_{s,0}. \quad (2.19)$$

Rearranging terms and ignoring terms higher than second-order, the equation of state can be written in the more common form of

$$p = c_0^2 \rho' + \frac{c_0^2}{\rho_0} \frac{B}{2A} \rho'^2 + \left(\frac{\partial P}{\partial s} \right)_{\rho,0} s'. \quad (2.20)$$

Here, the term B/A describes the nonlinearity of the medium [43]. Thus, (2.14), (2.15), (2.16), and (2.20) define the second-order equations of motion and equation of state for an acoustic wave in a thermoviscous fluid.

Through the manipulation of the second-order solutions found for the laws of conservation and thermodynamic equation of state, the nonlinear second-order wave equation can be derived. To enable this development, a cascaded approach is used whereby first-order terms can be substituted into second-order terms since the resulting error terms will be of third-order and, therefore, can be discarded. The second-order continuity (2.14) and momentum (2.15) equations can then be written [24]

$$\frac{\partial \rho'}{\partial t} + \rho_0 \nabla \cdot u = \frac{1}{\rho_0 c_0^4} \frac{\partial p^2}{\partial t} + \frac{1}{c_0^2} \frac{\partial \mathcal{L}}{\partial t}, \quad (2.21)$$

$$\rho_0 \frac{\partial u}{\partial t} + \nabla p = - \frac{1}{\rho_0 c_0^2} (\mu_B + \frac{4}{3}\mu) \nabla \frac{\partial p}{\partial t} - \nabla \mathcal{L}, \quad (2.22)$$

where $\mathcal{L} = \frac{1}{2} \rho_0 u^2 - p^2 / 2 \rho_0 c_0^2$ is the second-order Lagrangian density. (2.16) and (2.20) can then

be combined using the thermodynamic relations

$$\left(\frac{\partial P}{\partial s}\right)_\rho = \rho^2 \left(\frac{\partial T}{\partial \rho}\right)_s, \quad \left(\frac{\partial T}{\partial \rho}\right)_s = \frac{RTc^2}{c_v c_p \rho^2}, \quad (2.23)$$

to obtain

$$\rho' = \frac{p}{c_0^2} - \frac{1}{\rho_0 c_0^4} \frac{B}{2A} p^2 - \frac{\kappa}{\rho_0 c_0^4} \left(\frac{1}{c_v} - \frac{1}{c_p}\right) \frac{\partial p}{\partial t}. \quad (2.24)$$

By taking the divergence of (2.22) and subtracting the time derivative of (2.21) then using (2.24) to replace ρ' , the second-order wave equation is found [24],

$$\square^2 p + \frac{\delta}{c_0^4} \frac{\partial^3 p}{\partial t^3} = -\frac{\beta}{\rho_0 c_0^4} \frac{\partial^2 p^2}{\partial t^2} - \left(\nabla^2 + \frac{1}{c_0^2} \frac{\partial^2}{\partial t^2}\right) \mathcal{L}. \quad (2.25)$$

where $\square^2 = \nabla^2 - c_0^2(\partial^2/\partial t^2)$ is the d'Alembertian operator, $\beta = 1 + B/2A$ is the coefficient of nonlinearity, and δ is the diffusivity of sound [44]

$$\delta = v \left(\frac{4}{3} + \frac{\mu_B}{\mu} + \frac{\gamma - 1}{\text{Pr}}\right), \quad (2.26)$$

where $v = \mu/\rho_0$ is the kinematic viscosity.

From (2.25), the Westervelt equation can be established by eliminating the final term containing the Lagrangian density, \mathcal{L} , yielding [45]

$$\square^2 p + \frac{\delta}{c_0^4} \frac{\partial^3 p}{\partial t^3} = -\frac{\beta}{\rho_0 c_0^4} \frac{\partial^2 p^2}{\partial t^2}. \quad (2.27)$$

This approximation of the full second-order wave equation in (2.25) remains valid for progressive plane waves, where $\mathcal{L} = 0$, and when the nonlinear effects that accumulate from propagation can be considered much more significant than local nonlinear effects. The latter condition is true when the distance from the source is much greater than a wavelength, thus, local nonlinear effects can generally be ignored when considering quasi-plane waves, such as directional sound beams, for distances greater than a few wavelength from the source. Local nonlinear effects, however, become increasingly important when examining standing waves and the scattering of sound by sound (discussed in Section 2.2.2).

The most commonly used model describing the propagation of second-order sound waves while accounting for the medium nonlinearity and dissipation is the Burger's equation. This is derived from the one-dimensional form of the Westervelt equation (2.27),

$$\left(\frac{\partial^2}{\partial x^2} - \frac{1}{c_0^2} \frac{\partial^2}{\partial t^2}\right) p + \frac{\delta}{c_0^4} \frac{\partial^3 p}{\partial t^3} = -\frac{\beta}{\rho_0 c_0^4} \frac{\partial^2 p^2}{\partial t^2}, \quad (2.28)$$

whereby a slow scale is introduced corresponding to the retarded time τ and, through manipulation of the partial derivatives, the Burger's equation is found [46, 47],

$$\frac{\partial p}{\partial x} - \frac{\delta}{2c_0^3} \frac{\partial^2 p}{\partial \tau^2} = \frac{\beta}{\rho_0 c_0^3} \frac{\partial p^2}{\partial \tau}. \quad (2.29)$$

Thus, (2.29) is a one-dimensional model that accounts for the effects of dissipation and nonlinearity on progressive plane waves.

Expanding Westervelt's equation (2.27) to account for the effect of diffraction in addition to dissipation and nonlinearity, particularly in directional sound beams, the KZK equation is found by introducing a slow scale and manipulating the partial derivatives in a similar manner used to derive the Burger's equation. Defining z to be the direction of propagation with the source having a radius a located at $z = 0$ and operating at a frequency that satisfies the relation $ka \gg 1$ so that beam has reasonable directionality, the KZK equation is [12, 13]

$$\frac{\partial^2 p}{\partial z \partial \tau} - \frac{c_0}{2} \nabla_{\perp}^2 p - \frac{\delta}{2c_0^3} \frac{\partial^3 p}{\partial \tau^3} = \frac{\beta}{2\rho_0 c_0^3} \frac{\partial^2 p^2}{\partial \tau^2}. \quad (2.30)$$

where $\tau = t = z/c_0$ and $\nabla_{\perp}^2 = \partial^2/\partial x^2 + \partial^2/\partial y^2$ is the Laplacian in the plane perpendicular to the propagation of the wave.

2.2.1 Acoustic Source Modeling

The partial differential equations (PDEs) detailed in Section 2.2 describe the nonlinear propagation of an acoustic wave through a medium; however, to model the generation of a sound field from an acoustic source, such as a piston transducer, solutions to these equations need to be found. Restricting the sound pressure field p to the primary sound field p_1 consisting of fundamental frequencies linearly generated by an acoustic source and secondary sound field p_2 consisting of the second harmonic, sum frequency, and difference frequency produced from nonlinear propagation in a medium, solutions to the nonlinear PDEs can be found by assuming a quasilinear approximation for the pressure field,

$$p = p_1 + p_2. \quad (2.31)$$

Under this approximation, the linear summation of the primary and secondary sound fields is valid assuming $p_1 \gg p_2$, indicating that the secondary pressure is a small perturbation of the linear primary sound field. This section will examine the sound fields generated by a single acoustic source transmitting a single tone, thereby further limiting the analysis to the fundamental frequency f and only the second harmonic $2f$ in the secondary sound field. Section 2.2.2 will extend this investigation to incorporate the sum and difference frequencies

of the secondary sound field in addition to the second harmonic by considering multiple tones generated from a single acoustic source as well as an array of sources. Thus, the fundamental and second harmonic pressure fields can be defined as

$$p_n(r, z, \tau) = q_n(r, z, \tau)e^{jn\omega\tau}, \quad (2.32)$$

where $r = \sqrt{x^2 + y^2}$ is the cylindrical coordinate normal to the direction of propagation z and $n = 1$ or 2 for the fundamental and second harmonic frequencies, respectively. For either sound field n , $q_n(r, z, \tau)$ is the complex pressure amplitude, and $n\omega$ is the radian frequency of the pressure field where $\omega = 2\pi f$. By substituting (2.31) and (2.32) into the KZK equation (2.30), the quasilinear equations for the propagation of the fundamental and second harmonic frequencies in a nonlinear, dissipative medium can be written

$$\frac{\partial q_1}{\partial z} + \frac{j}{2k} \nabla_{\perp}^2 q_1 + \alpha_1 q_1 = 0, \quad (2.33)$$

$$\frac{\partial q_2}{\partial z} + \frac{j}{4k} \nabla_{\perp}^2 q_2 + \alpha_2 q_2 = \frac{\beta k}{2\rho_0 c_0^2} q_1^2, \quad (2.34)$$

where $k = \omega/c_0$ is the acoustic wavenumber and $\alpha_n = \delta(n\omega)^2/2c_0^3$ is the thermoviscous attenuation coefficient, however, the attenuation coefficient α_n can be determined through a variety of alternative methods [40, 48–51]. The right hand side of (2.33) and (2.34) represents the acoustic driving mechanism for the generation of the primary and secondary sound fields, respectively. The primary sound field is produced from the physical acoustic source and, therefore, this term is set to zero, whereas the secondary sound field is generated from the nonlinear propagation of the primary sound fields, thus becoming proportional to the square of the primary complex pressure amplitude, q_1^2 .

Solutions can be found for the fundamental and second harmonic frequencies in (2.33) and (2.34) by integrating over the product of the acoustic driving source and the appropriate Green's function, $G_n(r, z | r', z')$. Thus,

$$q_1(r, z) = 2\pi \int_0^\infty q_1(r', 0) G_1(r, z | r', 0) r' dr', \quad (2.35)$$

$$q_2(r, z) = \frac{\pi\beta k}{\rho_0 c_0^2} \int_0^z \int_0^\infty q_1^2(r', z') G_2(r, z | r', z') r' dr' dz', \quad (2.36)$$

where the integration occurs over the surface $dS' = 2\pi r' dr'$ for the primary sound fields since the source is solely located in the $z' = 0$ plane and over the volume $dV' = 2\pi r' dr' dz'$ for the secondary sound fields. The integration of (2.36) over a volume can be interpreted as the second harmonic being generated by an array of virtual sources in that volume, an assumption that is a product of the quasilinear approximation in (2.31). $q_1(r', 0)$ in (2.35) is the source function

for the primary sound field that is determined by type and shape of the source to be modeled (several of the more common source functions will be discussed in greater detail later in this section). Finally, to solve the integral equations in (2.35) and (2.36), the Green's function, defined as an impulse response to an inhomogeneous differential equation, can be ascertained as a solution of

$$\frac{\partial G_n}{\partial z} + \frac{j}{2nk} \nabla_{\perp}^2 G_n + \alpha_n G_n = \frac{1}{2\pi r} \delta(r - r') \delta(z - z'), \quad (2.37)$$

where $\frac{1}{2\pi r} \delta(r - r') \delta(z - z')$ is the three-dimensional Dirac delta function. Following the procedures outlined in [41] and [52] to solve (2.37), the Green's function can be expressed as

$$G_n(r, z | r', z') = \frac{jk}{2\pi(z - z')} J_0 \left(\frac{nkrr'}{z - z'} \right) \exp \left(-\frac{jk(r^2 + r'^2)}{2(z - z')} - \alpha_n(z - z') \right). \quad (2.38)$$

With the Green's function determined, the integral equations in (2.35) and (2.36) provide generic descriptions of the complex pressure amplitudes of the radiated primary and secondary sound fields. To describe the fields radiated from specific types of acoustic sources, the source function $q_1(r, 0)$ must be appropriately defined dependent upon the desired source to be modeled, the most common being Gaussian and circular piston sources, both of which will be analyzed here. The Gaussian source is an often modeled acoustic source because the mathematical description of the source lends itself well to developing closed form solutions for the sound fields under the quasilinear approximation. Therefore, to begin the analysis, the source function will be defined with a simple Gaussian distribution,

$$q_1(r, 0) = p_0 \exp \left(-(r/a)^2 \right), \quad (2.39)$$

where p_0 is the peak pressure from an acoustic source with a radius a . For purposes of normalizing the coordinates to simplify the model equations in later analysis, the radial coordinate of the Gaussian source function is shown divided by the acoustic source radius. This will be done for the axial coordinate z in the upcoming analysis as well where it will be divided by the distance to the limit between the near- and far-fields, $z_0 = \frac{1}{2}ka^2$. Substituting (2.39) into (2.35), the linear solution for the primary sound field of a Gaussian source is found to be

$$q_1(r, z) = \frac{p_0 e^{-\alpha_1 z}}{1 - jz/z_0} \exp \left(-\frac{(r/a)^2}{1 - jz/z_0} \right). \quad (2.40)$$

The solution for the second harmonic can then be found by substituting (2.40) into (2.36)

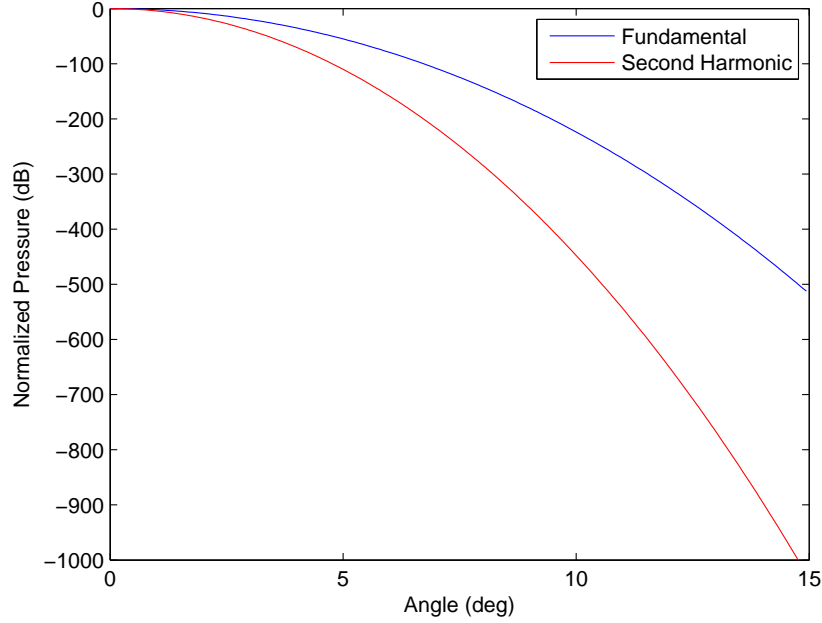


Figure 2.1: The normalized pressure amplitudes for the fundamental and second harmonic frequencies generated from a Gaussian source along the normalized radial axis, r/a , at a distance of 150 m from the source.

yielding [41]

$$q_2(r, z) = \frac{j\beta p_0^2 k^2 a^2}{4\rho_0 c_0^2} \frac{e^{-\alpha_2 z + j(2\alpha_1 - \alpha_2)z_0}}{1 - jz/z_0} \exp\left(-\frac{2(r/a)^2}{1 - jz/z_0}\right) \times \left[E_1(j(2\alpha_1 - \alpha_2)z_0) - E_1(j(2\alpha_1 - \alpha_2)(z_0 - jz))\right] \quad (2.41)$$

where $E_1(x) = \int_x^\infty t^{-1} e^{-t} dt$ is the exponential integral function [53]. Fig. 2.1 depicts the normalized pressure amplitudes for the fundamental and second harmonic frequencies at a distance of 150 m from a Gaussian source and are produced using (2.40) and (2.41), respectively. The parameters used to generate the results were given by [26] and [27]: $\rho_0 = 995.8 \text{ kg/m}^3$, $c_0 = 1497.7 \text{ m/s}$, $\beta = 3.59$, $a = 0.87 \text{ m}$, and $f = 16 \text{ kHz}$. The radial responses in Fig. 2.1 show that the beamwidth of the second harmonic is narrower than the fundamental, which is consistent with the analytic development of the secondary sound fields as $q_2 \propto q_1^2$.

For a circular piston source, the analytic closed form solutions for the primary and secondary sound fields cannot be as easily obtained as with the Gaussian source. To obtain closed form solutions, approximations must be made when solving the field integrals as, typically, they are only attainable for the primary sound fields in (2.35) along the axis of propagation and in the

far-field while only under asymptotic conditions can they be derived for the secondary sound fields in (2.36). As with the Gaussian source, the analysis begins by defining the source function for the circular piston as

$$q_1(r, 0) = p_0 H(a - r), \quad (2.42)$$

where $H(x)$ is the Heaviside step function. Substituting (2.42) into (2.35), the primary sound field for a circular piston source can be expressed [54]

$$q_1(r, z) = p_0 e^{-\alpha_1 z} \left(1 - e^{-jz_0/2} + 2e^{-jz_0/2} \int_0^{rz_0/az} e^{-jz\xi^2/z_0} J_1(2\xi) d\xi \right), \quad (2.43)$$

where $J_1(x)$ is the first-order Bessel function and ξ is the radial component to be integrated. Substituting (2.43) into (2.36), the solution for the secondary sound field will contain a quadruple integral since the field integral along the radial axis cannot be simplified for the primary sound field. Thus, in order to generate the secondary sound fields, direct numerical integration of (2.30) is the most common approach performed to determine the radiation patterns of these fields, discussed in further detail in Section 2.3. Since the radial component r is only present in the integral of (2.43), a simplified solution for the primary sound field can be obtained along the axis of propagation that could lead to a more desirable solution for the secondary sound fields, however, the solution would be restricted to use solely along that axis and have limited practical use. Therefore, to realize a closed form solution for the secondary sound fields of a circular piston, the analysis will be confined to only the far-field asymptotic conditions. Thus, following the derivations in [55] and [26] under the additional assumption that the attenuation of the second harmonic is greater than twice that of the fundamental frequency ($\alpha_2 > 2\alpha_1$), the solution for the second harmonic can be written [41]

$$q_2(\theta, z) = -\frac{\beta p_0^2 k^3 a^4}{8\rho_0 c_0^2 (\alpha_2 - 2\alpha_1)} \frac{e^{-2\alpha_1 z}}{z^2} D_1^2(\theta) \exp(-jkz \tan^2 \theta), \quad (2.44)$$

where

$$D_1(\theta) = \frac{2J_1(ka \tan \theta)}{ka \tan \theta} \quad (2.45)$$

and θ is the cylindrical coordinate denoting the angle off of the axis of propagation z . It is worth pointing out that under these similar conditions, the solution for the second harmonic produced by a Gaussian source (2.41) can be simplified to be identical to (2.44).

To avoid the restrictions imposed when using the closed form solution in (2.44) or having to use direct numerical integration of the KZK equation to determine the second harmonic (as well as the other second-order sound fields) for a circular piston source, much research effort has been put into finding solutions for the secondary sound fields that are valid under a wide range of

conditions. Tjotta and Tjotta [37] considered spherically spreading primary sound beams from collinear sources and developed asymptotic solutions of the generated sound, including contributions from the near-field. Aanonsen *et al.* [24] and Hamilton *et al.* [25] developed expressions for the primary and harmonic sound fields in the near- and far-field showing the validity of the fully nonlinear equation in both regions. However, a successful approach that capitalizes on the advantages in analytical simplicity that comes with Gaussian sources yet describes the radiated sound fields from a circular piston source is the use of expansion techniques based on the idea that sound beams can be expressed as a series of base functions. Cavanagh and Cook [14] and Wen and Breazeale [15] provided the initial development of numerical models for the primary field of a circular plane baffled transducer using a series of Gaussian-Laguerre and Gaussian base functions, respectively. Similarly, Hasegawa *et al.* [56] developed an expression for the velocity potential of a circular piston radiator using a series expansion consisting of spherical Bessel functions, spherical Hankel functions of the second kind, and Legendre polynomials. Ding has since presented a series of papers that expand upon Wen and Breazeale's work by extending the expansion technique with Gaussian base functions also describing the second-order sound fields [16–18], known as the multi-Gaussian beam (MGB) expansion model. The sound field expressions found for the primary and secondary fields using a series of base functions have the advantage of yielding simple analytic solutions that are computationally more efficient than previous methods. Therefore, by defining the acoustic source function $q_1(r, 0)$ as a linear superposition of Gaussian beams, this model provides the unique advantage of enabling closed form solutions to be found for the secondary sound fields produced by a circular piston source without requiring any assumptions or approximations that limit the validity of the solution.

Assuming linear superposition, a circular piston source (or any arbitrary axially symmetric source) can be defined by a series of base functions so that the linear combination of these functions describes the resultant sound field

$$q_1(r, z) = \sum_{n=1}^N q_{1n}(r, z) \quad (2.46)$$

where N is the total number of functions within the series. Wen and Breazeale [15] expanded upon this principle and showed that any axially symmetric beam field can be expressed as the linear superposition of a set of Gaussian base functions

$$q_1(r, 0) = p_0 \sum_{n=1}^N A_n \exp(-B_n(r/a)^2), \quad (2.47)$$

where A_n and B_n are the Gaussian coefficient set and beam waist parameters, respectively. These coefficients can be determined through any means of optimization but have been tradi-

tionally calculated by minimizing the mean square error between the objective function and Gaussian function series:

$$Q = \int_0^\infty \left[q_1(r, 0) - p_0 \sum_{n=1}^N A_n \exp(-B_n(r/a)^2) \right]^2 dr. \quad (2.48)$$

Substituting the MGB expansion definition for the source function of a circular piston (2.47) into (2.35) and ignoring the attenuation term, the primary sound field of an axially symmetric circular piston expressed as a linear superposition of Gaussian beams is [15]

$$q_1(\xi, \eta) = p_0 \sum_{n=1}^N \frac{A_n}{1 + jB_n\eta} \exp\left(-\frac{B_n\xi^2}{1 + jB_n\eta}\right), \quad (2.49)$$

where the cylindrical coordinates have been normalized such that the radial and axial coordinates are given by $\xi = r/a$ and $\eta = z/z_0$, respectively, and, again, N is the number of functions within the series as defined by the Gaussian coefficient set.

In Wen's original work, two sets of coefficients were presented defining an edge supported piston and a rigid piston with six and ten terms, respectively, but several sets have since been presented in the literature. Ding [57] derived a simplified method of calculating the coefficients also resulting in ten terms while Wei and Jun [58] provided an alternative optimization method where the coefficients were found by combining solutions of linear equations with Fourier series expansions, resulting in fifteen terms. Kim *et al.* [59] continued Ding's work by generating a new set of coefficients that increased the precision of the expansion for a piston radiator but also increased the number of terms to twenty five. More recently, Cervenka *et al.* [60] presented a heuristic evolutionary algorithm that minimized the number of coefficients in the set, yielding a solution with only four terms. Fig. 2.2 is a comparison of the primary sound fields produced using (2.49) along the acoustic axis illustrating the improvement in accuracy into the near-field as the number of coefficients is increased while the far-field accuracy can be maintained with fewer coefficients. The Gaussian coefficient sets are given in their entirety in Appendix A.

With the substitution of (2.49) into (2.36), the simplified solution for the second harmonic can be found following the derivation in [16]

$$q_2(\xi, \eta) = -\frac{\beta p_0^2 k^2 a^2}{2\rho_0 c_0^2} \sum_{n=1}^N \sum_{j=1}^N \frac{A_n A_j}{r_1} \exp\left(-\frac{s_1 \xi^2}{r_1}\right) \left[E_1\left(\frac{s_2 \xi^2}{r_1(r_1 \eta + r_2)}\right) - E_1\left(\frac{s_2 \xi^2}{r_1 r_2}\right) \right], \quad (2.50)$$

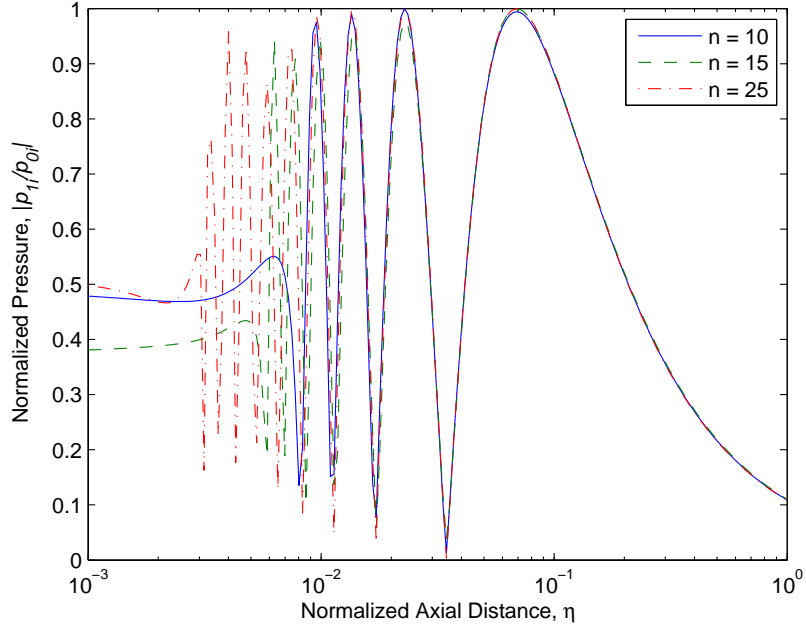


Figure 2.2: Comparison of the on-axis acoustic pressure for the primary frequency using the MGB method with $n = 10$, 15 , and 25 as given in [15], [58], and [59], respectively.

where

$$r_1 = (B_j + B_n) + 2\eta B_n B_j, \quad (2.51a)$$

$$r_2 = (B_n + B_j)\eta - 2j, \quad (2.51b)$$

$$s_1 = 4B_n B_j, \quad (2.51c)$$

$$s_2 = -2j(B_n - B_j)^2. \quad (2.51d)$$

The exponential integral function has several convenient asymptotic properties that allow further simplifications of (2.50) when the integrand is much greater or much less than unity: $E_1(x) \simeq x^{-1}e^{-x}$ for $x \gg 1$ and $E_1(x) \simeq -(\Gamma + \ln x)$ for $x \ll 1$ where $\Gamma = 0.577$ is Euler's constant. Additionally, by using the series expansion of the exponential integral function when on the acoustic axis, (2.50) further simplifies to

$$q_2(0, \eta) = -\frac{\beta p_0^2 k^2 a^2}{2\rho_0 c_0^2} \sum_{n=1}^N \sum_{j=1}^N \frac{A_n A_j}{r_1} \ln \left(1 + \frac{r_1}{r_2} \right). \quad (2.52)$$

Thus, the MGB expansion model produces a closed form solution for the second harmonic radiated from a circular piston source that is valid for all conditions under the quasilinear ap-

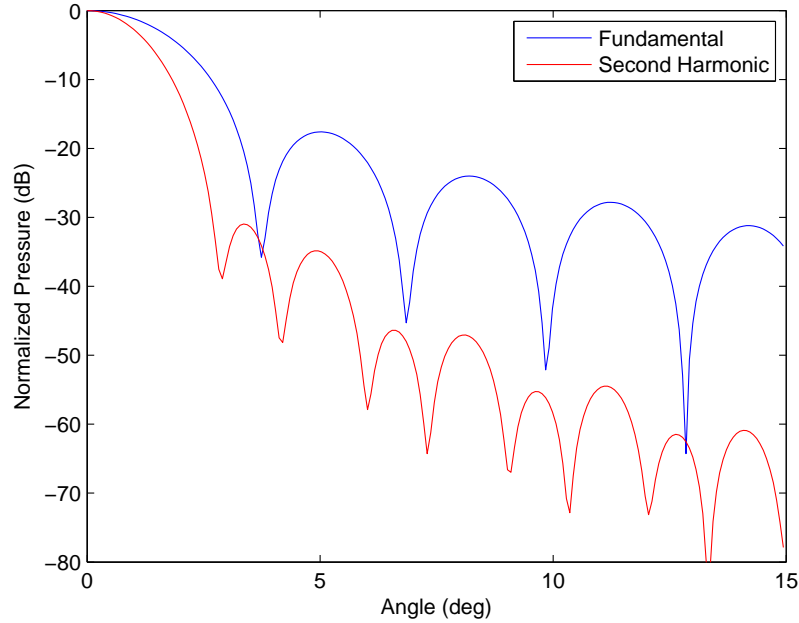


Figure 2.3: The normalized pressure amplitudes for the fundamental and second harmonic frequencies generated from a circular piston source using the MGB expansion model along the normalized radial axis ξ at a distance of 150 m from the source.

proximation. Similar to the depiction of the fields radiated from the Gaussian source, Fig. 2.3 describes the normalized pressure amplitudes for the fundamental and second harmonic frequencies generated from a circular piston source determined using (2.49) and (2.50), respectively. Again, the parameters used to produce the results were given by [26] and [27].

2.2.2 The Scattering of Sound by Sound and the Parametric Array

The analysis thus far has been limited to the radiation of a single acoustic tone; however, by expanding the investigation to account for the radiation of two or more tones, the resultant sound field will include the second-order sum and difference frequencies, in addition to the fundamental frequencies and the second harmonics for both acoustic tones, generated by the scattering of sound by sound. The scattering of sound by sound is a physical phenomenon whereby the nonlinear interaction of two or more sound fields produce intermodulation products that continue to propagate outside of the interaction region of the initial sound fields (i.e., the sum and difference frequencies for the second-order sound field) [19,20,61–63]. This phenomenon typically refers to the sound fields that are generated by noncollinear sources oriented so that their acoustic axes intersect at non-zero angles resulting in finite interaction regions. However,

the most commonly exploited use of the scattering of sound by sound is the generation of highly directional acoustic parametric arrays, a special case discovered by Westervelt during his investigations into the scattering of sound by sound [45] that lead to the development of his equation defining the nonlinear propagation of an acoustic wave (2.27). The parametric array is a virtual end-fire sound source that is generated by the beat pattern produced through the summing of two or more collinearly located ultrasonic sound fields where the nonlinear interaction of the fields create a directional sound beam at the intermodulation frequencies. Since the sources are collinearly located, the intermodulation frequencies propagate in the same direction as the primary frequencies and, therefore, are continuously pumped unlike the sound fields generated from noncollinear sources. While parametric radiation produces both the sum and difference frequencies, typically, parametric arrays refer to the generation of the difference frequency from two ultrasonic sound fields close in frequency so that this resultant tone will be located in the audio frequency range, thereby experiencing much less attenuation than the sum frequency that is located at much higher frequencies. Similar to the second harmonic, the Westervelt, Burgers, and KZK nonlinear equations developed in Section 2.2 are valid for the scattered sound fields and, thus, this section will follow a similar procedure as Section 2.2.1 to develop solutions that describe the scattered sound fields generated from a parametric array.

Considering a two tone primary sound field with fundamental frequencies f_1 and f_2 where $f_1 > f_2$, the secondary sound field will consist of the second harmonics $2f_1$ and $2f_2$, the sum frequency $f_S = f_1 + f_2$ and the difference frequency $f_D = f_1 - f_2$. Therefore, the sound pressure field p in (2.31) can be expanded as

$$p = p_1 + p_2 = \sum_{i=1}^2 p_{1i} + \sum_{\varsigma} p_{2\varsigma} = p_{11} + p_{12} + p_{21} + p_{22} + p_{2S} + p_{2D}, \quad (2.53)$$

where p_{1i} indicates the i th primary field and $p_{2\varsigma}$ indicates the second-order scattered field. The scattered field subscript ‘ ς ’ specifies the choice between one of the two second harmonics, sum, and difference frequencies, $\varsigma = 1, 2, S$, or D , respectively. Thus, the first subscript indicates the sound field order and the second subscript denotes the specific frequency component within that field (e.g., p_{12} and p_{21} are the pressure fields of the fundamental frequency f_2 and second harmonic $2f_1$, respectively). The two tone pressure field can then be written

$$p_1(r, z, \tau) = q_{11}(r, z, \tau)e^{j\omega_1\tau} + q_{12}(r, z, \tau)e^{j\omega_2\tau}, \quad (2.54)$$

$$p_2(r, z, \tau) = q_{21}(r, z, \tau)e^{j2\omega_1\tau} + q_{22}(r, z, \tau)e^{j2\omega_2\tau} + q_{2S}(r, z, \tau)e^{j\omega_S\tau} + q_{2D}(r, z, \tau)e^{j\omega_D\tau}. \quad (2.55)$$

Substituting (2.53), (2.54), and (2.55) into the KZK equation (2.30) yields equations for the primary and secondary sound fields that are identical to (2.33) and (2.34). Therefore, (2.35)

and (2.36) remain valid integral solutions for the fundamental and second harmonic frequencies within the two tone pressure field. Solutions can be found for the sum and difference frequencies by, again, integrating over the product of the acoustic driving source and appropriate Green's function producing a similar solution as for the second harmonic in (2.36), where the second-order field subscript \pm denotes the choice between the sum and difference frequencies. Thus, the integral solution can be found as

$$q_{2\pm}(r, z) = \pm \frac{\pi \beta k_{\pm}}{\rho_0 c_0^2} \int_0^z \int_0^\infty q_{11}(r', z') q_{12}^*(r', z') G_{\pm}(r, z | r', z') r' dr' dz', \quad (2.56)$$

where $k_{\pm} = \omega_{\pm}/c_0$ is the wavenumber determined by the selection of the sum or difference frequency ($\omega_{\pm} = \omega_1 \pm \omega_2$), the superscript $*$ indicates the complex conjugate taken only for the calculation of the difference frequency, nk and α_n in (2.38) are replaced with k_{\pm} and α_{\pm} , respectively, for the Green's function G_{\pm} , and the driving source q_1^2 in (2.36) is replaced with the interacting two tone primary field $q_{11}q_{12}$.

To determine solutions to the integral equation for the sum and difference frequencies (2.56), expressions for the two tone primary sound field must first be ascertained. Again, these solutions are dependent upon the type of acoustic source radiating the sound fields and their corresponding source function. Given a Gaussian source, the source functions for the two tone primary field are

$$q_{11}(r, 0) = p_{01} \exp(-(r/a)^2), \quad q_{12}(r, 0) = p_{02} \exp(-(r/a)^2). \quad (2.57)$$

where p_{0n} is the peak pressure amplitude for each of the fundamental frequencies f_n , $n = 1, 2$. The source functions in (2.57) yield the primary sound fields, found using (2.35), for each tone as

$$q_{11}(r, z) = \frac{p_{01} e^{-\alpha_{11} z}}{1 - jz/z_{01}} \exp\left(-\frac{(r/a)^2}{1 - jz/z_{01}}\right), \quad q_{12}(r, z) = \frac{p_{02} e^{-\alpha_{12} z}}{1 - jz/z_{02}} \exp\left(-\frac{(r/a)^2}{1 - jz/z_{02}}\right), \quad (2.58)$$

where k_n , z_{0n} , and α_{1n} are the wavenumber, limit between the near- and far-field, and attenuation coefficient for the fundamental frequencies f_n , $n = 1, 2$. Substituting (2.58) into (2.56), the solution for the sum and difference frequencies generated from a Gaussian source can be written [41]

$$q_{2\pm}(r, z) = \frac{j\beta k_{\pm}^2 z_{01} z_{02} p_{01} p_{02}}{2\rho_0 c_0^2 f_{\pm}} \exp\left(-\frac{k_{\pm}^2 r^2}{2f_{\pm}}\right) \times \left[E_1\left(\frac{k_1 k_2 (z_{01} \mp z_{02})^2 k_{\pm}^2 r^2}{2f_{\pm}(g_{\pm} \mp j f_{\pm} k_{\pm} z)}\right) - E_1\left(\frac{k_1 k_2 (z_{01} \mp z_{02})^2 k_{\pm}^2 r^2}{2f_{\pm} g_{\pm}}\right) \right] \quad (2.59)$$

where $f_{\pm}(z) = k_1 z_{01} + k_2 z_{02} - j k_{\pm} z$, and $g_{\pm}(z) = k_{\pm}^2 z_{01} z_{02} - j(k_2 z_{01} + k_1 z_{02}) k_{\pm} z$. On the acoustic

axis, the series expansion for the exponential integral functions in (2.59) can be utilized to simplify the expression to

$$q_{2\pm}(0, z) = \frac{j\beta k_{\pm}^2 z_{01} z_{02} p_{01} p_{02}}{2\rho_0 c_0^2 f_{\pm}} \ln(1 \mp jk_{\pm} z f_{\pm}/g_{\pm}). \quad (2.60)$$

Whereas (2.59) is derived assuming a single Gaussian source is simultaneously generating both fundamental frequencies, a similar result was obtained by Darvennes and Hamilton [30] using two noncollinear Gaussian sources with intersecting sound beams operating at unique frequencies.

The development of closed form solutions to the sum and difference frequencies generated from a circular piston requires similar approximations to be made as the development of the second harmonic in Section 2.2.1. To ease in the derivation, the analysis here will be restricted to the difference frequency solely. Considering only far-field conditions and that the circular piston is radiating collimated plane waves, closed form solutions to the primary sound fields can be expressed as

$$q_{11}(r, z) = p_{01}H(a - r)e^{\alpha_{11}z}, \quad q_{12}(r, z) = p_{02}H(a - r)e^{\alpha_{12}z}. \quad (2.61)$$

Under the far-field approximation and since the nonlinear interaction of the fields is primarily in the near-field, the axial component in the Green's function term $(z - z')^{-1}J_0(k_D r r'/(z - z'))$ can be simplified to $z^{-1}J_0(k_D r r'/z)$ and, therefore, the solution for the difference frequency generated from a circular piston source can be written [41]

$$q_{2D}(\theta, z) \simeq -\frac{j p_{01} p_{02} \beta k_D^2 a^2}{4\rho_0 c_0^2 \alpha_T} \frac{e^{-\alpha_D z}}{z} D_W(\theta) D_A(\theta) \exp\left(-\frac{1}{2} j k_D z \tan^2 \theta\right), \quad (2.62)$$

where $\alpha_T = \alpha_{11} + \alpha_{12} - \alpha_D$ and the Westervelt directivity $D_W(\theta)$ [45] and aperture factor $D_A(\theta)$ [64] are given by

$$D_W(\theta) = \frac{1}{1 + j(k_D/2\alpha_T) \tan^2 \theta}, \quad (2.63)$$

$$D_A(\theta) = \frac{2J_1(k_D a \tan \theta)}{k_D a \tan \theta}. \quad (2.64)$$

The Westervelt directivity accounts for the directionality gained by the end-fire effect of the parametric array while the aperture factor considers the directivity of a virtual source directly generating an acoustic wave at the difference frequency. Additionally, it can be seen that the amplitude of the difference frequency along the axis of propagation is proportional to the effective length of the parametric array, $L_a = \alpha_T^{-1}$.

While (2.62) has a convenient closed form solution describing the difference frequency, the assumptions required to enable the development of the solution dramatically limit its applicability. Therefore, much effort has been put into finding alternative methods to determine the radiation pattern of the difference frequency [26–36, 65], commonly done by implementing numerical integration techniques to directly solve (2.56). This was the procedure implemented by Garrett *et al.* [27] and Muir and Willette [65], both of which developed primary sound field solutions for circular piston sources and calculated the difference frequency in the far-field through direct numerical evaluation of (2.56) for comparison with experimental results. Less effort has been put into determining the radiation of the sum frequency, however, similar analytical complications are encountered in the development of the sum frequency solutions. Analogous to the methods taken to solve for the difference frequency, Berntsen *et al.* [26] solved (2.56) directly for the second harmonic and sum frequency for comparison with measurements.

As a means of avoiding the restrictions imposed by assumptions made in alternate methods or using less efficient numerical integration techniques, Ding [17, 18] was able to develop closed form solutions for the sum and difference frequencies radiated from a circular piston source through the implementation of the MGB expansion model. In a similar derivation as was performed for the second harmonic using the MGB expansion model, the primary sound fields can be expressed as

$$\begin{aligned} q_{11}(\xi, \eta) &= p_{01} \sum_{n=1}^N \frac{A_n}{1 + jB_{ln}\eta} \exp\left(-\frac{lB_{ln}\xi^2}{1 + jB_{ln}\eta}\right), \\ q_{12}(\xi, \eta) &= p_{02} \sum_{j=1}^N \frac{A_j}{1 + jB_{mj}\eta} \exp\left(-\frac{mB_{mj}\xi^2}{1 + jB_{mj}\eta}\right), \end{aligned} \quad (2.65)$$

where $l = k_1/k_0$ and $m = k_2/k_0$ are the wavenumbers of the fundamental frequencies normalized to the mean of the two fundamental frequencies $k_0 = (k_1 + k_2)/2$ and $B_{ln} = B_n/l$ and $B_{mj} = B_j/m$ are the normalized beam waist coefficients. The limit between the near- and far-field is also redefined to the mean of the primary frequencies as $z_0 = \frac{1}{2}k_0a^2$. Normalizing the wavenumber in the Green's function, $nk = l + m$, and substituting (2.65) into (2.56), the simplified solution for the sum and difference frequencies can be written [17]

$$\begin{aligned} q_{2\pm}(\xi, \eta) &= -\frac{\beta p_{01}p_{02}k_0^2a^2(l+m)^2}{4\rho_0c_0^2} \sum_{n=1}^N \sum_{j=1}^N \frac{A_nA_j}{r_1} \exp\left(-\frac{s_1\xi^2}{r_1}\right) \\ &\quad \times \left[E_1\left(\frac{s_2\xi^2}{r_1(r_1\eta + r_2)}\right) - E_1\left(\frac{s_2\xi^2}{r_1r_2}\right) \right], \end{aligned} \quad (2.66)$$

where

$$r_1 = (lB_j + mB_n) + j(l + m)\eta B_n B_j, \quad (2.67a)$$

$$r_2 = (lB_n + mB_j)\eta - j(l + m), \quad (2.67b)$$

$$s_1 = (l + m)^2 B_n B_j, \quad (2.67c)$$

$$s_2 = -j(l + m)lm(B_n - B_j)^2. \quad (2.67d)$$

and the selection of the sum or difference frequency defines the normalized wavenumbers (i.e., $l = k_1/k_0$ and $m = \pm k_2/k_0$ for the sum and difference frequencies, respectively). As with the second harmonic, (2.66) can be simplified along the acoustic axis by employing the series expansion of the exponential integral function,

$$q_{2\pm}(0, \eta) = -\frac{\beta p_{01} p_{02} k_0^2 a^2 (l + m)^2}{4\rho_0 c_0^2} \sum_{n=1}^N \sum_{j=1}^N \frac{A_n A_j}{r_1} \ln \left(1 + \frac{r_1}{r_2} \eta \right). \quad (2.68)$$

When the frequencies of the primary fields are equivalent denoting the second harmonic (i.e., $k_1 = k_2$ so that $l = m$), (2.66) simplifies to (2.50). As was the case for the second harmonic, the MGB expansion model produces a closed form solution for the scattered sound fields generated from a circular piston that is valid under the quasilinear approximation with no further restrictions. Fig. 2.4 shows the secondary sound fields produced using the MGB expansion equations (2.50) and (2.66) to model the radiated sound fields found in [26], [27], [16], and [17], and are reproduced here to verify the validity of the MGB expansion model to accurately determine the radiation patterns of the second-order scattered sound fields. In these results, the acoustic waves are transmitted through water and the parameter values are $\rho_0 = 995.8 \text{ kg/m}^3$, $c_0 = 1497.7 \text{ m/s}$, $\beta = 3.59$, $a_1 = 0.87 \text{ m}$, $a_2 = 0.83 \text{ m}$, $f_1 = 16 \text{ kHz}$, and $f_2 = 11 \text{ kHz}$ ($f_1 = 15 \text{ kHz}$ and $f_2 = 12 \text{ kHz}$ for the difference frequency). Fig. 2.4a describes the pressure amplitude on the acoustic axis for the second-order sound fields and Figs. 2.4b–2.4d show the normalized pressure amplitudes on various planes normal to the axis of propagation for the second harmonic, sum, and difference frequencies, respectively.

Westervelt's discovery of the parametric array, and the subsequent investigations into modeling the generation of the difference frequency, has prompted a vast amount of interest in the generation of highly directional audio. Yoneyama *et al.* [21] was the first to apply the concept of the parametric array in the development of a practical loudspeaker design and, since then, the highly directional loudspeaker has garnered attention in a variety of applications. For use in detection schemes, Haupt [66] investigated the detection of buried landmines by remotely exciting the landmine with the parametric array and using a laser Doppler vibrometer to measure the resultant response. Use of the parametric array has also grown in popularity in the fields of

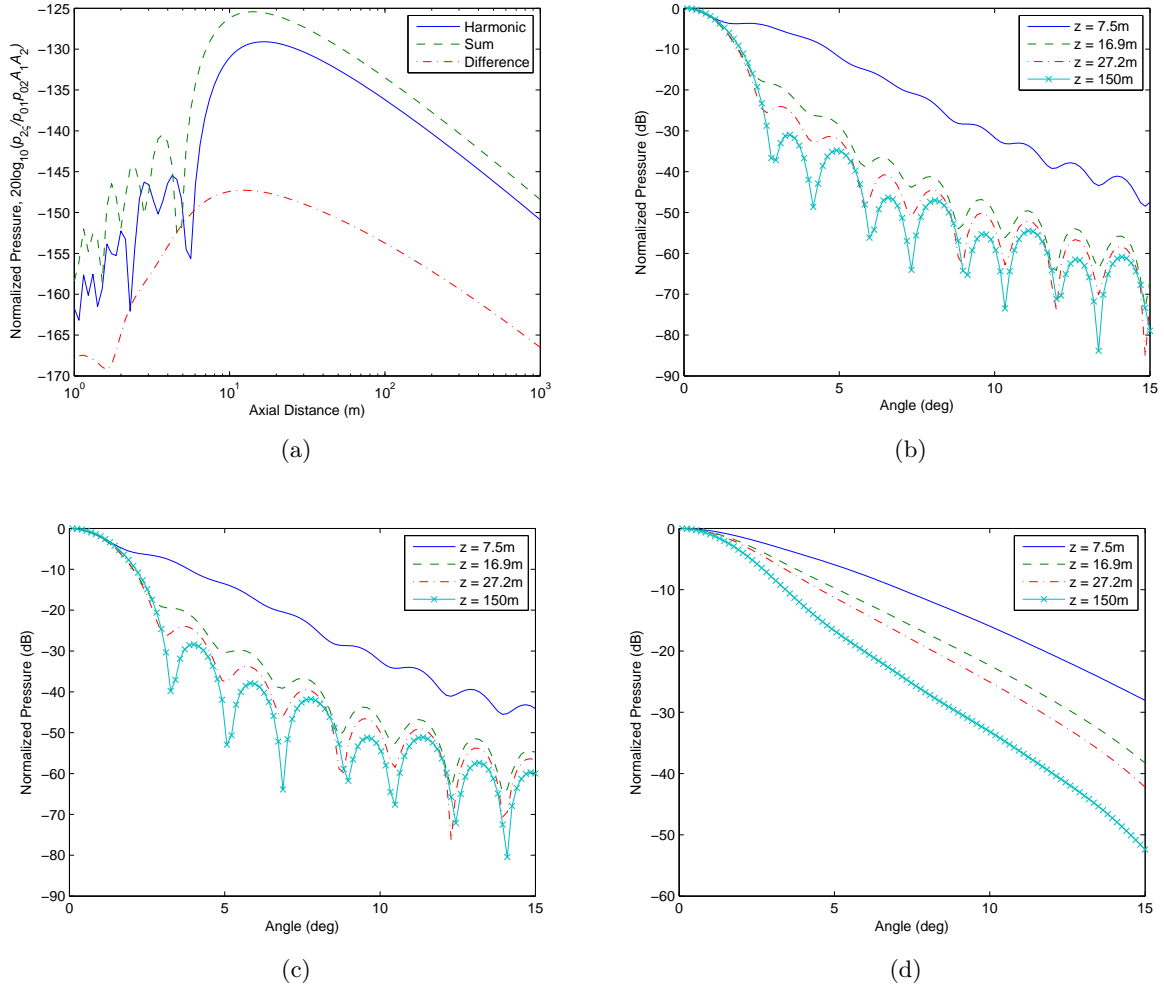


Figure 2.4: Normalized pressure amplitudes of the second-order sound field distributions (a) on the acoustic axis of the harmonic, sum, and difference frequencies where $A_i = \pi a^2$ is the area of the source for the i th primary frequency and at various distances from the source for (b) the second harmonic, (c) sum frequency, and (d) difference frequency as described in [16] and [17].

sound localization and active noise control as the highly directional beam produced by the array is ideal in controlling small regions of sound [67–72]. Ji *et al.* [67] studied the use of intersecting parametric beams to generate localized regions of sound and Shi and Gan [68] continued that investigation by discussing its use as a component of an audio system for gaming and immersive virtual reality simulations. Conversely, Tanaka and Tanaka [69, 70] investigated the use of the parametric array in the field of active noise control to generate localized cancellation regions. More recently, the parametric array has been investigated as a new method for delivering sound

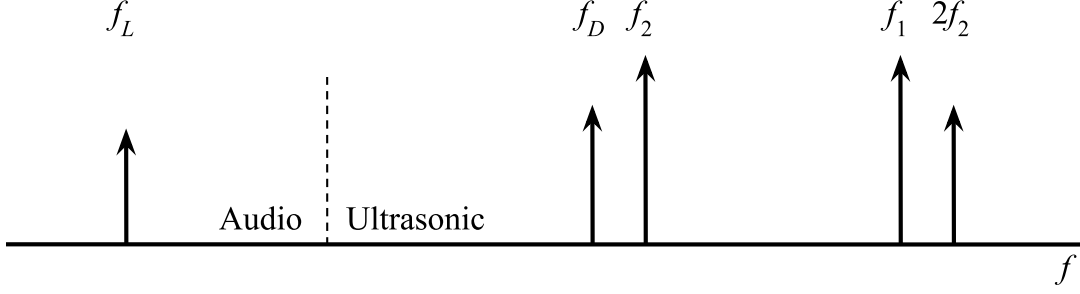


Figure 2.5: Frequency spectrum for the interacting primary (f_1 and f_2) and secondary ($2f_2$ and $f_D = f_1 - f_2$) sound fields with the resultant third-order fields ($f_L = (2f_2 - f_1) + (f_2 - f_D)$).

to individualized users of mobile phones and multimedia devices [73–75].

Primarily, research on the nonlinear acoustic properties that produce the scattering of sound by sound and the parametric array have focused on the second-order effects, ignoring third- and higher-order nonlinear processes. However, recent works by Garner and Steer [38, 39, 76] have shown that a third-order parametric array can be developed that offer advantages in directivity and sidelobe power over the more common second-order parametric array. Rather than using two primary sound fields close in frequency to produce a second-order difference tone in the audio frequency range, the third-order parametric array is generated from two ultrasonic primary sound fields distantly spaced so that one primary frequency is roughly twice that of the other ($2f_2 \gtrsim f_1$) resulting in a third-order intermodulation product in the audio frequency range, as illustrated in Fig. 2.5. Using a cascaded second-order approach and the concept of quadratic nonlinearity, the third-order sound fields are generated through the nonlinear interaction of the primary field with the secondary field during propagation to produce the third harmonics, $3f_1$ and $3f_2$, and the upper and lower third-order intermodulation (IM3) products, $f_U = 2f_1 - f_2$ and $f_L = 2f_2 - f_1$, respectively, along with several other fields that will be ignored in this discussion.

The sound pressure field p in (2.31) and (2.53) can, therefore, be expanded to incorporate the third-order sound fields as

$$\begin{aligned}
 p &= \sum_{i=1}^2 p_{1i} + \sum_{\varsigma} p_{2\varsigma} + \sum_{\zeta} p_{3\zeta} \\
 &= p_{11} + p_{12} + p_{21} + p_{22} + p_{2S} + p_{2D} + p_{31} + p_{32} + p_{3U} + p_{3L},
 \end{aligned} \tag{2.69}$$

where p_{1i} and $p_{2\varsigma}$ indicate the first- and second-order sound fields, as previously defined, and $p_{3\zeta}$ indicates the third-order sound fields. Similarly to its use in identifying the second-order scattered fields, the subscript ‘ ζ ’ specifies the choice of one of the two third harmonics, upper,

and lower IM3 tones, $\zeta = 1, 2, U$, or L , respectively. The third-order contribution to the two tone pressure field given by (2.54) and (2.55) can then be written

$$p_3(r, z, \tau) = q_{31}(r, z, \tau)e^{j3\omega_1\tau} + q_{32}(r, z, \tau)e^{j3\omega_2\tau} + q_{3U}(r, z, \tau)e^{j\omega_U\tau} + q_{3L}(r, z, \tau)e^{j\omega_L\tau}. \quad (2.70)$$

Under the cascaded second-order approach, (2.69) and (2.70) are substituted into the KZK equation (2.30) to yield the third-order quasilinear equation for propagation of the tertiary sound fields, written as

$$\frac{\partial p_3}{\partial z} + \frac{j}{8k} \nabla_{\perp}^2 p_3 + \alpha_3 p_3 = \frac{\beta k}{2\rho_0 c_0^2} (p_1 + p_2)^2, \quad (2.71)$$

where the source contributions for the third-order sound fields can be found by expanding the quadratic driving source $(p_1 + p_2)^2$ in the right hand term of (2.71) to determine the interacting primary and secondary fields. For the third-order fields of interest, these driving sources are

$$(p_1 + p_2)^2 = [q_{21}q_{11}] + [q_{22}q_{12}] + [q_{21}q_{12} + q_{11}q_{2D}] + [q_{22}q_{11} + q_{12}q_{2D}] + \dots \quad (2.72)$$

where the brackets $[\]$ indicate the distinct driving sources for the third harmonics $3f_1$ and $3f_2$, the IM3 upper f_U , and the IM3 lower f_L frequencies, respectively. It is worth bringing attention to the fact that the IM3 products are determined by two independent nonlinear interactions as each of the interactions yield a result at the IM3 frequency of interest. As with the primary and secondary sound fields, integrating over the product of the appropriate acoustic driving source and Green's function, solutions for the third harmonic and IM3 upper, and IM3 lower frequencies can be found as

$$q_{3i}(r, z) = \frac{4\pi\beta k_{3i}^2}{3\rho_0 c_0^2} \int_0^z \int_0^\infty [q_{1i}(r', z')]^3 G_3(r, z | r', z') r' dr' dz', \quad (2.73)$$

$$q_{3U}(r, z) = \frac{4\pi\beta k_U^2}{3\rho_0 c_0^2} \int_0^z \int_0^\infty [q_{21}(r', z')q_{12}^*(r', z') + q_{11}(r', z')q_{2D}(r', z')] G_{3U}(r, z | r', z') r' dr' dz', \quad (2.74)$$

$$q_{3L}(r, z) = \frac{4\pi\beta k_L^2}{3\rho_0 c_0^2} \int_0^z \int_0^\infty [q_{22}(r', z')q_{11}^*(r', z') + q_{12}(r', z')q_{2D}^*(r', z')] G_{3L}(r, z | r', z') r' dr' dz'. \quad (2.75)$$

Solutions to the third-order integral equations are not easily obtained and, similar to the procedure taken with the second-order sound fields, direct numerical integration of the KZK equation is often used to determine these fields. Chapter 3 explores methods for finding solutions to (2.73)–(2.75) and efficiently determining the radiation patterns of the third-order sound fields.

2.3 Computation of the Equations of Nonlinear Acoustics

Advancements in the fields of nonlinear acoustics and audio engineering [77–84] have improved the ability to generate and manipulate sound fields making the use of sound an intriguing option in a variety of applications, including radar [85, 86], detection [2, 3, 7, 9], and object characterization [11, 87, 88]. Practical implementation in many of these applications requires real-time analysis of the sound fields, however, as discussed in Section 2.2.1, solutions to the KZK equation and other governing equations of nonlinear acoustics are commonly found through numerical techniques necessitating substantial computation, thus, preventing real-time utilization. Chapters 3 and 4 address this issue by presenting computationally efficient methods of determining higher-order sound fields by employing expansion and transformation techniques that yield sound field integrals with fewer dimensions and smaller mesh sizing. This section explores commonly employed methods for solving the KZK equation and determining the radiation patterns of higher-order sound fields.

2.3.1 Direct Numerical Evaluation of the KZK Equation

Convenient, closed form solutions to the KZK equation (2.30) are typically unobtainable without the use of assumptions that limit their validity; therefore, a variety of methods have been developed to solve the KZK equation directly. The most common of these methods was developed at the Department of Mathematics, University of Bergen [89–91] where a solution to the KZK equation was found in the form of a Fourier series, expressed as

$$p(\xi, \eta) = \sum_{n=1}^{\infty} (g_n(\xi, \eta) \sin n\tau + h_n(\xi, \eta) \cos n\tau), \quad (2.76)$$

where n is the harmonic number, τ is the retarded time, and ξ and η are the normalized spatial coordinates. Thus, from (2.30) and (2.76), a set of coupled partial differential equations can be found for g_n and h_n as

$$\begin{aligned} \frac{\partial g_n}{\partial \eta} = & -n^2 \alpha r_0 g_n + \frac{1}{4n(1+\eta)^2} \nabla_{\perp}^2 h_n \\ & + \frac{nr_0}{2l_D(1+\eta)} \left(\frac{1}{2} \sum_{p=1}^{n-1} (g_p g_{n-p} - h_p h_{n-p}) - \sum_{p=n+1}^{\infty} (g_{p-n} g_p + h_{p-n} h_p) \right), \end{aligned} \quad (2.77)$$

$$\begin{aligned} \frac{\partial h_n}{\partial \eta} = & -n^2 \alpha r_0 h_n - \frac{1}{4n(1+\eta)^2} \nabla_{\perp}^2 g_n \\ & + \frac{nr_0}{2l_D(1+\eta)} \left(\frac{1}{2} \sum_{p=1}^{n-1} (h_p g_{n-p} + g_p h_{n-p}) + \sum_{p=n+1}^{\infty} (h_{p-n} g_p + g_{p-n} h_p) \right), \end{aligned} \quad (2.78)$$

where $n = 1, 2, \dots$ and l_D is the plane wave shock formation distance. The infinite series on the right hand side of (2.77) and (2.78) represent the physical flow of energy from the lower harmonics to the higher harmonics. To numerically integrate these equations, an implicit backward finite difference method is utilized where the infinite series are truncated for practical implementation. The effect of truncating the series is that the energy flow from the lower harmonics stops at the final harmonic in the series and, therefore, can result in a much larger amplitude for the final harmonic than expected. Thus, restrictions must be imposed on the numerical methods such that one harmonic does not exceed the amplitude of the next lower harmonic. The number of harmonics required to generate a stable solution can vary based upon the desired error bounds and acoustic source being modeled; thus, many works using this technique often repeat results with a varied number of total harmonics used in the infinite series. This approach was first implemented to compute the near-field of an acoustic source [24, 34] and finite amplitude wave propagation [92]. It was then extended to determine the nonlinear effects in the far-field of an acoustic source [25] as well as more complicated sound fields, such as propagation from a bifrequency sound source [93].

2.3.2 Calculation of Multidimensional Integrals

Direct numerical evaluation of the KZK equation yields highly accurate results given that the errors introduced by the truncated infinite series remain low. However, the implicit backward finite difference method and other numerical methods of this nature are not the most efficient and can take a considerable amount of time to generate a solution that is stable. Therefore, continued research efforts have gone into finding simplified solutions of the sound fields. The most straightforward simplification has come from the derivation of multidimensional integral solutions from the KZK equation that describe the primary sound field, (2.35), secondary sound field, (2.36) and (2.56), and tertiary sound field, (2.73)–(2.75), radiated from an acoustic source. As discussed in Sections 2.2.1 and 2.2.2, closed form solutions of these integrals can be found under the appropriate assumptions but this limits the range of validity of the results; thus, a variety of methods have been employed to numerically compute the multidimensional integrals. A popularly applied method to solve multidimensional integrals was developed by Berntsen *et al.* [94–98] that utilizes an adaptive quadrature integration routine, named DCUHRE, that splits the integral regions into increasingly small hyperrectangular segments until all regions can be solved within suitable error and stability bounds. This method has been exploited by

many works to solve for the second harmonic [26]

$$q_2(x, z) = -\frac{j\beta k_1^3}{2\pi z \rho_0 c_0^2} \int_0^\infty \int_0^\infty \int_0^\pi \left[E_1 \left(\frac{jk_1}{4z} (x_1^2 + x_2^2 - 2x_1x_2 \cos \phi) \right) \right]^* J_0 \left(\frac{xk_1 G^{1/2}}{z} \right) \\ \times \exp \left(\frac{jk_1}{4z} (4x^2 + G) \right) q_1(0, x_1) q_2^*(0, x_2) x_1 x_2 d\phi dx_1 dx_2, \quad (2.79)$$

where $G = x_1^2 + x_2^2 + 2x_1x_2 \cos \phi$ as well as the sum and difference frequencies [27, 29, 55]

$$q_\pm(x, z) = -\frac{j\beta k_1 k_2 k_\pm}{2\pi z \rho_0 c_0^2} \int_0^\infty \int_0^\infty \int_0^\pi E_1 \left(\frac{jk_1 k_2}{2k_\pm z} (x_1^2 + x_2^2 - 2x_1x_2 \cos \phi) \right) J_0 \left(\frac{x F^{1/2}}{z} \right) \\ \times \exp \left(\frac{j}{2k_\pm z} ((k_\pm x)^2 + F) \right) q_1(0, x_1) q_2^*(0, x_2) x_1 x_2 d\phi dx_1 dx_2, \quad (2.80)$$

where $F = (k_1 x_1)^2 + (k_2 x_2)^2 \pm 2k_1 x_1 k_2 x_2 \cos \phi$ and the complex conjugate is taken of the exponential integral instead of $q_2(0, x_2)$ for the sum frequency.

A common issue with solving the multidimensional integrals in acoustics is that the integrand is often highly oscillatory in nature, containing the product of functions that oscillate rapidly with different speeds, as seen in (2.79) and (2.80). Automated adaptive routines, such as those developed by Berntsen *et al.*, often address the oscillatory integrand by using integration rules with higher degree to minimize the number of evaluations required to find a stable solution, but this increases the computational complexity. An alternative approach was developed by Leble *et al.* [99–101] to solve the multidimensional integrals specifically when they contain highly oscillatory integrands. By rearranging the second-order integral solution to separate the integration terms as best as possible, the integral becomes

$$q_2(\xi, \eta) = -\frac{\beta(ka)^2}{\rho_0 c_0^2} e^{-\alpha_2 \eta} \int_0^\eta \exp \left(-\frac{2j\xi^2}{\eta - \eta'} + \alpha_2 r_0 \eta' \right) \frac{d\eta'}{\eta - \eta'} \\ \times \int_0^\infty q_1^2(\xi, \eta) \exp \left(-\frac{2j\xi'^2}{\eta - \eta'} \right) J_0 \left(\frac{4\xi\xi'}{\eta - \eta'} \right) \xi' d\xi'. \quad (2.81)$$

Focusing on the first of the two integrals in (2.81) so as to exclude the influence of the source $q_1^2(\xi, \eta)$, a special quadrature formula can be utilized [101],

$$q = \int_a^b f(x) e^{g(x)} dx = \sum_{k=1}^N \int_{x_k - h/2}^{x_k + h/2} f(x) e^{g(x)} dx \approx \sum_{k=1}^N B_k, \quad (2.82)$$

$$B_k = \begin{cases} f(x_k) e^{g(x_k)} h, & \text{if } |g'(x_k)h| \leq 0.1, \\ f(x_k) e^{g(x_k)} \sinh \left[\frac{h}{2} g'(x_k) \right] \frac{2}{g'(x_k)}, & \text{if } |g'(x_k)h| \geq 0.1, \end{cases} \quad (2.83)$$

to obtain an approximation for the integral. Repeating this quadrature formula for both integrals, (2.81) can be expressed as [100]

$$q_2(\xi_n, \eta_p) \cong -\frac{\beta(ka)^2}{\rho_0 c_0^2} e^{-\alpha_2 r_0 \eta} \times \sum_{k=0}^{p-1} \begin{cases} \frac{feg1_{p,n,k}}{\eta_p - \eta_k} \Delta\eta_k, & \text{if } |dg1_{p,n,k} \Delta\eta_k| \leq 0.1, \\ \frac{feg1_{p,n,k}}{\eta_p - \eta_k} \sinh\left[\frac{\Delta\eta_k}{2} dg1_{p,n,k}\right] \frac{2}{dg1_{p,n,k}}, & \text{if } |dg1_{p,n,k} \Delta\eta_k| > 0.1, \end{cases} \quad (2.84)$$

where

$$feg1_{p,n,k} = \exp\left(-\frac{2j\xi_n^2}{\eta_p - \eta_k} + \alpha_2 r_0 \eta_k\right) \times \sum_l \begin{cases} feg2_{p,n,k,l} \Delta\xi_l, & \text{if } |dg2_{p,k,l} \Delta\xi_l| \leq 0.1, \\ feg2_{p,n,k,l} \sinh\left[\frac{\Delta\xi_l}{2} dg2_{p,k,l}\right] \frac{2}{dg2_{p,k,l}}, & \text{if } |dg2_{p,k,l} \Delta\xi_l| > 0.1, \end{cases} \quad (2.85)$$

$$feg2_{p,n,k,l} = (q_1(\xi_l, \eta_k))^2 \xi_l J_0\left(\frac{4\xi_n \xi_l}{\eta_p - \eta_k}\right) \exp\left(-\frac{2j\xi_l^2}{\eta_p - \eta_k}\right), \quad (2.86)$$

and

$$dg1_{p,n,k} = -\frac{2j\xi_n^2}{(\eta_p - \eta_k)^2} + \alpha_2 r_0, \quad dg2_{p,k,l} = -\frac{4j\xi_l}{\eta_p - \eta_k}. \quad (2.87)$$

For proper application of this technique, the selection of the grid parameters η_{\min} and $\Delta\eta_k$ are critical to address the integrand oscillations. η_{\min} is dependent upon the source and wave parameters under the KZK equation,

$$\eta_{\min} < (ka)^{(1/3)} a/r_0, \quad (2.88)$$

and the step size $\Delta\eta_k$ must be defined such that

$$\eta_{\min} > -\frac{\Delta\eta_k}{2} \left(1 - \sqrt{1 + \frac{2}{\Delta\eta_k \pi}}\right). \quad (2.89)$$

The expressions given by (2.84)–(2.87) offer the advantage of simple numerical implementation over the automatic adaptive routine when dealing with rapidly oscillating functions in multidimensional integrals. This is the technique that is utilized to determine the radiation patterns of the third-order sound fields that are developed in Chapter 3.

2.4 Acousto-Electromagnetic Scattering

Acousto-EM scattering is a physical phenomenon whereby acoustic and electromagnetic waves interact to generate a scattered EM field, traditionally considered a Doppler spectrum produced by the mechanical vibration of an object under the illumination of the acoustic, or seismic, wave. In this process, the incident acoustic wave induces vibrations on the object, thereby displacing the boundary while simultaneously modulating the object density causing the incident EM wave to be modulated, producing the scattered EM fields. This phenomenon is commonly exploited in sensing systems as the use of two orthogonal modalities, acoustic and electromagnetic, offers many advantages over single mode systems that make acousto-EM sensing a highly attractive alternative to conventional sensing systems. Primarily, these advantages appear in the ability of the system to benefit from the combined capabilities of the individual sensing methods, relying on one modality when the other is insufficient or obtaining a unique set of information about the same object from each modality. For instance, acoustic- and EM-only sensing systems can have trouble obtaining information from objects under conditions that prevent penetration of the wave into the interior of the object or receipt of a reflected wave. For an acoustic system, the high reflection coefficient of the majority of materials prevents the coupling of acoustic energy into an object and, conversely for an EM system, electromagnetically lossy and metal objects prevent EM energy from coupling into the object interior, thereby making it difficult to obtain any information about the object in either situation. Additionally, in acoustically saturated environments where there is a large amount of background clutter or when dealing with acoustic shear waves where a directly reflected signal is not generated, acoustic detection of the desired reflected signal may not be possible. However, with a hybrid acousto-EM sensing system, information may be obtained in these scenarios where it was not previously feasible by detecting acoustic resonances for the metallic object in the EM-only system or simply adding EM interrogation capabilities in the acoustic-only system. Thus, with these improvements in the effectiveness of a sensing system, acousto-EM sensing systems have received growing interest for use in a variety of applications, such as landmine detection [1–10, 102], medical imaging [11], and structural integrity evaluation [11, 88].

The idea of scattering an EM signal with an acoustic wave was originally introduced by Brillouin [103] when he determined the interaction of a propagating EM wave with a fluctuating sound source in fluids and solids would result in a Doppler shift of the EM wave. This was later verified experimentally by Debye and Sears [104] by detecting a Doppler shift on scattered light from acoustic waves in a liquid while discussing the importance of the Bragg scattering condition on the results, which occurs when the EM wavelength is twice that of the acoustic wavelength. Interacting acoustic and EM waves has since been used in radio acoustic sounding systems (RASS) to measure meteorological conditions in the atmosphere by exploiting

the Bragg scattering condition [105, 106]. RASS systems simultaneously transmit a spherical acoustic wave and an EM signal that reflects off of the acoustic wave fronts when variations occur allowing for the acoustic propagation speed to be determined and atmospheric temperature calculated. More recently, acousto-EM scattering has been proposed as an alternative to conventional detection schemes [3–5, 7, 9–11, 102]. EM signals have long been used for probing, characterizing, and identifying targets in a variety of sensing applications, including interferometry [107], navigation [86], and ground penetrating radar (GPR) [108]; however, the use of EM signals in many detection schemes, particular GPR, has been greatly limited by the typically low contrast between the target object and the background environment. Therefore, as a means of improving the distinction between an object and its surrounding environment, acousto-EM sensing systems have been proposed to enhance the interrogated object contrast through mechanical vibration. Scott *et al.* [3, 4] developed an acousto-EM approach to detect buried objects by exciting the object with a seismic wave and using radio frequency (RF) antennas close to the surface of the soil to measure the scattered EM response while the objects are under seismic illumination. Lawrence, Buerkle, and Sarabandi [5, 7, 9–11] investigated theoretical implementations of the acousto-EM scattering by developing mathematical models for the scattered EM fields produced by an object excited with a high power acoustic source at stand-off ranges. Thus, Scott *et al.* and Lawrence, Buerkle, and Sarabandi show experimentally and theoretically that the resultant reflected and scattered EM signals are modulated with characteristics unique to the structure and composition of the vibrating object, thereby providing information about the structure of the target as well as distinguishing it from clutter.

To develop a mathematical model to describe the scattering of an EM signal in an acousto-EM sensing system, Sections 2.4.1 and 2.4.2 will discuss Doppler theory and amplitude modulation, respectively, as they pertain to EM waves in the presence of vibrating structures.

2.4.1 Doppler Theory

In the conventional analysis of interacting acoustic and EM waves, the Doppler effect is solely responsible for the resultant scattered EM fields, as the acoustic waves generate a sinusoidal vibrational motion on an object that shifts the frequency of an RF signal. The vibrational motion varies the distance of the object relative to the EM source which modulates the phase of the reflected RF signal. Thus, the reflected frequency f_r can be expressed as

$$f_r = f_{\text{RF}} \left(\frac{1 - v/c_{\text{RF}}}{1 + v/c_{\text{RF}}} \right), \quad (2.90)$$

where f_{RF} is the frequency of the transmitted RF signal, v is the velocity of the object, and c_{RF} is the speed of light. Using a Maclaurin series expansion and since the velocity of the object is

typically much less than the speed of light in most radar applications ($v \ll c_{\text{RF}}$), (2.90) can be simplified as

$$f_r = f_{\text{RF}} \left(1 - \frac{2v}{c_{\text{RF}}} \right). \quad (2.91)$$

Therefore, given the transmitted RF signal $g(t) = \cos \omega_{\text{RF}} t$, the reflected signal $s(t)$ can be expressed

$$s(t) = \cos \left[\omega_{\text{RF}} t \left(1 - \frac{2v}{c_{\text{RF}}} \right) \right] = \cos [\omega_{\text{RF}} t + 2k_{\text{RF}} v(t)], \quad (2.92)$$

where ω_{RF} is the radian frequency of the transmitted RF signal with the corresponding wavenumber k_{RF} and $v(t)$ is the velocity of the object at time t . Thus, from (2.92), it can be seen that the vibrational motion of the object modulates the phase of the transmitted RF signal. The phase term can be considered the change in phase over the distance between the EM source and vibrating object, therefore, the velocity can be replaced by the time-varying distance $r(t) = R_0 + d(t)$, where R_0 is the distance when the object is stationary and $d(t)$ is the vibrational displacement of the object. For the simple case of a constant velocity, $d(t) = vt$, the conventional Doppler equation in (2.92) is obtained. Considering a sinusoidal surface displacement, as would be encountered with a vibrating object under acoustic illumination, the displacement can be expressed as $d(t) = d_V \cos(\omega_V t)$ where d_V is the vibrational displacement amplitude and ω_V is the vibration radian frequency. The reflected signal, (2.92), can then be rewritten as

$$s(t) = \cos [\omega_{\text{RF}} t + 2k_{\text{RF}} d_V \cos(\omega_V t)], \quad (2.93)$$

where the $2k_{\text{RF}} R_0$ phase term has been ignored as it is produced by the propagation of the EM wave and not the vibrational motion of the object. Expanding (2.93) into its complex exponential form and using the Jacobi-Anger expansion, the reflected signal can again be rewritten as [109]

$$s(t) = \sum_{n=1}^{\infty} \frac{(2\pi)^n}{n!} \left(\frac{d_V}{\lambda_{\text{RF}}} \right)^n \cos [(\omega_{\text{RF}} \pm n\omega_V)t \pm n\frac{\pi}{2}]. \quad (2.94)$$

Thus, the RF signal reflected from a vibrating object produces a broad frequency spectrum containing the transmitted RF signal as well as modulation sidebands spaced at intervals of the vibration frequency, as illustrated in Fig. 2.6.

Considerable effort has been put into understanding the scattering of an RF signal by a vibrating structure [110–118]. Borkar and Yang [110] developed solutions for the fields scattered by oscillating plane and cylindrical surfaces. Kleinman and Mack [111] presented solutions accounting for the Doppler shift when determining the fields scattered by linearly vibrating objects. De Zutter [112] investigated the effect of translational motion in the generation of a scattered

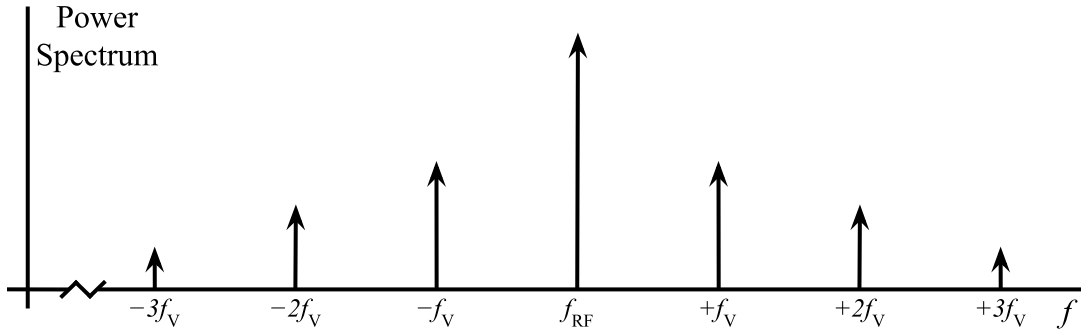


Figure 2.6: Frequency spectrum of an RF signal scattered by a vibrating object with modulation sidebands produced by the Doppler effect. The spectrum is centered at the frequency of the transmitted RF signal f_{RF} with modulation sidebands at $f_{\text{RF}} \pm n f_V$.

RF field and Cooper [113] and Gray and Addison [117] considered the effect of nonuniform motion on the resultant EM spectrum. Van Bladel and De Zutter [114] and De Zutter [115] derived solutions for the scattered fields from sinusoidally moving plates interrogated at normal and oblique incidences, respectively. From these works it can be seen that sidebands in the scattered EM spectrum resulting from a vibrating surface has traditionally been attributed solely to the Doppler effect. This assumption that the Doppler effect is the singular physical mechanism in which a scattered spectrum is generated has also been extended to a variety of applications in order to account for EM scattering from vibrating objects, particularly radar [116–118].

2.4.2 Amplitude Modulation

While the scattering of an EM wave has traditionally been attributed to the Doppler effect, which manifests as a phase modulation (PM), the modulation of an EM wave can also be produced from amplitude modulations (AM). Both modulation modes contain useful information, however, they are commonly interpreted differently depending on the sensing system implementation and processing performed on the received signal. Historically, AM has been ignored in the analysis of EM scattering from vibrating objects as the overall contribution to the power of the modulation sidebands has been considerably less than the PM introduced by the Doppler effect and often below the measurable noise floor of the system. However, advancement in analog cancellation technologies has significantly improved the dynamic range of RF measurement systems allowing for the improved detection capability of low-frequency and low-level sideband modulation in a reflected signal [102, 119–122], thus prompting an initial re-examination of the fundamental physical mechanisms that produce scattering of an RF signal from vibrating objects [109]. Therefore, AM contributions due to special relativity, path loss, and radar cross

section (RCS) were examined and reintroduced into the analysis of a scattered RF signal by a vibrating object, as these contributions were previously considered insignificant.

The investigation into the AM of an RF signal will begin by examining the modulation effects due to special relativity. An expression for the modulated signal can be written

$$s(t) = \gamma(t) \cos(\omega_{\text{RF}} t), \quad (2.95)$$

where $\gamma(t)$ is the amplitude modulation term due to special relativity which can be expressed using relativistic boundary conditions and the d'Alembertian solution [117] as

$$\gamma(t) = \frac{1 - v(t)/c_{\text{RF}}}{1 + v(t)/c_{\text{RF}}}. \quad (2.96)$$

As with the Doppler effect, the velocity of the object can be defined as a sinusoidal motion, $v(t) = d_V \omega_V \cos(\omega_V t)$, so that with the use of the Maclaurin series expansion, (2.96) can be rewritten

$$\gamma(t) = 1 + 2 \sum_{n=1}^{\infty} (-1)^n \left(\frac{v(t)}{c_{\text{RF}}} \right)^n = 1 + 2 \sum_{n=1}^{\infty} (-1)^n \left(\frac{d_V \omega_V}{c_{\text{RF}}} \right)^n [\cos(\omega_V t)]^n. \quad (2.97)$$

Using the trigonometric expansion of the cosine term in (2.97) and following the derivation in [109] to develop the Fourier series coefficients, the amplitude modulation term can be found to be

$$\gamma(t) = F_{\gamma,0} + \sum_{n=1}^{\infty} F_{\gamma,n} \cos(n\omega_V t), \quad (2.98)$$

where

$$F_{\gamma,0} \approx 1, \quad F_{\gamma,n} \approx 4 \left(\frac{d_V \omega_V}{2c_{\text{RF}}} \right)^n = 4\pi^n \left(\frac{d_V}{\lambda_V} \right)^n, \quad (2.99)$$

where $\lambda_V = c_{\text{RF}}/f_V$ is the vibrational wavelength. Substituting (2.98) and (2.99) into (2.95), the received modulated signal can be rewritten

$$\begin{aligned} s(t) &= \left[F_{\gamma,0} + \sum_{n=1}^{\infty} F_{\gamma,n} \cos(n\omega_V t) \right] \cos(\omega_{\text{RF}} t) \\ &= F_{\gamma,0} \cos(\omega_{\text{RF}} t) + \sum_{n=1}^{\infty} \left\{ \frac{F_{\gamma,n}}{2} \cos[(\omega_{\text{RF}} \pm n\omega_V) t] \right\}. \end{aligned} \quad (2.100)$$

Therefore, the AM due to special relativity produces modulation sidebands at the same frequencies as the Doppler PM. Additionally, the amplitude ratio of the contribution from special relativity to that of the Doppler effect for the lowest-order modulation sideband is the ratio of the RF to the vibration frequency, indicating that the power contribution from special relativity

remains negligible in remote sensing applications where the RF frequency is much greater than the vibrational frequency.

The contribution of the far-field path loss on the modulation of an RF signal is additionally considered since the RF power on the object decreases with distance due to the spherical spreading of the wave, a critical component in acousto-EM sensing systems as they interrogate objects at stand-off ranges. As an object vibrates, the path distance between the EM source and object will vary introducing a modulation on the signal; thus, an expression for the modulated signal when considering path loss is

$$s(t) = A_{\text{PL}}(t) \cos(\omega_{\text{RF}} t), \quad (2.101)$$

where, when surface displacement of the object is sinusoidal $d(t) = d_V \cos(\omega_V t)$, the path loss AM can be defined as

$$A_{\text{PL}}(t) \propto \frac{1}{[R_0 - d(t)]^2} = \frac{1}{[1 - B \cos(\omega_V t)]^2}, \quad (2.102)$$

where $B = d_V/R_0$ is the distance-normalized displacement amplitude. Again, using the Maclaurin series expansion and developing the Fourier series coefficients, (2.102) becomes [109]

$$A_{\text{PL}}(t) = \sum_{n=0}^{\infty} (n+1) [B \cos(\omega_V t)]^n = F_{\text{PL},0} + \sum_{n=1}^{\infty} F_{\text{PL},n} \cos(n\omega_V t), \quad (2.103)$$

where

$$F_{\text{PL},0} \approx 1, \quad F_{\text{PL},n} \approx 2(n+1) \left(\frac{B}{2}\right)^n = \left(\frac{2(n+1)}{2^n}\right) \left(\frac{d_V}{R_0}\right)^n. \quad (2.104)$$

Substituting (2.103) and (2.104) into (2.101), the received modulated signal can be rewritten

$$\begin{aligned} s(t) &= \left[F_{\text{PL},0} + \sum_{n=1}^{\infty} F_{\text{PL},n} \cos(n\omega_V t) \right] \cos(\omega_{\text{RF}} t) \\ &= F_{\text{PL},0} \cos(\omega_{\text{RF}} t) + \sum_{n=1}^{\infty} \left\{ \frac{F_{\text{PL},n}}{2} \cos[(\omega_{\text{RF}} \pm n\omega_V) t] \right\}. \end{aligned} \quad (2.105)$$

Again, the far-field path loss AM produces modulation sidebands at the same frequencies as the Doppler PM. Similar to AM due to special relativity, the power contribution will be much less than Doppler PM, however, unlike the other modulation types, path loss AM is independent of the RF wavelength.

Common examination of a vibrating object assumes only linear motion as to simplify the analysis, however, in practice, additional modes of motion are present, thereby requiring extra investigation into the effects of the physical geometry on the scattering of an EM wave. These

effects are typically accounted for by using RCS, which for simpler structures can have relatively simple approximations [123, 124]. An expression for an RCS modulated signal can be written

$$s(t) = A_{\text{RCS}}(t) \cos(\omega_{\text{RF}} t), \quad (2.106)$$

For the case of a flat, rectangular plate, the RCS, σ , expression is

$$\sigma_{\text{plate}} = \frac{4\pi A^2}{\lambda_{\text{RF}}^2} \cos^2 \theta \left[\frac{\sin(k_{\text{RF}} a \sin \theta)}{k_{\text{RF}} a \sin \theta} \right]^2, \quad (2.107)$$

where A is the area of the plate, a is the major dimension of the plate, and θ is the angle between the normal area vector of the plate and the propagation vector of the incident wave. Therefore, a plate that rotates in a rocking motion around its major axis will generate modulations as the angle θ changes over time. For a vibrational rocking motion where the angle varies sinusoidally, $\theta = \varphi \sin(\omega_V t)$, the RCS can be written

$$\sigma_{\text{plate}} \propto \cos^2(\varphi \sin \omega_V t) \left[\frac{\sin(k_{\text{RF}} a \sin(\varphi \sin \omega_V t))}{k_{\text{RF}} a \sin(\varphi \sin \omega_V t)} \right]^2, \quad (2.108)$$

where φ is the rotational amplitude of the vibration. The received modulated signal can then be found by inserting (2.108) into the radar equation [125] yielding

$$A_{\text{RCS}}(t) = \cos(\varphi \sin \omega_V t) \left[\frac{\sin(k_{\text{RF}} a \sin(\varphi \sin \omega_V t))}{k_{\text{RF}} a \sin(\varphi \sin \omega_V t)} \right]. \quad (2.109)$$

Similar to the approaches taken with AM due to special relativity and path loss, the expression for the received modulated signal is found by developing the Fourier series coefficients for RCS. Using the Jacobi-Anger expansion, (2.109) becomes [109]

$$\begin{aligned} A_{\text{RCS}}(t) &= \frac{2}{k_{\text{RF}} a \varphi} \sum_{m=0}^{\infty} J_{2m+1}(k_{\text{RF}} a \varphi) \frac{\sin[(2m+1)\omega_V t]}{\sin \omega_V t} \\ &= \frac{2}{k_{\text{RF}} a \varphi} \sum_{m=0}^{\infty} J_{2m+1}(k_{\text{RF}} a \varphi) \frac{4}{k_{\text{RF}} a \varphi} \sum_{n=1}^{\infty} \left[\sum_{m=0}^{\infty} J_{n+2m+1}(k_{\text{RF}} a \varphi) \right] \cos(2n\omega_V t) \\ &= F_{\text{RCS},0} + \sum_{n=1}^{\infty} F_{\text{RCS},n} \cos(2n\omega_V t), \end{aligned} \quad (2.110)$$

where

$$F_{\text{RCS},0} \approx 1, \quad F_{\text{RCS},n} \approx \frac{2}{(n+1)!} \left(\frac{k_{\text{RF}} a \varphi}{2} \right)^n = \frac{2(2\pi)^n}{(n+1)!} \left(\frac{a\varphi/2}{\lambda_{\text{RF}}} \right)^n. \quad (2.111)$$

Thus, substituting (2.110) and (2.111) in (2.106), the received modulated signal can be written

$$\begin{aligned} s(t) &= \left[F_{\text{RCS},0} + \sum_{n=1}^{\infty} F_{\text{RCS},n} \cos(2n\omega_V t) \right] \cos(\omega_{\text{RF}} t) \\ &= F_{\text{RCS},0} \cos(\omega_{\text{RF}} t) + \sum_{n=1}^{\infty} \left\{ \frac{F_{\text{RCS},n}}{2} \cos[(\omega_{\text{RF}} \pm 2n\omega_V) t] \right\}. \end{aligned} \quad (2.112)$$

Unlike the previous modulation types, the AM due to RCS produces only even modulation sidebands. Additionally, (2.112) has a similar form to that of Doppler PM as the plate linear edge deflection, $a\varphi/2$, takes the place of the vibrational displacement, d_V , in (2.94).

A comparison of the phase and amplitude modulations will be made in Chapter 5 as additional modulation effects caused by the propagation of a high powered acoustic wave through a medium are explored.

2.5 High Dynamic Range Nonlinear Measurement

Acousto-EM sensing systems offer many advantages over conventional remote sensing systems, however, a major issue is that they suffer from difficulty in measurement as acousto-EM scattering produces very low-level modulation sidebands close in frequency to the transmitted EM signal. This is a problem commonly encountered in modern day nonlinear measurement systems as noise and distortion on a signal, particularly from strongly nonlinear devices such as amplifiers, often appear in similar low-level, low-frequency conditions. The dynamic range of a system refers to its ability to detect these small signals in the presence of large signals and has received a significant amount of research as the desire to distinguish signals from background clutter and characterize signals that were previously undetectable has increased. Though there are several ways of defining dynamic range, depending upon the application, for the purposes of detecting the modulation sidebands produced within an acousto-EM sensing system, dynamic range is defined as the ratio of the measured input signal power to the minimum discernible signal at a given frequency offset from the input signal carrier. The dynamic range of a measurement system is critical in the detection of acousto-EM scattering as the interaction between the acoustic and EM waves is weakly nonlinear, requiring the use of high power signals to generate a detectable response. Thus, since the modulation sidebands will have significantly less power than the transmitted carrier signal and the frequency of the sidebands is dependent upon the vibration frequency, typically in the low kilohertz frequency range, a system with a high dynamic range is essential for practical implementation of an acousto-EM sensing system.

Conventional nonlinear measurement systems employ receivers, such as spectrum analyzers, that achieve dynamic range through designs that make them very linear, however, this approach

is unable to yield the dynamic ranges required to measure the low-level modulations produced by acousto-EM scattering, which are generally more than 100 dB below the received carrier signal. Therefore, to enable the measurement of small signals, the most common and successful approaches have attempted to eliminate the high power transmitted signal, routinely performed by implementing filtering and analog cancellation techniques to effectively lower the level of the minimum discernible signal and increase the system's dynamic range.

Filtering has been the long-established method for attempting to remove the high power signal from the measured response and is the most commonly implemented approach in commercially available nonlinear measurement systems. Analog filters are designed to operate across specific bandwidths where content at particular frequencies is passed through or strongly attenuated, with these frequency ranges termed passband and stopband, respectively. To remove the undesired high power signal, nonlinear measurement systems use bandstop filters where spectral content within a precise frequency range is attenuated while frequencies outside of this range remain unchanged, thereby lowering the power level of the measured input signal which, in turn, lowers the minimum discernible signal level. Ideal filters assume a direct transition between the bands at a single frequency but in real filters this transition takes place over a finite frequency range where there is a roll-off in attenuation, known as the filter skirt. Therefore, the use of filters can be inadequate if the small signals are close in frequency to the high power signal, locating them within the filter skirt and, thus, inaccurately attenuating the signals. To avoid these inaccuracies, a bandstop filter with a very narrow stopband and a steep filter skirt is required; however, in practical radar applications, this necessitates a filter designed with a quality factor higher than physically achievable, particularly in acousto-EM sensing applications where the small signals will be within a few kilohertz of the carrier signal. Thus, as an alternative approach for making high dynamic range nonlinear measurements, feedforward analog cancellation techniques have been developed to address the limitations of filter based measurement systems.

2.5.1 Analog Cancellation

Rather than attenuate an entire range of frequencies, as done with filtering based systems, feedforward analog cancellation eliminates only the high power input signal by combining it with a signal that has an equal amplitude but opposite phase resulting in a reduction in the power level of the measured input signal, thereby lowering the minimum discernible signal level. To implement this technique, the high power input signal is split and independently passed through the nonlinearity as well as amplitude and phase controls before being recombined to achieve cancellation, as shown in Fig. 2.7. The small signals are generated solely by the nonlinearity, therefore the feedforward signal that passed through the amplitude and phase controls will only

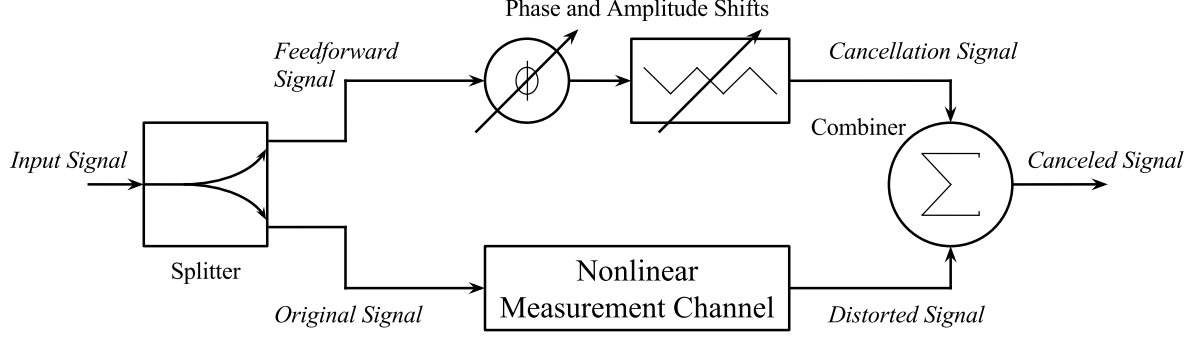


Figure 2.7: Feedforward analog cancellation implementation block diagram for use in high dynamic range nonlinear measurement systems.

effect the high power input signal upon recombination, thus improving the effective dynamic range of the system while leaving the small signals unaltered.

To achieve high levels of cancellation, accurate control of the amplitude and phase of the feedforward signal is critical as the the maximum achievable cancellation, given by (2.113), is determined by the ratio of the amplitudes of the feedforward and measurement signals and the discrepancy of the phase difference between the feedforward and measured signals and two perfectly anti-phased signals,

$$C_{A,\text{dB}} = -10 \log [1 + \epsilon_\alpha^2 - 2\epsilon_\alpha \cos(\epsilon_\phi)] , \quad (2.113)$$

where $C_{A,\text{dB}}$ is the achievable cancellation, ϵ_α is the amplitude error, and ϵ_ϕ is the phase error. Manual control of the amplitude and phase of the feedforward signal yields unsatisfactory results as amplitude and phase errors must be less than 0.1 dB and 0.6° , respectively, to achieve a cancellation of only 40 dB; therefore, measurement systems using analog cancellation typically automate control of the feedforward signal. Historically, automated control was performed with derivative-based iterative techniques that required a large number of iterations to achieve reasonable levels of cancellation, however, recent advancements have developed a predictive algorithm that determines the appropriate settings at each iteration of the system and performs calibrations during the cancellation process to better capture the nonlinear effects during measurement, thus enabling over 70 dB of cancellation to be achieved [109, 119, 120, 126].

By achieving such high levels of cancellation, the high dynamic range nonlinear measurement system developed by Wilkerson, Wetherington, and Steer [109, 119, 120, 126] is ideal for the measurement and characterization of acousto-EM scattering and Chapter 5 discusses its utilization as part of an acousto-EM sensing system employed to experimentally investigate the effect of medium fluctuations generated by a propagating acoustic wave on the scattering of an

EM signal.

2.6 Summary

Acousto-EM sensing is a hybrid sensing scheme that utilizes two orthogonal sensing modalities, acoustic and EM, to interrogate objects at distance, thereby providing the ability to ascertain unique information not attainable by conventional single modality remote sensing schemes. Practical implementation of acousto-EM sensing has been unattainable, however, as insufficient modeling capabilities for the nonlinear propagation of acoustic waves and the inability to measure the effects of the nonlinear interaction between acoustic and EM waves at stand off distances have limited the development of the sensing scheme. This chapter reviewed the current state of acousto-EM sensing by investigating recent theoretical and experimental developments pertaining to acoustically-induced scattering of an EM wave as well as examining the latest advancements in the generation and modeling of sound waves in nonlinear acoustics.

The KZK nonlinear parabolic wave equation is derived from the general motion of a fluid and is established as the fundamental equation of nonlinear acoustics, describing the propagation of an acoustic wave through a nonlinear medium. Common acoustic sources were then investigated with solutions to the KZK equation found for the primary and secondary sound fields radiated from each source. A review of several common numerical techniques used to solve the KZK equation, and the associated multiple field integrals, is also given since closed form solutions to the KZK equation can only be found under very limited conditions. The analysis was then extended to include the scattering of sound by sound whereby the acoustic field contains two or more interacting sound waves generated from collinear and noncollinear sources to produce second-order scattered acoustic fields. Primarily, previous research has focused on the parametric array, a special case of scattering of sound by sound, therefore, the development and application of these virtual sound sources was also discussed. The analytical models developed in Chapters 3 and 4 determine the scattered sound fields using methods that are computationally more efficient than the present theory. Chapter 3 extends the multi-Gaussian beam expansion technique to model the third-order scattered sound fields produced by the scattering of sound by sound. Chapter 4 implements a near-to-far-field transformation technique that enables far-field radiation patterns of the second-order scattered sound fields to be determined from data collected in the near-field.

Acousto-EM scattering is the physical phenomenon describing the scattering of an EM signal due to the nonlinear interaction with an acoustic wave. Traditionally, the scattering has been attributed solely to phase modulations introduced by the Doppler effect, however, recent investigations, prompted by advancements in nonlinear measurement systems, have shown that amplitude modulations due to special relativity, path loss, and radar cross section also con-

tribute to the scattering process. High dynamic range nonlinear measurement systems using feedforward analog cancellation techniques are critical in enabling the detection of these effects, as the modulations are quite small compared to the high power stimulus used in the sensing scheme. Chapter 5 continues this examination into the fundamental mechanisms that result in the scattering of an EM signal by exploring the effect acoustically-induced medium fluctuations have on an EM signal.

Chapter 3

Computationally Efficient Modeling of Third-Order Scattering of Sound by Sound

3.1 Introduction

Nonlinear interactions of high frequency acoustic signals in air produce a scattered sound field that radiates energy into the harmonics and the sum and difference frequencies of the primary interacting signals. The scattered sound fields can have very high directivity [39, 65] and are used in sound projection [21], acoustic radar [22], and sonar [23]. The source of both scattering and directivity is the nonlinearity of the acoustic medium and calculations of the scattered field using traditional methods is computationally intensive preventing the use of these calculations in real time. Such calculations are required to characterize the sound beam produced as the sound pressure level and the medium's characteristics such as density and, in the case of air, humidity change.

Westervelt initially described the scattering of sound by sound using two independent acoustic waves [19] and since then the modeling of this phenomenon has received much attention. As a one-dimensional manipulation of the Westervelt equation, the Burgers equation [46] accounts for the nonlinearity and dissipation of a plane wave as it propagates through a medium. By modifying the Burgers equation, Khokhlov, Zabolotskaya, and Kuznetsov incorporated the contributions of diffraction and absorption along with the nonlinearity and dissipation of the medium to produce the fully nonlinear wave equation known as the Khokhlov-Zabolotskaya-Kuznetsov (KZK) equation [12, 13]. This equation accurately represents the nonlinear propagation of a finite-amplitude sound beam generated by an arbitrarily shaped source and has become instrumental in modeling the nonlinear scattering of sound, with particular focus on

the development and application of ultrasonic parametric arrays [39, 41, 127].

With a well-defined expression describing nonlinear acoustic propagation, considerable effort has been put forth to expand upon Westervelt's original idea of the parametric array, in which a highly directional sound beam is generated from a two-tone primary field consisting of perfectly collimated, planar waves such that the resultant intermodulation products are continuously pumped and propagate in the same direction as the primary fields [45]. Tjøtta and Tjøtta [37] considered spherically spreading primary sound beams from collinear sources and developed asymptotic solutions of the generated sound, including contributions from the near-field. Aanonsen *et al.* [24] and Hamilton *et al.* [25] developed expressions for the primary and harmonic sound fields in the near- and far-field showing the validity of the fully nonlinear equation in both regions. Berntsen *et al.* [26] developed expressions for the secondary sound field valid into the far-field of an acoustic transducer. Garrett *et al.* [27], along with many others [28–36], analyzed the primary and secondary sound fields generated from parametric radiation comparing numerical results with theory and measurements from earlier works.

All of the techniques above require substantial computation which prevents their use in real-time simulation as required in some sensor applications. The long computation times derive from the use of numerical techniques such as finite difference methods that solve the nonlinear wave equation. To improve the computational efficiency of the sound field calculations, the use of expansion techniques based on the idea that sound beams can be expressed as a series of base functions has been proposed. Cavanagh and Cook [14] and Wen and Breazeale [15] provided the initial development of numerical models for the primary field of a circular plane baffled transducer using a series of Gaussian-Laguerre and Gaussian base functions, respectively. Similarly, Hasegawa *et al.* [56] developed an expression for the velocity potential of a circular piston radiator using a series expansion consisting of spherical Bessel functions, spherical Hankel functions of the second kind, and Legendre polynomials. Ding has since presented a series of papers that expand upon Wen and Breazeale's work by extending the expansion technique with Gaussian base functions also describing the second-order sound fields [16–18]. The sound field expressions found for the primary and secondary fields using a series of base functions have the advantage of yielding simple analytic solutions that are computationally more efficient than previous methods.

Nearly always, the second-order mixing is only considered although recently it has been shown that third-order interactions derived from cascaded second-order interactions result in very narrow sound beams [39]. The improvement in beam pattern gained by using higher-order fields has recently generated interest for use in a variety of applications, such as biomedical imaging [128–131] and non-destructive evaluation [87]. For use in biological media, Liu *et al.* [129] developed expressions for higher-order acoustic fields by including commonly ignored third-order terms in an investigation of the third-order nonlinear parameter. With similar applications

proposed, Zu-wen [130], with corrections by Mitri [131], derived third-order velocity and pressure equations that describe the harmonic generation of infinite plane acoustic waves within fluids. This chapter presents a computationally-efficient model for third-order nonlinear interaction of two primary sound beams using the series expansion of a set of Gaussian base functions. The model is then extended to show that it can accurately represent the sound fields generated from parametric transducer arrays—acoustic sources where the two-tone primary field is generated using multiple collinear transducers resulting in a radiated parametric sound field with higher power and greater directionality than achievable with a single transducer equivalent in size. Section 3.2 is a theoretical development of the first- and second-order field integrals derived from the Westervelt and KZK wave equations and describes the development of the third-order field integral that follows the cascaded second-order approach [38, 39]. Section 3.3 develops the sound field expressions for the primary, secondary, and tertiary waves in terms of the Gaussian base functions. Section 3.3.1 describes the radiated sound fields generated by the nonlinear interactions of the parametric transducer array in terms of the Gaussian base function solutions presented in the previous sections. Section 3.4 demonstrates that the analytical results of the third-order and parametric array sound field models are in good agreement with measurements and theory presented by previous authors. Section 3.5 compares the computational efficiency of the results achieved using the Gaussian base function solutions with the efficiency obtained using conventional numerical methods. Section 3.6 details the design criteria required to enhance the performance of the third-order parametric array.

3.2 Third-Order Quasilinear Solution

Westervelt’s derivation of the inhomogeneous wave equation [19] from Lighthill’s equation for arbitrary fluid motion [47] is the fundamental statement of nonlinear acoustics, as derived in Section 2.2. Given in (2.27), the Westervelt equation is reproduced here, ignoring effects from sound diffusivity, as

$$\nabla^2 p - \frac{1}{c_0^2} \frac{\partial^2 p}{\partial t^2} = -\frac{\beta}{\rho_0 c_0^4} \frac{\partial^2 p^2}{\partial t^2}, \quad (3.1)$$

where p is the acoustic pressure comprised of the primary and scattered sound fields as a function of position and time t , c_0 is the small-signal sound speed, ρ_0 is the medium density, β is the coefficient of nonlinearity, and ∇^2 is the Laplace operator. Khokhlov, Zabolotskaya, and Kuznetsov expanded upon Westervelt’s work by combining the effects of diffraction and absorption with the medium nonlinearity, thus developing the KZK nonlinear parabolic wave equation in which this theory is based [12, 13]. The KZK equation is given in (2.30) for nondissipative

fluids and reproduced here, also ignoring the effects from sound diffusivity, as

$$\frac{\partial^2 p}{\partial z \partial \tau} - \frac{c_0}{2} \nabla_{\perp}^2 p = \frac{\beta}{2\rho_0 c_0^3} \frac{\partial^2 p^2}{\partial \tau^2}, \quad (3.2)$$

where z is the Cartesian coordinate in the direction of wave propagation, $\nabla_{\perp}^2 = \partial^2/\partial x^2 + \partial^2/\partial y^2$ is the second-order spatial gradient transverse to the direction of propagation, $\tau = \omega_i t - k_i z$ is the retarded time, and $k_i = \omega_i/c_0$ is the wave number of the acoustic wave at angular frequency ω_i . The subscript ‘ i ’ denotes the desired primary frequency, where $i = 1, 2$ and $\omega_1 > \omega_2$.

In order to solve the KZK equation, linearized solutions for the primary fields and quasilinear solutions for the secondary fields can be derived as is commonly done in the literature. This approach is used to obtain integral equations for the second- and third-order sound fields in a form which can be easily discretized. Following the standard approach under the quasilinear approximation, the acoustic pressure in (3.1) and (3.2) is restricted to consist only of the two primary frequencies and the second-order sound field resulting from the interaction of the primary fields. Therefore, as was given in (2.53), the acoustic pressure, p , can be written for the primary and secondary sound fields as

$$p = \sum_{i=1}^2 p_{1i} + \sum_{\varsigma} p_{2\varsigma} = p_{11} + p_{12} + p_{21} + p_{22} + p_{2S} + p_{2D} \quad (3.3)$$

where p_{1i} indicates the i th primary field and $p_{2\varsigma}$ indicates the second-order scattered field. The scattered field subscript ‘ ς ’ specifies the choice of one of the two second harmonics, sum, and difference frequencies, $\varsigma = 1, 2, S, D$ respectively, as explained in Section 2.2.2.

The development of the solution begins by expressing the sound field equations in terms of the nondimensional field variables $\xi = r/a$ and $\eta_i = 2z/k_i a^2$ that correspond to the radial and axial coordinates, r and z respectively, where a is the radius of the source. The linearized solution of the primary sound field for angular frequency ω_i can then be written [41]

$$p_{1i}(\xi, \eta_i, \tau_i) = \Re \{ p_{0i} e^{-j\tau_i} q_{1i}(\xi, \eta_i) \}, \quad (3.4)$$

where the integral solution for the primary sound field given in (2.35) is normalized as

$$q_{1i}(\xi, \eta_i) = 2\pi \int_0^\infty q_{1i}(\xi', 0) G_1(\xi, \eta_i | \xi', \eta'_i) \xi' d\xi'. \quad (3.5)$$

In (3.5), $q_{1i}(\xi', 0)$ is the function that describes the type of source for angular frequency ω_i located in the $\eta' = 0$ plane. For a simple Gaussian source, this is defined by a Gaussian function, as given in (2.39),

$$q_{1i}(\xi', 0) = p_{0i} \exp(-b\xi'^2), \quad (3.6)$$

where p_{0i} is the peak pressure and b is an arbitrary, real constant corresponding to the shape of the resultant beam. $G_1(\xi, \eta_i | \xi', \eta'_i)$ is the Green's function which is derived following the method in [41], as detailed in Section 2.2.1, and expressed here as a normalized form of (2.38)

$$G_\sigma(\xi, \eta_i | \xi', \eta'_i) = \frac{j\sigma}{(\eta_i - \eta'_i)} J_0 \left(\frac{2\sigma\xi\xi'}{\eta_i - \eta'_i} \right) \exp \left[\frac{j\sigma(\xi^2 + \xi'^2)}{\eta_i - \eta'_i} \right]. \quad (3.7)$$

Similarly, the quasilinear solution of the second-order sound field can be written [17]

$$p_{2\varsigma}(\xi, \eta, \tau) = \Re \left\{ -p_{01}p_{02}(l+m)^2 \left[\frac{\beta(ka)^2}{\rho_0 c_0^2} \right] e^{-j(l+m)\tau} q_{2\varsigma}(\xi, \eta) \right\}, \quad (3.8)$$

where the integral solution for the secondary sound field given in (2.56) is normalized as

$$q_{2\varsigma}(\xi, \eta) = \frac{1}{2} \int_0^\eta \int_0^\infty q_{11}(\xi', \eta') q_{12}(\xi', \eta') G_{2\varsigma}(\xi, \eta | \xi', \eta') \xi' d\xi' d\eta'. \quad (3.9)$$

Again, it is important to note that the second-order sound field, (3.8), is comprised of the second harmonics and tones at the sum and difference frequencies. In the above equations, $p_{0i} = \rho_0 c_0 u_{0i}$ is the peak acoustic pressure where u_{0i} is the amplitude of the vibration velocity of the source for the i th primary frequency. For the second-order sound fields, the parameters are normalized to the center of the primary wave numbers, $k = (k_1 + k_2)/2$. Therefore, the normalized wave numbers of the primary fields are $l = k_1/k$ and $m = k_2/k$, the retarded time becomes $\tau = \omega t - kz$ where $\omega = kc_0$, the nondimensional axial coordinate becomes $\eta = 2z/ka^2$, and the radius of the source, a , is chosen as the average radius of the two sources, $q_{11}(\xi', 0)$ or $q_{12}(\xi', 0)$. As previously stated, the subscript ' ς ' identifies the choice of one of the two second harmonics, and sum and difference frequencies, $\varsigma = 1, 2, S, D$ respectively. Thus, ς sets the values for l and m to select the identified frequency component. For example, the second harmonic of the first primary field, p_{21} , is selected when $k_1 = k_2$ ($l = m = k_1/k$), the sum frequency, p_{2S} , is selected when $l = k_1/k$ and $m = k_2/k$, and the difference frequency, p_{2D} , is selected when $l = k_1/k$ and $m = -k_2/k$. Similarly, when calculating the Green's function, σ is the normalized wave number and is set to 1 for the primary frequency, 2 for the second harmonic, and is replaced by $l + m$ for the sum and difference frequencies.

The development of the third-order solutions is based upon the cascaded second-order approach originally proposed by Garner and Steer [39]. This method takes the concept of quadratic nonlinearity that produces the second-order sound field through the interaction of two primary sound beams and applies it to the interaction of the secondary field with the primary field to generate the third-order sound fields. For the purposes of this chapter, the interactions of these fields are limited to only include the contributions of the fundamental, second harmonic, and difference frequencies to the generation of the third harmonics and the upper and lower

third-order intermodulation (IM3) products: $\omega_{3U} = 2\omega_1 - \omega_2$ and $\omega_{3L} = 2\omega_2 - \omega_1$. For the intermodulation tones to be produced in the audio band, the primary frequencies must be distantly spaced ($\omega_1 \leq 2\omega_2$) so that the secondary fields $2\omega_2$ and $\omega_1 - \omega_2$ interact with the primary fields to yield the third-order audio tones. Expanding the acoustic pressure, p , to include the third-order tones, as was done in (2.69), it can be written

$$\begin{aligned} p &= \sum_{i=1}^2 p_{1i} + \sum_{\varsigma} p_{2\varsigma} + \sum_{\zeta} p_{3\zeta} \\ &= p_{11} + p_{12} + p_{21} + p_{22} + p_{2S} + p_{2D} + p_{31} + p_{32} + p_{3U} + p_{3L} \end{aligned} \quad (3.10)$$

where p_{1i} and $p_{2\varsigma}$ indicate the first- and second-order sound fields, as previously defined, and $p_{3\zeta}$ indicates the third-order tones. Similarly to its use in identifying the second-order scattered fields, the subscript ‘ ζ ’ specifies the choice of one of the two third harmonics, upper, and lower IM3 tones, $\zeta = 1, 2, U, L$ respectively.

Under these conditions the solutions for the desired third-order sound fields can be found. The solution for these fields can be written

$$p_{3\zeta}(\xi, \eta, \tau) = \Re \left\{ P_{3\zeta}(l + m + h)^2 \left[\frac{\beta(ka)^2}{\rho_0 c_0^2} \right]^2 e^{-j(l+m+h)\tau} q_{3\zeta}(\xi, \eta) \right\}, \quad (3.11)$$

where the integral solutions for the tertiary sound fields given in (2.73), (2.74), and (2.75) are normalized as

$$q_{3i}(\xi, \eta) = \frac{4}{3} \int_0^\eta \int_0^\infty (q_{1i}(\xi', \eta'))^3 G_3(\xi, \eta \mid \xi', \eta') \xi' d\xi' d\eta', \quad (3.12)$$

$$q_{3U}(\xi, \eta) = \frac{4}{3} \int_0^\eta \int_0^\infty [q_{21}(\xi', \eta') q_{12}^*(\xi', \eta') + q_{11}(\xi', \eta') q_{2D}(\xi', \eta')] G_{3U}(\xi, \eta \mid \xi', \eta') \xi' d\xi' d\eta', \quad (3.13)$$

$$q_{3L}(\xi, \eta) = \frac{4}{3} \int_0^\eta \int_0^\infty [q_{22}(\xi', \eta') q_{11}^*(\xi', \eta') + q_{12}(\xi', \eta') q_{2D}^*(\xi', \eta')] G_{3L}(\xi, \eta \mid \xi', \eta') \xi' d\xi' d\eta'. \quad (3.14)$$

As can be seen in (3.11)–(3.14), the third-order sound field solutions consist of contributions from second-order sound fields interacting with the primary waves. It is worth mentioning that the upper and lower IM3 tones are composed of a pair of interactions between both primary sound fields and corresponding second-order fields. Since each pair consists of a different combination of primary and secondary interacting sound fields, it is required to calculate them separately, as will be discussed below and in Section 3.3.

As with the second-order sound fields, the wave numbers corresponding to the primary and

secondary fields are normalized to the center of the primary wave numbers, $k = (k_1 + k_2)/2$. The normalized wave numbers $l = k_1/k$ and $m = k_2/k$ are defined in such a way as to describe the second-order sound field contribution, where $k_1 = k_2$ ($l = m = k_1/k$) for the second harmonic and $l = k_1/k$ and $m = -k_2/k$ for the difference frequency. The additional wave number, h , is the normalized wave number of the contributing primary sound field component. As previously stated, the subscript ‘ ζ ’ identifies the choice of one of the two third harmonics, upper, and lower IM3 tones, $\zeta = 1, 2, U, L$ respectively. Thus, ζ sets the values for l , m , and h to select the identified frequency component as well as the peak acoustic pressure amplitude, $P_{3\zeta}$. For example, the third harmonic of the first primary field, p_{31} , is defined in (3.12) with $P_{3\zeta} = p_{01}^3$ and is selected when $k_1 = k_2$ ($l = m = h = k_1/k$). The upper IM3 tone, p_{3U} , is defined in (3.13) with $P_{3\zeta} = p_{01}^2 p_{02}$ and is given by the addition of the first pair of interacting fields, the second harmonic of the first primary field with the second primary field (selected when $l = k_1/k$, $m = k_1/k$, and $h = -k_2/k$), and the second pair of interacting fields, the difference frequency with the first primary field (selecting $l = k_1/k$, $m = -k_2/k$, and $h = k_1/k$). Similarly, the lower IM3 tone, p_{3L} , is defined in (3.14) with $P_{3\zeta} = p_{01} p_{02}^2$ and is given by the addition of the first pair of interacting fields, the second harmonic of the second primary field with the first primary field (selected when $l = k_2/k$, $m = k_2/k$, and $h = -k_1/k$), and the second pair of interacting fields, the difference frequency with the second primary field (selected when $l = k_2/k$, $m = -k_1/k$, and $h = k_2/k$). While both pairs of interacting fields for a given IM3 tone have the same sum of the normalized wave numbers ($l + m + h$), the definition of the value for each wave number differs between the pairs and, therefore, the pairs require separate calculation. As before, when calculating the Green’s function, σ is the normalized wave number and is set to 3 for the third harmonic and is replaced by $l + m + h$ for the intermodulation frequencies.

3.3 Gaussian Beam Expansion

The fundamental sound field of an axially symmetric circular piston can be described using the multi-Gaussian beam (MGB) expansion model whereby the acoustic source is defined as a linear superposition of Gaussian beams [15], as developed in Section 2.2.1 and given by (2.49),

$$q_{1i}(\xi, \eta_i) = \sum_{n=1}^N \frac{A_n}{1 + jB_n\eta_i} \exp\left(-\frac{B_n\xi^2}{1 + jB_n\eta_i}\right). \quad (3.15)$$

where, again, A_n and B_n are the Gaussian coefficient set and beam waist parameters, respectively, and N is the number of functions within the series as defined by the Gaussian coefficient set. By defining the primary sound field in this manner, it has been shown that a closed form solution for the second-order sound fields can be developed that is computationally more effi-

cient than traditional methods used to determine the fields. Therefore, with the substitution of (3.15) into (3.9), the simplified solution for the second-order sound fields can be found following the derivation in [17], as shown in Section 2.2.2, yielding

$$q_{2s}(\xi, \eta) = \sum_{n=1}^N \sum_{j=1}^N \frac{A_n A_j}{4r_1} \exp\left(-\frac{s_1 \xi^2}{r_1}\right) \left[E_1\left(\frac{s_2 \xi^2}{r_1(r_1 \eta + r_2)}\right) - E_1\left(\frac{s_2 \xi^2}{r_1 r_2}\right) \right], \quad (3.16)$$

where

$$r_1 = (lB_j + mB_n) + j(l+m)\eta B_n B_j, \quad (3.17a)$$

$$r_2 = (lB_n + mB_j)\eta - j(l+m), \quad (3.17b)$$

$$s_1 = (l+m)^2 B_n B_j, \quad (3.17c)$$

$$s_2 = -j(l+m)lm(B_n - B_j)^2, \quad (3.17d)$$

and $E_1(x) = \int_x^\infty t^{-1} e^{-t} dt$ is the exponential integral function.

Since the first- and second-order sound field solutions are expressed in closed-form, they can be used to find a solution for the third-order sound fields. Substituting (3.15) and (3.16) into (3.12)–(3.14), the third-order sound field can be expressed as

$$\begin{aligned} q_{3s}(\xi, \eta) = & \sum_{n=1}^N \sum_{j=1}^N \sum_{f=1}^N \frac{1}{3} \int_0^\eta \int_0^\infty \frac{A_n A_j A_f \xi'}{(\eta - \eta')(1 + jB_f \eta')(r'_1)} J_0\left(\frac{2(l+m+h)\xi \xi'}{\eta - \eta'}\right) \\ & \times \exp\left(-\frac{hB_f \xi'^2}{1 + jB_f \eta'}\right) \exp\left(-\frac{s_1 \xi'^2}{r'_1} + \frac{j(l+m+h)(\xi^2 + \xi'^2)}{\eta - \eta'}\right) \\ & \times \left[E_1\left(\frac{s_2 \xi'^2}{r'_1(r'_1 \eta' + r'_2)}\right) - E_1\left(\frac{s_2 \xi'^2}{r'_1 r'_2}\right) \right] d\xi' d\eta'. \end{aligned} \quad (3.18)$$

Using the Taylor series expansion for the exponential integral function, given by

$$E_1(z) = -\gamma - \ln z - \sum_{n=1}^{\infty} \frac{(-z)^n}{nn!} \quad (3.19)$$

where γ is the Euler-Mascheroni constant, and the known integral formulas for Bessel and Gaussian functions in (3.20) and (3.21), the third-order sound field solution in (3.18) can be simplified, yielding an expression in terms of only the axial field integral, η' :

$$\int_0^\infty e^{-a^2 t^2} t^{\mu+1} J_\mu(bt) dt = \frac{b^\mu}{(2a^2)^{\mu+1}} e^{-(b^2/4a^2)} \quad (3.20)$$

and

$$\int_0^\infty e^{-a^2 t^2} t^{\mu-1} J_\nu(bt) dt = \frac{\Gamma\left(\frac{1}{2}\nu + \frac{1}{2}\mu\right) \left(\frac{1}{2}\frac{b}{a}\right)^\nu}{2a^\mu \Gamma(\nu+1)} M\left(\frac{1}{2}\nu + \frac{1}{2}\mu, \nu+1, -\frac{b^2}{4a^2}\right), \quad (3.21)$$

where the gamma function is given by

$$\Gamma(n) = (n-1)!, \quad (3.22)$$

for all positive integers n and

$$M(a, b, z) = \sum_{n=0}^{\infty} \frac{a^{(n)} z^n}{b^{(n)} n!} \quad (3.23)$$

is the confluent hypergeometric function [53] where

$$a^{(0)} = 1, \quad (3.24)$$

$$a^{(n)} = a(a+1)(a+2) \dots (a+n-1), \quad (3.25)$$

is the rising function. (3.23) is Kummer's function of the first kind and is a generalized hypergeometric series that is considered a function of a , b , or z (with the other two held constant).

Thus, by assuming an axially symmetric source and simplifying (3.18), the third-order sound field for the given interaction pair can be expressed using the MGB expansion method as

$$\begin{aligned} q_{3\zeta}(\xi, \eta) = & \sum_{n=1}^N \sum_{j=1}^N \sum_{f=1}^N \exp\left(-\frac{s_3 \xi^2}{r_3}\right) \int_0^\eta \frac{A_n A_j A_f}{6(r_3 \eta' + r_4)} \exp\left(-\frac{s_4 \xi^2}{r_3(r_3 \eta' + r_4)}\right) \\ & \times \left[\ln\left(1 + \frac{r'_1}{r'_2} \eta'\right) + \sum_{u=1}^{\infty} \frac{(-1)^{u+1}}{u u!} \Gamma(u+1) \left[\left(\frac{s_2}{r'_1(r'_1 \eta' + r'_2)}\right)^u - \left(\frac{s_2}{r'_1 r'_2}\right)^u \right] \right. \\ & \times \left. \left(\sqrt{\frac{r'_1(1 + j B_f \eta')(\eta - \eta')}{r_3 \eta' + r_4}} \right)^{u+1} M\left(-u, 1, \frac{s_5 \xi^2}{(r_3 \eta' + r_4)(\eta - \eta')}\right) \right] d\eta', \quad (3.26) \end{aligned}$$

where

$$r_3 = (l + m) [(lB_jB_f + mB_nB_f + hB_jB_n) + j(l + m + h)B_jB_nB_f\eta], \quad (3.27a)$$

$$r_4 = [(l + m)^2B_jB_n + hB_f(lB_j + mB_n)]\eta - j(l + m + h)(lB_j + mB_n), \quad (3.27b)$$

$$s_3 = (l + m + h)^2(l + m)^2B_jB_nB_f, \quad (3.27c)$$

$$s_4 = j(l + m + h)(l + m)^2 [(lB_j + mB_n)(2(l + m) + h)hB_jB_nB_f \\ - (l + m)^2h(B_f^2 + B_jB_n)B_jB_n - (l + m)h(B_n^2(h(B_j + mB_f) + B_j^2(hB_n + lB_f))], \quad (3.27d)$$

$$s_5 = (l + m + h)^2 [(lB_j + mB_n) - (l + m)B_jB_nB_f\eta'^2 \\ + j((l + m)B_jB_n + B_f(lB_j + mB_n))\eta']. \quad (3.27e)$$

Additionally, r'_1 and r'_2 are equivalent to (3.17a) and (3.17b) where η is replaced by η' . On the acoustic axis where $\xi = 0$, this simplifies to

$$q_{3\zeta}(0, \eta) = \sum_{n=1}^N \sum_{j=1}^N \sum_{f=1}^N \int_0^\eta \frac{A_n A_j A_f}{6(r_3\eta' + r_4)} \left[\ln \left(1 + \frac{r'_1}{r'_2} \eta' \right) + \sum_{u=1}^{\infty} \frac{(-1)^{u+1}}{uu!} \Gamma(u+1) \right. \\ \left. \times \left[\left(\frac{s_2}{r'_1(r'_1\eta' + r'_2)} \right)^u - \left(\frac{s_2}{r'_1 r'_2} \right)^u \right] \left(\sqrt{\frac{r'_1(1 + jB_f\eta')(\eta - \eta')}{r_3\eta' + r_4}} \right)^{u+1} \right] d\eta'. \quad (3.28)$$

Again, it is necessary to solve (3.26) for both pairs of interacting sound fields to generate the complete third-order sound field for a given IM3 tone.

It can be seen that the third-order sound field solution derived in (3.26) and (3.28) is considerably simplified relative to previously reported methods. The single field integral in (3.26) is computationally more efficient than the triple field integral method used in [39] and the implicit backward finite difference method to solve the coupled partial differential equations in [34], along with many other implementation schemes for second- and third-order sound fields, as discussed in Section 2.3.

3.3.1 Application to Parametric Transducer Arrays

The sound field solutions generated using the MGB technique can also be applied to describe and efficiently calculate the resultant sound fields radiated from a parametric transducer array. The parametric array is the virtual end-fire sound source that is generated by the beat pattern that is produced by summing two ultrasonic sound beams and can be modeled as a linear array of sources. The nonlinear interactions of the sound fields from each ultrasonic transducer comprising the array creates a focused sound source with scattered sound fields of higher direc-

tionality than achievable by a linear transducer of the same size as the ultrasonic transducer array, as described in Section 2.2.2. Since most of the nonlinear interaction is produced through collinear rather than noncollinear scattering, the arrays, comprising T transducers in a single plane, can be modeled using the summation of the contributions from each individual transducer. With the location of each transducer in the array denoted by ξ_{0t} , the primary, secondary, and tertiary sound field solutions of the parametric array can be written as

$$q_1(\xi, \eta) = \sum_{t=1}^T \sum_{n=1}^N \frac{A_n}{1 + jB_n\eta} \exp\left(-\frac{B_n(\xi - \xi_{0t})^2}{1 + jB_n\eta}\right), \quad (3.29)$$

$$q_{2s}(\xi, \eta) = \sum_{t=1}^T \sum_{n=1}^N \sum_{j=1}^N \frac{A_n A_j}{4r_1} \exp\left(-\frac{s_1(\xi - \xi_{0t})^2}{r_1}\right) \left[E_1\left(\frac{s_2(\xi - \xi_{0t})^2}{r_1(r_1\eta + r_2)}\right) - E_1\left(\frac{s_2(\xi - \xi_{0t})^2}{r_1 r_2}\right) \right], \quad (3.30)$$

and

$$\begin{aligned} q_{3s}(\xi, \eta) = & \sum_{t=1}^T \sum_{n=1}^N \sum_{j=1}^N \sum_{f=1}^N \exp\left(-\frac{s_3(\xi - \xi_{0t})^2}{r_3}\right) \int_0^\eta \frac{A_n A_j A_f}{6(r_3\eta' + r_4)} \exp\left(-\frac{s_4(\xi - \xi_{0t})^2}{r_3(r_3\eta' + r_4)}\right) \\ & \times \left[\ln\left(1 + \frac{r'_1}{r'_2}\eta'\right) + \sum_{u=1}^{\infty} \frac{(-1)^{u+1}}{uu!} \Gamma(u+1) \left[\left(\frac{s_2}{r'_1(r'_1\eta' + r'_2)}\right)^u - \left(\frac{s_2}{r'_1 r'_2}\right)^u \right] \right. \\ & \times \left. \left(\sqrt{\frac{r'_1(1 + jB_f\eta')(\eta - \eta')}{r_3\eta' + r_4}} \right)^{u+1} M\left(-u, 1, \frac{s_5(\xi - \xi_{0t})^2}{(r_3\eta' + r_4)(\eta - \eta')}\right) \right] d\eta', \quad (3.31) \end{aligned}$$

respectively. Therefore, by adding an additional summation layer, it is straightforward to extend the MGB expansion to describe the sound fields radiated from the transducer array.

It is important to note that the simplifications of the MGB expansion method are valid only when the sound beam is generated from an axially symmetric source, allowing for the simplifications shown in the secondary, and thus tertiary, sound fields to be achieved. For non-axially symmetric sources, the sound field solutions require numerical integration of a single field integral [60, 127, 132]. Additionally, since the MGB expansion method is derived from the KZK equation, the method has similar validity for all nondissipative fluids.

3.4 Sound Field Measurement

The simulation results calculated using the MGB expansion technique for the scattered sound fields are obtained in this section and compared to both measured responses and results calculated using the quasi-analytic theory presented in Section 3.3. These calculations were performed

on a Dell Precision R5500 having 48 GB of RAM and 500 GB of hard disk drive space with a processor speed of 3.470 GHz. The amplitude distributions for the second- and third-order sound fields generated from a single uniform planar piston source on the acoustic axis and at various planes perpendicular to the axis of propagation are considered. In addition, the amplitude response of the scattered sound fields produced by parametric arrays of various sizes are explored, illustrating the applicability of the expansion method to arrays. In this section, the Gaussian coefficient set for a rigid piston radiator as given in Table I of [15] is used, however, any of the coefficient sets given in Appendix A could alternatively be utilized.

3.4.1 Measurement Equipment

The experimental results presented in the following sections were found inside of a dual acoustic-RF anechoic chamber with an insertion loss up to 100 dB and 90 dB and a return loss up to 45 dB and 50 dB for the acoustic and RF waves, respectively, as described by Garner *et al.* [133]. The sound fields were transmitted using several acoustic sources, including individual circular pistons as well as parametric transducer arrays, as detailed in Sections 3.4.2 and 3.4.3, and the pressure levels were measured using a 6.4 mm PCB Piezotronics, Inc. Model 377B01 Type 1 precision condenser microphone that is pre-polarized with has a frequency range of 4 Hz to 80 kHz and operating on a constant 2-20 mA current supply provided from a Piezotronic 482A22 signal conditioner. The signals that were sent to the acoustic sources and received by the microphone were generated and recorded using a National Instruments (NI) PXI-4461 data acquisition card performing with a sampling rate of 204.8 kS/s. As shown in Fig. 3.1, the acoustic source was placed at a distance R from the microphone and rotated using a Kaidan Magellan MDT-19 turntable to measure the sound field radiation pattern at angle θ from the acoustic axis. These spherical coordinates were then converted to cylindrical coordinates for use in (3.16) and (3.26) using the simple transformations for the radial coordinate, $\rho = R \sin \theta$, and axial coordinate, $z = R \cos \theta$.

3.4.2 Single Uniform Planar Piston

To verify the suitability of the MGB method to modeling the third-order sound field solutions, the third harmonic and intermodulation sound fields nonlinearly generated by interaction of the primary and secondary fields from a uniform planar piston source are considered. That is, the third-order response is the result of the two cascaded second-order interactions. The solution of the third harmonic in (3.26) is compared to that given in [34], where $\rho_0 = 1.2 \text{ kg/m}^3$, $c_0 = 344.8 \text{ m/s}$, $\beta = 1.2$, and $a = 0.21 \text{ m}$. Fig. 3.2a describes the pressure amplitude on the acoustic axis for the first three harmonic sound fields driven at $f_1 = 30 \text{ kHz}$ and $p_0 = 116 \text{ dB SPL}$ while Fig. 3.2b describes the normalized pressure amplitudes of the first three harmonics at a

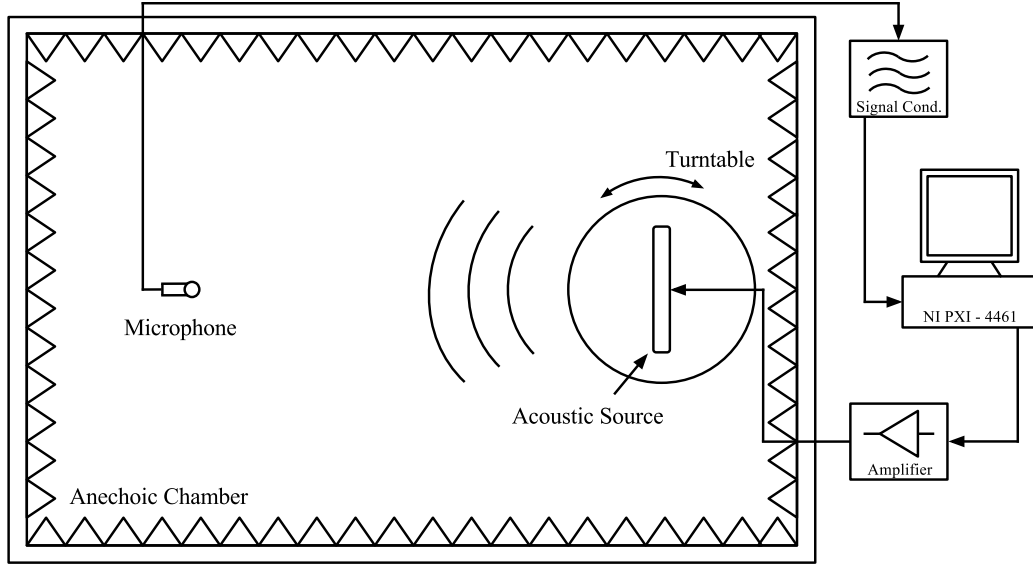


Figure 3.1: Acoustic measurement system used to determine the sound field distributions of the acoustic sources discussed in Sections 3.4.2 and 3.4.3.

distance of 6 m from the source driven at $f_1 = 25$ kHz and $p_0 = 117$ dB SPL, as found in Figs. 2 and 4 of [34]. The results obtained using the MGB expansion are in agreement with [34], with a slight discrepancy in the near-field of the third harmonic. For comparison to the intermodulation frequencies, measured data was obtained using an AirmarTM AT-50 ultrasonic transducer with a radius of 22 mm, a center frequency of 50 kHz, and driven at $f_1 = 51$ kHz and $f_2 = 49$ kHz with primary sound pressure amplitudes of $p_{01} = p_{02} = 95$ dB SPL. The sound fields were transmitted through air (with $\rho_0 = 1.2$ kg/m³, $c_0 = 343$ m/s, and $\beta = 1.21$) and are measured at a distance of 2 m from the source. Using the parameters given, Figs. 3.2c and 3.2d show the measured and theoretical normalized pressure amplitudes of the upper and lower IM3 tones, $f_U = 53$ kHz and $f_L = 47$ kHz, at a distance of 2 m from the source. The amplitude of the side lobes of the IM3 tones does not exceed the level of the measurement noise floor at angles greater than 30° off the acoustic axis, thus accounting for the discrepancy between the MGB expansion method and the measured results in the figures. Since the transducer and driving amplifier are nonlinear, they generate intermodulation distortion that contributes to the sound field. To account for this contribution in Figs. 3.2c and 3.2d, the equipment is characterized following the method outlined in [39] and [38]. From Fig. 3.2, it can be seen that the MGB expansion technique accurately models the third-order sound fields.

In computing the solutions for the third-order sound fields as shown in Fig. 3.2, the infinite series found in (3.26) and (3.28) resulting from the simplification of (3.12)–(3.14) by the MGB

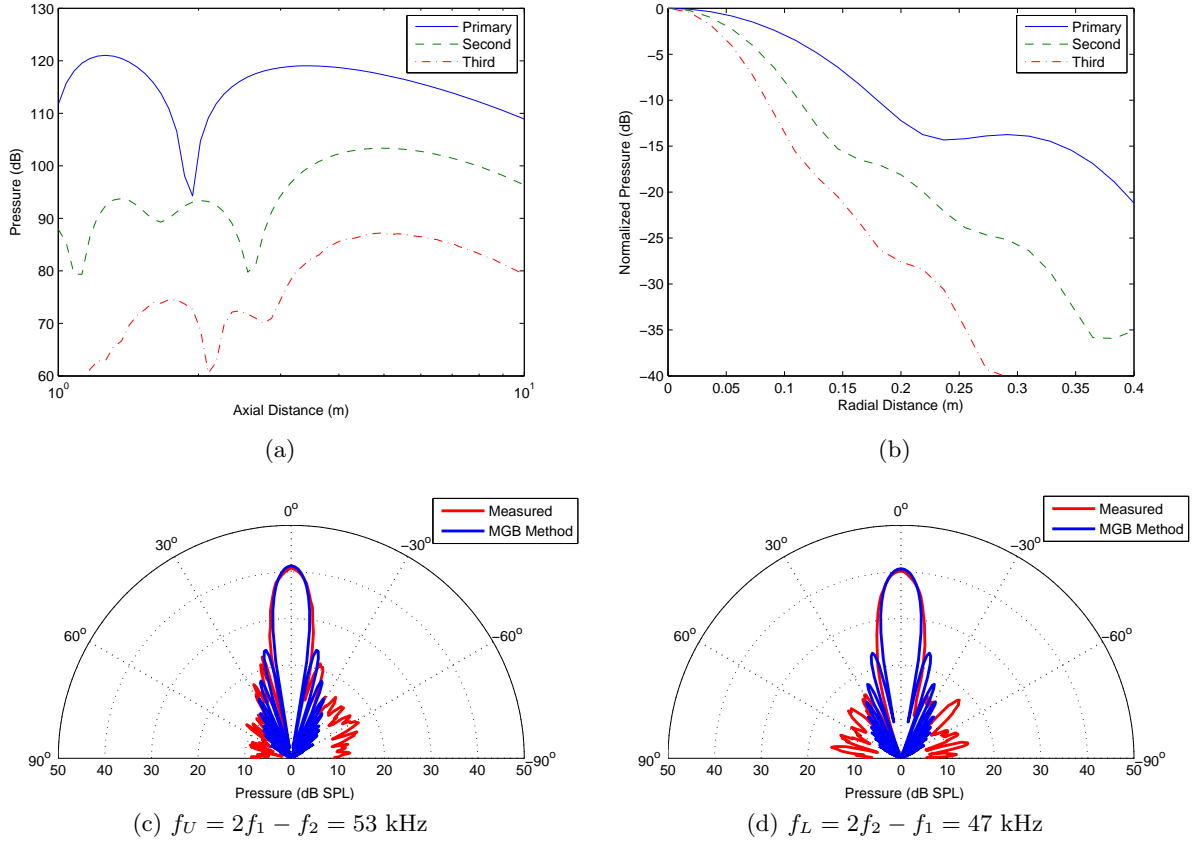


Figure 3.2: The third-order sound field distribution. The pressure amplitudes of the first three harmonic sound fields (a) on the acoustic axis and (b) normalized at a distance of 6 m from the source as described in [34]. The measured and theoretical pressure amplitude at a distance 2 m from the source for (c) the IM3 upper and (d) the IM3 lower tones.

expansion method converge, on average, in fewer than ten terms. A small percentage of the field points converge more slowly, requiring as much as several hundred terms, however, restricting the number of terms has a minimal effect on the resultant sound fields and the scarcity of these series prevents any significant increases in computation time. Additionally, changes in the source and medium parameters cause negligible variations in series convergence and simulation speeds due to the normalization of these parameters in the implementation of the MGB expansion method. At increased angles off the acoustic axis, however, the average number of terms required within the series to reach convergence increases slightly as the highly oscillatory nature of the functions within the third-order integrals imposes greater difficulty in generating the proper solutions. To address the challenges encountered by these types of functions and help improve simulation performance, the third-order integrals were solved using the numerical simulation

technique proposed by Kshevetsky and Leble [99].

3.4.3 Parametric Transducer Array

Since the sound field solutions generated by a parametric transducer array are linear superpositions of the contributions from each acoustic transducer, the MGB expansion method can be extended to accurately represent the fields from more complex sources. To verify the accuracy of the expansion, two distinct parametric array configurations are measured, comprising transducers that are different in size, number, and frequency. The first transducer array consists of 19 AirmarTM AT-50 ultrasonic transducers (each as described in Section 3.4.2 hexagonally arranged with spacing between the center of adjacent transducers of 66 mm. The transducers are driven at $f_1 = 51$ kHz and $f_2 = 49$ kHz with primary sound pressure amplitudes $p_{01} = p_{02} = 95$ dB SPL yielding a difference tone at $f_D = 2$ kHz and IM3 upper and lower tones at $f_U = 53$ kHz and $f_L = 47$ kHz. Figs. 3.3a–3.3b show the measured and theoretical results for the primary frequencies generated by the parametric array. Figs. 3.3c–3.3d show the measured and theoretical results for the difference and IM3 lower frequencies, respectively. Similar to the results for the IM3 tones from a single planar piston, the amplitude of the side lobes of the difference frequency does not exceed the level of the measurement noise floor at angles greater than 15 degrees off the acoustic axis. Additionally, the series convergence of the third-order sound field solutions for the parametric transducer array follow a similar behavior as discussed for the single planar piston. Thus, Fig. 3.3 illustrates the ability of the MGB expansion to represent the sound fields generated by a parametric transducer array.

The second transducer array considered is a 45 cm. diameter Audio SpotlightTM 416296 from Holosonic Labs Inc., comprising 81 circular piezoelectric transducers each with a radius of 16 mm, also hexagonally arranged with spacing between the center of adjacent transducers of 45 mm. A complete hexagonal array with this configuration would contain 91 elements, however, six transducers have been removed from the corners of the sound source to fit into the round bezel housing the transducers and four additional transducers were removed from the center column to allow for the mounting and wiring of the device. The acoustic system also utilized a Holosonic Labs AS-18-3 amplifier that was modified to bypass its pre-distortion circuitry, thereby enabling the transmission of pure frequency tones. The transducers are driven at $f_1 = 51$ kHz and $f_2 = 49$ kHz with primary sound pressure amplitudes $p_{01} = p_{02} = 115$ dB SPL with nonlinear scattering yielding second- and third-order sound fields. Again, Figs. 3.4a–3.4b show the measured and theoretical results for the primary frequencies generated by the Holosonic parametric array. Figs. 3.4c–3.4d show the measured and theoretical results for the difference and IM3 lower frequencies, respectively. For a comparison to the results in Figs. 4 and 5 of [39], the primary frequencies are set to $f_1 = 72$ kHz and $f_2 = 70$ kHz with primary

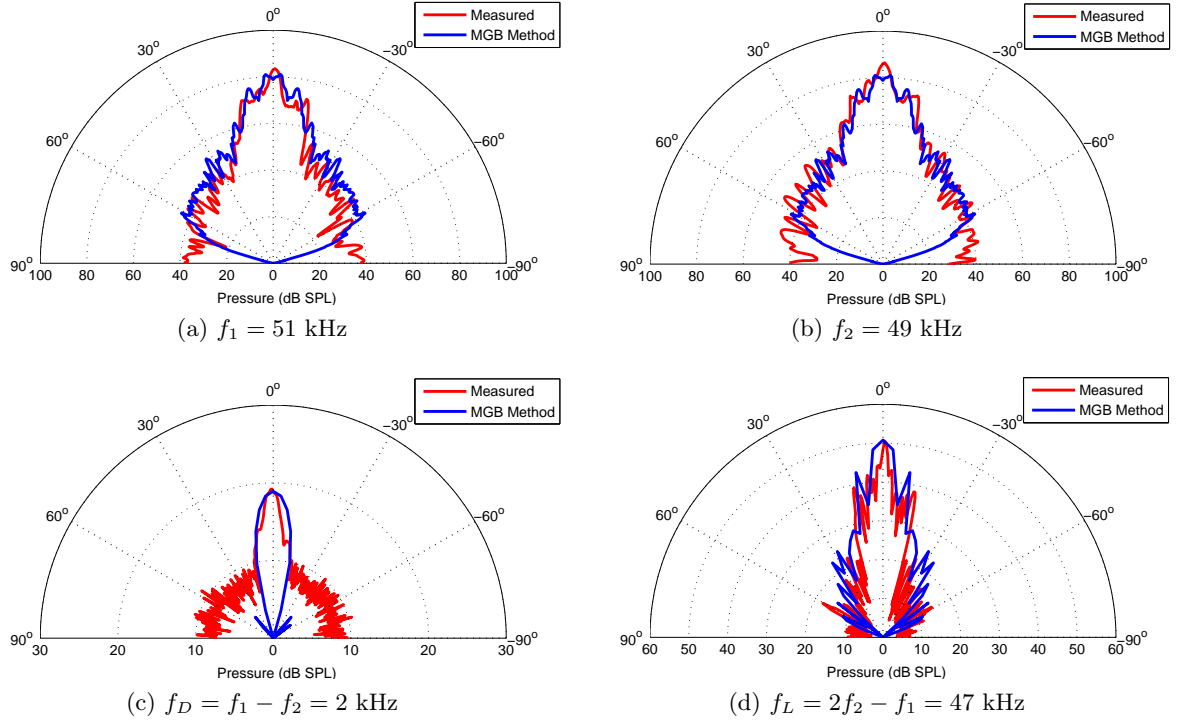


Figure 3.3: The sound field distribution generated by a 19 element parametric array. The measured and theoretical pressure amplitudes of the primary frequencies, (a) $f_1 = 51$ kHz and (b) $f_2 = 49$ kHz. The measured and theoretical pressure amplitudes of (c) the difference and (d) the IM3 lower frequencies.

sound pressure amplitudes of $p_{01} = p_{02} = 115$ dB and then $f_1 = 72$ kHz and $f_2 = 36$ kHz with primary sound pressure amplitudes of $p_{01} = p_{02} = 128$ dB to yield difference and IM3 lower tones at 2 kHz. Fig. 3.5 matches those given in [39] and further verifies the ability of the expansion method to model resultant sound fields of parametric arrays. Again, the amplitude of the side lobes of the IM3 tones does not exceed the level of the measurement noise floor at angles greater than 30 degrees off the acoustic axis for Figs. 3.4d and 3.5f.

While the results presented focus primarily on the scattering of sound by sound within air, it is important to note that the MGB expansion method can easily be extended to model similar scattering effects within water, biological media, and other fluids throughout the audible and ultrasonic frequency ranges. Thus, use of the method can provide computational advantages in practical applications, such as diagnostic ultrasound and harmonic imaging, where it is common to use the KZK equation to model nonlinear acoustic wave propagation.

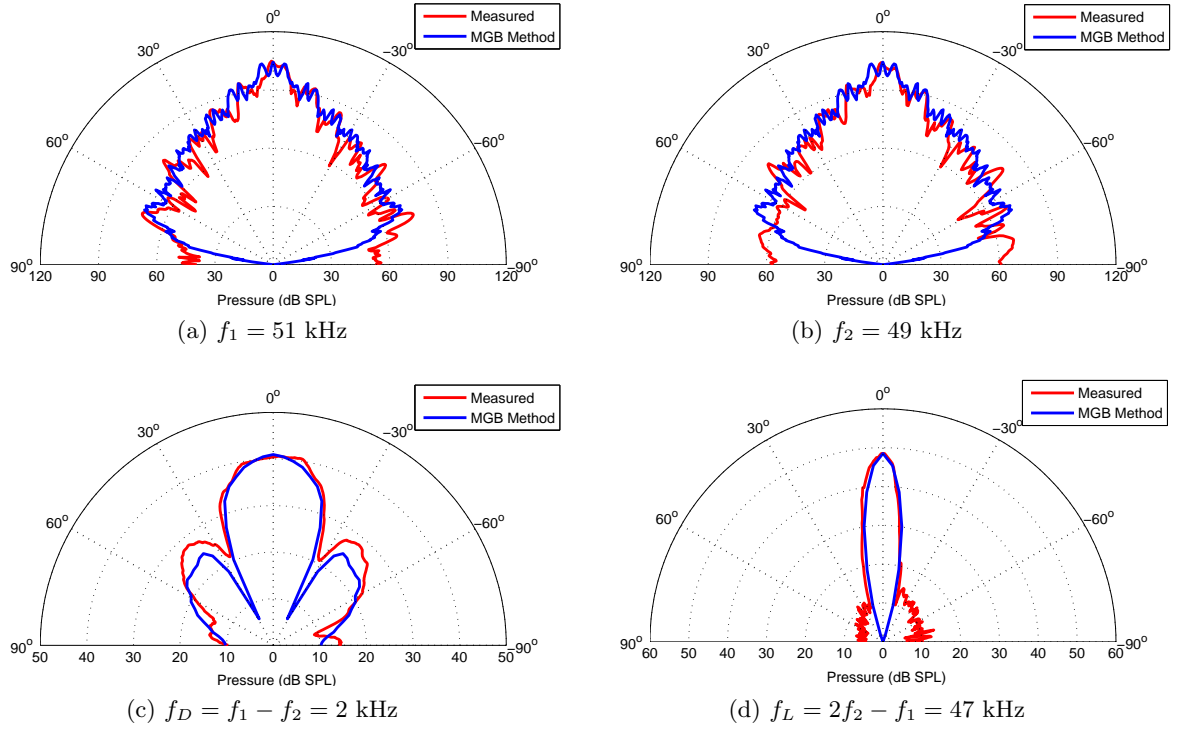


Figure 3.4: The sound field distribution generated by a 81 element parametric array. The measured and theoretical pressure amplitudes of the primary frequencies, (a) $f_1 = 51$ kHz and (b) $f_2 = 49$ kHz. The measured and theoretical pressure amplitudes of (c) the difference frequency and (d) the IM3 lower tone.

3.5 Comparison of Computation Methods

To determine the computation efficiency of the MGB expansion technique, the results in Sections 3.4.2 and 3.4.3 were compared to the traditional methods outlined in Section 2.3. Figs. 3.2a and 3.2b were simulated using the solutions for the harmonic fields given by (2.77) and (2.78), as utilized by Kamakura *et al.* [34] and developed at the University of Bergen [89–91]. Implementing the implicit backward finite difference method to solve the KZK equation directly as done by Kamakura *et al.*, the computation time required in the generation of the harmonic field was significantly increased compared to the MGB expansion method, greater than a 40x increase in computation time compared to the MGB expansion which generated the third harmonic fields in Figs. 3.2a and 3.2b in roughly 3.5 sec. This is the result of the requirement of these types of simulation techniques to simultaneously compute additional harmonics in order to calculate the field of interest, yielding larger memory requirements and longer computation times.

Similarly, the solutions for the third-order intermodulation products in Figs. 3.2c and 3.2d

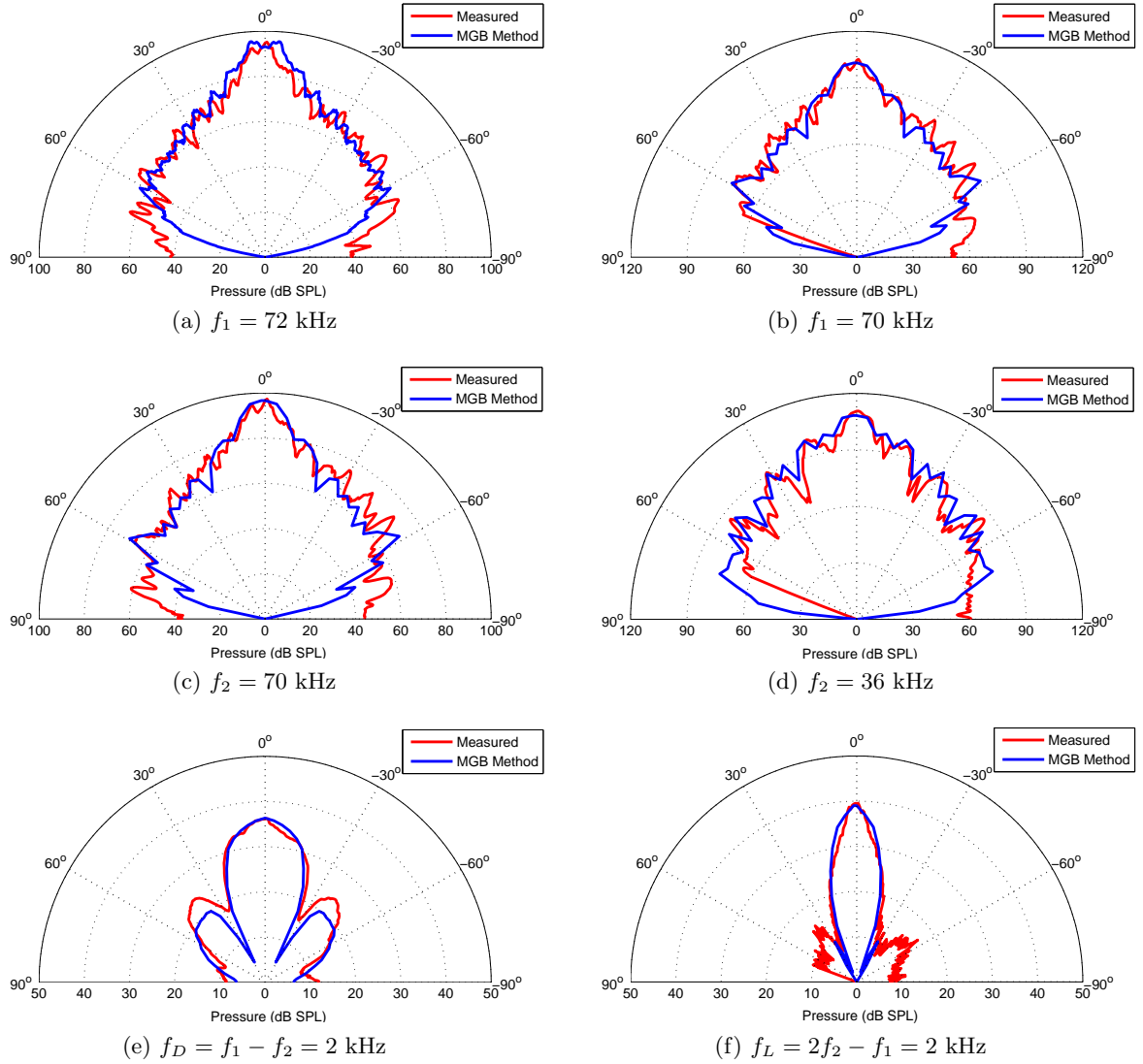


Figure 3.5: The sound field distribution generated by a 81 element parametric array as a comparison to [39]. The measured and theoretical pressure amplitudes of the primary frequencies (a) $f_1 = 72$ kHz and (c) $f_2 = 70$ kHz that generate (e) the difference frequency at $f_D = f_1 - f_2 = 2$ kHz. Additionally, the measured and theoretical pressure amplitudes of the primary frequencies (b) $f_1 = 70$ kHz, and (d) $f_2 = 36$ kHz that generate (f) the third-order lower frequency at $f_L = 2f_2 - f_1 = 2$ kHz.

were computed using the method given by Garner and Steer [39], whereby the three-dimensional field integrals were solved using the composite Simpson's Rule. Again, the computation time required in the generation of the third-order fields was significantly increased compared to the MGB expansion method, a 25x increase in computation time when generating the third-order

intermodulation products in Figs. 3.2c and 3.2d which the MGB expansion completed in about 8 sec. This is due to the need for much finer mesh sizing to account for a larger number of integral dimensions as well as from the use of Bessel functions that are more difficult in computing than the exponentials employed by the MGB expansion.

The advantages in computation efficiency over traditional simulation methods discussed for single planar pistons also apply for the transducer arrays, becoming even more pronounced as the number of elements within the arrays increases, which is evident in the generation of the sound field distributions in Figs. 3.3–3.5.

3.6 Third-Order Parametric Array Design Enhancements

The initial development of the third-order parametric array by Garner and Steer [38, 39, 76] demonstrated the ability to achieve an acoustic source having a higher directivity and lower sidelobe power than the more common second-order parametric array by exploiting the effects of third-order scattering of sound by sound. Since the third-order parametric array is generated by two ultrasonic primary sound fields that are distantly spaced in frequency as opposed to close in frequency as is the case for the second-order parametric array, the design criteria to efficiently produce the third-order parametric array differs from its second-order counterpart. The third-order parametric arrays reported in the works by Garner and Steer and analyzed in Section 3.4, however, are produced by modifying a system developed specifically for the generation of a second-order parametric array, thereby resulting in the highly inefficient production of sound fields in the audio frequency range (e.g., the Holosonic Labs Inc. acoustic system described in Section 3.4.3 yields a maximum sound pressure level for the third-order intermodulation products of 40 dB SPL despite transmitting the primary sound fields at close to 130 dB SPL, the maximum achievable pressure level of the system). Therefore, to enhance the generation of the third-order parametric array, an improved design of the acoustic system producing the third-order sound fields needs consideration.

3.6.1 Relationship of Transmitted Signals

The fundamental difference in the design of the second- and third-order parametric arrays is the frequency relationship between the two primary sound fields, as they are required to be either close in frequency [83, 134] or distantly spaced with one frequency roughly twice that of the other [38, 39, 76] to yield a second-order difference tone or third-order intermodulation product, respectively, in the audio frequency range. The maximum achievable sound pressure for the desired signal in the audio frequency range is dependent upon the power levels of the primary sound fields as they interact while propagating away from the acoustic source.

Thus, to increase the sound pressure level of the second-order difference tone or third-order intermodulation product, the sound pressure of the primary sound signals must be maximized. The transmitted power levels of the primary sound signals can be directly increased, however, this is limited by the ability of transducers to produce sound waves with significantly high pressure levels. The improved performance of transducers is a major area of interest within audio engineering [77–80] and, although the maximum obtainable pressure levels of the transducers effect the performance of the third-order parametric array, the design will ignore this factor and instead focus on alternative methods for enhancing the system. One factor that limits the production of sound fields with high pressure levels is the development of shock waves. Shock waves are formed by the nonlinear steepening of an ordinary sound wave with a high enough pressure amplitude to generate significant heat in the medium near the wave front to cause the pressure front to overtake the pressure trough, thereby creating a discontinuity. However, the shock formation limit increases as the transmitted ultrasonic frequency is lowered, thereby enabling higher power levels to be transmitted before reaching shock saturation. The lowering of the ultrasonic frequency also improves the ability to maintain the pressure level of the primary sound signals as they propagate away from the acoustic source, as a signal amplitude is attenuated during propagation through a nonlinear medium, with the attenuation increasing quickly as the frequency increases. Therefore, by lowering the ultrasonic frequency, the primary sound signals will experience less attenuation and maintain higher sound pressure levels. Thus, by moving the primary sound fields as close as possible to the boundary between the audio and ultrasonic frequency ranges, the maximum achievable sound pressure level of the primary sound fields is increased, resulting in an increase in the maximum obtainable sound pressure level for the desired signals in the audio frequency range. For the third-order parametric array, this implies that the lower frequency primary sound field, f_2 in Fig. 2.5, would be chosen so that it is close to the audible sound boundary while still maintaining a frequency relationship of roughly twice that of the other primary sound signal.

In general, ultrasonic signals can be driven at substantially higher sound pressure levels than lower frequency audible signals due to safety concerns with human hearing and moving the primary sound signals close to the audible boundary can result in it being within the range of sound detection by some individuals, so caution is required in the system design to avoid this effect.

3.6.2 Modulation Schemes

Since the generation of a directed single frequency sound beam, as has been discussed thus far, has minimal practical application, modulation schemes are necessary to properly convert an ultrasonic signal with a finite bandwidth to the audio frequency range. To achieve the

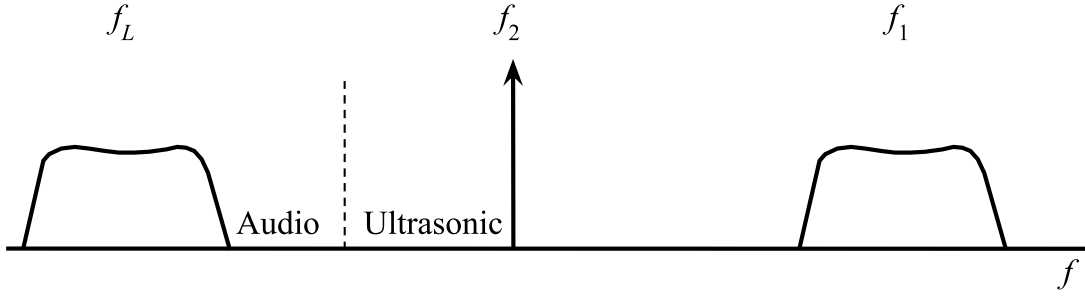


Figure 3.6: Frequency spectrum for the interacting primary sound fields utilized to produce the third-order parametric array having a finite bandwidth, with a single frequency signal, f_2 , a finite bandwidth signal, f_1 , and the resultant finite bandwidth third-order intermodulation product, f_L .

desired demodulated signal in the audio frequency range, a variety of amplitude modulation schemes have been employed, the most common of which are full amplitude modulation, truncated double-sideband modulation (with and without a suppressed carrier), and single-sideband modulation [81,82]. Single-sideband modulation schemes have become the most popular because it allows for the ultrasonic frequencies of the transmitted signals to be lowered closer to the threshold of audible human hearing, as described in the previous section, particularly for the second-order parametric array systems. Either of the primary sound fields can have a finite bandwidth when implementing the third-order parametric array, however, due to the loss associated in generated the second harmonic, $2f_2$, required for producing the third-order intermodulation product, the most efficient design locates the content bearing finite bandwidth signal as the higher frequency primary sound signal, f_1 , as shown in Fig. 3.6. The system can then employ a modulation scheme to convert the finite bandwidth signal to the audio frequency range in the third-order parametric array implementation. Similar to the second-order parametric array, single-sideband modulation would be the ideal modulation scheme to utilize since less power is required as only one sideband is transmitted. The required power can be further reduced by using single-sideband suppressed-carrier modulation whereby the carrier is also eliminated so that only the sideband containing the desired signal is transmitted.

3.6.3 System Architecture

To further improve the power efficiency of the acoustic system designed to produce the third-order parametric array, the architecture of the system must be constructed in such a manner as to optimize the generation of the transmitted primary sound signals. Developing amplifiers and transducers to operate efficiently over a large bandwidth, as is required for the third-order

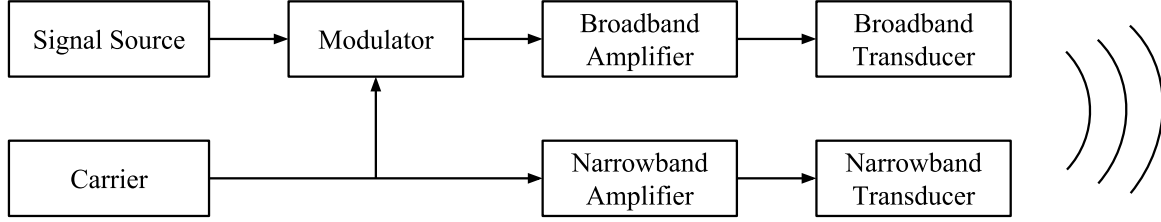


Figure 3.7: Block diagram of the third-order parametric array implementation utilizing separate narrowband and broadband amplifiers and transducers as to improve the efficiency of generating the interacting primary sound fields that produce the third-order intermodulation product.

parametric array due to the distantly spaced primary sound fields being transmitted, is quite difficult. A more efficient approach is to separately generate and transmit the primary sound signals using independent amplifiers and transducers designed specifically to operate at the frequency location of the respective primary signal. This is the preferred implementation as the design of both amplifiers and transducers operating over a small frequency range is simple, and inexpensive to produce, yet still provides an improvement in the performance of the devices over those designed to operate over much larger frequency ranges (e.g., higher gains for the amplifiers are achievable while consuming less power). The system would, therefore, have two sets of amplifiers and transducers thereby doubling the number of components of the second-order parametric array, however, the performance of each set would be significantly better. Since only one of the primary sound signals will have a finite bandwidth, as shown in Fig. 3.6, the efficiency of the system can be further enhanced by using a narrowband amplifier and transducer set, having all of the advantages in simplistic design, gain, and power consumption, for the lower frequency primary sound signal, f_2 , and a broadband amplifier and transducer for the finite bandwidth signal, f_1 . Fig. 3.7 illustrates a potential system configuration utilizing separate narrowband and broadband components to realize the third-order parametric array. By employing a narrowband amplifier and transducer that easily produces high sound pressure levels, the requirements for the broadband amplifier and transducer can be relaxed so that only low-to-moderate pressure levels need to be attained to yield acceptable pressure levels for the third-order intermodulation product, thereby simplifying the design of the broadband components and lowering the production cost. Additionally, as frequency increases the relative bandwidth of the primary sound signal reduces making it is easier to realize the transducers that would be required, again easing the design of the higher frequency broadband amplifier and transducer.

3.7 Summary

An analytical description of the scattered sound fields was presented using the MGB expansion technique. A method for deriving the Gaussian coefficients for the MGB technique was also discussed. With the use of the linear and quasilinear solutions of the KZK nonlinear equation, it was shown that the expressions for the MGB expansion of the first- and second-order solutions agree with previous theoretical and experimental results. Using these expressions, solutions for the third-order sound fields were obtained and compared with measurements and results found in the literature. In addition, the method was shown to be accurate for use with higher-order parametric transducer arrays.

The MGB expansion is computationally more efficient than previously reported methods in finding solutions to higher-order sound fields due to the ability to mathematically reduce the required number of field integrals. In addition, commonly used closed-form second-order sound field solutions require that the two primary frequencies are either close in frequency [45] or distantly spaced [28] in order to be simplified, whereas the MGB solution for the second-order fields does not have these frequency constraints, thus making them valid over a wider range of conditions.

Chapter 4

Determination of Nonlinearly Generated Scattered Acoustic Fields using a Near-to-Far-Field Transformation Method

4.1 Introduction

Scattered sound fields produced by the nonlinear interactions of high frequency acoustic signals radiate energy into the harmonics, sum and difference frequencies, and third-order intermodulation products of the primary interacting signals [135]. The radiation pattern of these nonlinearly generated scattered fields offer advantages over their primary signal counterparts, including an increase in beam directivity, decreased power in the sidelobes, and the ability to use smaller sized sources when generating low-frequency sound signals. These have been explored in a variety of research areas and applications, such as acoustic radar [85] and sonar [136], non-destructive evaluation [137], and 3D sound field reproduction [138]. However, with the scattered sound fields being generated through a nonlinear process, the determination of the far-field response is challenging, as computation of these fields using traditional methods is time consuming and intensive, often requiring calculation over hundreds of wavelengths, and measurement at sufficient distances to be in the far-field is typically impractical, especially for large transducers. With these concerns and the increased deployment of acoustic sources intended for use over very large distances, such as long range acoustic devices (LRAD), an alternative approach to simply but accurately determine the far-field characteristics of an acoustic source is desired. The main contribution of this chapter is the development of a nonlinear near-to-far-field (NTFF)

transform that enables the far-field radiation pattern of nonlinearly generated scattered acoustic fields to be determined from amplitude measurements sampled in the near-field.

The problem of determining sound fields as they propagate into the far-field is not unique to acoustics as similar issues are encountered in determining the electromagnetic (EM) radiation patterns of antennas. In EM, a common approach that mitigates the need for lengthy simulations and impractical measurements, yet still ascertains the far-field radiation pattern, is utilizing a linear NTFF transformation, whereby data collected in the near-field of the source is used to determine the value at points in the far-field [139–144]. This technique is widely used and has been applied through an assortment of methods to determine antenna far-field characteristics. To account for varying antenna apertures and applications, various near-field scanning geometries have been employed to support the transformation. These geometries include plane-polar [145], spiral [146], and spheroidal [147]. Similarly, a considerable number of algorithms have been proposed to implement the transformation [148–155]. Ludwig [148] and Ricciardi and Stutzman [147] developed series expansions to define their algorithms using spherical waves and eigenfunctions, respectively. Petre and Sarkar [149] developed a transformation method utilizing an array of dipole probes to improve the near-field measurements. Kobayashi *et al.* [150] presented a transformation algorithm using antenna array-factor as a simplified alternative to the expansion methods. Ohashi and Arai [151], Bucci *et al.* [152], and Costanzo and Di Massa [153] considered methods where phase was extrapolated from amplitude measurements on two different planes in order to overcome the difficulty of measuring phase.

While linear NTFF transformations have been extensively explored in EM, the use of similar techniques in acoustics has only occurred in recent years as their application has proven beneficial in a variety of research areas. In the initial development by Ballantine [156], a proof was given of the wave-potential theorem based on Kirchhoff’s [157] solution of Huygens’ principle that he applied to acoustic systems. Horton and Innis [158] and Baker [159] continued this work by experimentally applying Ballantine’s solution to determine the far-field characteristics of underwater acoustic transducers from measurements made in the near-field using a special application of the Helmholtz integral equation and multiple measurement surfaces. A variety of techniques have since been proposed to improve measurement in the near-field of the acoustic sources [160–163]. Predominantly, the linear NTFF transformation technique presented in these works has been used to determine the characteristics of the primary frequency signal as it radiates into the far-field. However, Wang [164] demonstrated the usefulness of the application of the NTFF transformation by implementing the technique as a means of computing the acoustic far-field directional pattern for primary fields scattered by objects modeled in the near-field using finite-difference time-domain acoustic simulations.

More recently, near-field transformation techniques have been applied in the fields of acoustic holography and imaging. Williams and Maynard [165–168] introduced the concept of near-field

acoustic holography (NAH) as a means of reconstructing the acoustic pressure on the surface of a radiating structure from near-field data. Typically, the conversion of the near-field data is performed using a series of Fourier transforms, however, generalized approaches using Green's functions that satisfy the homogeneous Dirichlet and Neumann conditions have also been developed for simple geometries where a Green's function can be derived for the desired structure [169, 170]. Implementation of these techniques is challenging due to the difficult derivations required, therefore, a variety of alternative methods have been developed. The Fourier-based techniques have been improved by the development of patch NAH which enables a reduction in the number of measurement points required [171, 172]. Additionally, inverse boundary element methods have emerged as a numerical approach to solve the Helmholtz integral, thereby enabling the reconstruction of the acoustic radiation from arbitrary structures [173–175]. This technique employs spatial discretization that requires multiple nodes per wavelength to accurately reconstruct the acoustic source, which can result in a large number of data points leading to lengthy computation times. To address this issue, the Helmholtz equation least squares method [176], as well as subsequent hybrid techniques built upon this method [177, 178], was developed that approximates the acoustic field using an expansion of the particular solution to the Helmholtz equation and minimizing the error using least squares, thus yielding simple mathematical results to improve computation efficiency. These advancements in NAH techniques have prompted its use in many research areas, including noninvasive imaging [179, 180], nonstationary acoustic field visualization [181, 182], and object characterization [183].

This chapter focuses on developing a nonlinear NTFF transformation concept that can be used when nonlinear scattering of sound by sound also occurs outside the near-field region. A nonlinear NTFF transform model is presented that computes the far-field characteristics of higher-order fields generated by acoustic scattering of sound by sound through the nonlinear interaction of two primary sound beams based on their radiation characteristics in the near-field; thereby effectively extending linear NTFF theory to include the scattered nonlinear second-order acoustic fields. By establishing the near-field characteristics of the scattered sound fields either with measurements made near the source or simple calculation, the scattered far-field radiation patterns are determined without requiring measurements to be taken at large, impractical distances and without performing lengthy computations. Section 4.2 is a theoretical development of the NTFF transformation as it pertains to the first- and second-order sound fields. Section 4.3 demonstrates that the far-field radiation patterns of the higher-order sound fields produced by the transformation are in good agreement with measurements and theory presented by previous authors for both single transducer sound sources and parametric transducer arrays.

4.2 Transformation Development for Acoustic Fields

In this section, nonlinear NTFF transformations are developed to calculate the far-field radiation patterns of higher-order sound fields. Expanding upon Kirchhoff's solution to Huygens' principle, the Khokhlov-Zabolotskaya-Kuznetsov (KZK) equation, a fully nonlinear parabolic wave equation that has been shown to accurately describe second- and third-order sound fields [135], is used to derive expressions for the higher-order transformations.

Kirchhoff's theorem [156, 157] is a mathematical solution to Huygens' principle that states that any point exterior to an enclosed surface can be determined from the amplitude and phase information along that surface if all sources are interior to the surface. Assuming the amplitude of the pressure wave is small enough to enable use of the linear Helmholtz equation,

$$\nabla^2 p + k^2 p = 0, \quad (4.1)$$

then the surface integral form of Kirchhoff's theorem is [156, 157]

$$p(P) = \frac{1}{4\pi} \iint_S \left[p(Q) \frac{\partial}{\partial n} U(P | Q) - U(P | Q) \frac{\partial p(Q)}{\partial n} \right] dS, \quad (4.2)$$

where p is the acoustic pressure located at the field point and a point on the closed surface, P and Q , respectively, $k = \omega/c_0$ is the wave number of the acoustic wave having angular frequency ω , c_0 is the small-signal sound speed, ∇^2 is the Laplace operator, and $U(P | Q)$ is a solution to the Helmholtz equation. The Green's function, $G(P | Q)$, is a simple expression that serves as a solution to the linear Helmholtz equation, therefore,

$$U(P | Q) = G(P | Q) e^{-j\omega t} = \frac{e^{-j\omega t} e^{jkR}}{R}, \quad (4.3)$$

where R is the distance from point Q on the closed surface to the field point P , t is time, and $\omega = kc_0$ is the angular frequency of the acoustic wave. Then the Helmholtz formula [184] becomes

$$p(P) = \frac{e^{-j\omega t}}{4\pi} \iint_S \left[p(Q) \frac{\partial}{\partial n} \frac{e^{jkR}}{R} - \frac{e^{jkR}}{R} \frac{\partial p(Q)}{\partial n} \right] dS. \quad (4.4)$$

It can be seen from (4.4) that any point in the far-field can be determined by measuring the amplitude and phase of the pressure, p , and the normal gradient of the pressure, $\partial p / \partial n$, in the near-field. However, due to the difficulty of measuring the normal component of the pressure gradient, this term is commonly approximated as jkp , the exact solution given by a plane wave propagating in the normal direction of the closed surface. This remains valid for cylindrical transducers given that the radius of curvature of the transducer is comparable to a wavelength, or less, and the rate of variation of the phase over the transducer surface is not large [185]. With

this limitation, the near-field pressure wave, $p(Q)$, can be approximated as a quasi-plane wave, as has been shown to be acceptable in several previous works [158, 159, 185]. Since the field point is located in the far-field where $kR \gg 1$, the expression can be further reduced by using the Fraunhofer approximation to simplify the normal gradient of the Green's function [158]:

$$\frac{\partial}{\partial n} \frac{e^{jkR}}{R} = jk \frac{e^{jkR}}{R} \frac{\partial R}{\partial n} = -jk \frac{e^{jkR}}{R} \cos \phi, \quad (4.5)$$

where ϕ is the angle between the normal component and a line connecting P to Q . Thus, with discrete frequency components, a linear expression for the far-field pressure determined by near-field contributions can be written as [159]

$$p(P) = -\frac{jk e^{-j\omega t}}{4\pi} \iint_S (1 + \cos \phi) \frac{e^{jkR}}{R} p(Q) dS. \quad (4.6)$$

By assuming that the pressure wave is described by the Helmholtz equation in (4.1), the far-field solution in (4.6) accounts solely for the linearly propagating primary waves generated from an acoustic source, this is the linear NTFF transformation. To extend Kirchhoff's theorem to include nonlinearly generated higher-order sound fields, the nonlinear Khokhlov-Zabolotskaya-Kuznetsov (KZK) parabolic wave equation, which considers the effects of diffraction, absorption, and medium nonlinearity on a sound field as it propagates through a medium, as detailed in Section 2.2, is used to describe the pressure wave as it propagates into the far-field [12, 13]. Given in (3.2), the KZK equation is again reproduced here as

$$\frac{\partial^2 p}{\partial z \partial \tau} - \frac{c_0}{2} \nabla_{\perp}^2 p = \frac{\beta}{2\rho_0 c_0^3} \frac{\partial^2 p^2}{\partial \tau^2}, \quad (4.7)$$

where p is the acoustic pressure comprised of the primary sound field and higher-order sound fields as a function of position and time $\tau = \omega_i t - k_i z$, ρ_0 is the medium density, β is the coefficient of nonlinearity, z is the Cartesian coordinate in the direction of wave propagation, and $\nabla_{\perp}^2 = \partial^2/\partial x^2 + \partial^2/\partial y^2$ is the second-order spatial gradient transverse to the direction of propagation. The subscript ' i ' denotes the primary frequency component, where $i = 1, 2$, and $\omega_1 > \omega_2$.

Traditionally, quasilinear solutions are derived to solve the KZK equation for the higher-order sound fields, as demonstrated in Chapter 3. Under the quasilinear approximation, the acoustic pressure in (4.7) is restricted to consist only of two primary frequencies, the second-order sound field resulting from the interaction of the primary fields, and the third-order sound field resulting from the cascaded interactions of the primary and secondary sound fields [39, 135]. Therefore, as was given in (2.53) and (3.3), the acoustic pressure, p , can be written for the

primary and secondary sound fields as

$$p = \sum_{i=1}^2 p_{1i} + \sum_{\varsigma} p_{2\varsigma} = p_{11} + p_{12} + p_{21} + p_{22} + p_{2S} + p_{2D}, \quad (4.8)$$

where p_{1i} indicates the i th primary field and $p_{2\varsigma}$ indicates the second-order scattered field. As discussed in Sections 2.2.2 and 3.2, the second-order sound field includes the second harmonic and the sum and difference frequencies ($\omega_{2S} = \omega_1 + \omega_2$ and $\omega_{2D} = \omega_1 - \omega_2$) where the second-order field subscript ‘ ς ’ identifies the second harmonics of the two primary frequencies, sum, or difference frequency, $\varsigma = 1, 2, S$, or D , respectively.

To solve Kirchhoff’s theorem for the second-order sound fields, the Green’s function must be utilized to derive a solution to the KZK equation in (4.7). Again, following the method in [41] where a linearized version of the KZK equation is developed, the corresponding Green’s function for the higher-order fields generated by an axially symmetric source, as given in (2.38) and (3.7), can be expressed as

$$G_{\sigma}(\xi, \eta \mid \xi', \eta') = \frac{j\sigma e^{-j\sigma\tau}}{(\eta - \eta')} J_0 \left(\frac{2\sigma\xi\xi'}{\eta - \eta'} \right) \exp \left[\frac{j\sigma(\xi^2 + \xi'^2)}{\eta - \eta'} \right]. \quad (4.9)$$

As before, the parameters are normalized to the center of the primary wave numbers, $k_0 = (k_1 + k_2)/2$, so that the normalized angular frequency is $\omega_0 = k_0 c_0$, the normalized wave numbers of the primary fields are k_1/k_0 and k_2/k_0 , and the nondimensional axial and radial coordinates become $\eta = 2z/k_0 a^2$ and $\xi = r/a$, respectively, where a is the radius of the source. The selection of the second-order field ς sets the values for l and m to select the identified frequency component, $\sigma = l + m$; therefore, the second harmonic of the first primary field, p_{21} , is selected when $l = m = k_1/k_0$, the sum frequency, p_{2S} , is selected when $l = k_1/k_0$ and $m = k_2/k_0$, and the difference frequency, p_{2D} , is selected when $l = k_1/k_0$ and $m = -k_2/k_0$. Additionally, in cylindrical coordinates, (ξ, η) and (ξ', η') are the normalized radial and axial distances of the field point and closed surface, respectively. Thus, as a solution to (4.7), $U(P \mid Q)$ can be found using (4.9) and following the derivations in Sections 2.2.1 and 3.3, where it is shown that the second-order sound fields generated from an axially symmetric piston source can be expressed as a series of Gaussian functions, as given in (2.66) and (3.16), resulting in

$$U(P \mid Q) = \sum_{n=1}^N \sum_{j=1}^N \frac{A_n A_j e^{-j(l+m)\tau}}{4r_1} \exp \left(-\frac{s_1 \xi^2}{r_1} \right) \left[E_1 \left(\frac{s_2 \xi^2}{r_1(r_1 \eta + r_2)} \right) - E_1 \left(\frac{s_2 \xi^2}{r_1 r_2} \right) \right], \quad (4.10)$$

where

$$r_1 = (lB_j + mB_n) + j(l + m)\eta B_n B_j, \quad (4.11a)$$

$$r_2 = (lB_n + mB_j)\eta - j(l + m), \quad (4.11b)$$

$$s_1 = (l + m)^2 B_n B_j, \quad (4.11c)$$

$$s_2 = -j(l + m)lm(B_n - B_j)^2, \quad (4.11d)$$

$E_1(x) = \int_x^\infty t^{-1}e^{-t}dt$ is the exponential integral function, and, again, A_n and B_n are the Gaussian coefficient set and waist parameters, respectively. It is important to note that the normalized axial and radial distances, η and ξ , are the distances from the closed surface to the field point for each of the dimensions.

Using an approach similar to that used to develop a solution to the linear Helmholtz formula, the normal gradient of the pressure and the solution to the KZK equation given in (4.10) are approximated to solve the surface integral in (4.2) for the second-order sound field. Again, assuming that the radius of curvature of the transducer is comparable to a wavelength of the lowest frequency primary tone and the phase variation over the transducer surface is minimal, the normal gradient of the pressure can be approximated as a plane wave at the higher-order frequency propagating in the normal direction of the closed surface, $j(l + m)p$. Since the wave is propagating in the axial direction, as indicated by the KZK equation and implied by the form of the Green's function in (4.9), the normal gradient of (4.10) can be restricted to the direction of propagation and, thus, can be expressed as

$$\frac{\partial U}{\partial n} = \sum_{n=1}^N \sum_{j=1}^N \frac{A_n A_j e^{-j(l+m)\tau}}{4} \frac{\partial}{\partial \eta} \frac{1}{r_1} \exp\left(-\frac{s_1 \xi^2}{r_1}\right) \left[E_1\left(\frac{s_2 \xi^2}{r_1(r_1 \eta + r_2)}\right) - E_1\left(\frac{s_2 \xi^2}{r_1 r_2}\right) \right] \frac{\partial \eta}{\partial n}. \quad (4.12)$$

As with the simplification of the Green's function in the linear Helmholtz equation, the normal gradient of η can be found as $-\cos \phi$, where ϕ is the angle between the normal component and a line connecting the field point to the closed surface. Then ignoring the components of the normal gradient on the order of η^{-3} or smaller, (4.12) simplifies to

$$\begin{aligned} \frac{\partial U}{\partial n} = & \sum_{n=1}^N \sum_{j=1}^N \frac{-j(l + m) A_n A_j B_n B_j e^{-j(l+m)\tau}}{r_1^2} \exp\left(-\frac{s_1 \xi^2}{r_1}\right) \\ & \times \left[E_1\left(\frac{s_2 \xi^2}{r_1(r_1 \eta + r_2)}\right) - E_1\left(\frac{s_2 \xi^2}{r_1 r_2}\right) \right] \cos \phi. \end{aligned} \quad (4.13)$$

Substituting (4.10) and (4.13) into (4.2) and using the approximation $\partial p / \partial n \approx j(l + m)p$, the far-field pressure of the second-order fields determined by their near-field contributions can

be written as

$$p_{2\varsigma}(P) = - \iint_S \sum_{n=1}^N \sum_{j=1}^N \frac{j(l+m)A_n A_j e^{-j(l+m)\tau}}{4\pi r_1} \left(\frac{B_n B_j}{r_1} \cos \phi + k_0 \right) \exp \left(-\frac{s_1 \xi^2}{r_1} \right) \\ \times \left[E_1 \left(\frac{s_2 \xi^2}{r_1(r_1 \eta + r_2)} \right) - E_1 \left(\frac{s_2 \xi^2}{r_1 r_2} \right) \right] p_{2\varsigma}(Q) dS. \quad (4.14)$$

This, (4.14), is the nonlinear NTFF transformation for the second-order sound fields produced by the scattering of sound by sound enabling the far-field radiation patterns to be determined for the second-order sound fields from measurements made in the near-field, without requiring a detailed knowledge of the acoustic source enclosed within the surface.. As previously stated, the choice of $l+m$ in (4.14) is dependent upon the far-field sound field component of interest (e.g., $l = k_1/k_0$ or k_2/k_0 and $m = k_1/k_0$, k_2/k_0 , or $-k_2/k_0$ selects the second harmonic, sum, and difference frequencies, respectively). Additionally, since the nonlinear NTFF transformation is derived from a solution of the KZK equation that is valid in the paraxial region for sound beams generated from axially symmetric sources propagating in nondissipative fluids, (4.10) is only valid under similar conditions.

4.3 Measurement with High Powered Acoustic Sources

In this section, the linear and nonlinear NTFF transforms, (4.6) and (4.14), are used to determine the far-field primary and secondary scattered sound fields, respectively, from near-field data. These are compared to the response found by calculating the far-field pressure amplitudes directly using the closed form expansions given in Chapter 3. Section 4.3.2 considers the near- and far-field amplitude responses for the primary and secondary sound fields generated from a single uniform planar piston. Similarly, application of the transformation method to determine the far-field amplitude distribution of the sound fields produced by the scattering of sound by sound from transducer arrays are investigated in Section 4.3.3. To determine the far-field radiation patterns in this section, the near-field data is obtained on the surface of the cylinder enclosing the acoustic source, as shown in Fig. 4.1. Found by either measurement taken inside of an anechoic chamber [133], as detailed in Section 4.3.1, or calculation using the implicit backward finite difference method given by [89–91] that employs a set of coupled partial differential equations to solve Westervelt’s nonlinear wave equation as discussed in Section 2.3, the data collected within the near-field has less than λ separation between adjacent measurement points to ensure appropriate representation of the near-field for accurate far-field computations (Baker [159] reported that less than 0.8λ separation should be used otherwise spurious scallops arise in the far-field radiation patterns of the primary fields). Under Kirchhoff’s theorem, the

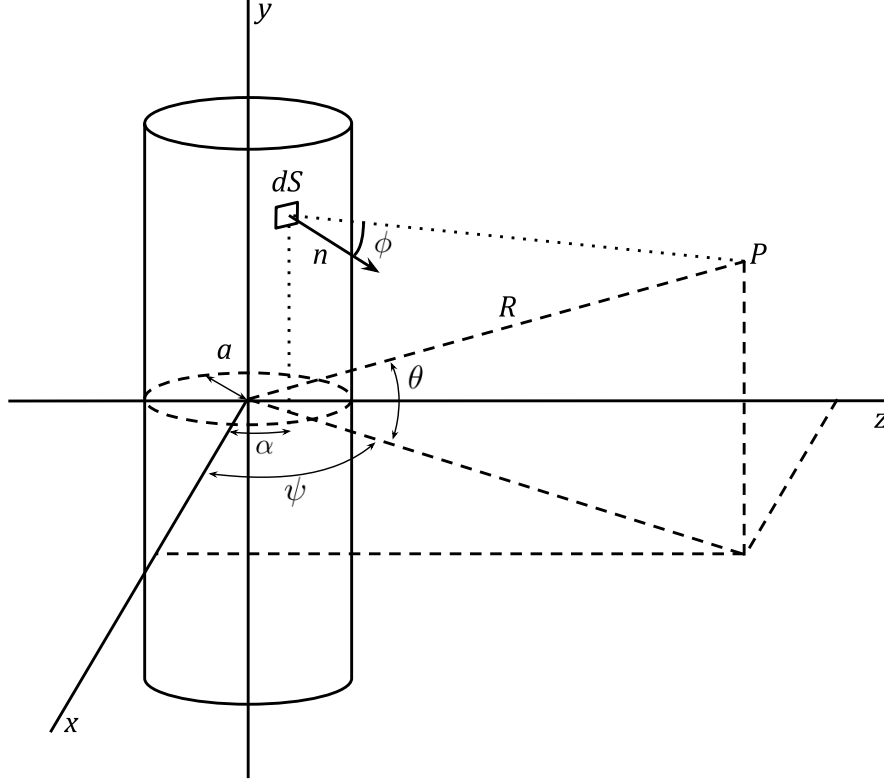


Figure 4.1: Geometry of coordinate system used in the NTFF transformation. The near-field points along the closed surface are at an angle α from the x -axis and at a distance a and elevation y from the source. Similarly, the field point is located at $P (R, \psi, \theta)$.

surface of integration in (4.2) should be a completely closed surface, however, if the pressure amplitudes are negligible away from the paraxial region, a partially closed surface centered on the axis of radiation can be used. The coordinate system in Fig. 4.1 is employed to define the relationship between the closed surface in the near-field and the observation point in the far-field, where the near-field data points along the closed surface are given by (a, α, y) and the far-field observation point is located at (R, ψ, θ) .

4.3.1 Near-Field Measurement Architecture

Similar to the methods utilized to determine the experimental results in Chapter 3, the near-field data was measured inside of the dual acoustic-RF anechoic chamber using the PCB Piezotronics, Inc. condenser microphone. Again, the sound fields were transmitted from individual circular piston sources as well as parametric transducer arrays, as discussed in Sections 4.3.2 and 4.3.3, with the acoustic sources rotated by a Kaidan Magellan MDT-19 turntable employed to capture

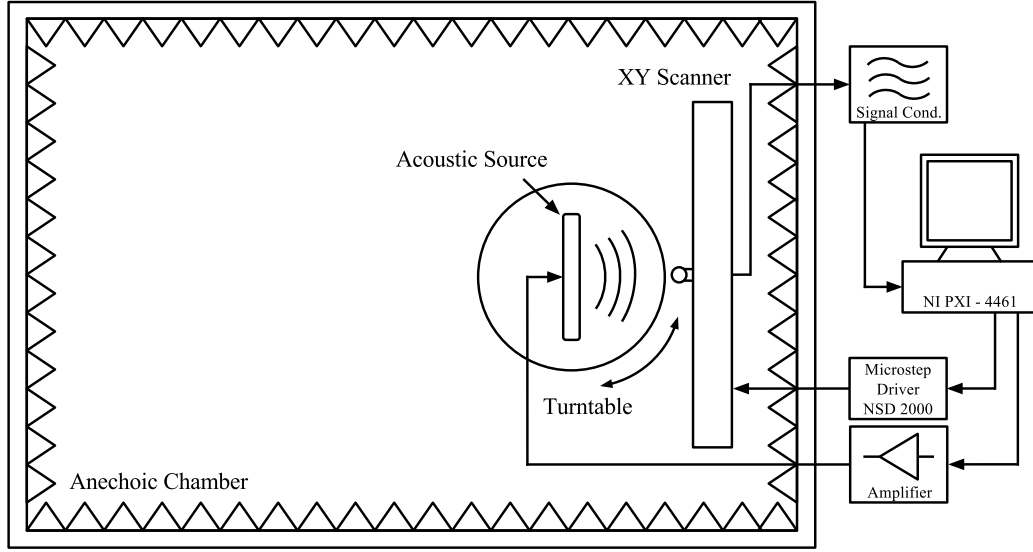


Figure 4.2: Acoustic measurement system employed to ascertain the near-field data on the surface of a cylinder enclosing the acoustic sources required by the linear and nonlinear NTFF transformations to determine the far-field responses discussed in Sections 4.3.2 and 4.3.3.

the measurement of the near-field data along an arc in the XZ plane. The microphone was attached to an XY scanner controlled by a Newark Systems NSD 2000 high-precision microstep driver to provide the ability to measure the near-field data at fractions of a wavelength in the y -axis, thus, yielding the data for a full near-field surface enclosing the acoustic sources when combined with the turntable rotation, as illustrated in Fig. 4.1, that can be used in (4.6) and (4.14) to determine the far-field response. The complete measurement configuration is shown in Fig. 4.2.

4.3.2 NTFF Transformation for a Single Uniform Planar Piston

Acoustic far-field radiation patterns calculated for primary frequencies using the Helmholtz formula have been shown to produce accurate results for a variety of transducer types operating in water [158, 159]. A similar method was used to calculate the far-field radiation pattern at 150 m at the fundamental frequency of a high power acoustic signal produced by a piston source driven at 50 kHz [38, 135], shown as the direct profile in Fig. 4.3b. The piston source has a radius of 22 mm, a moderate pressure amplitude, p_0 , of 90 dB SPL, and is operating in air with the corresponding medium parameters: density, ρ_0 , of 1.2 kg/m³, sound speed, c_0 , of 343 m/s, and coefficient of nonlinearity, β , of 1.21. The near-field was measured over a hemisphere at 10λ from the source with sample points spaced approximately $\frac{1}{3}\lambda$ apart, shown in Fig. 4.3a. Evaluating

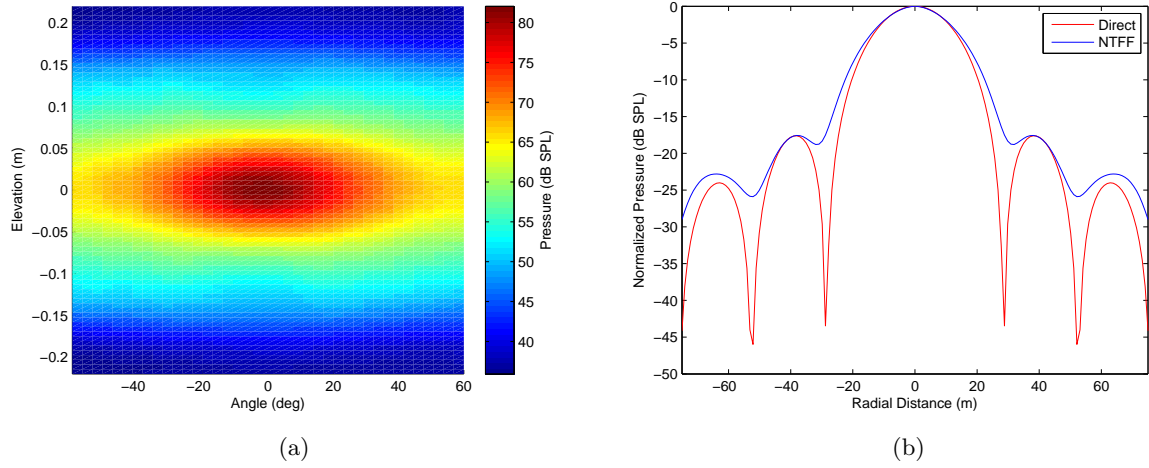


Figure 4.3: The primary sound field generated from a 22 mm diameter transducer operating at $f = 50$ kHz demonstrating the ability of the linear NTFF transformation, (4.6), to accurately produce the far-field pressure amplitude from near-field data: (a) the measured near-field data obtained at 10λ from the source and (b) a comparison of the normalized far-field pressure amplitude at 150 m obtained using direct calculation and using the linear NTFF transformation of the measured near-field data.

(4.6), this near-field data was linearly transformed into the far-field yielding the results identified as NTFF in Fig. 4.3b. The result of the linear transformation follows the general envelope of the directly calculated far-field radiation pattern; however, the nulls that are produced are not as deep as those obtained with the directly calculated results. This is a consequence of the finite number of near-field measurement points used in the transform. We have observed that increasing the near-field resolution increases the depth of the notches in the results in the far-field, yielding a closer agreement with the results from direct far-field calculation. Furthermore, the plane wave and Fraunhofer approximations made in the derivation of (4.6) account for the minor deviations in the far-field amplitude pressure for the outer sidelobes in Fig. 4.3b.

A more sophisticated use of the NTFF method is the determination of the second-order sound fields in the far-field. In Figs. 4.4 and 4.5, the solution to the second-order fields in (4.14) is compared to the results given in [135], where $\rho_0 = 995.8$ kg/m³, $c_0 = 1497.7$ m/s, and $\beta = 3.59$, using the near-field data given in [26] and [27] at 100λ from the source with sample points spaced approximately $\frac{1}{5}\lambda$ apart and shown in Figs. 4.4a, 4.5a, and 4.5c (calculated here using the implicit backward finite difference method previously discussed). The large transducer is driven at frequencies $f_1 = 16$ kHz and $f_2 = 11$ kHz for the second harmonic and sum frequency and at $f_1 = 15$ kHz and $f_2 = 12$ kHz for the difference frequency, where the effective radii of the transducer at these frequencies are found to be $a_1 = 0.87$ m and $a_2 = 0.83$ m using the method

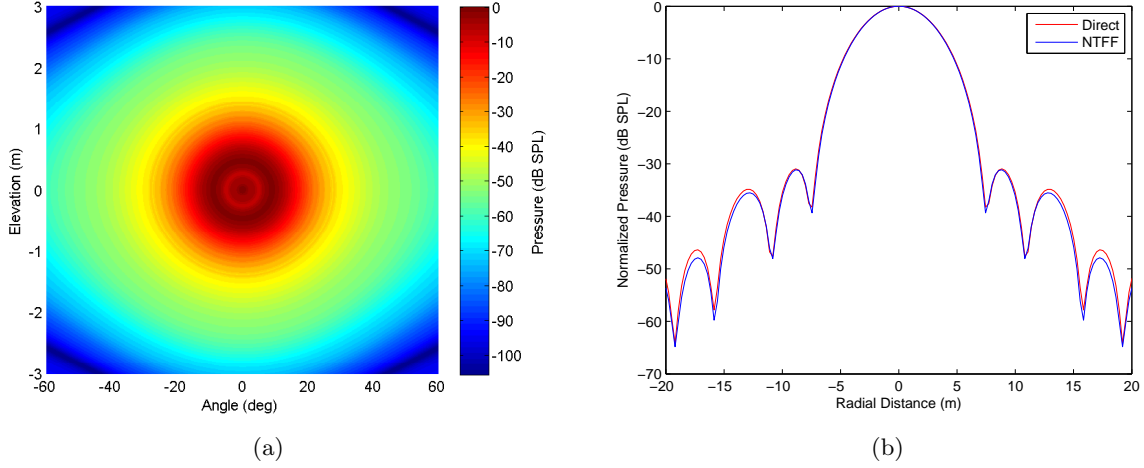


Figure 4.4: The pressure amplitudes for the second harmonic: (a) the near-field data at 100λ from the source used in the nonlinear NTFF transformation and (b) a comparison of the normalized far-field pressure amplitudes produced using the nonlinear NTFF transformation and direct computation. The radial distance is the distance from the axis normal to the direction of propagation.

outlined in [186]. Figs. 4.4b, 4.5b, and 4.5d present the normalized pressure amplitudes of the second harmonic, sum, and difference frequencies, respectively, at a distance of 150 m from the source generated using the nonlinear NTFF transformation and compared to the previously published results. Thus, it can be seen from Figs. 4.4 and 4.5 that the results obtained using the nonlinear NTFF transformation method are in agreement with the directly calculated profile for the second-order sound fields. The far-field agreement of the transformed and directly calculated far-field results is high. The close match is a result of the high density of the near-field sampled data points made possible by calculating the near-field (using the finite difference method). This can be compared to the more moderate agreement shown in Fig. 4.3b where near-field samples were experimentally measured using a coarser grid. Additionally, since the nonlinear NTFF transformation was derived from the KZK equation which is only valid at small angles in the paraxial region, the transformation is restricted to a similar region of validity. Therefore, due to this constraint, the far-field NTFF results for the second harmonic in Fig. 4.4b and sum frequency in Fig. 4.5b begin to develop discrepancies in their pressure amplitudes as the far-field angle increases off axis. The far-field pressure amplitude of the difference frequency is affected less by this constraint as the steady slope of the near-field pattern enables a more accurate integration than that of the second harmonic and sum frequencies. The many sidelobes of the second harmonic and sum frequency result in less accurate integration, thus, the the far-field

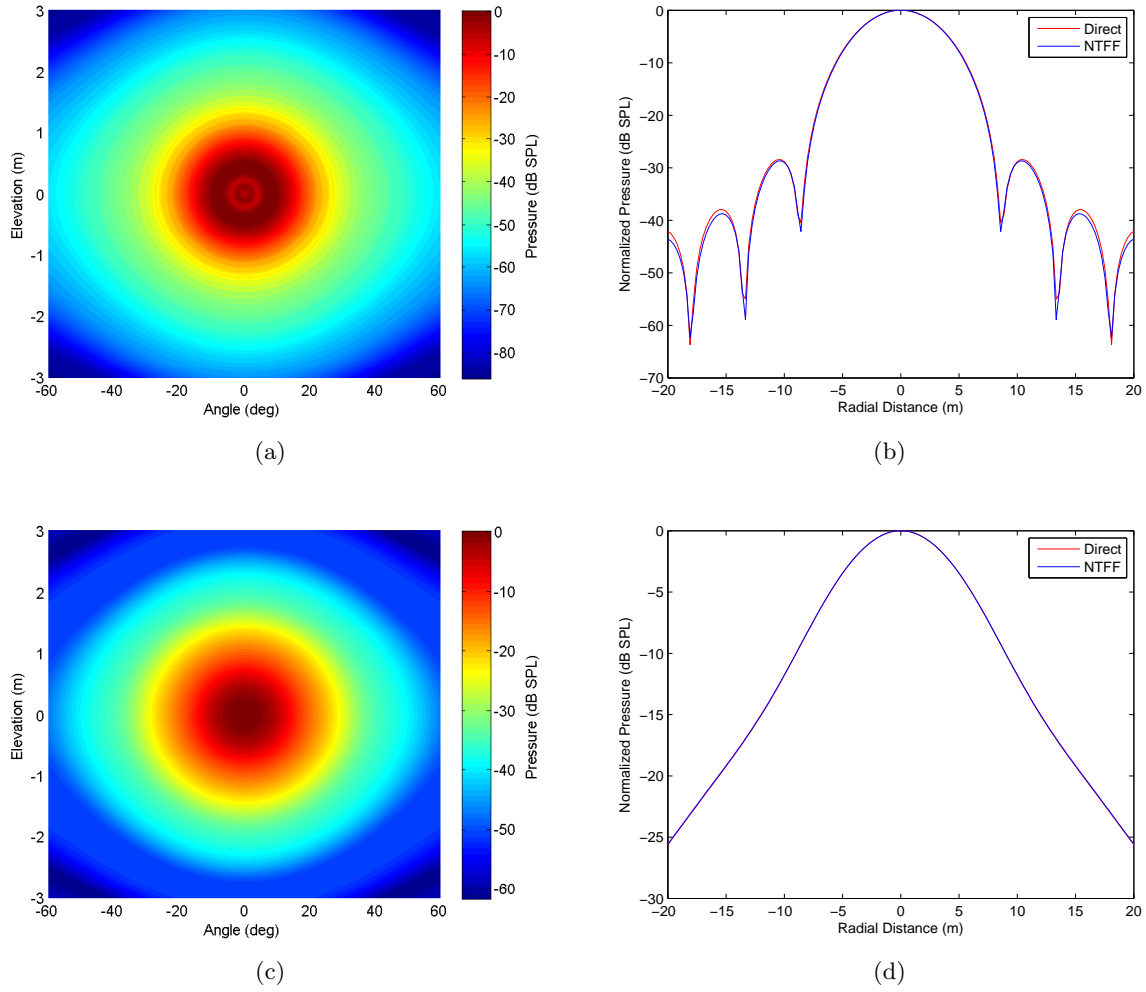


Figure 4.5: Sound pressure amplitudes for the second-order sum and difference frequencies: the near-field data at 100λ from the source used in the nonlinear NTFF transformation for (a) the sum frequency and (c) the difference frequency and a comparison of the normalized far-field pressure amplitudes calculated using the nonlinear NTFF transformation of the near-field data found using the implicit backward finite difference method and direct computation for (b) the sum frequency and (d) the difference frequency. The radial distance is the distance from the axis normal to the direction of propagation.

radiation pattern determined using the nonlinear NTFF transformation is more accurate for the difference frequency, shown in Fig. 4.5d, than for the sum frequency, shown in Fig. 4.5b.

4.3.3 NTFF Transformation for a Parametric Transducer Array

Since the NTFF transformation is valid as long as all sources are within a closed surface, the method can be applied to parametric transducer arrays given that the surface is large enough to enclose the entire physical transducer array. Therefore, to verify the accuracy of the transformation method when applied to arrays, the response of two distinct parametric transducer arrays is measured in air within the near-field and the transformation employed to determine their far-field radiation patterns. The first transducer array consists of 19 AirmarTM AT-50 ultrasonic transducers with a diameter of 31 mm hexagonally arranged with spacing between the centers of adjacent transducers of 66 mm. The transducers were driven by two tones with frequencies $f_1 = 51$ kHz and $f_2 = 49$ kHz with primary sound pressure amplitudes $p_{01} = p_{02} = 115$ dB SPL. The far-field secondary sound fields, with sum frequency $f_S = 100$ kHz and difference frequency $f_D = 2$ kHz, were calculated at a distance of 150 m from the transducers, again using the method described in [38, 135]. The sound profiles of the primary sound fields and the nonlinearly generated scattered sound fields were measured in the near-field at a distance of 25λ from the source (i.e., 17 cm) with sample points spaced approximately 0.9λ apart, given in Figs. 4.6a, 4.7a, and 4.7c. The NTFF transformations were then employed to evaluate the measured near-field data yielding the far-field characteristics shown in Figs. 4.6b, 4.7b, and 4.7d. Fig. 4.6b shows the pressure amplitude of the fundamental frequency at a distance of 150 m found using (4.6) and Figs. 4.7b and 4.7d show the pressure amplitudes of the sum and difference frequencies, respectively, at a distance of 150 m found using (4.10). The expected results for the far-field radiation pattern determined by direct calculation for the 19 element transducer array can be seen to be close to the results obtained by transforming the near-field measurements. As with the single transducer, the results of the linear NTFF transform follows the general envelope of the directly calculated far-field profile, however, there is an inconsistency between the transformation and directly calculated pressure amplitudes for the first sidelobe. The error in pressure amplitude is caused by insufficient sampling of the near-field along the horizontal axis, as the near-field measurements were not extended beyond the active face of the array, visible in Fig. 4.6a, leading to inaccuracies in the far-field radiation pattern. Additionally, the second-order far-fields in Figs. 4.7b and 4.7d suffer from similar problems in pressure amplitude accuracy due to the insufficient near-field sampling, as well as having errors introduced by the applicability of the KZK equation which become more apparent as the angle increases away from the direction of propagation. Again, the difference frequency does not encounter similar pressure amplitude discrepancies from the limitations imposed by the KZK equation since the near-field integration surface is less complex and the change in far-field amplitude is less than 3 dB.

The second transducer array considered is a 92 cm LRAD-1000XTM long range acoustic

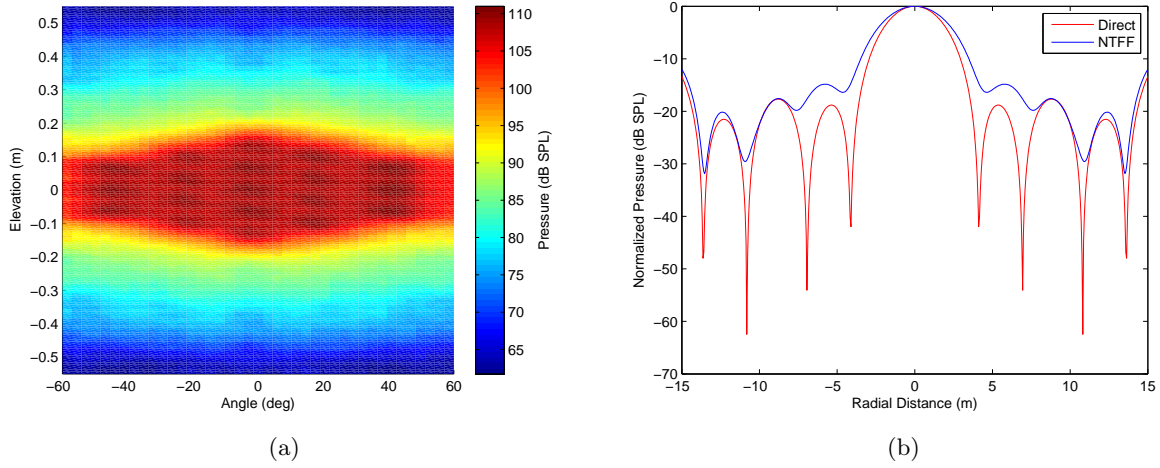


Figure 4.6: The primary sound field at 51 kHz for the 19 element parametric transducer array: (a) the near-field data experimentally sampled at 25λ from the source and (b) a comparison of the normalized far-field pressure amplitudes using the linear NTFF transformation of the measured near-field data and direct computation.

device from American Technology Corp. that consists of 7 hexagonally arranged circular transducers each with a diameter of 81 mm and spacing between the centers of adjacent transducers of 28 cm. The transducers are driven at the lower frequencies of $f_1 = 4$ kHz and $f_2 = 3$ kHz with primary sound pressure amplitudes $p_{01} = p_{02} = 140$ dB SPL producing a sum frequency $f_S = 7$ kHz and difference frequency $f_D = 1$ kHz. Again, the near-field data is measured inside of the anechoic chamber at a distance of 10λ (i.e., 98 cm) from the source with sample points spaced approximately $\frac{1}{10}\lambda$ apart and shown in Figs. 4.8a, 4.9a, and 4.9c. Figs. 4.8b, 4.9b, and 4.9d describe the pressure amplitudes of the fundamental, sum, and difference frequencies, respectively, at a distance of 150 m from the LRAD and are shown to agree with the expected results found via direct computation. As with the first transducer array, the far-field radiation pattern for the fundamental frequency in Fig. 4.8b was generated using (4.6) while the secondary sound fields in Figs. 4.9b and 4.9d were generated used (4.10). The far-field radiation pattern found using the linear NTFF transformation for the fundamental frequency generated by the LRAD experiences the same inaccuracies in the pressure amplitude of the first sidelobe as the 19 element transducer array. As before, the size of the measurement surface in the near-field was insufficient, due to the constraints caused by the physical dimensions of the transducer array inside of the anechoic chamber, yielding amplitude errors in the far-field of both the primary and secondary sound fields. Again, it is evident from the discrepancy between the nonlinear transformation and directly calculated far-field results as the angle increases away

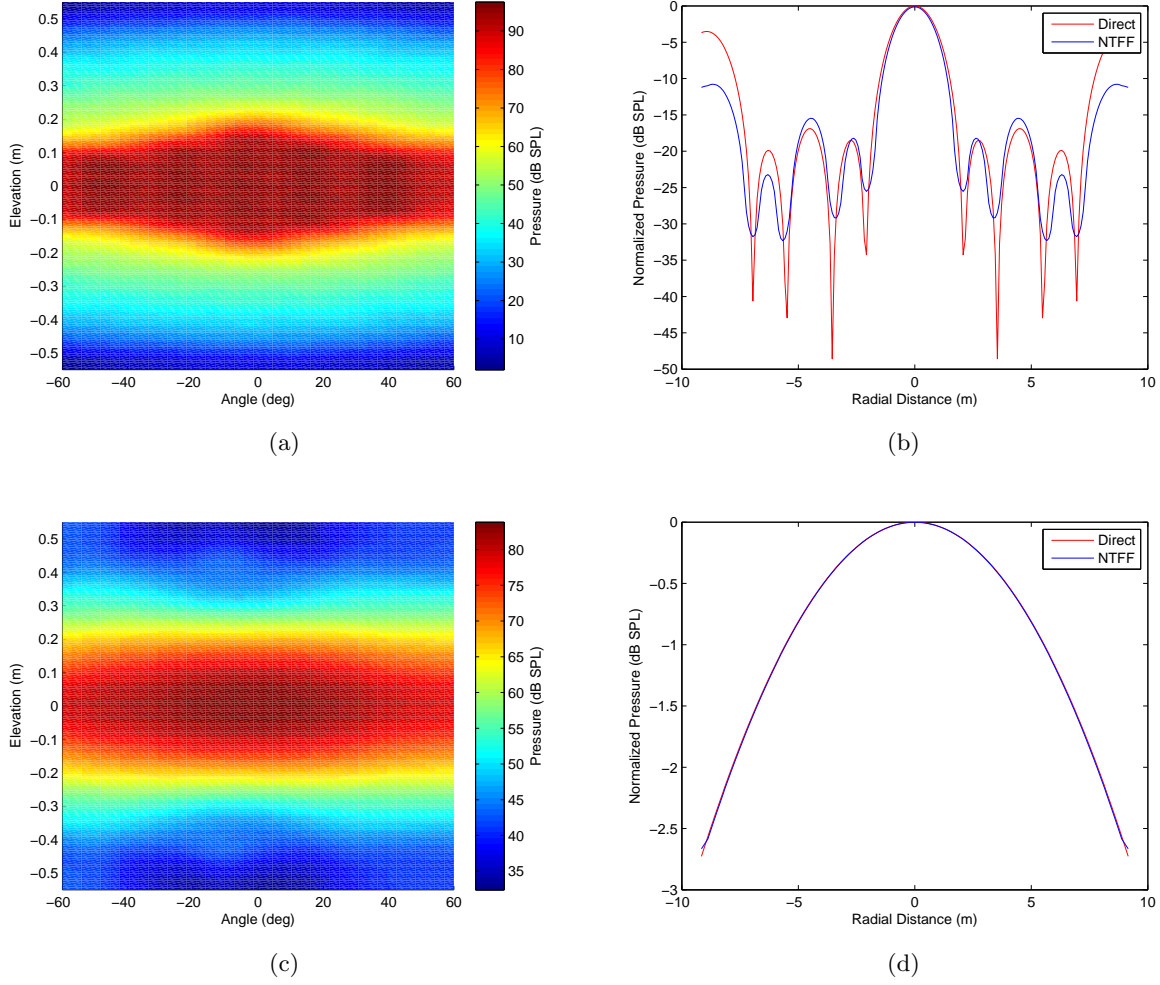


Figure 4.7: Sound pressure amplitudes for the second-order sum and difference frequencies generated from the 19 element parametric transducer array: the near-field data experimentally sampled at 25λ from the source for (a) the sum frequency and (c) the difference frequency and a comparison of the normalized far-field pressure amplitudes calculated using the nonlinear NTFF transformation of the measured near-field data and direct computation for (b) the sum frequency and (d) the difference frequency.

from the propagation axis for the sum frequency in Fig. 4.9b that as the accuracy of the KZK equation declines, so does the accuracy of the nonlinear NTFF transform. Additionally, the nonlinear transformation of the difference frequency is, once again, in excellent agreement with the directly calculated results as the far-field radiation pattern varies by less than 1 dB across the computed region.

Therefore, as is suggested by Kirchhoff in his theorem, Figs. 4.6, 4.7, 4.8, and 4.9 show that

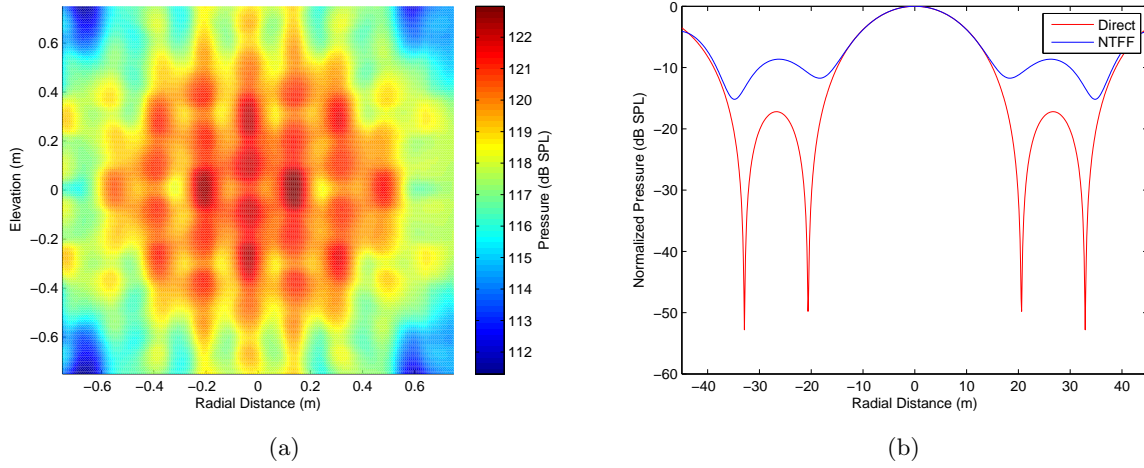


Figure 4.8: The primary sound field for the LRAD parametric transducer array: (a) the near-field data experimentally sampled at 10λ from the source and (b) a comparison of the normalized far-field pressure amplitudes calculated using the linear NTFF transformation and direct computation.

solutions to (4.2) remain valid for determining the far-field radiation patterns of multiple sources as long as all sources are contained within the closed surface used for integration. There are slight discrepancies, however, between the directly calculated results and the NTFF transformation for the amplitude of the first sidelobe of the primary sound field from the transducer arrays. This is due to the plane wave approximation for the change in the pressure normal to the source, $\partial p / \partial n = jkp$, and the Fraunhofer approximation made in the derivation of the solution given in (4.6). Additionally, the KZK equation is strictly valid only for sound beams and the accuracy decreases at large angles from the primary axis; thus, the second-order solutions suffer similar accuracy disparity at large off-axis angles, which can be seen in Figs. 4.7b and 4.9b. Insufficient near-field sampling, particularly when measurements do not exceed the dimensions of the active face of the acoustic source, can also significantly effect the accuracy of the linear and nonlinear NTFF transformations.

4.4 Summary

A nonlinear near-to-far-field, NTFF, transformation was presented that accurately models the far-field characteristics of second-order acoustic fields produced by the scattering of sound by sound. Using solutions to the KZK nonlinear parabolic wave equation in place of Kirchhoff's solution to the linear Helmholtz equation, it was shown that the expressions for the NTFF

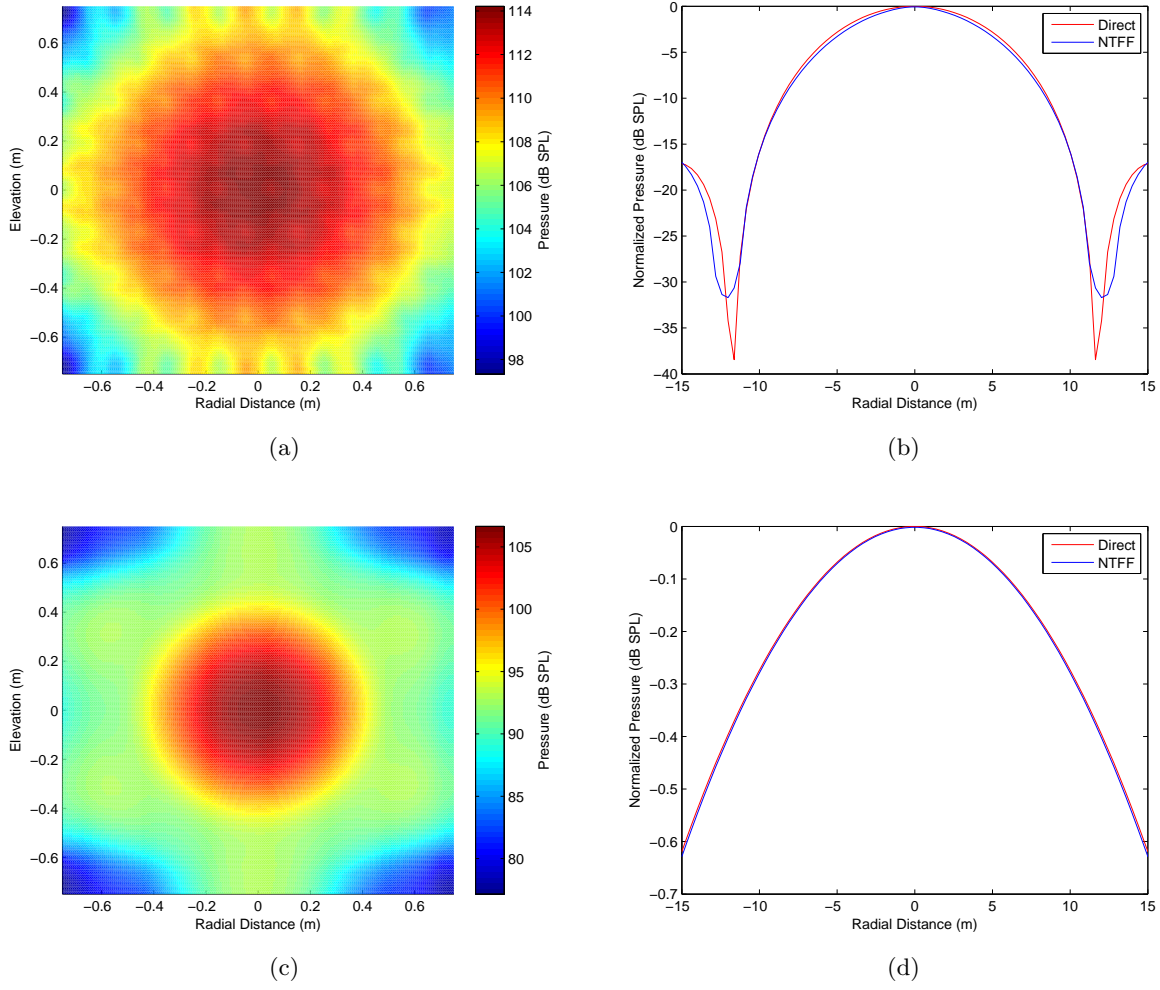


Figure 4.9: Sound pressure amplitudes for the second-order sum and difference frequencies generated from the LRAD parametric transducer array: the near-field data experimentally sampled at 10λ from the source for (a) the sum frequency and (c) the difference frequency and a comparison of the normalized far-field pressure amplitudes calculated using the nonlinear NTFF transformation of the measured near-field data and direct computation for (b) the sum frequency and (d) the difference frequency.

transformation yield solutions for the second-order sound fields (i.e., second harmonic, sum, and difference frequencies) that agree with previous theoretical and experimental results. It was also shown that the transformation remains valid when multiple sources are enclosed within the near-field surface enabling its use with more complex acoustic sources, such as parametric transducer arrays, as long as the sources are axially symmetric. Since the nonlinear NTFF transformation, (4.10), was derived from a solution of the KZK equation, the validity of the transformation

is similar to that for the KZK equation, particularly its restriction to the paraxial region. Computationally, the NTFF transformation is comparable to the results from direct calculation in terms of time and memory. Deviations between the far-field radiation patterns produced by the NTFF transformation and the expected results arise from the approximations made in derivations of (4.6) and (4.10), particularly the plane wave and paraxial approximations; however, the general envelope of the NTFF transform provides an accurate portrayal of the far-fields generated by the acoustic sources.

The NTFF transformation yields accurate far-field characteristics given that the near-field data is sampled properly. The sampled near-field data must have less than λ separation between adjacent measurement points to produce valid results from the transformation. As the separation between the sampled points decreases, the accuracy of the far-field results increases, in particular, the depth of the nulls in the far-field response determined by the NTFF transformation increases thereby providing a closer agreement with the results from direct far-field calculation. Additionally, the sampled near-field data should compose a completely closed surface containing the acoustic source, however, a partially closed surface can be utilized given that the pressure amplitudes outside of the surface are negligible. If the sampled surface does not exceed the dimensions of the active face of the acoustic source, thus yielding an insufficient sampling in the near-field, significant errors are introduced into the results of the transformation. The location of the near-field surface is also critical to a proper sampling of the near-field data. The surface must reside at a sufficient distance from the acoustic source to allow for the sound wave to travel multiple wavelengths but not far enough away to begin to approach the Fraunhofer distance, which denotes the boundary of the far-field.

As the ability to determine the far-field characteristics of higher-order sound fields has grown in importance with their increased use in a variety of applications, the NTFF transformation provides the unique capability of computing the far-field radiation patterns of an acoustic source by requiring measured or calculated information only from the near-field of the source. The primary interests when analyzing sound field radiation patterns are the directivity of the main beam and the sidelobe levels, both of which are accurately calculated in the far-field under conditions in which the KZK equations is valid using the NTFF transformation. Of the first- and second-order sound fields, the difference frequency signal holds significant importance as the primary, harmonic, and sum tones will be rapidly attenuated in mediums such as air and water when the frequencies of the primary tones are sufficiently high. Additionally, the difference frequency has high directivity but it is often impractical to physically measure the profile of this signal's far-field response. The work presented in this chapter enables the determination of far-field acoustic radiation pattern of the difference frequency, along with the other second-order sound fields, by using near-field data easily obtained through computationally simple calculation or practical measurement.

Chapter 5

Near-Field Radio Frequency Scattering from Vibrating Structures in an Acoustically-Excited Environment

5.1 Introduction

The previous chapters addressed limitations in the practical implementation of acousto-EM sensing schemes by developing improved methods for determining the acoustic radiation patterns generated from a variety of sound sources. This chapter, however, will enhance the understanding of the fundamental processes that produce the nonlinear interaction between acoustic and EM waves by developing a mathematical description of the modulation induced on an EM signal by the periodic change in the medium characteristics due to the propagation of a high powered acoustic wave, experimentally verifying the model using bistatic radar and a long range acoustic device (LRAD) for the generation of high powered acoustic waves.

Radio frequency (RF) signals have long been used for probing, characterizing, and identifying targets in a variety of sensing applications, including interferometry [107], navigation [86], and ground penetrating radar (GPR) [108]. However, the use of RF signals in many detection schemes, particular GPR, is greatly limited by the typically low contrast between the target object and the background environment. As a means of improving the distinction between an object and its surrounding environment, recent works have proposed using an acoustic or seismic wave to induce a mechanical vibration on the object, thereby modulating a scattered electromagnetic (EM) signal and enhancing the interrogated object contrast [3–5, 7, 11, 88, 102, 121].

The resultant reflected and scattered RF signals are modulated with characteristics unique to the structure and composition of the vibrating object; thus, providing information about the structure of the target as well as distinguishing it from clutter.

Acoustically- or seismically-induced mechanical vibrations of buried objects tend to be in the one hertz to hundreds of hertz region so that the modulation sidebands on the scattered EM signal are very close in frequency to the relatively large, directly reflected transmitted signal which, for many cluttered or embedded environments, is usually very large. This is a common problem arising when attempting to employ acousto-EM sensing schemes as the acoustically- or seismically-excited mechanical vibrations often lead to low-level close-in modulated sidebands from objects such as landmines.

This chapter considers an additional sensing modality beyond the Doppler effect and more commonly examined effects, such as path loss, radar cross section, and special relativity, arising from the scattering of an EM wave by a propagating high powered acoustic wave in the medium and develops a theoretical analysis that enables the various near- to mid-field sensing modalities to be compared. Enhanced detectability and identifiability of reflected radar returns embodying scattering resulting from mechanical vibrations and rotations from targets such as aircraft is well known [187]; however, in these cases, the modulating signal is often hundreds of hertz to many tens of kilohertz with a distant target and the clutter environment is typically much less severe than with ground-based sensing. Exploitation of the induced acousto-EM interaction, therefore, enables the improvement of RF probing in near-field non-contact characterization and stand-off non-destructive evaluation applications, such as landmine detection [3, 4, 7], medical imaging [11], and structural integrity evaluation [11, 88].

Considerable effort has been put into understanding the scattering of an RF signal by a vibrating structure [110–118]. Borkar and Yang [110] developed solutions for the fields scattered by oscillating plane and cylindrical surfaces. Kleinman and Mack [111] presented solutions accounting for the Doppler shift when determining the fields scattered by linearly vibrating objects. De Zutter [112] investigated the effect of translational motion in the generation of a scattered RF field and Cooper [113] and Gray and Addison [117] considered the effect of nonuniform motion on the resultant EM spectrum. Van Bladel and De Zutter [114] and De Zutter [115] derived solutions for the scattered fields from sinusoidally moving plates interrogated at normal and oblique incidences, respectively. From these works it can be seen that sidebands in the scattered EM spectrum resulting from a vibrating surface has traditionally been attributed solely to the Doppler effect. This assumption that the Doppler effect is the singular physical mechanism in which a scattered spectrum is generated has also been extended to a variety of applications in order to account for EM scattering from vibrating objects, particularly radar [116–118].

A major issue in developing an understanding of the effects of acousto-EM scattering is that numerical analyses of the scattering processes, particularly for motions that are more com-

plex, provide little intuition into the fundamental mechanism generating the scattering, as the analyses are typically limited to full-field EM solutions [5,7,188] or to arbitrary waveform analysis [117,118]. Experimental investigations also provide little insight since many of the identifying characteristics of the reflected RF signal (i.e., vibration-induced modulation of the signal) occur at small signal levels that are not detectable because of the limited dynamic range of traditional sensors. With recent developments in sensor technologies due to enhancements in analog cancellation techniques, however, the dynamic range of RF sensors has greatly improved, thereby enabling better detection of low-frequency and low-level sideband modulation in a reflected signal [102,119–122]. Therefore, with the improved detection capabilities, fundamental physical processes that result in the scattering of an RF signal that were previously undetectable, such as modulations induced by medium fluctuations due to a propagating acoustic wave, can be examined. This understanding of the fundamental sensing limits of RF systems can prove useful in the determination of new sensing modalities that utilize responses in a physical domain orthogonal to the RF sensing probe, such as is the case with acousto-EM interactions.

This chapter presents an analytical description of the scattering of an RF signal from fluctuations in the electrical properties of the embedding medium caused by the propagation of an acoustic wave. This enhances the understanding of the fundamental physics behind the the generation of scattered EM fields produced by the nonlinear interaction of acoustic and EM waves in an acoustically-excited environment. Section 5.2 theoretically develops an analytical solution for the modulation effects introduced when a high-powered acoustic wave propagates through a medium to induce vibrations on a structure and compares the analytical results with the predominant modulation effects emerging as a direct result of an object vibrating, including Doppler phase modulation and amplitude modulation due to special relativity, path loss, and radar cross section (RCS). Section 5.3 describes the detection of acoustically-induced modulation of an RF signal using zero span frequency measurement as an alternative approach to measure the modulation sideband power over time instead of over a frequency range. Section 5.4 demonstrates that the analytical solutions for the combined modulation effects are in good agreement with near-field radar scattering measurements while providing key insights into the fundamental physics behind the production of the scattered RF signals due to presence of high powered acoustic waves.

5.2 Radio Frequency Scattering from Medium Property Fluctuations due to High Powered Acoustic Sources

Conventional analysis of interacting acoustic and EM waves attributes the generation of the resultant scattered EM fields solely to the Doppler effect, as the sinusoidal vibrational motion

induced on an object by the incident acoustic waves shifts the frequency of an RF signal, as discussed in Section 2.4.1. A recent investigation [109] reexamining the fundamental physical mechanisms that result in the scattering of an EM signal in an acoustically-excited environment focused primarily on modulation effects resulting directly from vibrations induced on a target, as detailed in Section 2.4.2, however, when an acoustic or seismic wave induces vibrations, the electrical properties of the embedding medium, especially its permittivity, fluctuate. Thus, a complicating modulated signal will be introduced into the clutter return. As the sound wave propagates, the dielectric constant of the medium, $\epsilon(t)$, varies periodically due to density variation created by the traveling pressure wave. This can be expressed mathematically as [189, 190]

$$\epsilon(t) = \epsilon_0 \epsilon_r [1 + \delta(t)], \quad (5.1)$$

where

$$\delta(t) = \frac{K p_A(t)}{\epsilon_r} = \frac{p_A(t)}{\rho_0 c_A^2} \frac{(\epsilon_r - 1)(\epsilon_r + 2)}{3\epsilon_r} \quad (5.2)$$

is the amplitude fluctuation of the permittivity, K is a constant of proportionality obtained as an approximation of the Lorentz-Lorenz relation, $p_A(t)$ is the propagating acoustic pressure at a particular position, ϵ_0 is the free-space permittivity, and ϵ_r , ρ_0 , and c_A are the at-rest relative permittivity, density, and the acoustic sound speed of the medium, respectively. It can be seen from (5.2) that the fluctuations in permittivity are directly proportional to the acoustic frequency and amplitude over time. Therefore, an EM signal in the sound perturbed medium will experience modulation corresponding to the frequency of the propagating acoustic signal, ω_A , and its harmonics.

Assuming that the transmitted RF signal is a linearly polarized plane wave traveling in the z direction, Maxwell's equations in the absence of sources become

$$\frac{\partial \mathcal{E}_y(t)}{\partial z} = \frac{\partial \mathcal{B}_x(t)}{\partial t}, \quad \frac{\partial \mathcal{H}_x(t)}{\partial z} = \frac{\partial \mathcal{D}_y(t)}{\partial t}, \quad (5.3)$$

where the constitutive relations for the nonmagnetic medium, incorporating (5.1), are given by

$$\mathcal{D}_y(t) = \epsilon(t) \mathcal{E}_y(t) = \epsilon_0 \epsilon_r \left[1 + \frac{p_A(t)}{\rho_0 c_A^2} \frac{(\epsilon_r - 1)(\epsilon_r + 2)}{3\epsilon_r} \right] \mathcal{E}_y(t), \quad (5.4)$$

$$\mathcal{H}_x(t) = \frac{1}{\mu_0} \mathcal{B}_x(t). \quad (5.5)$$

Realizing that the acoustic frequencies will be relatively close to the RF carrier so that the differentiation of the EM signal with respect to time may be simplified in the phasor form to $-j\omega_{\text{RF}}$, the wave equation describing the propagation of the RF signal in the sound perturbed

medium can be written

$$\frac{\partial^2 \mathcal{E}_y(t_A)}{\partial z^2} + k_{\text{RF}}^2 \epsilon_r \left[1 + \frac{p_A(t_A)}{\rho_0 c_A^2} \frac{(\epsilon_r - 1)(\epsilon_r + 2)}{3\epsilon_r} \right] \mathcal{E}_y(t_A) = 0, \quad (5.6)$$

where $k_{\text{RF}} = \omega_{\text{RF}}/c$ is the free-space EM wave number and $\mathcal{E}_y(t_A)$ is the phasor of the y -directed \mathcal{E} field varying slowly at the acoustic time scale, t_A .

If the periodic acoustic pressure wave, $p_A(t)$, is defined as having a radian frequency and wavenumber of ω_A and $k_A = \omega_A/c_A$, respectively, so as to be expressed

$$p_A(t) = \sum_{n=1}^{\infty} p_n \cos(n\omega_A t) \cos(nk_A z), \quad (5.7)$$

where p_n is the amplitude of the acoustic source at the n -th harmonic, then it can be seen that the EM wave equation in (5.6) takes the canonical form of Mathieu's differential equation, written in a generic form as

$$\frac{\partial^2 y}{\partial z^2} + [a - 2q \cos(2z)] y = 0. \quad (5.8)$$

Therefore, by following the method in [189] to solve Mathieu's differential equation, a solution for the acoustically-modulated EM wave equation can be found as

$$s(t) = a_0 \cos(\omega_{\text{RF}} t + k_{\text{RF}} \sqrt{\epsilon_r} z) \times \left\{ 1 + \sum_{\substack{n=-\infty \\ n \neq 0}}^{\infty} \frac{2p_n (k_{\text{RF}}/nk_A)^2 (\epsilon_r - 1)(\epsilon_r + 2)}{3\rho_0 c_A^2 [1 - 4(k_{\text{RF}}/nk_A)^2 \epsilon_r]} \cos(n\omega_A t) \cos(nk_A z) \right\}, \quad (5.9)$$

where a_0 is an amplitude term. Thus, from (5.9), it is seen that an RF signal propagating in a sound perturbed medium will be amplitude modulated by the acoustic signal. Therefore, by omitting the attenuation terms as the signal propagates, an expression for the modulation signal when considering acoustically-induced fluctuations in a medium can be written

$$s(t) = A_{\text{Acoust}}(t) \cos(\omega_{\text{RF}} t). \quad (5.10)$$

Examining (5.9), a simple expression for the normalized amplitude modulation can then be

obtained as

$$\begin{aligned}
A'_{\text{Acoust}}(t) &= 1 + \sum_{\substack{n=-\infty \\ n \neq 0}}^{\infty} \frac{2p_n (k_{\text{RF}}/nk_A)^2 (\epsilon_r - 1)(\epsilon_r + 2)}{3\rho_0 c_A^2 \left[1 - 4 (k_{\text{RF}}/nk_A)^2 \epsilon_r\right]} \cos(n\omega_A t) \\
&= F_{\text{Acoust},0} + 2 \sum_{n=1}^{\infty} F_{\text{Acoust},n} \cos(n\omega_A t)
\end{aligned} \tag{5.11}$$

with Fourier coefficients

$$F_{\text{Acoust},0} = 1, \quad F_{\text{Acoust},n} = \frac{p_n (k_{\text{RF}}/nk_A)^2 (\epsilon_r - 1)(\epsilon_r + 2)}{3\rho_0 c_A^2 \left[1 - 4 (k_{\text{RF}}/nk_A)^2 \epsilon_r\right]}. \tag{5.12}$$

Substituting (5.11) and (5.12) into (5.10), the received modulated signal can be written

$$\begin{aligned}
s'(t) &= \left[F_{\text{Acoust},0} + 2 \sum_{n=1}^{\infty} F_{\text{Acoust},n} \cos(n\omega_A t) \right] \cos(\omega_{\text{RF}} t) \\
&= F_{\text{Acoust},0} \cos(\omega_{\text{RF}} t) + \sum_{n=1}^{\infty} F_{\text{Acoust},n} \cos[(\omega_{\text{RF}} \pm n\omega_A)t].
\end{aligned} \tag{5.13}$$

Thus, the amplitude of the n -th acoustic AM sideband tone relative to the RF carrier tone is

$$\begin{aligned}
A_{\text{Acoust},n} &= \frac{p_n (k_{\text{RF}}/nk_A)^2 (\epsilon_r - 1)(\epsilon_r + 2)}{3\rho_0 c_A^2 \left[1 - 4 (k_{\text{RF}}/nk_A)^2 \epsilon_r\right]} \\
&= \frac{p_n (\lambda_A/n\lambda_{\text{RF}})^2 (\epsilon_r - 1)(\epsilon_r + 2)}{3\rho_0 c_A^2 \left[1 - 4 (\lambda_A/n\lambda_{\text{RF}})^2 \epsilon_r\right]},
\end{aligned} \tag{5.14}$$

where λ_A is the acoustic wavelength in the medium and λ_{RF} is the free-space EM wavelength.

Note that when a vibrating structure is acoustically excited, the frequency of vibration is that of the acoustic frequency ($\omega_V = \omega_A$). Thus, the vibration induced modulation and the modulation produced by the acoustic wave in an embedding medium are at the same frequency.

Thus, it can be seen that the effect of the propagating pressure wave on the characteristics of a medium causes modulation on an RF carrier. The amplitude of the modulation due to acoustic propagation is directly proportional to the sound pressure level of the wave and, therefore, this modulation effect can be magnified by the use of high powered acoustic sources. Additionally, there is a resonance point corresponding to when the RF wavelength is equal to $2/n$ of the acoustic wavelength,

$$\frac{2}{n} \frac{\lambda_A}{\lambda_{\text{RF}}} \sqrt{\epsilon_r} = 1. \tag{5.15}$$

Therefore, for a lossless medium, the solution for the modulation induced by a propagating acoustic wave will mathematically blow up under the condition in (5.15). However, in practical application where the medium is lossy, the amplitude of the resonance will be limited. To minimize the situation where the permittivity modulation effect masks detection of an acoustically-excited vibrating target, the RF wavelength in the medium, $\lambda_{\text{RF}}/\sqrt{\epsilon_r}$, should not be submultiples of twice the acoustic wavelength. However, in some circumstances, it may be desirable to maximize the coupling of the acoustic and RF waves in a medium in which case the RF wavelength should be twice the acoustic wavelength.

5.2.1 Comparison with Other Acousto-Electromagnetic Modulation Effects

To determine the significance of the modulation due to acoustically-induced medium fluctuations, the results derived in Section 5.2 were compared to the phase and amplitude modulations that appear on a signal propagating in an acoustically-excited environment and reflected from a vibrating surface, particularly a linearly vibrating plate, as discussed in Sections 2.4.1 and 2.4.2. By combining all of these effects, the modulated received signal for an acoustically-induced linearly vibrating plate can be written

$$s(t) = \alpha_0 A_{\text{Acoust}}(t) A_{\text{PL}}(t) A_{\text{RCS}}(t) \gamma(t) \cos [\omega_{\text{RF}} t - \phi_{\text{Doppler}}(t)], \quad (5.16)$$

where

$$A_{\text{PL}}(t) = 1 + \sum_{n=1}^{\infty} \left(\frac{2(n+1)}{2^n} \right) \left(\frac{d_V}{R_0} \right)^n \cos(n\omega_V t), \quad (5.17)$$

$$A_{\text{RCS}}(t) = 1 + \sum_{n=1}^{\infty} \frac{2(2\pi)^n}{(n+1)!} \left(\frac{a\varphi/2}{\lambda_{\text{RF}}} \right)^n \cos(2n\omega_V t), \quad (5.18)$$

$$\gamma(t) = 1 + \sum_{n=1}^{\infty} 4\pi^n \left(\frac{d_V}{\lambda_V} \right)^n \cos(n\omega_V t), \quad (5.19)$$

are the amplitude modulations due to path loss variation, a rocking target, and special relativity, as given by (2.103), (2.110), and (2.97), respectively, $\phi_{\text{Doppler}}(t)$ is the phase modulation from the Doppler effect yielding the reflected signal, as given by (2.94),

$$s(t) = \sum_{n=1}^{\infty} \frac{(2\pi)^n}{n!} \left(\frac{d_V}{\lambda_{\text{RF}}} \right)^n \cos [(\omega_{\text{RF}} \pm n\omega_V)t \pm n\frac{\pi}{2}], \quad (5.20)$$

$A_{\text{Acoust}}(t)$ is amplitude modulation from propagation in the sound perturbed medium, as given by (5.11), and α_0 is a constant accounting for transmitted power, non time-dependent effects, and amplitude solution of the Mathieu's equation for path loss, radar cross section, and medium

fluctuations, respectively. Therefore, substituting the Fourier series expansions for (5.11) and (5.17)–(5.20) into (5.16), and assuming that the AM effects are multiplicative, the normalized signal becomes

$$\begin{aligned}
s'(t) = & \left[\sum_{n=-\infty}^{\infty} A_{\text{Doppler},n} \cos \left(\omega_{\text{RF}} t + n\omega_V t + n\frac{\pi}{2} \right) \right] \\
& \times \left[F_{\text{Acoust},0} + \sum_{n=1}^{\infty} F_{\text{Acoust},n} \cos(n\omega_A t) \right] \\
& \times \left[F_{\text{PL},0} + \sum_{n=1}^{\infty} F_{\text{PL},n} \cos(n\omega_V t) \right] \\
& \times \left[F_{\text{RCS},0} + \sum_{n=1}^{\infty} F_{\text{RCS},n} \cos(2n\omega_V t) \right] \\
& \times \left[F_{\gamma,0} + \sum_{n=1}^{\infty} F_{\gamma,n} \cos(n\omega_V t) \right], \tag{5.21}
\end{aligned}$$

which is a similar expression for the normalized signal due to the combined modulation effects given in [109] with the addition of the AM due to a sound perturbed medium. Following a similar development as performed in [109], (5.21) can be simplified to

$$\begin{aligned}
s'(t) \approx & \left[\sum_{n=-\infty}^{\infty} A_{\text{Doppler},n} \cos \left(\omega_{\text{RF}} t + n\omega_V t + n\frac{\pi}{2} \right) \right] \\
& + \left[\sum_{n=1}^{\infty} F_{\text{PL},n} \cos(n\omega_V t) \right] \cos(\omega_{\text{RF}} t) \\
& + \left[\sum_{n=1}^{\infty} F_{\text{Acoust},n} \cos(n\omega_A t) \right] \cos(\omega_{\text{RF}} t) \\
& + \left[\sum_{n=1}^{\infty} F_{\text{RCS},n} \cos(2n\omega_V t) \right] \cos(\omega_{\text{RF}} t) \\
& + \left[\sum_{n=1}^{\infty} F_{\gamma,n} \cos(n\omega_V t) \right] \cos(\omega_{\text{RF}} t), \tag{5.22}
\end{aligned}$$

since the zero-order terms in the Fourier series expansions of the contributing modulation mechanisms are approximated as unity resulting in a single first-order term for each of the processes discussed with additional modulation tones that are the product of the higher-order Fourier coefficients of multiple modulation mechanisms; however, these higher-order products have amplitudes that are much lower than those produced by a single process alone and, therefore, can be discarded. Using trigonometric expansions to combine the carrier and modulated signal

frequencies, the normalized modulated signal can be further simplified as

$$\begin{aligned}
s'(t) \approx & \cos(\omega_{\text{RF}} t) \\
& + \sum_{n=1}^{\infty} \left[A_{\text{Doppler},n} \cos \left(\omega_{\text{RF}} t \pm n\omega_V t \pm n\frac{\pi}{2} \right) \right] \\
& + \sum_{n=1}^{\infty} [A_{\text{Acoust},n} \cos (\omega_{\text{RF}} \pm n\omega_A) t] \\
& + \sum_{n=1}^{\infty} [A_{\text{PL},n} \cos (\omega_{\text{RF}} \pm n\omega_V) t] \\
& + \sum_{n=1}^{\infty} [A_{\text{RCS},n} \cos (\omega_{\text{RF}} \pm 2n\omega_V t)] \\
& + \sum_{n=1}^{\infty} [A_{\gamma,n} \cos (\omega_{\text{RF}} \pm n\omega_V) t].
\end{aligned} \tag{5.23}$$

Therefore, the AM due to fluctuations in the medium is accounted for as a simple addition to the previously reported modulation effects. It is important to note, again, that when the vibrations are acoustically-induced, $\omega_V = \omega_A$ and the modulation tones occur at the same frequencies.

For a comparison of the results of the modulation processes, the modulation due to the acoustically-induced medium fluctuations is added to the presented summary of modulation tone amplitudes given by Table 4.1 in [109], shown here in Table 5.1. While the sideband tone amplitudes for Doppler PM, special relativity AM, and path loss AM are all proportional to the vibrational amplitude raised to the order of the tone, for the case of an acoustically-induced linearly vibrating plate, the acoustic AM is proportional to the pressure of the harmonic tone and the ratio of the acoustic and RF wavelengths. For moderate acoustic pressure levels, the phase modulation introduced by the Doppler effect remains the most dominant as $\omega_{\text{RF}} \gg \omega_V$ and $R_0 \gg \lambda_{\text{RF}}$, thereby minimizing the contributions from special relativity, path loss, and acoustically-induced medium fluctuation modulations. However, as the amplitude of the sound pressure increases, as is the case with high powered acoustic sources, the modulation from the acoustic excitation of the medium becomes more important since the amplitude is proportional to the acoustic pressure level. Fig. 5.1 is a comparison of the modulation powers of each of the processes relative to the RF carrier for the first eight modulation tones, as an extension of Fig. 4.4 in [109] using similar input parameters, where $d_V = \frac{3}{100}\lambda_{\text{RF}}$, $R_0 = 3\lambda_{\text{RF}}$, $\lambda_{\text{RF}} = \frac{1}{3}$ m, and $f_V = f_A = 2$ kHz which represent a ground penetrating radar operating at 900 MHz, with 1 m standoff from an object vibrating with an amplitude of 1 cm at 2 kHz. (2.94), (2.97), (2.103), and (5.11) were employed to produce the plots in Fig. 5.1, with the sound pressure level p_0 at the source in (5.11) being 100 dB SPL where the subsequent harmonic pressure

Table 5.1: Comparison of sideband tone power for various modulation types normalized to the RF carrier. The sideband amplitude is normalized to the primary unmodulated RF signal amplitude.

Type, equation	Normalized n -th order tone amplitude	valid n
Doppler PM, (2.94)	$\frac{(2\pi)^n}{n!} \left(\frac{d_V}{\lambda_{\text{RF}}} \right)^n$	$n = 1, 2, \dots$
Special Relativity AM, (2.97)	$\frac{2}{2^n} \left(\frac{d_V}{\lambda_V} \right)^n$	$n = 1, 2, \dots$
Path Loss AM, (2.103)	$\frac{n+1}{2^n} \left(\frac{d_V}{R_0} \right)^n$	$n = 1, 2, \dots$
Rocking AM, (2.110)	$\frac{(2\pi)^n}{(n+1)!} \left(\frac{a\varphi/2}{\lambda_{\text{RF}}} \right)^n$	$n = 2, 4, \dots$
Acoustic AM, (5.14)	$\frac{p_n(\epsilon_r - 1)(\epsilon_r + 2) \left(\frac{\lambda_A}{n\lambda_{\text{RF}}} \right)^2}{3\rho_0 c_A^2 \left[1 - 4 \left(\frac{\lambda_A}{n\lambda_{\text{RF}}} \right)^2 \epsilon_r \right]}$	$n = 1, 2, \dots$

levels, p_n , are found using the methods described in [25, 135]. While the contribution from the acoustic AM is minimal under these conditions, it can be seen that by increasing the sound pressure level closer to the threshold in which shock waves appear (roughly 194 dB SPL), the modulation amplitude steadily approaches that produced by the Doppler effect. The significance of this effect will be further analyzed in Section 5.4 whereby a high powered acoustic source is utilized to induce vibrations on an aluminum annular disc creating conditions in which the amplitudes of the modulation tones produced by the Doppler effect and acoustically-induced medium fluctuations are separated by less than 6 dB.

5.3 Vibration Modulation Detection from Stand-off Excitation

The improved detection of modulation sidebands on RF signals has been enabled by advancements in analog cancellation techniques that have increased the dynamic range capabilities of sensor systems, particularly for low-level low-frequency modulations, as discussed in Section 2.5. While these advancements have facilitated the detection and characterization of many nonlinear effects typically below the noise floor of conventional sensing systems, they often require

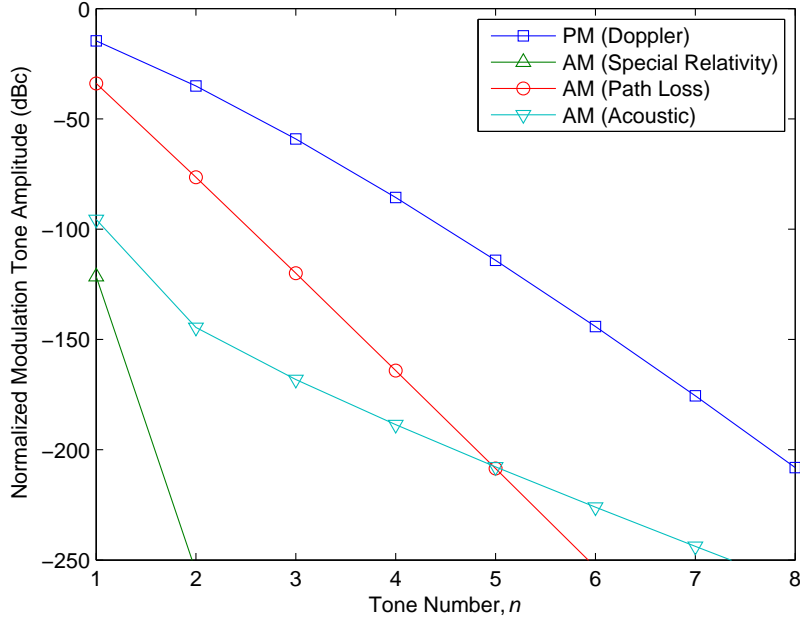


Figure 5.1: Expected power relative to the RF carrier tone of the first eight normalized modulation sideband tones for an acoustically-induced linearly vibrating plate using $d_V = 0.03\lambda_{\text{RF}}$, $R_0 = 3\lambda_{\text{RF}}$, $\lambda_{\text{RF}} = \frac{1}{3}$ m, and $f_V = 2$ kHz

the systems to operate solely in the frequency domain due to the time constraints imposed by the process of canceling the carrier signal and sweeping the desired frequency span with a narrow resolution bandwidth. However, for the measurement of vibrational responses due to acoustic excitation, this is often inadequate as systems employing sound fields commonly pulse the acoustic signals, thus, a transient measurement is needed to capture the pulsed response over time. Therefore, Sections 5.3.1 and 5.3.2 develop an implementation of a zero span frequency measurement for the high dynamic range nonlinear measurement system developed by Wilkerson, Wetherington, and Steer [109, 119, 120, 126], thereby extending the capabilities of the current system to include transient measurement.

5.3.1 Measurement Architecture

Zero span frequency measurement extends the capabilities of the current architecture of the high dynamic range nonlinear measurement system [109, 119, 120, 126] by taking a pseudo-transient approach for determining the measured transient response. To implement this approach, the cancellation algorithm of the system is utilized to obtain the initial cancellation of the RF carrier, which requires some time to achieve, as discussed in Section 2.5, followed by the con-

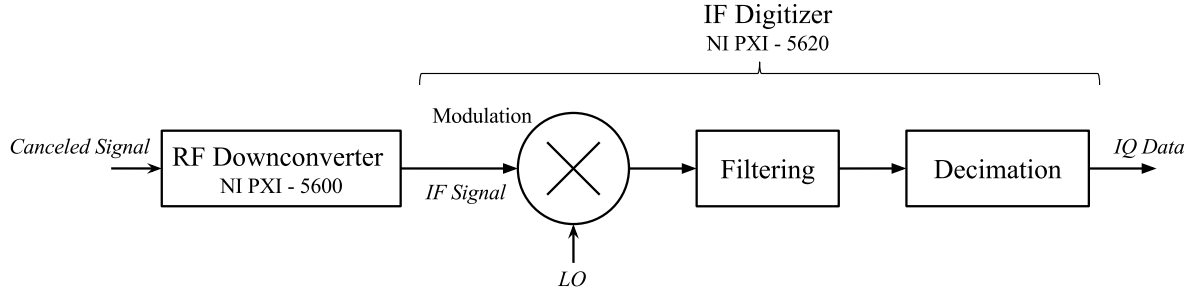


Figure 5.2: Block diagram of the pseudo-transient zero span frequency measurement architecture as an extension of the analog canceller used in the high dynamic range nonlinear measurement system.

tinuous measurement of the received power over time. Once the cancellation is realized, the In-phase (I) and Quadrature-phase (Q) components of the received signal are measured using the NI PXI-5660 RF Vector Signal Analyzer, which is comprised of the NI PXI-5600 RF Downconverter and NI PXI-5620 Intermediate Frequency (IF) Digitizer. The canceled signal, obtained using the feedforward analog cancellation implementation shown in Fig. 2.7, is downconverted to an intermediate frequency which is then shifted to baseband and centered around DC by mixing the signal with a local oscillator. A lowpass filter is then applied to eliminate any higher frequency spectral content and the resultant signal is decimated to obtain the I/Q data, as shown in Fig. 5.2. With this implementation, the system can be configured to perform transient measurements by specifying the desired center frequency, filter bandwidth for which the zero span frequency measurement will record the power, and duration of time for which to acquire the I/Q data (see Appendix B.2 for more detail on configuring the system for transient measurement).

5.3.2 Zero Span Frequency Measurement

The ability to capture transient data was incorporated into the high dynamic range nonlinear measurement system using a zero span frequency measurement. Zero span frequency measurement is a measurement configuration offering the ability to effectively measure the power in a frequency band as a function of time. Rather than perform a power versus frequency sweep using a narrow resolution bandwidth across a given frequency span, the zero span frequency measurement centers a filter at the frequency of the signal of interest and measures the power across the entire bandwidth versus time, thereby enabling a response to be evaluated in the time domain. The analog canceller was developed for a steady-state operation, as its current implementation requires several iterations of the cancellation algorithm to occur while the spectrum

analyzer slowly sweeps the desired frequency span with a very narrow resolution bandwidth making instantaneous measurement infeasible. Therefore, to enable a transient measurement, the cancellation process of the measurement system is performed and, after the proper cancellation is found, held at the canceled state while the zero span frequency measurement is performed over the desired length of time.

This pseudo-transient approach enables the response of the system in the time domain to be measured, however, several limitations remain in generating the time domain responses. The accuracy of the cancellation is temporary, as the phase and amplitude will drift over time increasing error and deteriorating the cancellation of the carrier signal. Therefore, the maximum measurement length must be limited in this approach to avoid the introduction of errors as the quality of the cancellation diminishes. Additionally, the zero-span frequency measurement captures the spectral content within a specified bandwidth centered at the transmitted frequency, however, in the case where acoustically-induced vibrations create modulation sidebands that are close in frequency to the transmitted RF carrier, the bandwidth of the filter is larger than the distance between the transmitted frequency and the modulation frequency. Therefore, the power levels detected with the zero span frequency band include both the transmitted signal as well as the sideband signals, thereby yielding a transient signal response with a noise floor equivalent to the canceled power level of the carrier, making the ability to measure low-level modulation sidebands difficult.

5.4 Spectral Measurement

To verify the theoretical developments in Section 5.2 and examine the transient capabilities introduced by the zero span frequency measurement, modulation effects within an acoustically-excited environment were explored using a long range acoustic device (LRAD), capable of generating sound waves up to 155 dB SPL, to excite an aluminum annular disc with a diameter of 17.5 cm and thickness of 1.2 cm inside of the dual acoustic-RF anechoic chamber, as detailed previously in Section 3.4.1, with the experimental setup as shown in Fig. 5.3. The high dynamic range nonlinear measurement system was configured as a bistatic radar operating at 915 MHz transmitting 1 W total power at a standoff distance of 2 m from the disc, which was hung horizontally and supported by two looped threads positioned through the center of the disc. To generate the largest vibrational displacement, the plate was acoustically-excited at its mechanical resonance of 2.18 kHz using the LRAD, which provided an incident sound pressure level of 130 dB SPL yielding a surface displacement of 1.5 μm . The mechanical resonance was found by producing a linear frequency modulation (LFM) chirp signal, a pulsed signal which increases in frequency over time, to excite the disc over a large frequency range with the resultant vibrational response measured using a laser Doppler vibrometer (LDV).

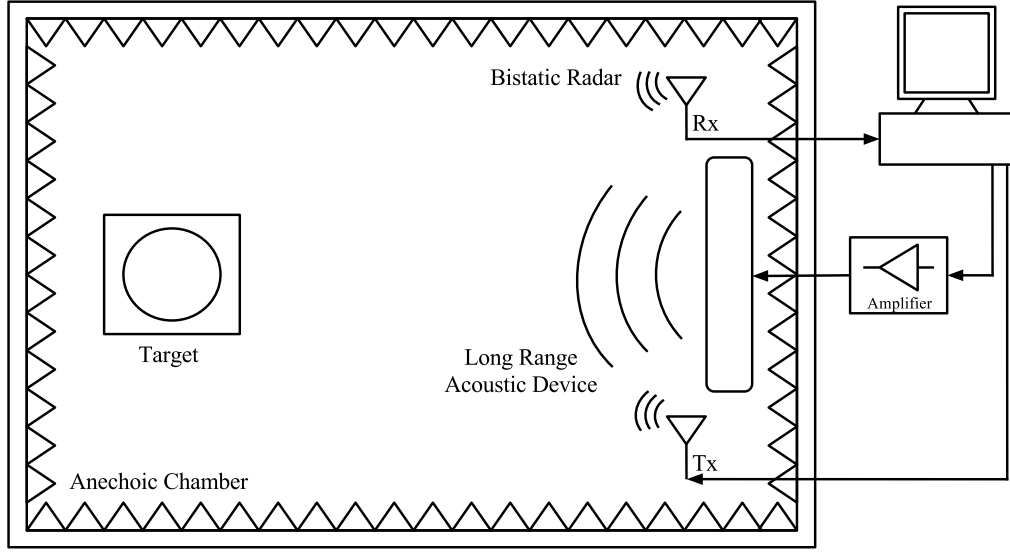


Figure 5.3: Top view of the experimental setup for the bistatic radar measurement of the vibrating plate acoustically-induced by an LRAD.

Under these conditions, the solution for the combined modulation effects in (5.23) is compared to the results obtained using the bistatic radar detailed above. Fig. 5.4 shows the theoretical and experimental resultant power spectrums where it can be seen that the modulation offset on either side of the RF carrier is equivalent to the acoustic excitation frequency. The modulation sideband power levels predicted by (5.23) are highly accurate, producing a very good agreement with the measured results. It is important to note that the discrepancy between the RF carrier power levels for the predicted and measured results is due to reporting the RF carrier power level before and after cancellation, respectively. Additionally, as predicted, the higher-order tones were well below the dynamic range of the measurement system and, therefore, could not be detected. Thus, it can be seen that the model equations, (5.23), can accurately represent the modulation effects on an RF signal within an acoustically-excited environment.

In contrast to the conditions considered previously in Fig. 5.1, the amplitude modulation contributions are much more significant as the relative power of the contributions from Doppler PM, path loss AM, and AM due to medium fluctuations for the first tone are separated by less than 6 dB, whereas contributions from special relativity and RCS remain negligible. This is a consequence of the fact that the actual surface displacement generated on an object by an incident acoustic wave is relatively small, $1.5 \mu\text{m}$ in this scenario, thereby decreasing the absolute difference in power between the modulation effects generated from the vibrations on the surface of the object (i.e., Doppler PM, special relativity AM, and path loss AM). The

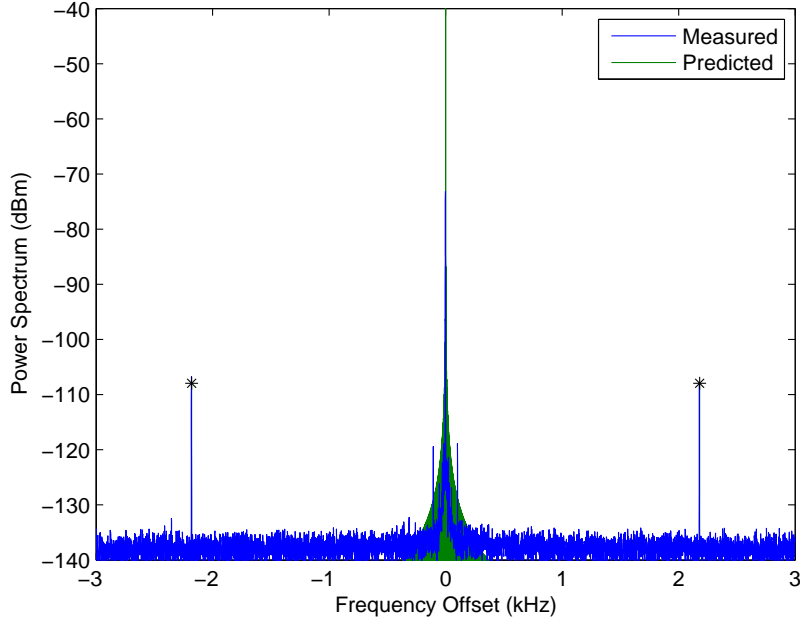


Figure 5.4: Measured narrowband RF power spectrum showing the modulation of an RF carrier at 915 MHz by an acoustic excitation tone at 2.18 kHz compared to the expected model results, i.e., using (5.23). On this scale, the predicted spectrum consists of the RF carrier at 0 kHz and the modulation tones offset from the carrier at ± 2.18 kHz. Except for noise evident in the measured results, the responses are almost identical.

achievable level of surface displacement is heavily dependent upon the material properties of the object and the medium in which the acoustic wave is propagating. For instance, in air, the majority of the acoustic power incident upon a metal object is reflected with only a small portion of the incident power being transmitted to the object, thus yielding very little surface displacement. This can be further exacerbated if the mass of the object increases, as the amount of power required to initiate the displacement of larger, heavier objects increases proportionally. Therefore, when vibrations are acoustically-induced, AM has a much larger influence on the overall generated modulation, with the dominance of Doppler PM being significantly reduced.

By employing the zero span frequency measurement system detailed in Section 5.3, the transient response of the aluminum annular disc was measured, as shown in Fig. 5.5. Fig. 5.5a is the measured frequency response of the disc during acoustic excitation, similar to the results produced in Fig. 5.4, and Fig. 5.5b is the corresponding transient response for a single modulation sideband while the acoustic source was pulsed. The modulation sidebands are present while under acoustic interrogation, however, when the excitation ceases the sideband power levels ring down at the mechanical resonance of the object, which can be seen in Fig. 5.5b as

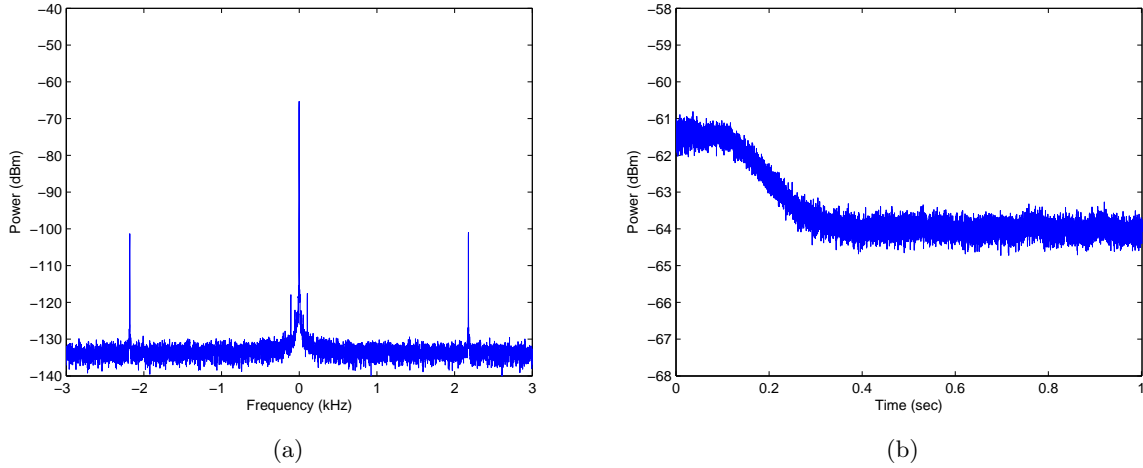


Figure 5.5: Measured response showing the modulation of an RF carrier at 915 MHz by an aluminum annular disc excited at its mechanical resonance of 2.18 kHz in the (a) frequency and (b) time domains. The transient response in (b) was found using a zero span frequency measurement centered around a single modulation sideband.

the power level reduces to the noise floor when the excitation is terminated. Since the modulation sideband is close in frequency to the RF carrier, the power in the filter band of the zero span frequency measurement includes the carrier resulting in power levels higher than that of the modulation sideband. This undesirable effect can be avoided by introducing filters into the nonlinear measurement system that have much smaller bandwidths, capable of isolating narrow frequency ranges of only a few kilohertz when operating at mega- and gigahertz frequencies.

5.5 Summary

Analytical descriptions of the fundamental physical mechanisms of RF scattering by a vibrating object in an acoustically-excited environment were explored. It was shown that the interaction between a vibrating structure and an incident EM wave produces modulation sidebands detectable on a reflected wave. Additionally, the fluctuations of the permittivity of an embedding medium, due to the propagation of a acoustic wave, generates detectable modulation sidebands. For moderate acoustic pressure levels, the Doppler effect is the most critical process in determining the modulation of an RF signal by a linearly vibrating object, however, amplitude modulation from fluctuations in the medium permittivity become quite significant when acoustic pressure levels are increased, as possible through the use of high powered acoustic sources similar to an LRAD. Furthermore, in an environment where the vibrations are acoustically-

induced yielding relatively small surface displacements, the influence of amplitude modulation from medium fluctuations on the overall modulation of a signal increases substantially, as the resultant power levels of the modulation process become comparable to that of Doppler phase modulation.

EM sensing of an acoustically-induced vibrating target provides improved detectability of buried targets compared to EM scattering alone. This has been enabled by the development of high dynamic range cancelers that suppress the carrier of scattered EM signals while allowing the passage of low frequency modulation sidebands. This increased sensing capability of sensor systems prompted the re-investigation of EM scattering from vibrating objects. This chapter provided a thorough investigation of scattered EM responses from such embedded targets.

Chapter 6

Conclusions

6.1 Summary of Research and Original Contributions

This dissertation addressed the limitations in the practical implementation of acousto-EM sensing schemes by developing alternative methods for efficiently computing the nonlinearly generated scattered acoustic fields as well as by investigating additional fundamental physical properties that result in the scattering of an EM signal. A growing interest in the development of alternative sensing modalities that can provide unique object characterization has been the motivation for improving the fundamental principles behind acousto-EM sensing schemes. With the advancements in computational efficiency when calculating higher-order sound fields and the model enhancements describing the scattering of an EM wave in an acoustically-excited environment that are presented in this dissertation, improvements have been made to the performance of acousto-EM remote sensing technologies.

A mathematical model was developed that improves the computational efficiency of higher-order sound fields produced by the scattering of sound by sound, particularly when applied to more complex acoustic sources, such as transducer arrays. By defining the acoustic source as a series of Gaussian functions, an analytical solution for the third-order sound fields was realized that provided computational advantages over traditional methods for solving the partial differential equations of nonlinear acoustics, enabling a computation speed of over 40x faster than methods employing finite difference schemes and over 25x faster than methods solving multidimensional field integrals. The higher-order sound fields have a high directionality that make them ideal for use in detection and characterization systems, thus, the computational enhancements demonstrated improve the ability to implement acousto-EM sensing schemes, which rely on the real-time calculation of the radiated sound fields.

Design criteria detailing the necessary modifications to enhance the performance of the current third-order parametric array system were also introduced. The requirements for pro-

ducing a highly directional sound beam in the audio band using third-order scattering of sound by sound necessitate the use of two sets of transducers and driving amplifiers to efficiently generate the primary sound fields that will result in the desired third-order intermodulation frequency. The design demonstrates that by utilizing a narrowband amplifier with a high power level that is located lower in frequency along with a broadband amplifier that drives the content bearing signal, the third-order parametric array system will operate much more efficiently, requiring less electrical power to drive acoustic signals with high sound pressure levels. The current third-order parametric array system produces third-order intermodulation products that have a maximum sound pressure level of 40 dB SPL, which is inadequate for use in any real application, however, with the modifications proposed, the maximum achievable pressure levels can easily double the current amount using relatively moderate primary sound field pressure levels (i.e., 120–130 dB SPL). Additionally, by increasing the primary sound field pressure levels through the use of high powered acoustic signals, such as a long range acoustic device, the maximum achievable third-order intermodulation product sound pressure level can increase even further. With the increased power levels achieved by the improved design and advantages gained in directivity by employing third-order sound fields, the enhanced third-order parametric array system is an exceptional option for the acoustic source that is an essential component in an acousto-EM sensing scheme.

As an additional means of determining the radiation patterns generated by an acoustic source, a near-to-far-field transformation was developed that demonstrated the ability to determine the far-field radiation patterns of second-order sound fields produced by the scattering of sound by sound from data obtained in the near-field of the source. The nonlinear transformation was derived from the KZK equation as an extension to Kirchhoff’s theorem and demonstrated the ability to determine the far-field characteristics of an arbitrary configuration of acoustic sources as long as the sources resided completely within the chosen near-field surface. This enables the far-field radiation patterns to be ascertained without a detailed knowledge of the actual acoustic sources, which can be useful in remote sensing schemes, particularly those utilizing acousto-EM scattering, by establishing the effect an unknown source may have on the environment. The transformation provides an alternative method for computing far-field radiation patterns that becomes especially useful when the sound fields from physical acoustic sources that lack simple analytical expressions are desired.

To enable a better fundamental understanding of the nonlinear processes resulting in acousto-EM scattering, the effect of a high powered acoustic source on the medium in which an EM wave propagates thereby yielding a scattered EM signal was investigated. An analytical solution was derived for the modulation of an EM signal due to the fluctuations in the permittivity of the embedding medium caused by the propagation of an acoustic source. This was compared to additional known modulation processes occurring in an acoustically-excited environment caused

by vibrating structures, including phase modulation due to the Doppler effect as well as amplitude modulation from special relativity, path loss, and radar cross section. It was demonstrated that while Doppler phase modulation was a considerable contributor to the overall modulation detected, the effect of the modulation due to the fluctuating medium was quite significant, particularly when high sound pressure levels existed with low levels of vibration, which resulted in a modulation power level that was within 6 dB of that produced by the Doppler phase modulation. The analytical model combining the contribution from each of the modulation processes was shown to correlate well with an RF signal reflected from an acoustically-induced vibrating plate measured using the high dynamic range nonlinear measurement system. Therefore, as measurement capabilities continue to improve enabling further advancements in the understanding of known scattering mechanisms, especially for the nonlinear interactions between acoustic and EM waves, systems looking to exploit acousto-EM scattering, such as buried object detection schemes, can be more effectively designed.

The research presented in this dissertation establishes a foundation for the continued improvement in the design of a system utilizing acousto-EM sensing.

6.2 Future Research

While the research presented in this dissertation establishes important advancements in the development of acousto-EM sensing schemes, additional efforts may be applied to expand upon the topics introduced, thereby continuing the evolution of the hybrid remote sensing scheme.

A major opportunity area for future research lies in the continued development of the third-order parametric array. Section 3.6 established important design criteria required to improve the performance of the third-order parametric array, which currently has been demonstrated only as a modification to a second-order parametric array system. Therefore, to fully investigate the advantages provided over the second-order parametric array, a third-order parametric array system needs to be developed implementing the design enhancements detailed in Chapter 3. The most critical developmental components will reside with the design of the driving amplifiers for each of the primary frequencies and the transducer array configuration, as to efficiently produce a third-order intermodulation frequency in the audio band, the primary frequencies must be distantly spaced in frequency thereby requiring two unique sets of amplifiers and transducers. As per the design enhancements proposed, the amplifier pair will consist of a narrowband amplifier, which can easily be designed to operate with a very high efficiency, and a broadband amplifier. Broadband amplifiers are much more difficult to produce as achieving a uniform gain across the desired frequency band is challenging and often leads to designs that are physically much larger than narrowband amplifiers. Additionally, it has been shown that the most efficient means of generating the nonlinearly generated scattered sound fields is with collinearly located sources,

therefore, the third-order parametric array should have both sets of transducers residing within a single array. However, the configuration of the transducers within the array and the method in which the elements are driven, whether continuously or alternating dependent upon frequency and array location, needs to be determined.

The nonlinear near-to-far-field transformation developed in Chapter 4 to determine the far-field radiation patterns from near-field data was derived under the quasilinear approximation considering only the primary and secondary sound fields generated from the scattering of sound by sound. The demonstrated results show that the transformation yields highly accurate results when the far-field remains in the paraxial region, as is the valid range of the KZK equation from which the transformation is derived, however, errors quickly accumulate as the transformation advances beyond this region. The validity constraint in the far-field imposed by the KZK equation can be quite limiting, therefore, it would be advantageous to develop an alternative nonlinear transformation based on solutions derived from the Westervelt equation, particularly for applications in which the sound fields at large angles away from the acoustic axis are desired. With significant research efforts being given to the application of third-order sound fields and the development of third-order parametric arrays, an extension of the nonlinear transformation to account for third-order sound fields can be developed. Since closed form solutions for the third-order sound fields have yet to be established, the resulting transformation will contain additional layers of integration not encountered with the nonlinear transformation presented in Chapter 4. Therefore, it may be worthwhile to investigate a closed form solution for the third-order sound fields, which may require additional validity approximations to obtain a viable expression, to enable a more ideal near-to-far-field transformation for use in ascertaining the far-field radiation patterns for the tertiary sound fields generated by the scattering of sound by sound. This work focused solely on determining the far-field radiation patterns of nonlinearly generated scattered sound fields, however, it can also be extended to include the modeling of the far-field characteristics of the sound fields scattered by objects in the near-field. This extension would be similar to the research being performed in the field of acoustic holography and could provide useful results for application in object detection and biomedical research.

An analytical solution for the modulation of an EM signal by permittivity fluctuations from periodic pressure changes as an acoustic wave propagates through the embedding medium was derived in Chapter 5. A comparison of the resultant relative power level of the amplitude modulation from the medium fluctuations with the more commonly considered processes that generate modulation sidebands (e.g., Doppler effect, path loss, special relativity, and radar cross section) shows that the propagating acoustic wave can produce modulation sidebands with power levels comparable to those generated by the phase modulation introduced by the Doppler effect, with the theoretical model incorporating the additional modulation source shown to match experimental results. While the experimental results correlate with the theoretical

model when considering the effects of all of the modulation processes, individually verifying the contribution from each source of modulation has not been done as isolating each effect during measurement is currently infeasible. To better characterize the modulation effects, effort can be put forth to investigate the development of a set of experiments that have parameters chosen specifically to emphasize the effects of a single modulation process at a time, thereby improving the analytical solutions describing the contribution from each process. Improved experimental configurations may also prove beneficial in better characterizing the modulation processes, as the acoustic sources and antennas were located very closely due to the confinements of the anechoic chamber, which may have contributed to the difficulties in isolating the individual modulation processes.

Additionally, there are several opportunities to enhance the performance of the transient response of the high dynamic range nonlinear measurement system. The current system employs a pseudo-transient implementation where the full cancellation algorithm is performed followed by a continuous capture of the I/Q data over time, achieved by fixing a filter with a given bandwidth at a single frequency and rapidly evaluating the power within that band as a function of time. In the current configuration of the measurement system, the minimum bandwidth of the filter able to measure I/Q data is 10 MHz, which is significantly larger than frequency of the modulation sidebands generated by acousto-EM scattering. Therefore, when attempting to measure these modulation sidebands, the power of the carrier signal will also be captured as the frequency separation between the carrier and the modulation sideband is not large enough to measure the power level of the sideband without distortion and allow for the transition between the passband and stopband of the filter. Furthermore, all of the power within the passband of the filter is summed at each point in time, therefore, with such a large bandwidth, low level frequency content drops below the cumulative noise floor. Thus, the measurement system needs to be reconfigured as to contain a filter with a much smaller bandwidth that is capable of continuously capturing the data if transient measurement is to be achieved. The pseudo-transient implementation also assumes that the environment remains in a relatively steady-state condition so that the cancellation remains accurate for the duration of the measurement, which is inadequate for any practical application and limits the actual time allotted for a valid measurement in a laboratory environment. For true transient capabilities, the speed in which the analog cancellation algorithm completes must be drastically reduced as to enable continuous cancellation in a changing environment, which would require tremendous engineering effort; however, it would facilitate the extension of the high dynamic range nonlinear measurement system for use with more complex applications, such as wireless systems.

REFERENCES

- [1] W. R. Scott Jr, C. T. Schroeder, and J. S. Martin, “An acousto-electromagnetic sensor for locating land mines,” in *Proceedings of SPIE*, vol. 3392, Apr. 1998, pp. 176–186.
- [2] W. R. Scott Jr and J. S. Martin, “Experimental investigation of the acousto-electromagnetic sensor for locating land mines,” in *Proceedings of SPIE*, vol. 3710, Apr. 1999, pp. 204–214.
- [3] W. R. Scott Jr, C. T. Schroeder, J. S. Martin, and G. D. Larson, “Investigation of a technique that uses both elastic and electromagnetic waves to detect buried land mines,” *Proceedings of the AP2000 - Millennium Conference on Antennas and Propagation*, 2000.
- [4] W. R. Scott Jr, C. Schroeder, and J. S. Martin, “A hybrid acoustic/electromagnetic technique for locating land mines,” in *Proc. 1998 IEEE Int. Geoscience and Remote Sensing Symposium*, vol. 1, 1998, pp. 216–218.
- [5] D. E. Lawrence and K. Sarabandi, “Acoustic and electromagnetic wave interaction: analytical formulation for acousto-electromagnetic scattering behavior of a dielectric cylinder,” *IEEE Trans. Antennas Propag.*, vol. 49, no. 10, pp. 1382–1392, Oct. 2001.
- [6] —, “Electromagnetic scattering from vibrating metallic objects using time-varying generalized impedance boundary conditions,” in *Antennas and Propagation Society International Symposium, 2002. IEEE*, vol. 2, 2002, pp. 782–785.
- [7] K. Sarabandi and D. E. Lawrence, “Acoustic and electromagnetic wave interaction: estimation of doppler spectrum from an acoustically vibrated metallic circular cylinder,” *IEEE Trans. Antennas Propag.*, vol. 51, no. 7, pp. 1499–1507, 2003.
- [8] D. E. Lawrence and K. Sarabandi, “Electromagnetic scattering from vibrating penetrable objects using a general class of time-varying sheet boundary conditions,” *IEEE Trans. Antennas Propag.*, vol. 54, no. 7, pp. 2054–2061, 2006.
- [9] —, “Acousto-electromagnetic interaction in the detection of buried objects,” in *Geoscience and Remote Sensing Symposium, 2001. IGARSS '01. IEEE 2001 International*, vol. 4, 2001, pp. 1989–1991.
- [10] A. M. Buerkle and K. Sarabandi, “Analysis of acousto-electromagnetic wave interaction using sheet boundary conditions and the finite-difference time-domain method,” *IEEE Trans. Antennas Propag.*, vol. 55, no. 7, pp. 1991–1998, 2007.
- [11] A. Buerkle and K. Sarabandi, “Analysis of acousto-electromagnetic wave interaction using the finite-difference time-domain method,” *IEEE Trans. Antennas Propag.*, vol. 56, no. 8, pp. 2191–2199, 2008.
- [12] E. A. Zabolotskaya and R. V. Khokhlov, “Quasi-plane waves in the nonlinear acoustics of confined beams,” *Sov. Phys. Acoust.*, vol. 15, no. 1, pp. 35–40, Jul. 1969.

- [13] V. P. Kuznetsov, "Equations of nonlinear acoustics," *Sov. Phys. Acoust.*, vol. 16, no. 4, pp. 467–470, Apr. 1971.
- [14] E. Cavanagh and B. D. Cook, "Gaussian-laguerre description of ultrasonic fields—numerical example: Circular piston," *J. Acoust. Soc. Am.*, vol. 67, no. 4, pp. 1136–1140, Apr. 1980.
- [15] J. J. Wen and M. A. Breazeale, "A diffraction beam field expressed as the superposition of gaussian beams," *J. Acoust. Soc. Am.*, vol. 83, no. 5, pp. 1752–1756, May 1988.
- [16] D. Ding, Y. Shui, J. Lin, and D. Zhang, "A simple calculation approach for the second harmonic sound field generated by an arbitrary axial-symmetric source," *J. Acoust. Soc. Am.*, vol. 100, no. 2, pp. 727–733, Aug. 1996.
- [17] D. Ding, "A simplified algorithm for the second-order sound fields," *J. Acoust. Soc. Am.*, vol. 108, no. 6, pp. 2759–2764, Dec. 2000.
- [18] —, "A simplified algorithm for second-order sound beams with arbitrary source distribution and geometry (I)," *J. Acoust. Soc. Am.*, vol. 115, no. 1, pp. 35–37, Jan. 2004.
- [19] P. J. Westervelt, "Scattering of sound by sound," *J. Acoust. Soc. Am.*, vol. 29, no. 2, pp. 199–203, Feb. 1957.
- [20] —, "Scattering of sound by sound," *J. Acoust. Soc. Am.*, vol. 29, no. 8, pp. 934–935, Aug. 1957.
- [21] M. Yoneyama, J. Fujimoto, Y. Kawamo, and S. Sasabe, "The audio spotlight: An application of nonlinear interaction of sound waves to a new type of loudspeaker design," *J. Acoust. Soc. Am.*, vol. 73, no. 5, pp. 1532–1536, 1983.
- [22] I. A. Bourne and T. D. Keenan, "High power acoustic radar," *Nature*, vol. 251, no. 5472, pp. 206–208, Sep. 1974.
- [23] L. Lasdon, A. Waren, and D. Suchman, "Optimal design of acoustic sonar transducer arrays," in *IEEE Int. Conf. on Eng. in the Ocean Environment*, Aug. 1974, pp. 3–9.
- [24] S. I. Aanonsen, T. Barkve, J. N. Tjøtta, and S. Tjøtta, "Distortion and harmonic generation in the nearfield of a finite amplitude sound beam," *J. Acoust. Soc. Am.*, vol. 75, no. 3, pp. 749–768, Mar. 1984.
- [25] M. F. Hamilton, J. N. Tjøtta, and S. Tjøtta, "Nonlinear effects in the farfield of a directive sound source," *J. Acoust. Soc. Am.*, vol. 78, no. 1, pp. 202–216, Jul. 1985.
- [26] J. Berntsen, J. N. Tjøtta, and S. Tjøtta, "Nearfield of a large acoustic transducer. Part IV: Second harmonic and sum frequency radiation," *J. Acoust. Soc. Am.*, vol. 75, no. 5, pp. 1383–1391, May 1984.
- [27] G. S. Garrett, J. N. Tjøtta, and S. Tjøtta, "Nearfield of a large acoustic transducer, Part II: Parametric radiation," *J. Acoust. Soc. Am.*, vol. 74, no. 3, pp. 1013–1020, Sep. 1983.

- [28] H. O. Berktaay and D. J. Leahy, “Farfield performance of parametric transmitters,” *J. Acoust. Soc. Am.*, vol. 55, no. 3, pp. 539–546, Mar. 1974.
- [29] J. Berntsen, J. N. Tjøtta, and S. Tjøtta, “Interaction of sound waves. Part IV: Scattering of sound by sound,” *J. Acoust. Soc. Am.*, vol. 86, no. 5, pp. 1968–1983, Nov. 1989.
- [30] C. M. Darvennes and M. F. Hamilton, “Scattering of sound by sound from two gaussian beams,” *J. Acoust. Soc. Am.*, vol. 87, no. 5, pp. 1955–1964, May 1990.
- [31] F. H. Fenlon, “A recursive procedure for computing the nonlinear spectral interactions of progressive finite-amplitude waves in nondispersive fluids,” *J. Acoust. Soc. Am.*, vol. 50, no. 5B, pp. 1299–1312, Nov. 1971.
- [32] F. H. Fenlon and F. S. McKendree, “Axisymmetric parametric radiation—a weak interaction model,” *J. Acoust. Soc. Am.*, vol. 66, no. 2, pp. 534–547, Aug. 1979.
- [33] M. F. Hamilton, J. N. Tjøtta, and S. Tjøtta, “Noncollinear interaction of two sound beams from displaced gaussian sources, with application to parametric receiving arrays,” *J. Acoust. Soc. Am.*, vol. 82, no. 1, pp. 311–318, Jul. 1987.
- [34] T. Kamakura, N. Hamada, K. Aoki, and Y. Kumamoto, “Nonlinearly generated spectral components in the nearfield of a directive sound source,” *J. Acoust. Soc. Am.*, vol. 85, no. 6, pp. 2331–2337, June 1989.
- [35] J. N. Tjøtta and S. Tjøtta, “Nonlinear equations of acoustics, with application to parametric acoustic arrays,” *J. Acoust. Soc. Am.*, vol. 69, no. 6, pp. 1644–1652, June 1981.
- [36] J. N. Tjøtta, S. Tjøtta, and E. H. Vefring, “Propagation and interaction of two collinear finite amplitude sound beams,” *J. Acoust. Soc. Am.*, vol. 88, no. 6, pp. 2859–2870, Dec. 1990.
- [37] J. N. Tjøtta and S. Tjøtta, “Nonlinear interaction of two collinear, spherically spreading sound beams,” *J. Acoust. Soc. Am.*, vol. 67, no. 2, pp. 484–490, Feb. 1980.
- [38] G. Garner and M. B. Steer, “A cascaded second-order approach to computing third-order scattering of noncollinear acoustic beams,” *Appl. Acoust.*, vol. 73, no. 12, pp. 1220–1230, Dec. 2012.
- [39] —, “Third-order parametric array generated by distantly spaced primary ultrasonic tones,” *IEEE Trans. Ultrason., Ferroelectr., Freq. Control*, vol. 59, no. 4, pp. 776–784, Apr. 2012.
- [40] L. E. Kinsler, A. R. Frey, A. B. Coppers, and J. V. Sanders, *Fundamentals of Acoustics*, 4th ed. New York: Wiley, 1976.
- [41] M. Hamilton, *Nonlinear Acoustics*. San Diego, CA: Academic Press, 1998.
- [42] D. T. Blackstock, *Fundamentals of Physical Acoustics*. New York: Wiley, 2000.

- [43] R. T. Beyer, "Parameter of nonlinearity in fluids," *J. Acoust. Soc. Am.*, vol. 32, no. 6, pp. 719–721, Jun. 1960.
- [44] M. J. Lighthill, *Waves in Fluids*. Cambridge, England: Cambridge University Press, 1980.
- [45] P. J. Westervelt, "Parametric acoustic array," *J. Acoust. Soc. Am.*, vol. 35, no. 4, pp. 535–537, Apr. 1963.
- [46] J. M. Burgers, *A Mathematical Model Illustrating the Theory of Turbulence*, ser. Advances in Applied Mechanics. New York: Academic Press, 1948, vol. 1, pp. 171–199.
- [47] M. J. Lighthill, "On sound generated aerodynamically. i. general theory," *Proceedings of the Royal Society of London. Series A, Mathematical and Physical Sciences*, vol. 211, no. 1107, pp. 564–587, Mar. 20 1952.
- [48] International Organization for Standardization, Committee ISO/TC 43, Acoustics, Subcommittee S1, Noise, "Acoustics—Attenuation of sound during propagation outdoors—Part 1: Calculation of the absorption of sound by the atmosphere," International Organization for Standardization, Geneva, Switzerland, ISO 9613-1, 1993.
- [49] —, "Acoustics—Attenuation of sound during propagation outdoors—Part 2: General method of calculation," International Organization for Standardization, Geneva, Switzerland, ISO 9613-2, 1996.
- [50] American National Standards Institute, Committee S1, Acoustics, "Method for calculation of the absorption of sound by the atmosphere," American National Standards Institute, New York, NY, ANSI S1.26-1995, 1995.
- [51] E. J. Rickley, G. G. Fleming, and C. J. Roof, "Simplified procedure for computing the absorption of sound by the atmosphere," *Noise Control Eng.*, vol. 55, no. 6, pp. 482–494, Nov. 2007.
- [52] P. M. Morse and K. U. Ingard, *Theoretical Acoustics*. New York: McGraw-Hill, 1968.
- [53] M. Abramowitz, *Handbook of Mathematical Functions With Formulas, Graphs, and Mathematical Tables*. New York: Wiley, 1972.
- [54] J. N. Tjøtta and S. Tjøtta, "An analytical model for the nearfield of a baffled piston transducer," *J. Acoust. Soc. Am.*, vol. 68, no. 1, pp. 334–339, Jul. 1980.
- [55] G. S. Garrett, J. N. Tjøtta, and S. Tjøtta, "Nearfield of a large acoustic transducer. Part III: General results," *J. Acoust. Soc. Am.*, vol. 75, no. 3, pp. 769–779, Mar. 1984.
- [56] T. Hasegawa, N. Inoue, and K. Matsuzawa, "A new rigorous expansion for the velocity potential of a circular piston source," *J. Acoust. Soc. Am.*, vol. 74, no. 3, pp. 1044–1047, Sept. 1983.
- [57] D. Ding and Y. Zhang, "Notes on the gaussian beam expansion," *J. Acoust. Soc. Am.*, vol. 116, no. 3, pp. 1401–1405, Sep. 2004.

- [58] W. Liu and J. Yang, “A simple and accurate method for calculating the gaussian beam expansion coefficients,” *Chinese Physics Letters*, vol. 27, no. 12, p. 124301, Dec. 2010.
- [59] H.-J. Kim, J. S. L. W., and A. Sedov, “Generation of the basis sets for multi-gaussian ultrasonic beam models—an overview,” *J. Acoust. Soc. Am.*, vol. 119, no. 4, pp. 1971–1978, Apr. 2006.
- [60] M. Cervenka, M. Bednarik, and P. Konicek, “Numerical simulation of parametric field patterns of ultrasonic transducer arrays,” in *IEEE Int. Ultrason. Symp.*, 2009, pp. 1–4.
- [61] U. Ingard and D. C. Pridmore-Brown, “Scattering of sound by sound,” *J. Acoust. Soc. Am.*, vol. 28, no. 3, pp. 367–369, May 1956.
- [62] J. L. S. Bellin and R. T. Beyer, “Scattering of sound by sound,” *J. Acoust. Soc. Am.*, vol. 32, no. 3, pp. 339–341, Mar. 1960.
- [63] J. P. Jones and R. T. Beyer, “Scattering of sound by sound,” *J. Acoust. Soc. Am.*, vol. 48, no. 1B, pp. 398–402, 1970.
- [64] J. Naze and S. Tjøtta, “Nonlinear interaction of two sound beams,” *J. Acoust. Soc. Am.*, vol. 37, pp. 174–175, 1965.
- [65] T. G. Muir and J. G. Willette, “Parametric acoustic transmitting arrays,” *J. Acoust. Soc. Am.*, vol. 52, no. 5B, pp. 1481–1486, 1972.
- [66] R. W. Haupt and K. D. Rolt, “Standoff acoustic laser technique to locate buried land mines,” *Lincoln Laboratory Journal*, vol. 15, no. 1, pp. 3–22, 2005.
- [67] P. Ji, J. Yang, and W.-S. Gan, “The investigation of localized sound generation using two ultrasound beams,” *IEEE. Trans. Ultrason., Ferroelectr., and Freq. Control*, vol. 56, no. 6, pp. 1282–1287, Jun. 2009.
- [68] C. Shi and W.-S. Gan, “Development of a parametric loudspeaker: A novel directional sound generation technology,” *IEEE Potentials*, vol. 29, no. 6, pp. 20–24, Nov. 2010.
- [69] N. Tanaka and M. Tanaka, “Active noise control using a steerable parametric array loudspeaker,” *J. Acoust. Soc. Am.*, vol. 127, no. 6, pp. 3526–3537, Jun. 2010.
- [70] —, “Mathematically trivial control of sound using a parametric beam focusing source,” *J. Acoust. Soc. Am.*, vol. 129, no. 1, pp. 165–172, Jan. 2010.
- [71] T. Komatsuzaki and Y. Iwata, “Active noise control using high-directional parametric loudspeaker,” *J. Environ. and Eng.*, vol. 6, no. 1, pp. 140–149, 2011.
- [72] L. A. Brooks, A. C. Zander, and C. H. Hansen, “Investigation into the feasibility of using a parametric array control source in an active noise control system,” in *Proc. of Acoustics*, Nov. 2005, pp. 1–7.
- [73] Y. Nakashima, T. Yoshimura, and T. Ohya, “Prototype of parametric array loudspeaker on mobile phone and its acoustical characteristics,” in *Audio Eng. Soc. 118th Convention*, May 2005, pp. 1–6.

- [74] Y. Nakashima, T. Yoshimura, N. Naka, and Y. Ohya, "Prototype of mobile super directional loudspeaker," *NTT DoCoMo Tech.*, vol. 8, no. 1, pp. 25–32, 2006.
- [75] X. Li, L. Xu, and L. Xu, "Audio near-distance directional loudspeaker technology for portable multimedia devices," in *IEEE. Int. Conf. Mech. and Automation*, Aug. 2011, pp. 727–731.
- [76] G. Garner III, "Design of optimal directional parametric acoustic arrays in air," Ph.D. dissertation, North Carolina State University, Raleigh, NC, 2011.
- [77] I. Ladabaum, X. Jin, and B. T. Khuri-Yakub, "Acoustic transducers and method of microfabrication," Patent US 5 982 709 A, Nov. 9, 1999.
- [78] E. G. Norris, "Resonant tuned, ultrasonic electrostatic emitter," Patent US 6 044 160 A, Mar. 28, 2000.
- [79] F. J. Pompei, "Ultrasonic transducer for parametric array," Patent US 6 771 785 B2, Aug. 4, 2004.
- [80] —, "Parametric audio amplifier system," Patent US 6 914 991 B1, Jul. 5, 2005.
- [81] —, "Parametric array modulation and processing method," Patent US 7 596 228 B2, Sep. 29, 2009.
- [82] J. J. Croft III, M. E. Spencer, and J. O. Norris, "Modulator processing for a parametric speaker system," Patent US 7 729 498 B2, Jun. 1, 2010.
- [83] F. J. Pompei, "Parametric audio system," Patent US 20 120 051 556 A1, Mar. 1, 2012.
- [84] E. G. Norris, "Multi-dimensional parametric audio system and method," Patent US 20 140 050 325 A1, Feb. 20, 2014.
- [85] H. D. Parry and M. J. Sanders, "The design and operation of an acoustic radar," *IEEE Trans. Geoscience Electronics*, vol. 10, no. 1, pp. 58–64, Jan. 1972.
- [86] R. A. Smith, "Radar navigation," *Inst. of Electrical Engineers - Part IIIA: Radiolocation*, vol. 93, no. 1, pp. 331–342, 1946.
- [87] A. A. Shah, Y. Ribakov, and S. Hirose, "Nondestructive evaluation of damaged concrete using nonlinear ultrasonics," *Materials & Design*, vol. 30, no. 3, pp. 775–782, 2009.
- [88] A. Buerkle and K. Sarabandi, "Non-destructive evaluation of elastic targets using acousto-electromagnetic wave interaction and time reversal focusing," *IEEE Trans. Antennas Propag.*, vol. 57, no. 11, pp. 3628–3637, 2009.
- [89] J. Berntsen, "Numerical calculations of finite amplitude sound beams," in *Frontiers of Nonlinear Acoustics: Proceedings of 12th ISNA*, M. F. Hamilton and D. T. Blackstock, Eds. London: Elsevier, 1990, pp. 191–196.
- [90] J. Berntsen and E. Vefring, "Numerical computation of a finite amplitude sound beam," Dept. of Math., Univ. of Bergen, Bergen, Norway, Tech. Rep. 82, 1986.

- [91] S. I. Aanonsen, “Numerical computation of the nearfield of a finite amplitude sound beam,” Dept. of Math., Univ. of Bergen, Bergen, Norway, Tech. Rep. 73, 1983.
- [92] D. H. Trivett and A. L. V. Buren, “Propagation of plane, cylindrical, and spherical finite amplitude waves,” *J. Acoust. Soc. Am.*, vol. 69, no. 4, pp. 943–949, Apr. 1981.
- [93] E. H. Vefring, J. N. Tjøtta, and S. Tjøtta, “Nonlinear effects in the sound field of a bifrequency source,” in *Frontiers of Nonlinear Acoustics: Proceedings of 12th ISNA*, M. F. Hamilton and D. T. Blackstock, Eds. London: Elsevier, 1990, pp. 251–256.
- [94] J. Berntsen, T. O. Espelid, and A. Genz, “An automatic integration routine applicable in linear and nonlinear acoustics,” in *Frontiers of Nonlinear Acoustics: Proceedings of 12th ISNA*, M. F. Hamilton and D. T. Blackstock, Eds. London: Elsevier, 1990, pp. 609–614.
- [95] —, “A test of ADMINT,” Dept. of Math., Univ. of Bergen, Bergen, Norway, Tech. Rep. No. 31, Informatics, 1988.
- [96] —, “An adaptive algorithm for the approximate calculation of multiple integrals,” *ACM Trans. Math. Software*, vol. 17, no. 4, pp. 437–451, Dec. 1991.
- [97] J. Berntsen, “On the numerical calculation of multidimensional integrals appearing in the theory of underwater acoustics,” in *Numerical integration: Recent developments, software and applications*, T. O. Espelid and A. Genz, Eds. Netherlands: Kluwer Academic, 1992, pp. 249–265.
- [98] J. Berntsen and T. O. Espelid, “On the use of Gauss quadrature in adaptive automatic integration schemes,” *BIT Numerical Mathematics*, vol. 24, no. 2, pp. 239–242, 1984.
- [99] S. P. Kshevetsky and S. B. Leble, *Mathematical Methods of Theoretical Physics*. Kaliningrad State University, 1995.
- [100] S. B. Leble, K. Zachariasz, and I. S. Vereshchagina, “The estimation of virial coefficients via the third harmonics measurements,” in *Int. Symposium Hydroacoustics and Ultrasonics*, May 1997, pp. 83–88.
- [101] S. B. Leble and A. Sukhov, “On numerical calculation of acoustic field of plane source,” *TASK Quarterly*, vol. 7, no. 2, pp. 185–198, 2003.
- [102] J. M. Wetherington and M. B. Steer, “Sensitive vibration detection using ground-penetrating radar,” *IEEE Microw. Wireless Compon. Lett.*, vol. 23, no. 12, pp. 680–682, Dec. 2013.
- [103] L. Brillouin, “Diffusion de la lumiere et des rayons x par un corps transparent homogène,” *Annals of Physics*, vol. 17, pp. 88–122, 1922.
- [104] P. Debye and F. W. Sears, “On the scattering of light by supersonic waves,” *Proc. Nat. Acad. Sci.*, vol. 18, no. 6, pp. 409–414, Jun. 1932.

- [105] E. M. North, A. M. Peterson, and H. D. Parry, "RASS, a remote sensing system for measuring low-level temperature profiles," *Bulletin Amer. Meteor. Soc.*, vol. 54, no. 9, pp. 912–919, Sep. 1973.
- [106] M. S. Frankel and A. M. Peterson, "Remote temperature profiling in the lower troposphere," *Rad. Sci.*, vol. 11, no. 3, pp. 157–166, Mar. 1976.
- [107] D. Massonnet and T. Rabaute, "Radar interferometry: Limits and potential," *IEEE Trans. Geosci. Remote Sens.*, vol. 31, no. 2, pp. 455–464, Mar. 1993.
- [108] J. S. Mellett, "Ground penetrating radar applicaitons in engineering, environmental managment, and geology," *Journal of Applied Geophysics*, vol. 33, no. 1-3, pp. 157–166, 1995.
- [109] J. M. Wetherington, "Characterization of passive spectral regrowth in radio frequency systems," Ph.D. dissertation, North Carolina State University, Raleigh, NC, 2013.
- [110] S. Borkar and R. F. Yang, "Reflection of electromagnetic waves from oscillating surfaces," *IEEE Trans. Antennas Propag.*, vol. 23, no. 1, pp. 122–127, Jan. 1975.
- [111] R. Kleinman and R. Mack, "Scattering by linearly vibrating objects," *IEEE Trans. Antennas Propag.*, vol. 27, no. 3, pp. 344–352, 1979.
- [112] D. De Zutter, "Doppler effect from a transmitter in translational motion," *IEE J. Microwaves, Optics, and Acoustics*, vol. 3, no. 2, pp. 85–92, Mar. 1979.
- [113] J. Cooper, "Scattering of electromagnetic fields by a moving boundary: the one-dimensional case," *IEEE Trans. Antennas Propag.*, vol. 28, no. 6, pp. 791–795, Nov. 1980.
- [114] J. Van Bladel and D. De Zutter, "Reflections from linearly vibrating objects: plane mirror at normal incidence," *IEEE Trans. Antennas Propag.*, vol. 29, no. 4, pp. 629–637, Jul. 1981.
- [115] D. De Zutter, "Reflections from linearly vibrating objects: plane mirror at oblique incidence," *IEEE Trans. Antennas Propag.*, vol. 30, no. 5, pp. 898–903, Sep. 1982.
- [116] D. Censor, "Theory of the doppler effect: fact, fiction and approximation," *Radio Sci.*, vol. 19, no. 4, pp. 1027–1040, Jul. 1984.
- [117] J. E. Gray and S. R. Addison, "Effect of nonuniform target motion on radar backscattered waveforms," *IEE Proc.-Radar, Sonar, Navig.*, vol. 150, no. 4, pp. 262–270, 2003.
- [118] V. C. Chen, F. Li, S. S. Ho, and H. Wechsler, "Micro-Doppler effect in radar: phenomenon, model, and simulation study," *IEEE Trans. Aerosp. Electron. Syst.*, vol. 42, no. 1, pp. 2–21, Jan. 2006.
- [119] J. R. Wilkerson, K. G. Gard, and M. B. Steer, "Automated broadband high-dynamic-range nonlinear distortion measurement system," *IEEE Trans. Microw. Theory Tech.*, vol. 58, no. 5, pp. 1273–1282, May 2010.

- [120] J. M. Wetherington and M. B. Steer, "Robust analog canceller for high-dynamic-range radio frequency measurement," *IEEE Trans. Microw. Theory Tech.*, vol. 60, no. 6, pp. 1709–1719, Jun. 2012.
- [121] —, "Standoff acoustic modulation of radio frequency signals in a log-periodic dipole array antenna," *IEEE Antennas Wireless Propag. Lett.*, vol. 11, pp. 885–888, 2012.
- [122] M. B. Steer, J. R. Wilkerson, N. M. Kriplani, and J. M. Wetherington, "Why it is so hard to find small radio frequency signals in the presence of large signals," in *2012 Workshop on Integrated Nonlinear Microwave and Millimetre-Wave Circuits (INMMIC)*, Sep. 2012, pp. 1–3.
- [123] J. W. Crispin, Jr. and A. L. Maffett, "Radar cross-section estimation for simple shapes," *Proc. IEEE*, vol. 53, no. 8, pp. 833–848, Aug. 1965.
- [124] R. A. Ross, "Radar cross section of rectangular flat plates as a function of aspect angle," *IEEE Trans. Antennas Propag.*, vol. 14, no. 14, pp. 329–335, May 1966.
- [125] M. B. Steer, *Microwave and RF Design: A Systems Approach*, 2nd ed. Raleigh, NC: SciTech Pub., 2013.
- [126] J. R. Wilkerson, "Passive intermodulation distortion in radio frequency communication systems," Ph.D. dissertation, North Carolina State University, Raleigh, NC, 2010.
- [127] J. Yang, K. Sha, W.-S. Gan, and J. Tian, "Nonlinear wave propagation for a parametric loudspeaker," *IEICE Trans. Fundamentals*, vol. E87-A, no. 9, pp. 2395–2400, Sep. 2004.
- [128] Q. Ma, X. Gong, and D. Zhang, "Third order harmonic imaging for biological tissues using three phase-coded pulses," *Ultrasonics*, vol. 44, pp. e61–e65, 2006.
- [129] X. Liu, J. Li, X. Gong, Z. Zhu, and D. Zhang, "Theoretical and experimental study of the third-order nonlinearity parameter c/a for biological media," *Physica D: Nonlinear Phenomena*, vol. 228, no. 2, pp. 172–178, 2007.
- [130] Z. Qian, "Nonlinear acoustics in higher-order approximation," *Acta Physica Sinica*, vol. 4, no. 9, pp. 670–675, 1995 (overseas edition).
- [131] F. G. Mitri, "Nonlinear acoustics in higher-order approximation: Comment," *IEEE Trans. Ultrason., Ferroelectr., and Freq. Control*, vol. 57, no. 8, pp. 1715–1716, 2010.
- [132] K. Sha, J. Yang, and W.-S. Gan, "A complex virtual source approach for calculating the diffraction beam field generated by a rectangular planar source," *IEEE Trans. Ultrason., Ferroelectr., Freq. Control*, vol. 50, no. 7, pp. 890–897, Jul. 2003.
- [133] G. Garner, J. Wilkerson, M. Skeen, D. Patrick, R. Hodges, R. Schimizzi, S. Vora, Z. Feng, K. Gard, and M. Steer, "Acoustic-RF anechoic chamber construction and evaluation," in *2008 IEEE Radio and Wireless Symposium*, 2008, pp. 331–334.
- [134] F. J. Pompei, "Sound from ultrasound: The parametric array as an audible sound source," Ph.D. dissertation, Massachusetts Institute of Technology, Cambridge, MA, 2002.

- [135] S. J. Johnson and M. B. Steer, "An efficient approach to computing third-order scattering of sound by sound with application to parametric arrays," *IEEE Trans. Ultrason., Ferroelectr., and Freq. Control*, in press.
- [136] M. B. Porter, "Acoustic models and sonar systems," *IEEE J. Oceanic Engineering*, vol. 18, no. 4, pp. 425–437, Oct. 1993.
- [137] B. W. Drinkwater and P. D. Wilcox, "Ultrasonic arrays for non-destructive evaluation: a review," *NDTE International*, vol. 39, no. 7, pp. 525–541, Mar. 2006.
- [138] A. Gupta and T. D. Abhayapala, "Three-dimensional sound field reproduction using multiple circular loudspeaker arrays," *IEEE Trans. Audio, Speech, and Lang. Proc.*, vol. 19, no. 5, pp. 1149–1159, Jul. 2011.
- [139] C. A. Balanis, *Antenna Theory: Analysis and Design*, 3rd ed. Hoboken, NJ: Wiley, 2005.
- [140] J. H. Richmond and T. E. Tice, "Probes for microwave near-field measurements," *IRE Trans. Microwave Theory Tech.*, vol. 3, no. 3, pp. 32–34, Apr. 1955.
- [141] J. H. Richmond, "Simplified calculation of antenna patterns, with application to radome problems," *IRE Trans. Microwave Theory Tech.*, vol. 3, no. 4, pp. 9–12, July 1955.
- [142] R. C. Johnson, H. A. Ecker, and J. S. Hollis, "Determination of far-field antenna patterns from near-field measurements," *Proc. of the IEEE*, vol. 61, no. 12, pp. 1668–1694, Dec. 1973.
- [143] A. D. Yaghjian, "An overview of near-field antenna measurements," *IEEE Trans. Antennas and Propagation*, vol. 34, no. 1, pp. 30–45, Jan. 1986.
- [144] C. Gennarelli, A. Capozzoli, L. J. Foged, J. Fordham, and D. J. van Rensburg, "Determination of far-field antenna patterns from near-field measurements," *Inter. J. Antennas and Propagation*, vol. 2012, p. 243203, May 2012.
- [145] Y. Rahmat-Samii, V. Galindo-Israel, and R. Mittra, "A plane-polar approach for far-field construction from near-field measurements," *IEEE Trans. Antennas and Propagation*, vol. 28, no. 2, pp. 216–230, Mar. 1980.
- [146] F. D'Agostino, C. Gennarelli, G. Riccio, and C. Savarese, "Theoretical foundations of near-field far-field transformations with spiral scanings," *Prog. Electromagnetics Research*, vol. 61, pp. 193–214, 2006.
- [147] G. F. Ricciardi and W. L. Stutzman, "A near-field to far-field transformation for spheroidal geometry utilizing an eigenfunction expansion," *IEEE Trans. Antennas and Propagation*, vol. 52, no. 12, pp. 3337–3349, Dec. 2004.
- [148] A. C. Ludwig, "Near-field far-field transformation using spherical-wave expansions," *IEEE Trans. Antennas and Propagation*, vol. 19, no. 2, pp. 214–220, Sept. 1970.

- [149] P. Petre and T. K. Sarkar, "Planar near-field to far-field transformation using an array of dipole probes," *IEEE Trans. Antennas and Propagation*, vol. 42, no. 4, pp. 534–537, Apr. 1994.
- [150] H. Kobayashi, Y. Yamaguchi, and Y. Cui, "Simple near-field to far-field transformation method using antenna array-factor," *J. Wireless Networking and Communications*, vol. 2, no. 4, pp. 43–48, Dec. 2012.
- [151] E. Ohashi and H. Arai, "Spherical near-field to far-field transformation by phase retrieval method," *IEICE Communications Express*, vol. 2, no. 8, pp. 325–329, Dec. 2013.
- [152] O. M. Bucci, G. D'Elia, and M. D. Migliore, "An effective near-field far-field transformation technique from truncated and inaccurate amplitude-only data," *IEEE Trans. Antennas and Propagation*, vol. 47, no. 9, pp. 1377–1385, Sept. 1999.
- [153] S. Costanzo and G. D. Massa, "An integrated probe for phaseless near-field measurements," *Measurement*, vol. 31, no. 2, pp. 123–129, Mar. 2002.
- [154] M. B. Stephanson, "A fast near- to far-field transform algorithm," Master's thesis, The Ohio State University, Columbus, OH, 2007.
- [155] J. R. Watkins, "Utilizing near-field measurements to characterize far-field radar signatures," Master's thesis, Air Force Institute of Technology, 2004.
- [156] S. Ballantine, "An operational proof of the wave-potential theorem, with applications to electromagnetic and acoustic systems," *J. Franklin Institute*, vol. 221, pp. 469–484, Apr. 1936.
- [157] G. Kirchhoff, "Berliner sitzungsber." p. 641, 1882.
- [158] C. W. Horton and G. S. I. Jr., "The computation of far-field radiation patterns from measurements made near the source," *J. Acoust. Soc. Am.*, vol. 33, no. 7, pp. 877–880, July 1961.
- [159] D. D. Baker, "Determination of far-field characteristics of large underwater sound transducers from near-field measurements," *J. Acoust. Soc. Am.*, vol. 34, no. 11, pp. 1737–1744, Nov. 1962.
- [160] W. J. Trott, "Underwater sound transducer calibration from nearfield data," *J. Acoust. Soc. Am.*, vol. 36, no. 8, pp. 1557–1568, Aug. 1964.
- [161] I. D. Groves and V. P. Benedetti, "Acoustic measurements with a circular nearfield array in an anechoic water-filled tank," *J. Acoust. Soc. Am.*, vol. 54, no. 3, pp. 717–729, Apr. 1973.
- [162] R. D. Marcniak, "A nearfield, underwater measurement system," *J. Acoust. Soc. Am.*, vol. 66, no. 4, pp. 955–964, Oct. 1979.

- [163] L. Wright, S. P. Robinson, and V. F. Humphrey, "Prediction of acoustic radiation from axisymmetric surfaces with arbitrary boundary conditions using the boundary element method on a distributed computing system," *J. Acoust. Soc. Am.*, vol. 125, no. 3, pp. 1374–1383, Mar. 2009.
- [164] S. Wang, "Finite-difference time-domain approach to underwater acoustic scattering problems," *J. Acoust. Soc. Am.*, vol. 99, no. 4, pp. 1924–1931, Apr. 1996.
- [165] E. G. Williams and J. D. Maynard, "Holographic imaging without the wavelength resolution limit," *Phys. Rev. Lett.*, vol. 45, no. 7, pp. 554–557, Aug. 1980.
- [166] E. G. Williams, J. D. Maynard, and E. Skudrzyk, "Sound source reconstructions using a microphone array," *J. Acoust. Soc. Am.*, vol. 68, no. 1, pp. 340–344, Jul. 1980.
- [167] E. G. Williams, H. D. Dardy, and R. G. Fink, "Nearfield acoustical holography using an underwater, automated scanner," *J. Acoust. Soc. Am.*, vol. 78, no. 2, pp. 789–798, Aug. 1985.
- [168] J. D. Maynard, E. G. Williams, and Y. Lee, "Nearfield acoustic holography: I. Theory of generalized holography and the development of NAH," *J. Acoust. Soc. Am.*, vol. 78, no. 4, pp. 1395–1413, Oct. 1985.
- [169] E. G. Williams, H. D. Dardy, and K. B. Washburn, "Generalized nearfield acoustical holography for cylindrical geometry: Theory and experiment," *J. Acoust. Soc. Am.*, vol. 81, no. 2, pp. 389–407, Feb. 1987.
- [170] W. A. Veronesi and J. D. Maynard, "Nearfield acoustic holography (NAH) II. Holographic reconstruction algorithms and computer implementation," *J. Acoust. Soc. Am.*, vol. 81, no. 5, pp. 1307–1322, May 1987.
- [171] E. G. Williams, B. H. Houston, and P. C. Herdic, "Fast Fourier transform and singular value decomposition formulations for patch nearfield acoustical holography," *J. Acoust. Soc. Am.*, vol. 114, no. 3, pp. 1322–1333, Aug. 2003.
- [172] M. Lee and J. S. Bolton, "Patch near-field acoustical holography in cylindrical geometry," *J. Acoust. Soc. Am.*, vol. 118, no. 6, pp. 3721–3732, Dec. 2005.
- [173] B. K. Gardner and R. J. Bernhard, "A noise source identification technique using an inverse helmholtz integral equation method," *ASME J. Vib., Acoust., Stress, Reliab.*, vol. 110, pp. 84–90, Dec. 1988.
- [174] W. A. Veronesi and J. D. Maynard, "Digital holographic reconstruction of sources with arbitrarily shaped surfaces," *J. Acoust. Soc. Am.*, vol. 85, no. 2, pp. 588–598, Feb. 1989.
- [175] G. V. Borgiotti, A. Sarkissian, E. G. Williams, and L. Schuetz, "Conformal generalized near-field acoustic holography for axisymmetric geometries," *J. Acoust. Soc. Am.*, vol. 88, no. 1, pp. 199–209, Jul. 1990.
- [176] Z. Wang and S. F. Wu, "Helmholtz equation-least-squares method for reconstructing the acoustic pressure field," *J. Acoust. Soc. Am.*, vol. 102, no. 4, pp. 2020–2032, Oct. 1997.

- [177] S. F. Wu and X. Zhao, “Combined helmholtz equation least squares (CHELS) method for reconstructing acoustic radiation,” *J. Acoust. Soc. Am.*, vol. 112, no. 1, pp. 179–188, Jul. 2002.
- [178] S. F. Wu, “Hybrid near-field acoustic holography,” *J. Acoust. Soc. Am.*, vol. 115, no. 1, pp. 207–217, Jan. 2004.
- [179] G. S. Shekhawat and V. P. Dravid, “Nanoscale imaging of buried structures via scanning near-field ultrasound holography,” *Science*, vol. 310, no. 5745, pp. 89–92, Oct. 2005.
- [180] G. S. Shekhawat, A. Srivastava, S. Avasthy, and V. Dravid, “Ultrasound holography for noninvasive imaging of buried defects and interfaces for advanced interconnect architectures,” *Appl. Phys. Lett.*, vol. 95, no. 26, p. 263101, Dec. 2009.
- [181] J. H. Thomas, V. Grulier, S. Paillasseur, J. C. Pascal, and J. C. L. Roux, “Real-time near-field acoustic holography for continuously visualizing nonstationary acoustic fields,” *J. Acoust. Soc. Am.*, vol. 128, no. 6, pp. 3554–3567, Dec. 2010.
- [182] S. Pan and W. Jiang, “Optimized two-dimensional imaging of transient sound fields using a hybrid transient acoustic holography,” *Proc. Meet. Acoust.*, vol. 19, pp. 1–9, Jul. 2013.
- [183] S. A. Tsysar, Y. D. Sinelnikov, and O. A. Sapozhnikov, “Characterization of cylindrical ultrasonic transducers using acoustic holography,” *Acoust. Phys.*, vol. 57, no. 1, pp. 94–105, 2011.
- [184] B. B. Baker and E. T. Copson, *The mathematical theory of Huygens’ principle*, 2nd ed. Oxford, England: Clarendon Press, 1950.
- [185] C. W. Horton, “Acoustic impedance of an outgoing cylindrical wave,” *J. Acoust. Soc. Am.*, vol. 34, no. 10, p. 1663, 1962.
- [186] G. S. Garrett, J. N. Tjotta, and S. Tjotta, “Nearfield of a large acoustic transducer, Part I. linear radiation,” *J. Acoust. Soc. Am.*, vol. 72, no. 3, pp. 1056–1061, Sep. 1982.
- [187] M. I. Skolnik, “Introduction to radar,” *Radar Handbook*, p. 2, 1962.
- [188] J. Van Bladel, “Electromagnetic fields in the presence of rotating bodies,” *Proc. IEEE*, vol. 64, pp. 301–318, Mar. 1976.
- [189] H. J. Schmitt and T. T. Wu, “Electromagnetic reflection from sound waves,” *J. Acoust. Soc. Am.*, vol. 32, no. 12, pp. 1660–1667, 1960.
- [190] H. J. Schmitt, “Diffraction of electromagnetic waves by sound waves,” *J. Acoust. Soc. Am.*, vol. 33, no. 10, pp. 1288–1292, 1961.

APPENDICES

Appendix A

Gaussian Beam Expansion Coefficient Sets

The implementation of the MGB expansion technique described in Chapters 2 and 3 requires the optimization of the coefficients of the Gaussian base functions, A_n and B_n , as discussed in Section 2.2.1. As a means of determining these coefficients, an assortment of optimization methods have been employed to produce a variety of acceptable coefficient sets that vary in the number of terms required in each set. The following presents several Gaussian coefficient sets previously reported in the literature. This dissertation utilizes the ten term coefficient set given by Wen and Breazeale [15] and detailed in Table A.1.

n	A_n	B_n
1	$11.428 + 0.95175j$	$4.0697 + 0.22726j$
2	$0.06002 - 0.08013j$	$1.1531 - 20.933j$
3	$-4.2743 - 8.5562j$	$4.4608 + 5.1268j$
4	$1.6576 + 2.7015j$	$4.3521 + 14.997j$
5	$-5.0418 + 3.2488j$	$4.5443 + 10.003j$
6	$1.1227 - 0.68854j$	$3.8478 + 20.078j$
7	$-1.0106 - 0.26955j$	$2.5280 - 10.310j$
8	$-2.5974 + 3.2202j$	$3.3197 - 4.8008j$
9	$-0.14840 - 0.31193j$	$1.9002 - 15.820j$
10	$-0.20850 - 0.23851j$	$2.6340 + 25.009j$

Table A.1: Ten term coefficient set defining an edge supported piston, as given by Wen and Breazeale [15].

n	A_n	B_n
1	$-0.0366 + 0.0698j$	$0.9568 + 22.0499j$
2	$-0.2880 - 0.1072j$	$1.8966 + 17.3281j$
3	$0.0463 - 0.8593j$	$2.5687 + 12.2845j$
4	$2.4278 - 0.4273j$	$3.1522 + 7.1375j$
5	$-1.6515 + 6.9321j$	$3.7393 + 2.2497j$
6	$-1.6515 - 6.9321j$	$3.7393 - 2.2497j$
7	$2.4278 + 0.4273j$	$3.1522 - 7.1375j$
8	$0.0463 + .8593j$	$2.5687 - 12.2845j$
9	$-0.2880 + 0.1072j$	$1.8966 - 17.3281j$
10	$-0.0366 - 0.0698j$	$0.9568 - 22.0499j$

Table A.2: Ten term coefficient set given by Ding using a simplified method of calculation [57].

n	A_n	B_n
1	$-0.0647 - 0.0042j$	$1.21 + 35.6867j$
2	$0.0334 - 0.2398j$	$2.3108 + 31.3481j$
3	$0.5113 - 0.0972j$	$2.8161 + 26.2901j$
4	$0.5858 + 0.7912j$	$3.2223 + 21.1344j$
5	$-0.6908 + 1.5627j$	$3.486 + 15.8696j$
6	$-3.0363 + 0.5081j$	$3.6537 + 10.4523j$
7	$-3.6501 - 6.3857j$	$4.0206 + 5.0002j$
8	13.6222	4.3552
9	$-3.6501 + 6.3857j$	$4.0206 - 5.0002j$
10	$-3.0363 - 0.5081j$	$3.6537 - 10.4523j$
11	$-0.9608 - 1.5627j$	$3.486 - 15.8696j$
12	$0.5858 - 0.7912j$	$3.2223 - 21.1344j$
13	$0.5113 + 0.0972j$	$2.8161 - 26.2901j$
14	$0.0334 + 0.2398j$	$2.3108 - 31.3481j$
15	$-0.0647 + 0.0042j$	$1.21 - 35.6867j$

Table A.3: Fifteen term coefficient set given by Wei and Jun using an alternative optimization method that combines solutions of linear equations with Fourier series expansions [58].

n	A_n	B_n
1	$1.96364 + 1.28797j$	$4.90285 + 0.72127j$
2	$1.16005 - 2.30785j$	$5.64040 - 4.11116j$
3	$-1.73228 + 0.93175j$	$4.23459 - 4.52195j$
4	$-0.39524 + 0.09089j$	$2.95782 + 4.37533j$

Table A.4: Four term coefficient set given by Cervenka using a heuristic evolutionary algorithm [60].

n	A_n	B_n
1	$-0.051932 + 0.074854j$	$1.9598 - 68.491j$
2	$-0.001932 + 0.13338j$	$2.2259 - 62.801j$
3	$0.2038 + 0.15604j$	$2.6482 - 51.148j$
4	$0.49313 - 0.054592j$	$3.0329 - 39.309j$
5	$-0.01404 - 0.017898j$	$0.97296 - 79.031j$
6	$0.75146 - 0.7956j$	$3.4613 - 27.379j$
7	$-4.6458 - 6.3564j$	$4.4953 - 9.5366j$
8	$17.899 - 9.5721j$	$5.344 + 6.6418j$
9	$0.020451 + 0.4854j$	$4.2603 + 45.77j$
10	$-4.2364 - 3.8044j$	$4.9867 + 17.935j$
11	$0.1324 - 0.04058j$	$3.8823 + 60.869j$
12	$-0.064179 - 10.45j$	$5.1546 + 12.172j$
13	$-0.24048 + 0.96624j$	$4.9921 + 36.952j$
14	$-3.1798 + 0.057147j$	$4.8183 + 23.873j$
15	$0.24524 + 0.14556j$	$3.6069 + 52.531j$
16	$-1.308 + 1.0953j$	$4.658 + 30.099j$
17	$-0.000527 - 0.020896j$	$0.83072 + 68.991j$
18	$0.64227 - 0.32108j$	$3.2362 - 33.351j$
19	$0.086431 + 0.16529j$	$2.4479 - 57.008j$
20	$-0.05428 + 0.011274j$	$1.5995 - 73.994j$
21	$14.433 + 29.229j$	$5.3897 + 1.3751j$
22	$0.68906 - 1.6732j$	$3.7246 - 21.401j$
23	$-0.11112 - 3.4071j$	$4.0538 - 15.436j$
24	$-21.03 + 3.9134j$	$5.0621 - 3.8817j$
25	$0.34217 + 0.090409j$	$2.84 - 45.245j$

Table A.5: Twenty-five term coefficient set given by Kim *et al.* that increased the precision of the expansion for a piston radiator into the near-field [59].

n	A_n	B_n
1	$2.2097 - 0.39647j$	$3.7227 - 0.13038j$
2	$0.06733 - 0.00417j$	$3.0331 + 15.467j$
3	$-0.29108 - 0.10913j$	$2.2474 - 4.5275j$
4	$0.00901 - 0.01554j$	$2.3366 + 21.301j$
5	$0.11751 + 0.21108j$	$3.4625 + 9.7999j$
6	$-0.93941 + 0.30743j$	$3.7731 + 4.5318j$

Table A.6: Six term coefficient set defining a rigid piston, as given by Wen and Breazeale [15].

Appendix B

LabVIEW Measurement and Automation Code

The experimental results presented in this dissertation were enabled by the use of NI LabVIEW software to control the acoustic and RF equipment required to conduct each measurement. The following is a brief overview of the LabVIEW code employed to generate the presented results.

B.1 Acoustic Signal Generation and Measurement Code

The acoustic measurements performed relied heavily on the LabVIEW code developed by Dr. Glenwood Garner for the generation and recording of acoustic signals, a detailed description of which can be found in Appendix C of his Ph.D. dissertation titled “Design of Optimal Directional Parametric Acoustic Arrays in Air”. The appendix describes the operation and use of LabVIEW code designed to generate and receive acoustic signals (“Signal_Generation.vi”), maneuver the Magellan MDT-19 turntable used to obtain the radiation pattern of an acoustic source (“Turn_Table_Control.vi”), and control the XY scanner employed to determine the near-field characteristics for use in the NTF transformation (“Master_2D_Sweep_Controller.vi”). “Signal_Generation.vi” provides the capability of generating many commonly utilized acoustic signals (e.g., pulsed sinusoid, frequency sweeps, and two tone signals) while allowing for simultaneously recording up to four input channels (two microphone inputs, an input from the LDV, and a voltage input) through the use of two NI PXI-4461 data acquisition cards that transmit and receive the acoustic signals. “Turn_Table_Control.vi” automates the measurement of acoustic radiation patterns by synchronizing the rotation of the Magellan MDT-19 turntable with the acoustic measurements. When the turntable motor activates, thereby producing a sound signal exceeding a specified threshold, a secondary microphone located near the motor triggers the acoustic measurement to be taken using a similar signal acquisition process

as “Signal_Generation.vi”. “Master_2D_Sweep_Controller.vi” controls the two-dimensional XY scanner used to capture the near-field data that would be converted to its far-field counterpart using the NTFF transformation method. This code manages the acceleration and velocity of the scanner’s stepper motors to scan a plane in front of the acoustic source; however, it does not control the acoustic measurements, thus requiring “Signal_Generation.vi” (or another signal acquisition script) to be used simultaneously.

To suit the specific experiments performed in this dissertation, slight modifications were made to these LabVIEW codes, however, these modifications have a negligible impact on the configuration and performance as compared to the original version of the code. Thus, the reader is directed to the Garner dissertation as it details in depth the operation of the acoustic measurements, turntable, and XY scanner.

B.2 Zero Span Frequency Measurement Analog Cancellation Code

The RF measurements in this dissertation were found using the high dynamic range nonlinear measurement system originally developed by Wilkerson, Wetherington, and Steer. This system performs the feedforward analog cancellation operation, as described in Sec. 2.5, to obtain a maximum cancellation of the received carrier power of 60 dB, which is then passed to the spectrum analyzer where the final measurement is realized. To perform this measurement, a steady state environment is required (and assumed by the LabVIEW code) as many individual measurements are taken across the frequency spectrum over time to comprise the complete frequency spectrum. To obtain the transient measurement results in this dissertation, transient capabilities were incorporated into the nonlinear measurement system by adding the option of taking a zero span frequency measurement. This measurement function occurs immediately following the cancellation of the received carrier power and continues until the LabVIEW code is terminated. As specified in Chapter 5, this is a pseudo-transient technique as some time is required to achieve the cancellation of the carrier signal, however, the signal is measured at the given frequency in real-time once the cancellation algorithm completes. For a detailed description of the system along with system documentation, the reader is directed to the Ph.D. dissertation of Dr. Joshua Wetherington titled “Characterization of Passive Spectral Regrowth in Radio Frequency System”.

Since the zero span frequency measurement is incorporated into the existing system, the front panel of the LabVIEW code is very similar to that presented in the Wetherington dissertation, as shown in Fig. B.1, with the addition of inputs related to the zero span frequency measurement. The transient measurement is defined by the inputs provided for the desired mod-

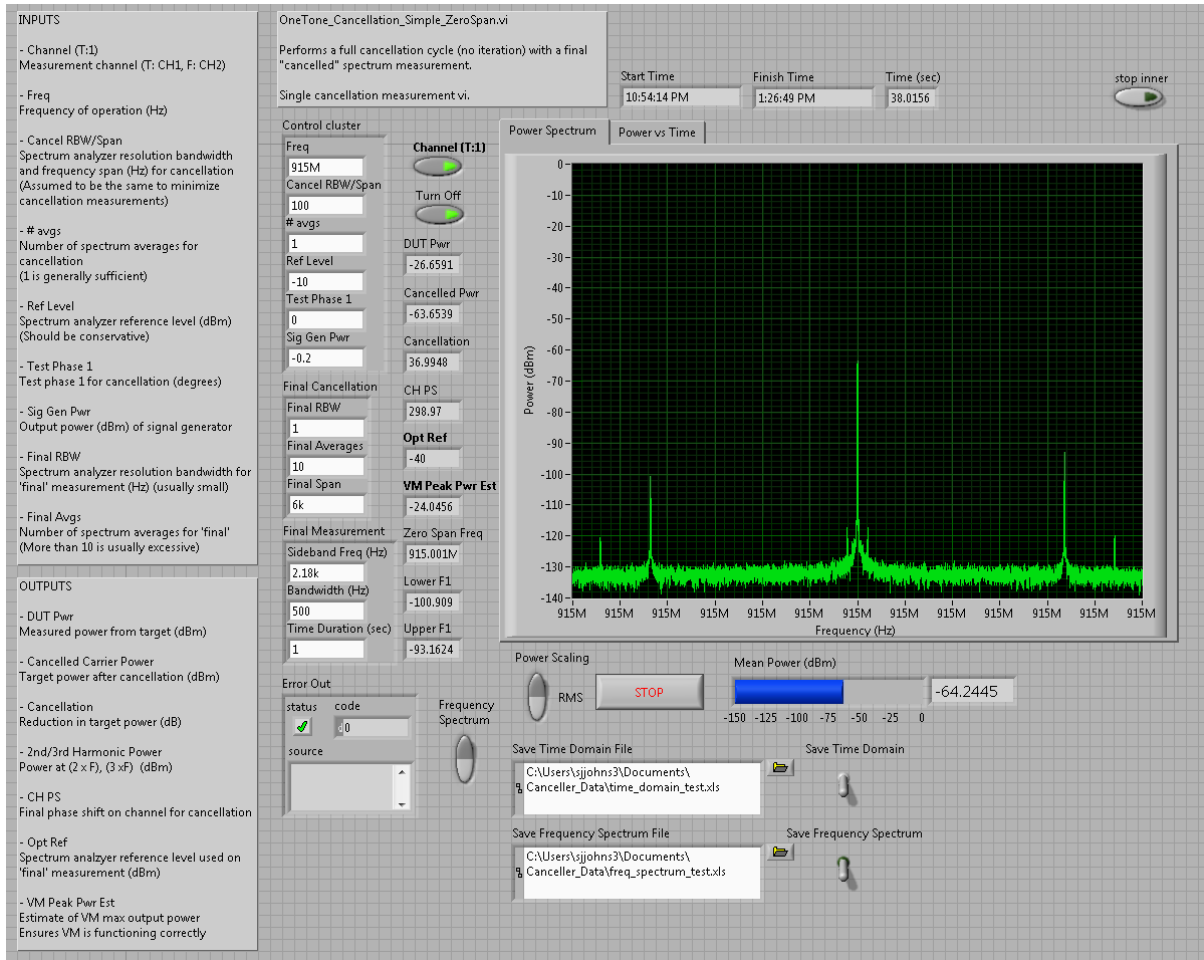


Figure B.1: Front panel of user interface of the high dynamic range nonlinear measurement system with zero span frequency measurement incorporated.

ulation sideband frequency, bandwidth of the measurement filter, and duration of the measurement. These settings center a stationary filter with the specified bandwidth at the modulation sideband frequency and display the measured results for the duration specified (however, since the code runs continuously, the display is refreshed at the completion of each measurement duration interval). Additionally, options for saving the frequency and time domain data are included, both producing a Microsoft Excel spreadsheet containing the data acquired during the measurement. Choosing to save the frequency domain data will record the power (in dB) across the entire frequency range specified after the carrier signal has been canceled. Choosing to save the time domain data will record the power (in dB) within the filter bandwidth centered at the specified sideband frequency and will continue to record the data until the LabVIEW code is terminated or the switch indicating to save the time domain data is deactivated.

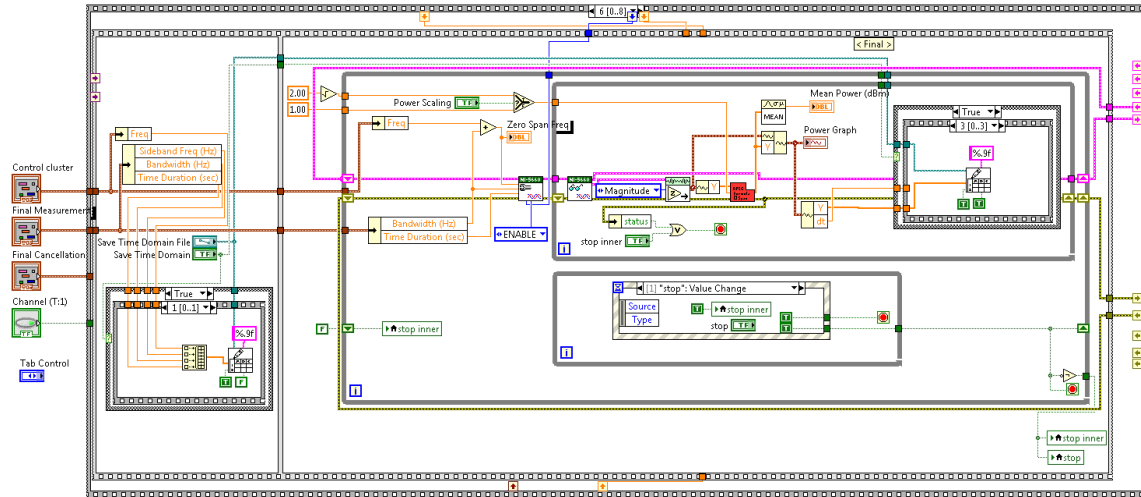


Figure B.2: Block diagram of zero span frequency measurement implementation in the measurement system.

Similar to the front panel, the back panel of the LabVIEW code strongly resembles the code presented in the Wetherington dissertation. To perform the zero span frequency measurement, an additional step was inserted into the system process, as shown in Fig. B.2, immediately following the cancellation algorithm and will run continuously until the user terminates the measurement process. This step configures the filter used in the zero span frequency measurement, captures the I/Q data of the received signal over time and saves it to a file, if indicated. When the measurement is terminated, the system continues to the appropriate shut down routine to properly power down the hardware used in the measurement, as specified in the original system documentation in the Wetherington dissertation.

Appendix C

MATLAB Simulation Code

This appendix details the MATLAB code used to generate the theoretical results presented in this dissertation.

C.1 Multi-Gaussian Beam Expansion Code

```
%% Multi-Gaussian Beam Expansion Technique
% Acoustic_Field_Generator.m is the main script in the generation of
% acoustic fields using the multi-Gaussian beam (MGB) expansion
% technique. This script generates the solutions for the primary,
% secondary, and tertiary acoustic fields under the specified
% conditions using the multi-Gaussian beam expansion technique as
% described in "An Efficient Approach to Computing Third-Order
% Scattering with Application to Parametric Arrays" by
% Spencer J. Johnson.
```

```
clear all; close all; clc;
```

```
%% Input Specifications
% The user is to input the specifications for the sound fields of
% interest in this section. Provide the two primary sound fields
% with the sound pressure levels, the medium properties, the
% transducer and sound source specifications with electrical
% nonlinearity configurations, and the resulting far-field area for
% the sound fields of interest.
```

```

% Select the desired frequencies
% Note: f_1 must be greater than f_2
f_1 = 60000;
f_2 = 49000;

% Select the medium properties
rho = 1.2056;          %medium density
c = 343;               %small signal sound speed
beta = 1.2;            %coefficient of nonlinearity

% Select the sound pressure level for each primary tone (in dB SPL)
p_1 = 128;
p_2 = 128;

% Select transducer specifications
a_t = 0.0161;          %transducer radius (Note: 0.0161 or 0.022)
trans_num = 81;        %number of transducers
                        %(Note: must be 1, 7, 19, 37, 61, or 81)
d = 0.04;              %distance between transducer elements

% Select sound field area specifications
r_f = 5;               %distance to observation point
theta_max = 15;        %maximum observation angle (in degrees)
                        %(Note: must be between 0 and 90)
theta_num = 36;        %numbers of points to be calculated in field

% Select desired sound field
order = 1;             %sound field order (Note: must be 1, 2, or 3)
field = 'one';          %sound field selection
                        %For Primary: 'one' or 'two'
                        %For Secondary: 'harmonic', 'sum', or 'diff'
                        %For Tertiary: 'harmonic', 'upper', or 'lower'

% Select transient simulation options
time = 'off';          %transient simulation: 'on' or 'off'
t_start = 0;           %start/stop selection should be in seconds
t_stop = 1e-5;

```

```

% Select electrical nonlinearity configuration
elec_non = 'none'; %nonlinearity contribution from
                    %amplifier/transducer
                    %For None: 'none'
                    %For Holosonic: 'holo'
                    %For Airmar: 'airmar'

%% DO NOT ALTER THE SCRIPT AFTER THIS POINT
% This section utilizes the input specifications to generate the
% output fields of interest.

% This loads the MGB coefficients for use in the simulation
ten_coefficient

% Check frequency configuration
if f_1 < f_2
    disp('f_1 must be greater than f_2. ');
    break
end

% Primary sound pressure conversion from dB SPL
p_1 = sqrt(2)*20e-6*10^(p_1/20);
p_2 = sqrt(2)*20e-6*10^(p_2/20);

% Check theta configuration
if (theta_max > 90) || (theta_max <= 0)
    disp('Theta_max must be between 0 and 90. ');
    break
end

% Generating sound field mesh
theta_f = linspace(0,theta_max,theta_num)*pi/180; %field point angle
z_f = r_f*cos(theta_f);
x_f = r_f*sin(theta_f);
y_f = zeros(1,length(z_f));
z_max = r_f*cos(theta_f(1));

```

```

x_max = r_f*sin(theta_f(end));

% Step number for mesh grid (r,phi are equivalent to x,z here)
x_step = 400;
z_step = 100;

% Define timing settings for transient simulations
t = linspace(t_start,t_stop,100);

% Check far-field criteria
lambda_1 = c/f_1;
lambda_2 = c/f_2;
S = pi*a_t^2; %transducer area
r_0 = S/((lambda_1+lambda_2)/2); %Rayleigh distance
if r_f<r_0
    disp('Increase distance, you are not in the farfield.');
```

break

```

end

% Defining transducer locations
switch trans_num
    case 1
        radius = 0;
    case 7
        radius = 1;
    case 19
        radius = 2;
    case 37
        radius = 3;
    case 61
        radius = 4;
    case 81
        radius = 5;
    otherwise
        disp('Select an appropriate number of transducers.')
```

break

```

end
```

```

[x_t , y_t , z_t ] = par_array_cord(radius ,d, 'vert ');

% Check element spacing within the transducer array
if d<=(2*a_t)
    disp('Increase element separation or decrease element radius. ');
    break
end

% Define desired sound field
switch order
    case 1
        ord = 'first ';
        name = 'Primary';
        switch field
            case 'one'
                f = f_1;
                type = 'Fundamental Frequency';
                ind = 'f_1';
            case 'two'
                f = f_2;
                type = 'Fundamental Frequency';
                ind = 'f_2';
        end
    case 2
        ord = 'second';
        name = 'Secondary';
        switch field
            case 'harmonic'
                f = 2*f_1;
                type = 'Second Harmonic';
                ind = '2f_1';
            case 'sum'
                f = f_1+f_2;
                type = 'Summation Frequency';
                ind = 'f_S';
            case 'diff'
                f = f_1-f_2;

```

```

        type = 'Difference Frequency';
        ind = 'f_D';
    end
case 3
    ord = 'third';
    name = 'Tertiary';
    switch field
        case 'harmonic'
            f = 3*f_1;
            type = 'Third Harmonic';
            ind = '3f_1';
        case 'upper'
            f = 2*f_1-f_2;
            type = 'IM3 Upper Frequency';
            ind = 'f_U';
        case 'lower'
            f = 2*f_2-f_1;
            type = 'IM3 Lower Frequency';
            ind = 'f_L';
    end
otherwise
    disp('Select an appropriate sound field.')
    break
end

% Define desired electrical nonlinearity contribution
switch elec_non
    case 'none'
        a_1 = 1;
        a_2 = 0;
        a_3 = 0;
    case 'holo'
        a_1 = 3e-1;
        a_2 = 2e-6;
        a_3 = -1.5e-10;
    case 'airmar'
        a_1 = 5.5e-1;

```

```

        a_2 = 1.8e-3;
        a_3 = -1.4e-2;
    otherwise
        disp('Select an appropriate electrical nonlinearity
              characterization.')
        break
    end

p = zeros(size(theta_f));

% Steps through the far-field points
for theta_ind = 1:length(theta_f)
    % Steps through the transducer elements in the sound source
    for tran_ind = 1:length(x_t)

        r = sqrt((x_f(theta_ind)-x_t(tran_ind))^2 ...
                  +(y_f(theta_ind)-y_t(tran_ind))^2);
        z = (z_f(theta_ind)-z_t(tran_ind));

        p_temp = Single_Piston_Function_Generator ...
            (r,z,f_1,f_2,p_1,p_2,a_t,z_max,x_max,z_step,...
             x_step,rho,c,beta,A,B,a_1,a_2,a_3,ord,field);

        p(theta_ind) = p(theta_ind) + p_temp;
    end
end

myTitleTop = strcat(name, ' Sound Field ');
myTitleBot = strcat(type, ' at \it ',ind, '\rm =',...
    sprintf(' %d kHz',f));

% Specifies whether the transient settings for the simulation are to
% be turned on. This section also plots the sound fields as a
% function of the angle off of the primary axis.
switch time
    case 'on'
        [P, T] = ndgrid(p,t);

```



```

P = P.*exp(-2*pi*f*T);
p_dB = 20*log10(abs(P)/(sqrt(2)*20e-6));
p_dB2 = p_dB;

for t_ind = 1:length(t)
    figure(1)
    cla(figure(1),'reset')
    h = subplot(2,2,1);
    plot(theta_f*180/pi,p_dB(:,1))
    xlabel('Angle (deg)')
    ylabel('Sound Pressure Level (dB SPL)')
    p = get(h,'pos');
    set(h,'pos',[p(1) p(2)-.075 p(3:4)]);

    h = subplot(2,2,2);
    plot(theta_f*180/pi,p_dB(:,t_ind))
    xlabel('Angle (deg)')
    ylabel('Sound Pressure Level (dB SPL)')
    axis([min(theta_f*180/pi) max(theta_f*180/pi) -50 100])
    p = get(h,'pos');
    set(h,'pos',[p(1) p(2)-.075 p(3:4)]);

    p_dB2(p_dB2 < 0) = 0;
    plot_step_max = ceil(max(p_dB2(:,1))/10)*10;
    if plot_step_max <= 0;
        plot_step_max = 10;
    end
    plot_step_min = 0;
    plot_step = plot_step_max/5;
    P_dB = transpose(p_dB2(:,1));

    h = subplot(2,2,3);
    halfPolar([pi/2-fliplr(theta_f) theta_f+pi/2],...
        [fliplr(P_dB) P_dB],{'b'},[plot_step_min ...
        plot_step 2*plot_step 3*plot_step 4*plot_step ...
        plot_step_max]);
    p = get(h,'pos');

```

```

    set(h, 'pos', [p(1) p(2) - .05 p(3:4)]);

    P_dB = transpose(p_dB2(:, t_ind));

    h = subplot(2, 2, 4);
    halfPolar([pi/2 - fliplr(theta_f) theta_f + pi/2], ...
        [fliplr(P_dB) P_dB], {'b'}, [plot_step_min ...
        plot_step 2*plot_step 3*plot_step 4*plot_step ...
        plot_step_max]);
    p = get(h, 'pos');
    set(h, 'pos', [p(1) p(2) - .05 p(3:4)]);

    suplabel({myTitleTop; myTitleBot}, 't');

    sec = .001;
    tic;
    while toc < sec
    end
end

case 'off'
    p_dB = 20*log10(abs(p)/(sqrt(2)*20e-6));

    figure(1)
    subplot(2, 1, 1)
    plot(theta_f*180/pi, p_dB)
    mtitle(myTitleTop, myTitleBot);
    xlabel('Angle (deg)')
    ylabel('Sound Pressure Level (dB SPL)')

    p_dB(p_dB < 0) = 0;
    plot_step_max = ceil(max(p_dB)/10)*10;
    if plot_step_max <= 0;
        plot_step_max = 10;
    end
    plot_step_min = 0;
    plot_step = plot_step_max/5;

```

```

subplot(2,1,2)
halfPolar([pi/2-fliplr(theta_f) theta_f+pi/2], ...
    [fliplr(p_dB) p_dB],{'b'},[plot_step_min plot_step ...
    2*plot_step 3*plot_step 4*plot_step plot_step_max]);
end

```

```

function [p] = SinglePistonFunctionGenerator(x_i , z_i , f_1 , f_2 , ...
    p_1 , p_2 , a_t , z_max , x_max , z_step , x_step , rho , c , beta , A , B , ...
    a_1 , a_2 , a_3 , order , choice)
% SinglePistonFunctionGenerator.m is called by
% AcousticFieldGenerator.m, sets the normalization conditions
% for the resultant sound fields of interest , and calls the
% appropriate scripts to generate the sound field.

% Radian frequencies
omega_1 = 2*pi*f_1 ;
omega_2 = 2*pi*f_2 ;

% Wave numbers
k_1 = omega_1/c ;
k_2 = omega_2/c ;
k0 = (k_1+k_2)/2 ;
z_0 = k0*a_t ^2/2 ;

% Attenuation coefficients
alpha_f1 = alpha_x(f_1 , 29.92 , 70 , 50) ;    %primary frequency #1
alpha_f2 = alpha_x(f_2 , 29.92 , 70 , 50) ;    %primary frequency #2
alpha_2f1 = alpha_x(2*f_1 , 29.92 , 70 , 50) ; %second harmonic #1
alpha_D = alpha_x(f_1-f_2 , 29.92 , 70 , 50) ; %difference tone
alpha_S = alpha_x(f_1+f_2 , 29.92 , 70 , 50) ; %difference tone

X1 = x_i/a_t ;
Z1 = z_i/z_0 ;

% Selects the normalization criterion based upon the input settings
switch order
case 'first'
    q1 = zeros(size(X1)) ;
    switch choice
    case 'one'
        l = k_1/k0 ;
        p0 = p_1 ;
        pOTHER = p_2 ;

```

```

        alpha_1 = alpha_f1;
    case 'two'
        l = k_2/k0;
        p0 = p_2;
        pOTHER = p_1;
        alpha_1 = alpha_f2;
    otherwise
        err = MException('TypeChk:UnknownDef', ...
            '''Choice'' selection for the primary (first)
            field should be ''one'' or ''two''.'');
        throw(err)
end

for n = 1:length(A)
    B1 = B(n)/l;
    q1 = q1 + A(n)./(1+1i.*B1.*Z1) ...
        .*exp(-l*B1.*X1.^2./(1+1i.*B1.*Z1)+1i*l*k0*z_0*Z1);
end

p = sum(sum((a_1*p0+a_3*(0.75*p0^3+1.5*p0*pOTHER^2)) ...
    *q1.*exp(-alpha_1*z_0*Z1)));

case 'second'
    switch choice
        case 'harmonic'
            k1 = k_1;
            k2 = k_1;
            l = k_1/k0;
            m = k_1/k0;
            p0 = p_1*p_1/2;
            alpha_2 = 4*alpha_f1;
            alpha_21 = alpha_2f1;
        case 'sum'
            k1 = k_1;
            k2 = k_2;
            l = k_1/k0;
            m = k_2/k0;

```

```

        p0 = p_1*p_2;
        alpha_2 = alpha_S;
        alpha_21 = alpha_S;
    case 'diff'
        k1 = k_1;
        k2 = k_2;
        l = k_1/k0;
        m = -k_2/k0;
        p0 = p_1*p_2;
        alpha_2 = alpha_D;
        alpha_21 = alpha_D;
    otherwise
        err = MException('TypeChk:UnknownDef', ...
            '''Choice'' selection for the secondary (second)
                field should be ''harmonic'', ''sum'', or ''
                diff''.'');
        throw(err)
    end

% Primary sound field
q21 = zeros(size(X1));
for n = 1:length(A)
    B1 = B(n)/(l+m);
    q21 = q21 + A(n)./(1+l*i.*B1.*Z1) ...
        .*exp(-(l+m)*B1.*X1.^2./(1+l*i.*B1.*Z1) ...
            +l*i*(l+m)*k0*z_0*Z1);
end

% Secondary sound field
q2 = Second_Order_MGB(X1,Z1,k1,k2,k0,A,B,choice);
p2 = (-p0*beta*(l+m)^2*(k0*a_t)^2/(rho*c^2) ...
    *q2.*exp(-alpha_2*z_0*Z1+l*i*(l+m)*k0*z_0*Z1));
p_temp = sum(sum(a_2*p0*q21 ...
    .*exp(-alpha_21*z_0*Z1+l*i*(l+m)*k0*z_0*Z1)));
p = p2 + p_temp;

case 'third'

```

```

syms u;
xi_min = 0;
xi_n = x_i/a_t;
xi_max = x_max/a_t;
xi_step = (xi_max-xi_min)/x_step;
sigma_p = z_i/z_0;
sigma_kzk = (k0*a_t)^(1/3)*a_t/z_0;
sigma_min = 3/4*sigma_kzk;
sigma_max = z_max/z_0;
sigma_step = (sigma_max-sigma_min)/z_step;

% Defining the mesh for the tertiary sound field
xi = linspace(xi_min,xi_max,floor((xi_max-xi_min)/xi_step));
sigma = linspace(sigma_min,sigma_max,...
    floor((sigma_max-sigma_min)/sigma_step));
xi_l = xi;
sigma_k = sigma(1:end-1);
sigma_step = sigma(2:end)-sigma(1:end-1);
[XI_L SIGMA_K] = ndgrid(xi_l,sigma_k);
[XI_L sigma_step] = ndgrid(xi_l,sigma_step);

% Tertiary sound field
[q3 qn lmh p0 alpha_3] = MGB_Integrand_Generator...
    (XI_L,SIGMA_K,p_1,p_2,f_1,f_2,c,xi_n,sigma_p,...
    xi_step,sigma_step,A,B,choice);
p3 = 1/2*p0*lmh^2*(beta*(k0*a_t)^2/(rho*c^2))^2 ...
    *q3.*exp(-alpha_3*z_0*Z1+1i*lmh*k0*z_0*Z1);
p_temp = sum(sum(3/4*a_3*p0*qn...
    .*exp(-alpha_3*z_0*Z1+1i*lmh*k0*z_0*Z1)));
p = p3 + p_temp;

otherwise
    err = MException('TypeChk:UnknownDef', ...
        '''Order'' selection should be ''first'', ''second'', or
        ''third''.'');
    throw(err)
end

```

```

function [THIRD, qn, lmh, p0, alpha_3] = MGB_Integrand_Generator...
    (xi_1, sigma_k, p_1, p_2, f_1, f_2, c, xi_n, sigma_p, ...
    xi_step, sigma_step, A, B, choice)
% MGB_Integrand_Generator.m is called by
% Single_Piston_Function_Generator.m and calculates the third order
% sound field using the MGB expansion technique.

X1 = xi_1;
Z1 = sigma_k;

% Wave numbers
k1 = 2*pi*f_1/c;
k2 = 2*pi*f_2/c;
k0 = (k1+k2)/2;

qf1 = zeros(size(X1));
qf2 = zeros(size(X1));
qn = zeros(size(X1));

% Selects the third order sound field based upon the input settings.
switch choice
    case 'harmonic'
        l = k1/k0;
        m = k1/k0;
        h = k1/k0;
        p0 = p_1^3;
        alpha_3 = alpha_x(3*f_1, 29.92, 70, 50);

        for n = 1:length(A)
            B1 = B(n)/l;
            B3 = B(n)/(l+m+h);
            qf1 = qf1 + A(n)./(1+1i.*B1.*Z1) ...
                .*exp(-l*B1.*X1.^2./(1+1i.*B1.*Z1));
            qn = qn + A(n)./(1+1i.*B3.*Z1) ...
                .*exp(-(l+m+h)*B3.*X1.^2./(1+1i.*B3.*Z1));
        end
end

```



```

    signal = qf1.*qf1.*qf1;

case 'upper'
    l = k1/k0;
    m = k1/k0;
    h = -k2/k0;
    p0 = p_1^2*p_2;
    alpha_3 = alpha_x(2*f_1-f_2,29.92,70,50);

    for n = 1:length(A)
        B1 = B(n)/l;
        B2 = B(n)/(-h);
        B3 = B(n)/(l+m+h);
        qf1 = qf1 + A(n)./(1+1i.*B1.*Z1) ...
            .*exp(-l*B1.*X1.^2./(1+1i.*B1.*Z1));
        qf2 = qf2 + A(n)./(1+1i.*B2.*Z1) ...
            .*exp(-(-h)*B2.*X1.^2./(1+1i.*B2.*Z1));
        qn = qn + A(n)./(1+1i.*B3.*Z1) ...
            .*exp(-(l+m+h)*B3.*X1.^2./(1+1i.*B3.*Z1));
    end
    [q2f1] = Second_Order_MGB(X1,Z1,k1,k1,k0,A,B,'harmonic');
    [qdiff] = Second_Order_MGB(X1,Z1,k1,k2,k0,A,B,'diff');

    signal = 1/2*q2f1.*conj(qf2) + (qf1).*conj(qdiff);

case 'lower'
    l = -k1/k0;
    m = k2/k0;
    h = k2/k0;
    p0 = p_1*p_2^2;
    alpha_3 = alpha_x(2*f_2-f_1,29.92,70,50);

    for n = 1:length(A)
        B1 = B(n)/(-l);
        B2 = B(n)/m;
        B3 = B(n)/(l+m+h);
        qf1 = qf1 + A(n)./(1+1i.*B1.*Z1) ...

```

```

        .*exp(-(1)*B1.*X1.^2./(1+1i.*B1.*Z1));
    qf2 = qf2 + A(n)./(1+1i.*B2.*Z1) ...
        .*exp(-m*B2.*X1.^2./(1+1i.*B2.*Z1));
    qn = qn + A(n)./(1+1i.*B3.*Z1) ...
        .*exp(-(l+m+h)*B3.*X1.^2./(1+1i.*B3.*Z1));

end

[ q2f2 ] = Second_Order_MGB(X1,Z1,k2,k2,k0,A,B, 'harmonic');
[ qdiff ] = Second_Order_MGB(X1,Z1,k1,k2,k0,A,B, 'diff');

signal = 1/2*q2f2.*conj(qf1) + (qf2).*conj(qdiff);

otherwise
    err = MException('TypeChk:UnknownDef', ...
        '''Choice'' selection for the tertiary (third) field
        should be ''harmonic'', ''upper'', or ''lower''.'');
    throw(err)
end

dg1 = 1i*xi_n.^2./(sigma_p-sigma_k).^2*(l+m+h);
dg2 = 2i*xi_l./(sigma_p-sigma_k)*(l+m+h);
feg2 = 4/3*xi_l.*besselj(0,2*(l+m+h)*xi_n*xi_l ...
    ./(sigma_p-sigma_k)).*exp(1i*(l+m+h)*xi_l.^2 ...
    ./(sigma_p-sigma_k)).*signal;
feg1 = exp(1i*(l+m+h)*xi_n.^2./(sigma_p-sigma_k)).*feg2.*xi_step;
feg1(abs(dg2*xi_step) > 0.1) = feg1(abs(dg2*xi_step) > 0.1) ...
    .*sinh(xi_step/2.*dg2(abs(dg2*xi_step) > 0.1)) ...
    .*2./(xi_step.*dg2(abs(dg2*xi_step) > 0.1));
THIRD = feg1./(sigma_p-sigma_k).*sigma_step;
THIRD(abs(dg1.*sigma_step) > 0.1) = ...
    THIRD(abs(dg1.*sigma_step) > 0.1) ...
    .*sinh(sigma_step(abs(dg1.*sigma_step) > 0.1)) ...
    ./2.*dg1(abs(dg1.*sigma_step) > 0.1)) ...
    .*2./(sigma_step(abs(dg1.*sigma_step) > 0.1)) ...
    .*dg1(abs(dg1.*sigma_step) > 0.1));

THIRD(isnan(THIRD)) = 0;

```

```
THIRD = sum(sum(THIRD));  
lmh = l+m+h;
```

```

function [q_2] = Second_Order_MGB(X,Z,k1,k2,k0,A,B,choice)
% Second_Order_MGB.m is called by Acoustic_Field_Generator.m
% and MGB_Integrator_Generator.m and calculates the second order
% sound field using the MGB expansion technique.

% Selects the second order sound field based upon the input settings
switch choice
    case 'harmonic'
        l = k1/k0;
        m = k2/k0;
    case 'sum'
        l = k1/k0;
        m = k2/k0;
    case 'diff'
        l = k1/k0;
        m = -k2/k0;
    otherwise
        err = MException('TypeChk:UnknownDef', ...
            '''Choice'' selection should be ''harmonic'', ''sum'', or
            ''diff''.'');
        throw(err)
end

siz = size(X);

X1 = X(:);
Z1 = Z(:);
q_2 = zeros(size(X1));

for n = 1:length(A)
    An = A(n);
    Bmn = B(n)/m;
    for k = 1:length(A)
        Ak = A(k);
        Blk = B(k)/l;
        r1 = (l.*Bmn+m.*Blk) + 1i.*(l+m).*Z1.*Blk.*Bmn;
        r2 = (l.*Blk+m.*Bmn).*Z1 - 1i.*(l+m);
    end
end

```

```

if Blk == Bmn
    q2_temp = An.*Ak./(4.*(l+m).*Blk.*(1+1i.*Blk.*Z1)) ...
        .*exp(-(Blk.*(l+m).*X1.^2)./(1+1i.*Blk.*Z1)) ...
        .*log(1+1i.*Blk.*Z1);
    q2_temp(X1==0) = An.*Ak./(4.*(l+m).*Blk.*...
        (1+1i.*Blk.*Z1(X1==0))).*log(1+1i.*Blk.*Z1(X1==0));
else
    s1 = (l+m).^2.*Blk.*Bmn;
    s2 = -1i.*(l+m).*l.*m.*(Blk-Bmn).^2;
    e1 = (s2./(r1.*(r1.*Z1+r2)).*X1.^2);
    e2 = (s2./(r1.*r2).*X1.^2);
    exp_e1 = expint(e1);
    exp_e2 = expint(e2);
    e_int = exp_e1-exp_e2;
    e_int(abs(angle(e1)-angle(e2)) > pi) = ...
        e_int(abs(angle(e1)-angle(e2)) > pi)+2i ...
        *pi*sign(angle(e1(abs(angle(e1)-angle(e2)) > pi)));
    q2_temp = An.*Ak./(4.*r1).*exp(-s1./r1.*X1.^2).*(e_int);
    q2_temp(X1==0) = An.*Ak./(4.*r1(X1==0)) ...
        .*log(1+r1(X1==0)./r2(X1==0).*Z1(X1==0));
end
q2_temp(isnan(q2_temp)) = 0;

q_2 = q_2 + q2_temp;
end
end

q_2 = reshape(q_2,siz);

```

```

function [x_t, y_t, z_t] = par_array_cord(R_tran,d,alignment)
% par_array_cord.m is called by Acoustic_Field_Generator.m
% and determines the location of the transducers used to define
% the sound source. The script was originally written by Glenwood
% Garner and can be found in his dissertation "Design of Optimal
% Directional Parametric Acoustic Arrays in Air".

A = d*cos(pi/6); %Adjacent distance

% Recursive termination
if R_tran == 0
    x_t = 0;
    y_t = 0;
    z_t = 0;
else
    x_t = [];
    y_t = [];
    % Compute coordinates for one pie slice
    for array_ind = 1:6
        % Compute coordinates of each edge element
        for edge_ind = 1:R_tran
            y_edge = (edge_ind-1)*A;
            x_edge = (R_tran-((edge_ind-1)*0.5))*d;

            array_angle = atan(y_edge/x_edge)+(array_ind-1)*pi/3;
            array_dist = sqrt(y_edge^2+x_edge^2);

            x_t = [x_t array_dist*cos(array_angle)];
            y_t = [y_t array_dist*sin(array_angle)];
        end
    end
    % Recursively call par_array_cord for next smaller radius
    if strcmp(alignment,'horiz')
        [x_t_rec, y_t_rec] = par_array_cord(R_tran-1,d,alignment);
        x_t = [x_t x_t_rec]; %concatenate current and previous
        y_t = [y_t y_t_rec]; %concatenate current and previous
        z_t = zeros(1,length(y_t));
    end
end

```

```

elseif strcmp(alignment, 'vert')
    [y_t_rec, x_t_rec] = par_array_cord(R_tran-1,d,alignment);
    x_t_temp = x_t; %switch x and y coordinates
    x_t = [y_t y_t_rec]; %concatenate current and previous
    y_t = [x_t_temp x_t_rec]; %concatenate current and previous
    z_t = zeros(1,length(y_t));
else
    disp('Error: alignment not specified');
end
end

remove = [1 6 11 15 16 21 26 85 88 91];
if R_tran == 5
    x_t(remove) = [];
    y_t(remove) = [];
    z_t(remove) = [];
end

```

```

function [alpha_Np_per_m] = alpha_x(f,ps_inch,F,hr)
% alpha_x.m is called by Single_Piston_Function_Generator.m
% and MGB_Integrand_Generator.m and determines the attenuation
% of the sound signal as it propagates through the atmosphere.
% The signal attenuation is given by the ISO 9613-1 international
% standard.

ps = .0334224599*ps_inch; %convert inches Hg to atmospheres
ps0 = 1;                  %standard atmospheric pressure
C = (5/9)*(F-32);        %convert degrees F to degrees Celcius
F = f/ps;                %normalize frequency to pressure
T = C+273.15;            %convert temp. to absolute temp.
T0 = 293.15;             %standard absolute temp.
T01 = 273.16;            %absolute freezing temp. of water

% Saturation pressure
psat = ps0*(10^((-6.8346*((T01/T) ^ 1.261))+4.6151));
% Absolute humidity
h = hr*psat/ps;

% Oxygen thermoviscous loss
FrO = (1/ps0)*(24+(4.04e4*h*((0.02+h)/(0.391+h))));
% Nitrogen thermoviscous loss
FrN = (1/ps0)*(T0/T)^(1/2)*(9+280*h*exp(-4.17*((T0/T)^(1/3)-1)));

alpha_Np_per_m = (ps*(F.^2)./ps0).*(1.84e-11*(T/T0)^(1/2)...
    +(T/T0)^(-5/2)*(0.01278*exp(-2239.1/T)./(FrO+(F.^2./FrO))...
    +0.1068*exp(-3352/T)./(FrN+(F.^2./FrN))));

% You could also return attenuation in dB/m
alpha_dB_per_m = 8.686*alpha_Np_per_m;

```



```

%% Ten Term MGB Coefficient Set
% ten_coefficient.m is called by Acoustic_Field_Generator.m
% and Near_to_Far_Field_Transformation_Technique.m and loads the
% ten term MGB coefficient set given by Wen and Breazeale.

A = [11.428+0.95175i 0.06002-0.08013i -4.2743-8.5562i ...
      1.6576+2.7015i -5.0418+3.2488i 1.1227-0.68854i ...
      -1.0106-0.26955i -2.5974+3.2202i -0.14840-0.31193i ...
      -0.20850-0.23851i];

B = [4.0697+0.22726i 1.1531-20.933i 4.4608+5.1268i ...
      4.3521+14.997i 4.5443+10.003i 3.8478+20.078i 2.5280-10.310i ...
      3.3197-4.8008i 1.9002-15.820i 2.6340+25.009i];

```

C.2 Near-to-Far-Field Transformation Code

```
%% Near-to-Far-Field Transformation Technique
% Near_to_Far_Field_Transformation_Technique.m is the main script
% utilized to implement the near-to-far-field (NTFF) transformation
% technique. This program generates the far-field solutions for
% the NTFF transformation method as described in "A Near-to-Far-
% Field Transformation method for the determination of nonlinearly
% generated scattered acoustic fields" by Spencer J. Johnson.

clear all; close all; clc;

% This loads the MGB coefficients for use in the simulation
ten_coefficient

%% Transmitted Sound Field Specifications
% The user is to input the specifications for the sound fields of
% interest in this section. Provide the two primary sound fields
% with the sound pressure levels, the medium properties, the
% transducer and sound source specifications, the near-field sound
% field sampled, and the resulting far-field area for the
% sound fields of interest.

% Select the desired frequencies
% Note: f_1 must be greater than f_2
f_1 = 4000;
f_2 = 3000;

% Select the medium properties
rho = 1.21;           %medium density
c = 344.8;           %small signal sound speed
beta = 1.2;           %coefficient of nonlinearity

% Select the sound pressure level for each primary tone (in dB SPL)
p_1 = 140;
p_2 = 140;
```

```

% Select transducer specifications
% Note: Holosonic, Airmar, or LRAD
a_t = 0.0404;          %transducer radius
                        %Note: 0.0161, 0.022, or 0.0404)
trans_num = 7;         %number of transducers
                        %Note: 81, 19, or 7
d = 0.279;             %distance between transducer elements
                        %Note: 0.045, 0.066, or 0.279

% Specify measured near-field conditions
choice = 'sum';
r_nf = 0.34;
theta_max = 60;
theta_num = 200;
y_max = 1;
num_y = 75;

% Specify desired far-field conditions
theta_max_ff = 15;
theta_num_ff = 150;
r_f = 150;

%% DO NOT ALTER THE SCRIPT AFTER THIS POINT
% This section utilizes the input specifications to generate the
% output fields of interest.

% Primary sound pressure conversion from dB SPL
p_1 = sqrt(2)*20e-6*10^(p_1/20);
p_2 = sqrt(2)*20e-6*10^(p_2/20);
S = pi*a_t^2;          %transducer area

% Radian frequencies
omega_1 = 2*pi*f_1;
omega_2 = 2*pi*f_2;

% Wave numbers
k_1 = omega_1/c;

```

```

k_2 = omega_2/c;

% Field selection
switch choice
    case 'harmonic'
        k1 = k_1;
        k2 = k_1;
        k0 = (k1+k2)/2;
        l = k_1/k0;
        m = k_1/k0;
        p0 = p_1*p_1;
    case 'sum'
        k1 = k_1;
        k2 = k_2;
        k0 = (k1+k2)/2;
        l = k_1/k0;
        m = k_2/k0;
        p0 = p_1*p_2;
    case 'diff'
        k1 = k_1;
        k2 = k_2;
        k0 = (k1+k2)/2;
        l = k_1/k0;
        m = -k_2/k0;
        p0 = p_1*p_2;
end

z_0 = k0*a_t^2/2;
lambda = 2*pi/k0;
r_0 = S/(lambda/2);

% Defining transducer locations
switch trans_num
    case 1
        radius = 0;
    case 7
        radius = 1;
    case 19

```

```

        radius = 2;
case 37
        radius = 3;
case 61
        radius = 4;
case 81
        radius = 5;
otherwise
        disp('Select an appropriate number of transducers.')
        break
end
[x_t,y_t,z_t] = par_array_cord(radius,d,'vert');

%% Near-Field and Far-Field Mesh Specifications
% Generates the mesh grids for the near- and far-field simulations
% in order to perform the NTFF transformation.

% Select sound field area specifications
theta_nf = (linspace(-theta_max,theta_max,theta_num))*pi/180;
x = r_nf*sin(theta_nf);
z = r_nf*ones(size(theta_nf));
y = linspace(-y_max,y_max,num_y);
a = sqrt(x.^2+z.^2);
delta_a = theta_nf(2)-theta_nf(1);
y_length = max(y)-min(y);
y_num = length(y);
delta_y = y(2)-y(1);
theta_y = asin(y);
M = (max(theta_nf)-min(theta_nf))/delta_a + 1;

% Determines the weighting for the integral solution
[y_i,w_y] = lgwt(y_num,y(1)/a_t,y(end)/a_t);
y_i = fliplr(y_i');
w_y = w_y';
[x_i,w_x] = lgwt(theta_num,x(1)/a_t,x(end)/a_t);
x_i = fliplr(x_i');

```

```

w_x = w_x';

[X,Y] = ndgrid(x,y);
[Z,Y1] = ndgrid(z,y);
[THETA,Y2] = ndgrid(theta_nf*180/pi,y);
[X_i,Y_i] = ndgrid(x_i,y_i);
[W_x,W_y] = ndgrid(w_x,w_y);
W = W_x.*W_y;
rho_nf = sqrt(X.^2+Y.^2);
X1 = rho_nf/a_t;
Z1 = Z/z_0;

% Far-field mesh
theta_ff = (linspace(-theta_max_ff,theta_max_ff,...
    theta_num_ff))*pi/180;
x_ff = r_f*sin(theta_ff);
z_ff = r_f*ones(size(theta_ff));
y_ff = zeros(size(x_ff));
R = sqrt(x_ff.^2+y_ff.^2+z_ff.^2);
X1_ff = sqrt(x_ff.^2+y_ff.^2)/a_t;
Z1_ff = z_ff/z_0;

% On-axis mesh
z_on = logspace(-3,1,theta_num_ff);
x_on = zeros(size(z_on));
y_on = zeros(size(z_on));

% Loads the Near-Field Data
addpath('C:\NearFieldDataPathName')

load DataFileName.mat

q1_nf = data_1;
q2_nf = data_2;

```

```

%% Primary Sound Field Generation
% This section determines the far-field radiation pattern for the
% primary sound fields using the NTFF transformation.

q1_on = zeros(size(z_on));
q1_ff = zeros(size(x_ff));
p1_ntff = zeros(size(x_ff));

phi = zeros(length(theta_nf),length(theta_ff));
alpha_f1 = alpha_x(f_1,29.92,70,50);

% Far-Field Primary Sound Field using the MGB expansion
for t = 1:length(x_t)
    X1_ff = sqrt(((x_ff-x_t(t))/a_t).^2 + ((y_ff-y_t(t))/a_t).^2);
    Z1_ff = (z_ff-z_t(t))/z_0;
    for n = 1:length(A)
        B1 = B(n)/l;
        q1_ff = q1_ff + p_1*A(n)./(1+1i.*B1.*Z1_ff)...
            .*exp(-1*B1.*X1_ff.^2./(1+1i.*B1.*Z1_ff));
    end
end
q1_ff = q1_ff/max(q1_ff);
q1_ff_dB = 20*log10(abs(q1_ff));

% Primary NTFF Expansion Technique
for n = 1:length(x_ff)
    phi(:,n) = theta_ff(n) - theta_nf;
end

for n = 1:M
    p1_ntff = p1_ntff - a(n)*(1+cos(phi(n,:)))...
        .*exp(-1i*k_1*a(n)*cos(phi(n,:))).*abs(q1_nf(n));
end
C = -1i*k_1*delta_a/(4*pi)*exp(-1i*k_1*R)./(R)*y_length/y_num;
p1_ntff = C.*p1_ntff;
p1_ntff = p1_ntff/max(p1_ntff);
p1_ntff_dB = 20*log10(abs(p1_ntff));

```

```

% Primary Sound Field Plots
figure(1)
halfPolar(theta_nf+pi/2,p1_nf_dB);
figure(1)
subplot(2,1,1)
semilogx(z_on,p1_on_dB)
hold on
vline(r_nf,'b')
hold on
vline(r_0,'r')
subplot(2,1,2)
semilogx(z_on,q2_on_dB)
hold on
vline(r_nf,'b')
hold on
vline(r_0,'r')

figure(2)
surf(THETA,Y,q1_nf_dB,'Edgecolor','none')
xlabel('Radial Distance (m)')
ylabel('Elevation (m)')
view(0,90)
axis([min(min(THETA)) max(max(THETA)) min(min(Y)) max(max(Y))])
h = colorbar;
ylabel(h,'Pressure (dB SPL)')
zlabel('Near-Field Surface Pressure')
title('Primary Near-Field')

figure(3)
plot(x_ff,q1_ff_dB,'r',x_ff,p1_ntff_dB,'b')
set(gca,'XTick',[-50,-40,-30,-20,-10,0,10,20,30,40,50])
xlabel('Radial Distance (m)')
ylabel('Normalized Pressure (dB SPL)')
legend('Direct','NTFF')
xlim([-50 50])
title('Far-Field Comparison — Primary Sound Field')

```



```

%% Secondary Sound Field Generation
% This section determines the far-field radiation pattern for the
% secondary sound fields using the NTFF transformation.

p2_ntff = zeros(size(x_ff));
p2_other = zeros(size(x_ff));
q2_harm_ff = zeros(size(x_ff));

% Far-Field Secondary Sound Field using the MGB expansion
for t = 1:length(x_t)
    X1_ff = sqrt(((x_ff-x_t(t))/a_t).^2 + ((y_ff-y_t(t))/a_t).^2);
    Z1_ff = (z_ff-z_t(t))/z_0;
    temp = Second_Order_MGB(X1_ff,Z1_ff,k1,k2,k0,A,B,choice);
    q2_harm_ff = q2_harm_ff + temp;
end
q2_harm_ff = -p0*beta*(1+m)^2*(k0*a_t)^2/(rho*c^2)*q2_harm_ff;
q2_harm_ff = q2_harm_ff/max(q2_harm_ff);
q2_harm_ff_dB = 20*log10(abs(q2_harm_ff));

% Second Order Solution
cos_B = zeros(size(rho_nf));
sin_B = zeros(size(rho_nf));
for p = 1:length(p2_ntff)
    z_p = z_ff(p);
    r_prime = sqrt(((x_ff(p) - X)/a_t).^2+(Y/a_t).^2);
    z_prime = (z_p - Z)/z_0;
    for n = 1:length(y)
        cos_B(:,n) = cos(theta_ff(p) - theta_nf).*cos(theta_y(n));
        sin_B(:,n) = sin(theta_ff(p) - theta_nf).*sin(theta_y(n));
    end
    p2_ntff(p) = Second_Order_NTFF(r_prime,z_prime,abs(q2_nf),...
        cos_B,sin_B,W,k1,k2,k0,A,B,choice);
end
C = 1/(4*pi)*delta_a*y_max/a_t;
p2_ntff = p2_ntff.*C;
p2_ntff = p2_ntff/max(p2_ntff);
p2_ntff_dB = 20*log10(abs(p2_ntff));

```

```

% Secondary Sound Field Plots
figure(4)
surf(X,Y,q2_nf,'Edgecolor','none')
xlabel('Radial Distance (m)')
ylabel('Elevation (m)')
view(0,90)
axis([min(min(X)) max(max(X)) min(min(Y)) max(max(Y))])
grid off;
h = colorbar;
ylabel(h,'Pressure (dB SPL)')
zlabel('Near-Field Surface Pressure')
title('Secondary Near-Field')

figure(5)
plot(x_ff,q2_harm_ff_dB,'r',x_ff,p2_ntff_dB,'b')
xlabel('Radial Distance (m)')
ylabel('Normalized Pressure (dB SPL)')
legend('Direct','NTFF')
xlim([-15 15])
ylim([-40 0])
title('Far-Field Comparison — Secondary Sound Field')

```

```

function [q_2_NTFF] = Second_Order_NTFF(X,Z,p_Q,cos_B,sin_B,...
    W,k1,k2,k0,A,B,choice)
% Second_Order_NTFF.m is called by
% Near_to_Far_Field_Transformation_Technique.m and calculates the
% far-field radiation patterns of the second order sound field
% using the NTFF transformation and MGB expansion techniques.

% Selects the second order sound field based upon the input settings
switch choice
    case 'harmonic'
        l = k1/k0;
        m = k2/k0;
    case 'sum'
        l = k1/k0;
        m = k2/k0;
    case 'diff'
        l = k1/k0;
        m = -k2/k0;
    otherwise
        err = MException('TypeChk:UnknownDef', ...
            ''Choice'' selection should be ''harmonic'', ''sum'', or
            ''diff''.');
        throw(err)
end

siz = size(X);

X1 = X(:);
Z1 = Z(:);
pQ = p_Q(:);
cosB = cos_B(:);
sinB = sin_B(:);
W1 = W(:);
q_2_NTFF = zeros(size(X1));

for n = 1:length(A)
    An = A(n);

```

```

Bmn = B(n)/m;
for k = 1:length(A)
    Ak = A(k);
    Blk = B(k)/l;
    r1 = (1.*Bmn+m.*Blk) + 1i.*(l+m).*Z1.*Blk.*Bmn;
    r2 = (1.*Blk+m.*Bmn).*Z1 - 1i.*(l+m);
    s1 = (l+m).^2.*Blk.*Bmn;
    if Blk == Bmn
        q2_temp = An.*Ak./(4.*(l+m).*Blk.*(1+1i.*Blk.*Z1)) ...
            .*exp(-(Blk.*(l+m).*X1.^2)./(1+1i.*Blk.*Z1)) ...
            .*log(1+1i.*Blk.*Z1);
        q2_temp(X1==0) = An.*Ak./(4.*(l+m).*Blk.*...
            (1+1i.*Blk.*Z1(X1==0))).*log(1+1i.*Blk.*Z1(X1==0));
        x_norm = 0;
    else
        s2 = -1i.*(l+m).*l.*m.*(Blk-Bmn).^2;
        e1 = (s2./(r1.*(r1.*Z1+r2)).*X1.^2);
        e2 = (s2./(r1.*r2).*X1.^2);
        exp_e1 = expint(e1);
        exp_e2 = expint(e2);
        e_int = exp_e1-exp_e2;
        e_int(abs(angle(e1)-angle(e2)) > pi) = ...
            e_int(abs(angle(e1)-angle(e2)) > pi)+2i ...
            *pi*sign(angle(e1(abs(angle(e1)-angle(e2)) > pi)));
        q2_temp = An.*Ak./(4.*r1).*exp(-s1./r1.*X1.^2).*(e_int);
        q2_temp(X1==0) = An.*Ak./(4.*r1(X1==0)) ...
            .*log(1+r1(X1==0)./r2(X1==0).*Z1(X1==0));

        x_norm = -2./(r1.*X1).*exp(-s1./r1.*X1.^2) ...
            .* (exp(e1)-exp(e2));
        x_norm(X1==0) = 0;
    end
    q2_temp(isnan(q2_temp)) = 0;

    q2_temp = W1.*(q2_temp.*(-1i.*(l+m).*(Blk.*Bmn...
        ./r1.*cosB+k0)-2.*s1./r1.*sinB) + x_norm.*sinB).*pQ;
    q2_NTFF = q2_NTFF + q2_temp;

```

```
        end
    end

q_2_NTFF = sum(sum(reshape(q_2_NTFF,siz)));
```

C.3 Acousto-Electromagnetic Interaction Code

```
%% Acousto-Electromagnetic Interaction
% Acousto_EM_Interaction.m is the main script in determining the
% modulation of an electromagnetic (EM) wave by an acoustic field.
% This program generates the solutions for the comparison data for
% the different modulation processes as described in "Near-Field
% Radio Frequency Scattering from Acoustically-Excited Vibrating
% Structures" by Spencer J. Johnson.

clear all; close all; clc;

addpath('C:\DataPathName')

%% Comparison of Power Levels of Modulation Tones
% Select the RF signal properties
f_rf = 915e6;
c_rf = 3e8;
lambda_rf = c_rf/f_rf;
omega_rf = 2*pi*f_rf;
k_rf = omega_rf/c_rf;

% Select the acoustic signal properties
f_a = 2e3;
c_a = 343;
lambda_a = c_a/f_a;
omega_a = 2*pi*f_a;
k_a = omega_a/c_a;

% Select the medium properties
rho = 1.21;
e_r = 1.00058986;

% Select the sound pressure level (in dB SPL)
p0_dBSPL = 150;

R0 = 3*lambda_rf;
```

```

d_v = 3/100*lambda_rf;
p0 = sqrt(2)*20e-6*10^(p0_dBSPL/20);

n = 1:1:8;
dopp = zeros(size(n));
spec = zeros(size(n));
path = zeros(size(n));
acoust = zeros(size(n));

% Transmitted RF signal power level (in W)
p = 1;

% Determines the contribution of the different modulation types
% for the first n tones.
for m = 1:length(n)
    dopp(m) = p*besselj(m,2*k_rf*d_v);
    spec(m) = 4*(d_v*omega_a/(2*c_rf))^m;
    path(m) = 2*(m+1)*((d_v/R0)/2)^m;
    acoust(m) = p0*(k_rf/(m*k_a))^2*(e_r-1)*(e_r+2)...
        /(3*rho*c_a^2*(1-4*(k_rf/(m*k_a))^2*e_r));
end
carrier_dB = 20*log10(abs(p));
dopp_dB = 20*log10(abs(dopp));
spec_dB = 20*log10(abs(spec));
path_dB = 20*log10(abs(path));
acoust_dB = 20*log10(abs(acoust));
combo_dB = 20*log10(abs(acoust)+abs(dopp)+abs(path)+abs(spec));

% Determines the doppler spectrum per um of surface displacement
disp_v = linspace(.01,2,100)*10^-6;
dopp_dv = besselj(1,2*k_rf*disp_v);
dopp_dv_dB = 20*log10(abs(dopp_dv));

% Plots the doppler spectrum and modulation tones
figure(1)
plot(disp_v*10^6,dopp_dv_dB)
xlabel('Displacement (\mm)')

```

```

ylabel('Power Spectrum (dBm)')

figure(2)
plot(n,dopp_dB,'s-',n,spec_dB,'^-',n,path_dB,'o-',n,acoust_dB,'v-')
axis([min(n) max(n) -250 0])
xlabel('Tone Number, \it{n}')
ylabel('Normalized Modulation Tone Amplitude (dBc)')
legend('PM (Doppler)', 'AM (Spec. Rel.)', 'AM (Path Loss)', ...
       'AM (Acoustic)')

%% Combined modulation effects on the RF carrier
% This plots the measured modulation data and compares it with the
% expected calculated results.

% Reads the measured modulation data in from an Excel worksheet and
% and selects the frequencies from the appropriate worksheet cell.
worksheet = 'DataFileName.xlsx';
start_freq = 'A8:A8';
step_freq = 'B8:B8';
carr_freq = 'A2:A2';
span_freq = 'C4:C4';

Radar_data = xlsread(worksheet, 'A:A');
Radar_data(1:8) = [];

freq_start = xlsread(worksheet, start_freq);
freq_step = xlsread(worksheet, step_freq);
freq_carr = xlsread(worksheet, carr_freq);
freq_span = xlsread(worksheet, span_freq);

freq_length = length(Radar_data);
freq_end = -freq_span/2 + (freq_length-1)*freq_step;
freq_data = -freq_span/2:freq_step:freq_end;

% Determines the sampling rate
Fs = freq_span;

```



```

samp_time = 1/Fs;
samp_num = 1e6;
time = 0:samp_time:samp_time*(samp_num-1);

% Combined modulation effects
omega_rf = 0; %carrier offset
combine = abs(p*besselj(1,2*k_rf*d_v))...
    .*(cos(omega_rf*time+omega_a*time+pi/2))...
    +cos(omega_rf*time-omega_a*time-pi/2))...
    +abs(2*(1+1)*((d_v/R0)/2))+abs(p0*(k_rf/(k_a))^2...
    *(e_r-1)*(e_r+2)/(3*rho*c_a^2*(1-4*(k_rf/(k_a))^2*e_r)))...
    .*(cos(omega_rf*time+omega_a*time))...
    +cos(omega_rf*time-omega_a*time))+abs(p)*cos(omega_rf*time);

% Performs the FFT of the modulation signal to generate the
% frequency domain plot.
freq_length = pow2(nextpow2(samp_num));
freq_step = freq_span/freq_length;
freq_end = -freq_span/2 + (freq_length-1)*freq_step;
freq = -freq_span/2:freq_step:freq_end;
combine2 = [combine.*hamming(length(combine)).',...
    zeros(1,freq_length-length(combine))];
combined = 2/length(combine2)*fft(combine2,freq_length);
combined2 = combined(1:length(combined)/2+1);
combined = combined(length(combined)/2+2:end);
combined = horzcat(combined,combined2);
combined = 20*log10(abs(combined));

[peak,loc] = findpeaks(combined,'MinPeakHeight',-120,...
    'MinPeakDistance',10e3);
peak(2) = [];
loc(2) = [];

% Plot of the modulation effects and the RF carrier
figure(3)
set(gcf,'DefaultAxesColorOrder',[0 0.5 0 ; 0 0 0 ; 0 0.5 0]);
h = plot(freq/1e3,combined,freq_data/1e3,Radar_data,'b',...

```

```

        freq(loc)/1e3,peak,'*');
xlabel('Frequency Offset (kHz)')
ylabel('Power (dBm)')
legend_name = {'Predicted','Measured'};
order = [2 1];
legend(h(order),legend_name{order})
title(sprintf('Acoustically-Induced Modulation onto RF Carrier, F-{\n
    RF} = %d MHz',freq_carr/1e6));
axis([-3 3 -140 -40])

```

```

%% Reading the Frequency Spectrum Radar Data from Excel Spreadsheet
% Radar-Frequency-Domain-Excel-Read.m is called by
% Acousto-EM-Interaction.m and loads and plots the frequency
% spectrum data from the high dynamic range nonlinear measurement
% system.

```

```

clear all; close all; clc;

```

```

addpath('C:\DataPathName')

```

```

worksheet = 'DataFileName.xlsx';
start_freq = 'A8:A8';
step_freq = 'B8:B8';
carr_freq = 'A2:A2';
span_freq = 'C4:C4';

```

```

Radar_data = xlsread(worksheet, 'A:A');
Radar_data(1:8) = [];

```

```

freq_start = xlsread(worksheet, start_freq);
freq_step = xlsread(worksheet, step_freq);
freq_carr = xlsread(worksheet, carr_freq);
freq_span = xlsread(worksheet, span_freq);

```

```

freq_length = length(Radar_data);
freq_end = -freq_span/2 + (freq_length-1)*freq_step;
freq = -freq_span/2:freq_step:freq_end;

```

```

figure(1)
set(gca, 'FontSize', 16)
plot(freq/1e3, Radar_data)
xlabel('Frequency (kHz)')
ylabel('Power (dBm)')
title(sprintf('Acoustically-Induced Modulation onto RF Carrier, F-{'
    RF} = %d MHz', freq_carr/1e6));
axis([-3 3 -140 -40])

```

```

%% Reading the Time Domain Radar Data from Excel Spreadsheet
% Radar_Time_Domain_Excel_Read.m is called by
% Acousto_EM_Interaction.m and loads and plots the transient data
% from the high dynamic range nonlinear measurement system.

clear all; close all; clc;

addpath('C:\DataPathName')

worksheet = 'DataFileName.xlsx';

carr_freq = xlsread(worksheet, 'A2:A2');
mod_freq = xlsread(worksheet, 'B2:B2');

data = xlsread(worksheet, 'A:A');
data(1:5) = [];

dt = xlsread(worksheet, 'A4:A4');
time = 0:dt:dt*(length(data)-1);

myTitleBottom = sprintf('F_{RF} = %d MHz and F_{AC} = %0.3f kHz', ...
    carr_freq/1e6, mod_freq/1e3);

h = figure(1);
plot(time, data)
xlabel('Time (sec)')
ylabel('Power (dBm)')
mtitle('Acoustically-Induced Modulation onto RF Carrier', ...
    myTitleBottom);
p = get(h, 'pos');
set(h, 'pos', [p(1) p(2) - .075 p(3:4)]);
axis([min(time) max(time) -68 -58])

```